Flexure Pivot Oscillators for Mechanical Watches

Etienne Frédéric Gabriel THALMANN

■ École
polytechnique
fédérale
de Lausanne

2020

Contents

Contents

Contents

Acknowledgements

I would like to thank my thesis directors, Simon Henein and Ilan Vardi, for the opportunity to work on this exciting research topic. I am grateful for their guidance, support, flexibility, constructive criticism and their overall contribution to my thesis.

I wish to show my appreciation to my partner Ramya, whose love, encouragement and expectations have been an important driving force for this work.

I wish to express my deepest gratitude to all the members of my research team at Instant-lab who were always kind and ready to put their sharp skills to help, in particular:

- Mohammad Kahrobaiyan whose insight and creativity gave birth to some of the most promising architectures presented in this thesis.
- Billy Nussbaumer for his technical expertise and invaluable contributions to the design of the experimental setup.
- Arnaud Maurel for his precious computer-aided design skills and being always available and motivated to help in the experiments.
- Romain Gillet for his dexterity and experience in watchmaking without whom manipulating my prototypes would have been extremely complicated.
- Emmanuelle Brusq and Julia Bierent whose summer internships contributed to the research on the RDCO oscillator.
- Simón Prêcheur Llarena for the beautiful and instructive laser-cut mockups of the new flexure pivot architectures.
- Hubert Schneegans and Thomas Füssinger for their help in the acquisition of experimental signals.
- Roland Bitterli for his help with finite element software.

I wish to extend my special thanks to the industrial partners following this research for their interest, resources and insightful comments, for teaching me some of their methods and for providing a practical context to this work.

My sincere thanks to the members of my thesis jury, Yves Bellouard, Jürgen Brugger, Michel Despont and Fabienne Marquis Weible, for generously offering their time and for their constructive and insightful comments.

I would like to also acknowledge Pere Llosas, Toralf Scharf and Pierre Thomann for their expertise and tips regarding the experimental phase of this research.

Finally, I would like to thank my parents, Muriel and Philippe, for sparking my scientific curiosity and imparting some of the values that make a good researcher. I am grateful for the love and encouragement of my entire family.

Neuchâtel, June 3, 2020   E. T.

Abstract

It appears that the concerted efforts of the watchmaking industry are leading towards a limit in mechanical watch accuracy. The general consensus in horology is that the time base's quality factor, a dimensionless number that characterizes the oscillator damping, needs to be improved in order to significantly increase timekeeper accuracy. The three classical mechanical time bases all suffer from limitations for mechanical watch applications. The pendulum used in precision mechanical clocks reaches quality factors of order 100 000 but is too sensitive to the orientation of gravity to be used in portable timekeepers (watches). The balance and hairspring oscillator used in classical mechanical watches sees its quality factor limited to about 300 (450 in partial vacuum) by the friction in its bearings. The tuning fork used in electronic watches can reach quality factors of order 100 000 but its high frequency and very small oscillation amplitude makes it very challenging to sustain mechanically. The solution appears to be flexure-pivot oscillators in silicon. Flexure-pivot oscillators use the elastic deformation of thin beams to guide the rotational motion of an inertial body and to exert a force opposed to its displacement, thus providing all the elements for a one degree-of-freedom mechanical oscillator. The use of flexures instead of bearings eliminates contact friction and monocrystalline silicon minimizes internal friction, leading to significant improvements in quality factor in comparison to balance and hairspring oscillators. Moreover, the rotational amplitude is compatible with existing sustaining mechanisms (escapements).

Accurate timekeeping requires the period of oscillation of the time base to stay as regular as possible regardless of changes in operating conditions such as amplitude of oscillation, orientation with respect to gravity, temperature and shocks. This thesis focuses on minimizing the effects of amplitude and gravity that arise from the use of flexures. First, the nonlinear elastic behavior of flexures introduces a dependence of oscillation period on amplitude called isochronism defect. Second, the weight-bearing function of the flexures and their deviation from the motion of ideal linkages result in a contribution of gravity to their effective stiffness and hence an effect on their period. It is assumed that the other effects, i.e., temperature and shocks, can be solved with existing techniques.

The first technical contribution of this thesis is to note that the isochronism defect is a second order phenomenon, and to deal with it by modifying the second order behavior of flexure spring stiffness or inertia. The second technical contribution is a design method to reduce the effect of gravity for all orientations of the time base to within the specifications of current mechanical watches, this by ingeniously placing the flexures and exploiting the position of the center of mass.

These findings are embodied in three new flexure pivot architectures called Gravity Insensitive

Abstract

Flexure Pivot, co-RCC flexure pivot oscillator and Rotation-Dilation Coupled Oscillator. A silicon co-RCC prototype satisfying typical mechanical watch specifications is manufactured. The technical contributions of the thesis are validated by finite element simulations and experimentally. This thesis only deals with time bases and a new method has been developed to measure their chronometric performance without a sustaining mechanism (escapement).

Keywords: Flexure Pivot Oscillators – Compliant Mechanisms – Mechanical Oscillators – Isochronism – Gravity Sensitivity – Horology – Mechanical Watches

Résumé

Les efforts concertés de l'industrie horlogère semblent indiquer que l'on se rapproche d'une limite de la précision des montres mécaniques. Le consensus général en horlogerie est qu'il est essentiel d'améliorer le facteur de qualité des bases de temps, un nombre adimensionnel qui caractérise leur amortissement, pour améliorer de manière significative la précision des garde-temps. Pour une application en montre mécanique, les trois bases de temps classiques se heurtent à des limites. Le pendule utilisé dans les horloges mécaniques de précision atteint des facteurs de qualité de l'ordre de 100 000 mais est trop sensible à l'orientation de la gravité pour être utilisé dans un garde-temps portable tel qu'une montre. Le balancier-spiral utilisé dans les montres mécaniques classiques voit son facteur de qualité limité par le frottement dans son pivot à environ 300 (450 sous vide partiel). Le diapason utilisé dans les montres électroniques atteint des facteurs de qualité de l'ordre de 100 000 mais présente des difficultés à être implémenté mécaniquement dû à sa haute fréquence et faible amplitude d'oscillation. La solution semble être les oscillateurs à pivot flexible en silicium. Ces oscillateurs se basent sur la déformation de fines lames élastiques pour guider le mouvement de rotation d'un corps inertiel et exercer une force de rappel opposée au déplacement, formant ainsi un oscillateur rotatif à un degré de liberté. L'utilisation de guidages flexibles au lieu de pivots rigides élimine tout frottement entre surfaces et le silicium monocristallin minimise le frottement interne au matériau, contribuant ainsi à une amélioration significative du facteur de qualité par rapport au balancier-spiral. De plus, le mouvement rotatif de ces oscillateurs est compatible avec les mécanismes d'entretien existants (échappements).

Un chronométrage précis nécessite une base de temps dont la période d'oscillation est aussi régulière que possible, indépendamment des conditions d'opération tels que son amplitude, son orientation par rapport à la gravité, la température ou les chocs. Cette thèse a pour objectif de minimiser les effets de l'amplitude et de la gravité sur la période d'oscillation causés par l'utilisation de guidages flexibles. Premièrement, le comportement élastique non linéaire des guidages flexibles crée une dépendance entre période d'oscillation et amplitude appelée défaut d'isochronisme. Deuxièmement, le fait que les guidages flexibles supportent le poids de l'oscillateur et que leur mouvement ne correspond pas parfaitement à celui de guidages idéaux donne lieu à une contribution de la gravité à la rigidité effective de l'oscillateur et donc un effet sur sa période. On suppose que les autres effets, tels que la température et les chocs peuvent être annulés au moyen de techniques existantes.

La première contribution technique de cette thèse est de remarquer que le défaut d'isochronisme est un phénomène de deuxième ordre et de le contrôler en modifiant les termes de deuxième ordre de la rigidité et de l'inertie des oscillateurs. La deuxième contribution technique est une méthode de conception permettant de restreindre aux caractéristiques

Résumé

des montres mécaniques actuelles l'influence de la gravité sur la période de l'oscillateur, en plaçant ingénieusement les éléments flexibles et en exploitant la position du centre de masse.

Ces résultats sont matérialisés sous la forme de trois nouvelles architectures d'oscillateurs à pivot flexible appelés *Gravity Insensitive Flexure Pivot oscillator*, oscillateur à pivot flexible co-RCC et *Rotation-Dilation Coupled Oscillator*. Un prototype satisfaisant un cahier des charges horloger typique est fabriqué en silicium. Les contributions techniques de la thèse sont validées par simulation numérique (éléments finis) et expérimentalement. Cette thèse ne traite que des bases de temps et une nouvelle méthode a été développée pour mesurer leur performance chronométrique sans mécanisme d'entretien (échappement).

Mots clés : Oscillateurs à pivot flexible – Guidages flexibles – Oscillateurs mécaniques – Isochronisme – Sensibilité à la gravité – Horlogerie – Montres mécaniques

List of Figures

List of Tables

List of Acronyms

CFP   **C**rossed **F**lexure **P**ivot

COM   **C**enter **o**f **M**ass

DOF   **D**egree **o**f **F**reedom

DRIE   **D**eep **R**eactive **I**on **E**tching

FEM   **F**inite **E**lements **M**ethod

GIFP   **G**ravity-**I**nsensitive **F**lexure **P**ivot

MEMS **M**icro**e**lectro**m**echanical **S**ystems

RCC   **R**emote **C**enter **C**ompliance (flexure pivot)

RDCO   **R**otation-**D**ilation **C**oupled **O**scillator

SEM   **S**canning **E**lectron **M**icroscope

1 Introduction

1.1 Goal of the thesis

The goal of this thesis is to invent new flexure pivot oscillators in silicon in order to break through the apparent limit of mechanical watch accuracy, about 1 s/day accuracy, by increasing oscillator quality factor while overcoming two of the principal challenges of portable timekeepers: isochronism defect and influence of the orientation of gravity.

Remark 1.1.1. We express the accuracy of a timekeeper by its *daily rate*, that is, the gain or loss of the timekeeper in seconds per day (s/day) with respect to a reference frequency, see Eq. (5.7).

1.2 Motivation of the thesis

First, this work is motivated by the potential improvement in the accuracy of mechanical watches made possible by recent advances in materials and techniques. Nowadays, the accuracy of the best mechanical watches does not exceed a few seconds per day despite concerted efforts by the watchmaking industry.[1] The general consensus in horology is that the quality factor of the time base, a dimensionless number that characterizes the damping of an oscillator, needs to be improved for the accuracy of the watch to increase, see Sec. 1.4.1. Yet, the friction in the currently used time base, the balance and hairspring,[2] limits its quality

---

[1]Different norms exist to certify the accuracy of mechanical watches. The Official Swiss Chronometer Testing Institute (COSC) issues the "Chronometer" certificate to mechanical movements that comply with the ISO 3159 norm, with an average daily rate between -4 and +6 s/day in various positions and at different temperatures (full requirements: www.cosc.swiss/en/certification/mechanical-movements). A similar certification is issued by The Besançon Observatory and the Glashütte Observatory (DIN 8319) with the main difference that the movement must be assembled in its case. The Swiss Federal Institute of Metrology (METAS) delivers the "Master Chronometer" certificate to mechanical watches having an average daily rate between 0 and +5 s/day in various positions, at different temperatures and exposed to magnetic fields (full requirements: www.metas.ch/dam/data/metas/ Dokumentation/rechtliches/zertifizierung-uhren/metas-n001-v-1-1-e.pdf). Note that some watch manufactures also define their own certification.

[2]We use this term for the mechanical oscillator also known as "sprung balance" consisting of a spiral spring (the hairspring) attached to a balance wheel rotating on a pivot and called "balancier-spiral" in French.

factor, see Sec. 1.3.2. The other existing mechanical time bases, the pendulum and the tuning fork also suffer from limitations in the mechanical watch application, hence the search for new time bases, see Sec. 1.3. The recent adoption of silicon by the very traditional watch industry (Noell et al., 2004) and the progress made in the Deep Reactive Ion Etching (DRIE) manufacturing technique make it now possible to manufacture watch-scale flexure-based time bases in silicon. The absence of contact friction of flexure-based mechanisms and the minimal internal friction of monocrystalline silicon pave the way to a significant increase in quality factor that could lead to a new level in mechanical watch accuracy.

Second, this work seeks to establish a scientific framework, give context and provide tools to the understanding of flexure-based oscillators which have, until now, mostly been developed in an industrial context and often not in the public domain. The recent interest of the watch-making industry for flexure-based oscillators has led to a number of prototypes and patents covering new architectures, see Chapter 2, but they have not been documented scientifically and their key issues have not been discussed.

Finally, the exploration of flexure-based time bases brings other valuable contributions than the potential improvement in mechanical watch accuracy. For example, in the field of mechanical watchmaking, the solution avenues proposed in Sec. 1.4 could suppress the need for lubrication, a traditional concern with the balance and hairspring,[3] decrease power consumption (Barrot et al., 2014), and simplify assembly through monolithic fabrication. The new experimental method needed to characterize our time bases is also an important contribution as it frees the evaluation of the time base from its energy source and facilitates early experimental characterization of prototypes. The findings of this work could also benefit other sectors where flexure pivots are used such as aerospace engineering (Henein et al., 2003) and precision robotics (Cosandier et al., 2017).

1.3 The three classical mechanical time bases

In order to give historical and scientific context to the new time bases presented in this work, it is important to mention the existing mechanical time bases. There are three classical mechanical time bases: the pendulum, the balance and hairspring, and the tuning fork, by chronological order of invention. They all suffer from a limitation in the mechanical watch application, justifying the search for new time bases.

1.3.1 The pendulum

The pendulum was first considered as an accurate time base by Galileo around 1600 due to its apparent *isochronism*, the property of independence of oscillation period from amplitude

---

[3] Watchmaking lore attributes a famous but most likely apocryphal quote to Abraham-Louis Breguet (1747-1823), one of the greatest watchmakers in history. When King Louis XVI asked him to make the perfect watch, he replied: "Give me the perfect oil and I will make you a perfect watch."

essential to accurate timekeeping, see Sec. 1.5.1.[4] In 1641, Galileo designed the first known idea of a pendulum clock, see Fig. 1.1, but neither he nor his son Vincenzio lived to finish it (Drake, 1995; Defossez, 1946). Christiaan Huygens invented the first working pendulum clock in 1657 and in the 1660s pendulum clocks reached an accuracy of order 15 seconds/day, which was a significant improvement from the 15 minutes/day of the typical clocks of the time (Bennett et al., 2002). By 1921, with the invention of the Shortt free pendulum, pendulum clocks reached an impressive accuracy of order 1 s/year (Matthys, 2004). This clock, which uses an electromechanical sustaining mechanism, was used as standard clock in observatories for over 20 years. For purely mechanical clocks, one of the highest level of accuracy was reached by *Clock B*, built following John Harrison's 18th century design, which reached an accuracy of about 1 second per 100 days (McKie, 2015). The pendulum can however not be used in a mechanical watch since its restoring force depends on gravity and any change in the orientation or magnitude of the gravity force affects its period of oscillation.[5]
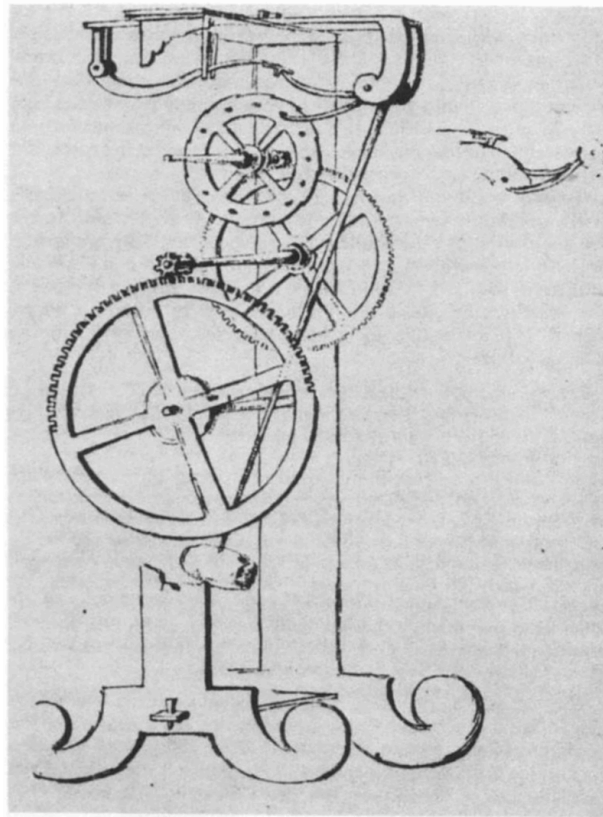
Figure 1.1 – Galileo's 1641 design for a pendulum clock, drawn by Vincenzo Viviani in 1659.

---

[4]Galileo was mistaken in his observation as the pendulum is only approximately isochronous for small amplitudes, see Sec. 1.5.1.

[5]For example, Christiaan Huygens' attempt to make a marine pendulum clock in 1662 to determine the longitude at sea was abandoned as it suffered from the ship's motion and the variation of Earth gravity with latitude (Leopold, 1996).

1.3.2 The balance and hairspring

The balance and hairspring oscillator was invented by Christiaan Huygens in 1675 while seeking an isochronous time base whose period of oscillation does not depend on gravity.[6] It consists of a spiral spring, called hairspring or balance-spring (Berner, 2002), attached to a balance wheel rotating on a rigid pivot, see Fig. 1.2. The hairspring closely follows Hooke's law, i.e., its restoring force is proportional to displacement, which is the necessary condition for isochronism for a mechanical oscillator with constant inertia. The chronometric precision of this oscillator was validated by John Harrison with his 1759 marine chronometer H4 (Gould, 2013), and is still used today in virtually all mechanical watches. As mentioned in Sec. 1.2, the friction in the pivot of this time base limits improvements in mechanical watch accuracy, see Sec. 1.4.1.
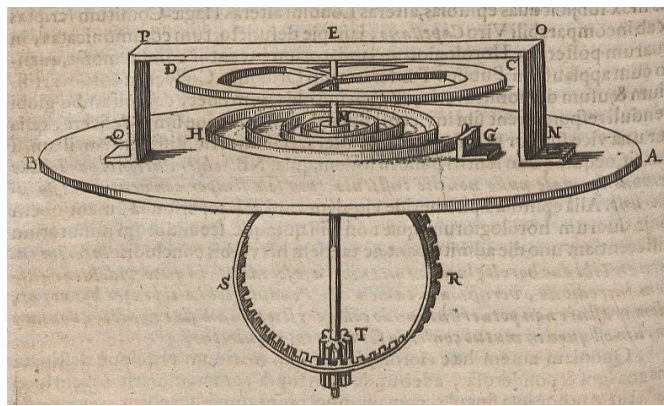
Figure 1.2 – balance and hairspring oscillator drawn by Huygens in (Académie des inscriptions et belles-lettres, 1675).

1.3.3 The tuning fork

The tuning fork was invented by John Shore, trumpeter and lutenist to H. Purcell and G.F. Händel, in 1711 (Feldmann, 2008). Lissajous was the first to sustain its oscillation electrically in 1857 and Breguet (1866) and Niaudet-Breguet (1866) were the first to sustain its oscillation mechanically. Figure 1.3 shows a mechanical tuning fork clock realized by Louis-Clément Breguet in 1867 with a 100 Hz time base. Note that the accuracy of tuning fork clocks was lower than that of the precision pendulum clocks of the same period (Jaspers, 1986). A breakthrough happened in 1960, when Bulova commercialized the Accutron wristwatch invented by Max

---

[6] There is controversy surrounding the inventor of the balance and hairspring (Vardi and Henein, 2019). Christiaan Huygens announced his invention on January 30, 1675, in a letter to Henry Oldenburg, secretary of the Royal Society (Huygens, 1897, Correspondence N⁰ 2003), but Robert Hooke claimed that he had already invented the balance and hairspring oscillator years before. Later that year, Oldenburg published an explanation stating that Hooke never published or built a watch similar to Huygens' and Hooke was forced to apologize to the Royal Society as Huygens was also a member of the Royal Society (Oldenburg, 1675, p. 440-442). Others also claimed the invention such as Isaac Thuret, the watchmaker who built Huygens' first balance-hairspring assembly and ultimately admitted Huygens' authorship (Huygens, 1897, Correspondence N⁰ 2055) or Philippe de la Hire and Jean de Hautefeuille who both used a balance and a spring, but not a spiral spring (Defossez, 1946).

Hetzel. This watch used an electromagnetic system to sustain a 360 Hz tuning fork time base having a guaranteed accuracy of 2 s/day. Being flexure-based, the tuning fork oscillator makes it possible to overcome the quality factor limit of the balance and hairspring. Indeed, Fig. 1.4 shows that with a quality factor of order 1000, an acoustic tuning fork watch can have an accuracy near 1 s/day and, with a quality factor of order 100 000, a quartz tuning fork watch can have an accuracy near 0.01 s/day. However, the high frequency and small amplitude oscillations of a watch-scale tuning fork makes it very challenging to sustain mechanically. Trials done in the 1960s did not succeed in sustaining mechanically an oscillator with a frequency of order greater than 10 Hz (Perotto, 2009) but researchers built a successful prototype using a 84 Hz tuning fork in 2013. The project was discontinued thereafter and the only available documentation is the patent (Vardi and Déhon, 2015). More details are given in Sec. 2.1.

Figure 1.3 – Louis-Clément Breguet's 1867 tuning fork clock with a frequency of 100 Hz (Musée International d'Horlogerie, La Chaux-de-Fonds).

1.4   Solution avenues

1.4.1   Increasing the quality factor

Horologists agree that there is a correlation between the accuracy of a timekeeper and the quality factor of its timebase (Bateman, 1977; Matthys, 2004; Vardi, 2014). This phenomenon, first noted by British engineer Douglas Bateman (1977), is not totally understood but is backed by the data gathered on different oscillators and represented in Fig. 1.4. The quality factor of an oscillator is a measure of its efficiency and is defined as (Green, 1955)

$$Q = 2\pi \frac{\text{Energy stored}}{\text{Energy dissipated per cycle}}.$$

(1.1)
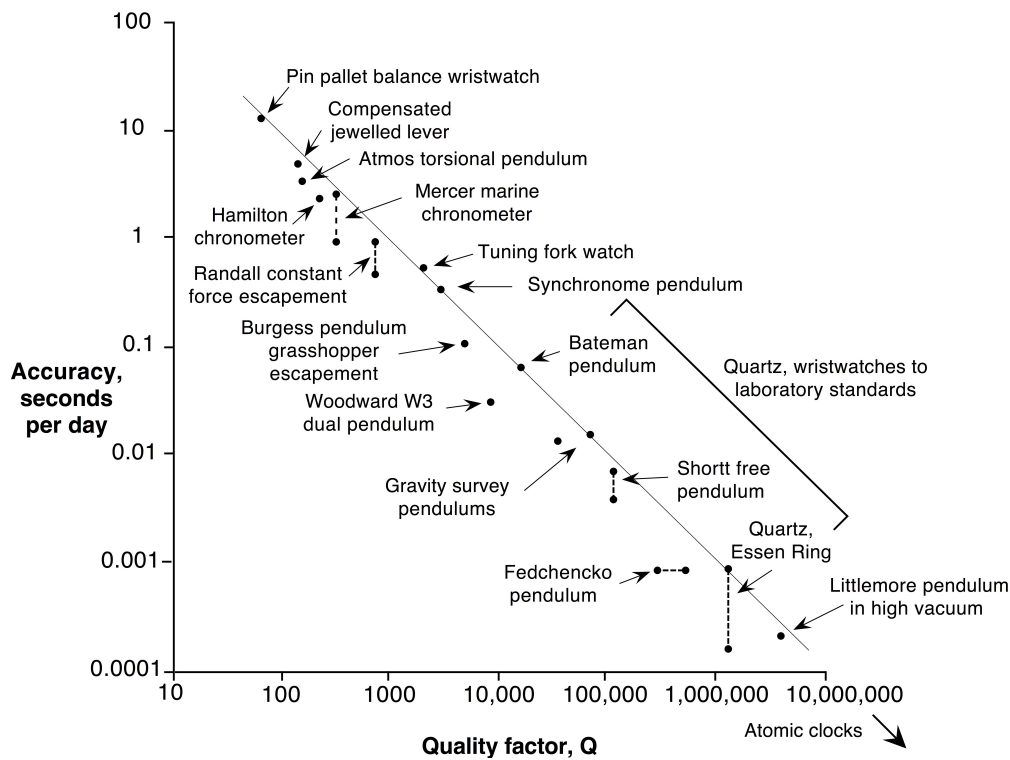
Figure 1.4 – Correlation between accuracy and quality factor (Vardi, 2014).

To give a more concrete definition, the value of Q corresponds to the number of cycles that a free oscillator performs before reaching 4.3% $(= e^{-\pi})$ of its initial amplitude (Vardi, 2014). In the case of a maintained oscillator, such as is the case in a timekeeper, Q quantifies the amount of energy that has to be restored to the oscillator per cycle to maintain its oscillation.

A more intuitive explanation for the effect of increasing the quality factor on timekeeping accuracy follows: increasing Q decreases the energy restored per cycle and thus the perturbation of the oscillator caused by the sustaining mechanism (usually an escapement, see Sec. 1.5.4). This phenomenon can be seen in practice: the balance and hairspring of classical mechanical watches ($Q \approx 200$) is impulsed twice per cycle, see Fig. 1.6, whereas that of marine chronometers ($Q \approx 800$) is impulsed once per cycle and accurate pendulum clocks such as the Shortt–Synchronome clock ($Q \approx 100\,000$) are impulsed every fifteenth cycle (Matthews, 1994).

Bateman (1977) formalized this principle by rewriting Airy's formula (Airy, 1830), which quantifies the timekeeping error caused by perturbations on the oscillator, in terms of quality factor. He derived that the timekeeping error over a period of oscillation T is

$$dT = T\frac{\cot\phi}{2Q}, \tag{1.2}$$

where ϕ is the phase of oscillation at which the perturbation, i.e., the impulsion by the sustaining mechanism, happens. According to this formula, a systematic impulsion at the same phase causes a constant gain or loss of the timekeeper. In the measure of time, any

error, if it is always the same (systematic error) can be taken into account (e.g., by adjusting the display), so it is the variation which really affects timekeeping accuracy (Woodward, 1995; Rawlings, 1993). This is done by taking the derivative of Eq. (1.2)

$$\frac{\Delta T}{T} = -\frac{\Delta\phi}{2Q\sin^2\phi} \tag{1.3}$$

and shows that, without modifying the sustaining mechanism, increasing Q decreases the error caused by variations $\Delta\phi$ of the phase of the impulsion.

1.4.2 Flexure-based oscillators

In the previous section, we explained that the quality factor of portable mechanical time-keepers needs to be increased in order to fulfil the goal of Sec. 1.1. The main obstacle to this increase is the friction in the bearings of the balance. Air friction also has a significant influence but eliminating it only increases the quality factor by about 50%: it was increased from 300 to 450 for a balance and hairspring in 99.8% vacuum (Cartier, 2012; Clymer, 2012). The elimination of contact friction needed for the desired increase in quality factor can be obtained by replacing the balance and hairspring with a flexure-based oscillator. We define a flexure-based oscillator as an inertial mass whose motion is guided by the deformation of elastic elements that provide a restoring force opposed to this motion, leading to an oscillatory behavior. In addition to eliminating contact friction, flexure-based oscillators can be manufactured using materials with minimal internal friction such as monocrystalline silicon, which also contributes to increasing the quality factor compared to the classical metals.

Currently, there are three promising types of flexure-based oscillators that could fulfil the goal of Sec. 1.1.

1. *The tuning fork.* This time base has already proven its performance, see Sec. 1.3.3, but is difficult to maintain mechanically at the watch scale.

2. *The flexure pivot oscillator.* This time base follows the principle of the balance and hairspring, where the rotational motion of an inertial mass is opposed by an elastic restoring torque, but uses elastic flexures to guide the rotational motion instead of a rigid pivot, thus drastically reducing the friction (Eastman, 1935).

3. *The IsoSpring.* This two degree-of-freedom (DOF) oscillator first introduced in (Henein et al., 2014) uses elastic flexures to guide the elliptical motion of an inertial mass. In addition to increasing the quality factor, it aims at eliminating the need for escapements in mechanical timekeepers.

In this thesis, we explore the second avenue: the flexure pivot oscillator. This solution seems to be the most directly implementable due to its similarity with the commonly used balance and hairspring system and is the one stirring the most interest from the industry, see Chapter 2.

The IsoSpring is currently being studied by a team of scientists under the guidance of Prof. Henein (Henein et al., 2014; Vardi et al., 2018) and will not be considered in this thesis. The mechanically-sustained tuning fork has been the topic of a project that resulted in a working prototype in 2013. The project was discontinued but recent patents by Winkler et al. (2017) show that the topic has not been buried. More details are given in Sec. 2.1.

1.5   Main challenges

The introduction of flexure pivot oscillators in portable mechanical timekeepers comes with new issues that need to be solved before they can be implemented. The main ones are discussed in this section.

1.5.1   Isochronism

Accurate timekeeping is essentially equivalent to having an oscillator with a period that is as regular as possible. Among the factors affecting the period are: amplitude, orientation of gravity, temperature, magnetism and shocks. The most important of these factors is amplitude and the independence of period from amplitude, called isochronism, is one of the main issues addressed in this work.

Isochronism was first identified by Galileo who remarked around 1600 that the period of oscillation of the pendulum was independent of oscillation amplitude. However, Mersenne and Descartes noted in 1636 that this was not accurate as they observed that the period of the pendulum slightly increases with amplitude (Matthews, 1994). Huygens then analyzed the problem mathematically and devised in 1656 a theoretically isochronous pendulum by replacing the rod with a flexible cord which unwinds off a cycloid (Huygens, 2007), as depicted in Fig. 1.5. More details are given in Chapter 2.
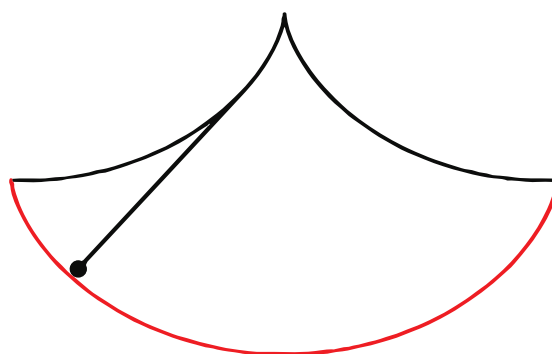
Figure 1.5 – Huygens' isochronism corrector for the pendulum using cycloidal cheeks.

In the case of a rotational oscillator consisting of a spring coupled to an inertial mass (such as a balance and hairspring), the condition for isochronism is that the spring restoring torque must follow Hooke's law, i.e., be a linear function of the angular displacement. This condition

complicates the use of flexures as oscillator springs since they exhibit nonlinear elastic properties. Different solutions already exist in order to achieve isochronism with flexure pivots but they all suffer from some limitation, see Sec. 2.2.7.

Note that rather than making our time bases isochronous, we are interested in controlling their isochronism defect in order to be able to compensate external defects that are independent from the oscillator. For example, it is known that escapements introduce isochronism defects and this property has already been used in clocks to compensate the intrinsic defect of pendulums (Beckett, Lord Grimthorpe, 1903, pp. 33-34) (Woodward, 1995, pp. 79-80).

1.5.2 Gravity sensitivity

A second crucial property for mechanical watch time bases is gravity insensitivity, the independence of oscillator frequency from its orientation with respect to gravity. When the position of the center of mass (COM) of an oscillator changes as it moves from its equilibrium position, the gravity force can either assist or oppose the motion, resulting in a respective softening or stiffening of the oscillator. This change in stiffness affects the frequency of the oscillator and is dependent on its orientation with respect to gravity. In the case of flexure-based oscillators, this phenomenon is likely to happen since the flexures only approximate ideal joints and their so-called parasitic motion can lead to translation of the COM. This work will help lay the foundations to make flexure-based oscillators gravity-insensitive.

1.5.3 Temperature sensitivity

Temperature is another important factor that can influence the accuracy of a time base. However, this has already been the topic of considerable research and we believe that the existing compensation techniques and materials are transferable to our new time bases. For instance, temperature-invariant materials have been described by Guillaume (1920), Ching and Ko (2016) and Musy et al. (2008), Temperature compensation techniques also exist such as bimetallic balances (Rawlings, 1993, p. 189) or bimetallic compensating elements (Harrison, 1767, p. xii), (Ditisheim, 1920). This topic is thus not discussed further in this work.

1.5.4 Mechanically sustaining the oscillation

In order to keep time, a timekeeper counts the oscillations of a time base. In parallel, energy has to be restored to the time base in a cyclical manner for it to operate continuously. In a mechanical timekeeper with a 1-DOF time base (such as a flexure pivot oscillator), these two functions are typically performed by a mechanical system called *escapement*, see Fig. 1.6. First, the escapement allows the back and forth motion of the time base to regulate the one directional motion of the mechanism driven by its power source and second, it transfers energy from the power source to the time base in the form of cyclical impulses.

The study of escapements is a research topic in itself and experience indicates that rigorous scientific analysis is problematic and of limited value for the development of new escapements. See (Conus, 2007) for a survey. For these reasons we limited our scope to satisfying a few criteria, assuming that they are sufficient to make our new time bases compatible with the existing escapements:

1. The frequency of the time base should stay under 32 Hz. This reference frequency is based on the results of Forster and Rolland (2019) who were able to make a lever escapement work at a frequency of 32 Hz in an experimental setup aimed at accelerating the ageing of the *Swiss lever escapement*.[7]

2. The oscillator should have a minimum operation amplitude of ±15 degrees to be potentially compatible with existing escapements. Typically, the lift angle of lever escapements is between 30 and 60 degrees (Pellaton, 1949, p. 13). The lift angle refers to the angle travelled by the oscillator between its first contact with the lever (Fig. 1.6a) and the end of the impulse.

It is worth noting that examples of flexure pivot oscillators with escapements exist, though their behavior is not fully described. Robuschi et al. (2017) simulated a 25 Hz flexure pivot oscillator with a maximal amplitude of 6 degrees working with a deadbeat escapement, but no working prototype is shown. Semon et al. (2017) showed a prototype with a rudimentary clock lever escapement combined to a 15 Hz oscillator with a 6 degree nominal amplitude (Markl, 2017) but no scientific account is given on its performance, see Sec. 2.2.6. Flexure pivot oscillators with escapements are also presented in a number of patents (Winkler et al., 2018a; Semon et al., 2017; Mercier et al., 2019; Ypma and Weeke, 2019) but no prototype has been disclosed. An interesting alternative using a magnetic escapement is also presented by Di Domenico et al. (2018).

| (a) | (b) | (c) | (d) |
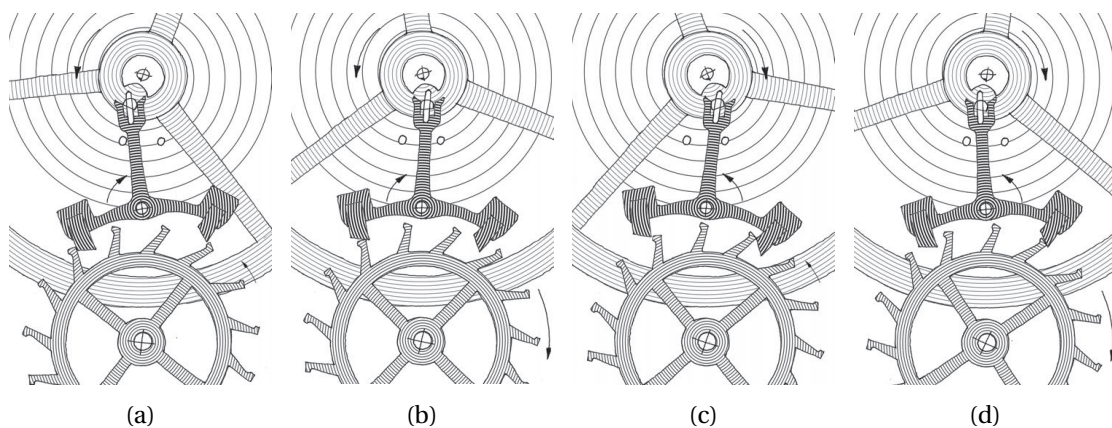
Figure 1.6 – Working principle of the lever escapement used in most mechanical watches: (a) entry lock, (b) entry impulse, (c) exit lock, (d) exit impulse. Illustrations by Olivier Laesser, 2015.

---

[7]The Swiss lever escapement is the most frequently used escapement in today's mechanical watches.

1.5.5 Magnetism

Magnetic fields from everyday objects such as mobile phones, medical and security scanners, magnetic clasps and induction stoves can affect the timekeeping accuracy of watches. As a reference, the "Master Chronometer" certificate tests the accuracy of mechanical watches subjected to a magnetic field of 1.5 T (15 000 gauss).[8] This is usually dealt with by using non-magnetic materials. In our case, we assume that a non-magnetic silicon construction solves this issue.

1.5.6 Shocks

Shocks can be an important source of perturbation in portable timekeepers. Their impact is usually limited through technical solutions such as mechanical stops and elastic elements at the attachment point of the flexures rather than conceptual advances and we thus leave this issue to the watchmakers. Some examples of embodiments can be found in (Winkler et al., 2018b; Léchot et al., 2018; Born, 2019; Winkler and Helfer, 2019).

1.5.7 Manufacturing

One of the requirements formulated in Sec. 1.1 is that the time base must be implementable at small scale. To ensure miniaturization and make it possible to use thin and slender flexures, we designed our architectures such that they are planar or consist of a stack of planar layers, see Chapter 3. This facilitates the compatibility of our designs with proven silicon manufacturing techniques such as Deep Reactive Ion Etching (DRIE).

1.5.8 Experimental characterization

As we explained in Sec. 1.5.4, we decided to develop our time bases without a dedicated escapement. The classical method for measuring the chronometric performance of balance and hairspring oscillators is thus not applicable as it relies on the acoustic signal resulting of the shocks between the oscillator and the escapement (Su and Du, 2007). Additionally, the absence of a sustaining mechanism makes it impossible to measure the time base at a constant amplitude, which is challenging since the signal keeps changing amplitude. We thus devised a new experimental method based on an optical signal that can evaluate the chronometric performance of the time base in free oscillation from an arbitrary start amplitude, see Chapter 7.

---

[8]See the requirements for the "Master Chronometer" certificate of the Swiss Federal Institute of Metrology (METAS) at www.metas.ch/dam/data/metas/Dokumentation/rechtliches/zertifizierung-uhren/metas-n001-v-1-1-e.pdf.

1.6   Structure of the thesis

In Chapter 2, we start by reviewing the latest stages of development of the three solution avenues introduced in Sec. 1.4.2. In Chapter 3, we present three new flexure-based oscillator architectures aiming at fulfilling the goal of Sec. 1.1. We derive models for the rotational stiffness of the new oscillators in Chapter 4 and use these models to solve the challenges of isochronism defect in Chapter 5 and influence of gravity in Chapter 6. In Chapter 7, we show the design and manufacturing of a silicon prototype satisfying typical mechanical watch specifications and use this prototype to validate our models experimentally.

2 State of the Art

Chapter 1 presented flexure-based oscillators as avenue to break through the apparent limit of mechanical watch accuracy and introduced three promising solutions: the tuning fork, the flexure pivot oscillator and the IsoSpring. This section summarizes the highest levels of development of these solutions, how they address some of the main challenges listed in Sec. 1.5, and their limitations.

2.1 The tuning fork

The groundwork for using the tuning fork as a portable mechanical time base was laid by Max Hetzel, inventor of the Accutron in 1960. With a very small amplitude of motion compared to the length of its blades, the tuning fork has an excellent isochronism.[1] Hetzel (1962) calculated that, for a ±50% amplitude variation of the Accutron tuning fork, the geometric isochronism defect is negligible and that the isochronism defect of its material was responsible for a ±0.5 s/day error. In the clock application by Breguet (1866) and Niaudet-Breguet (1866), the gravity sensitivity of the tuning fork was not a concern but when Max Hetzel first used it in a wristwatch, he calculated that there would be a ±4.5 s/day difference between the two vertical positions of the tuning fork. This difference is caused by the upward, respectively downward, motion of the centers-of-mass of the blades in the two different positions due to circular deflection of the blades. This change in gravitational potential energy affects the restoring force and thus the frequency of the time base. Hetzel suggested various architectures to compensate this effect, depicted in Fig. 2.1. He found that these solutions where not practical for a wristwatch and preferred an approach using two oscillator placed at a 180 degree angular offset that are electrically connected in parallel, resulting in an averaging of their frequencies.

After the Accutron, piezoelectric crystal oscillators became the reference time base for electronic timekeepers. For low frequency quartz oscillators (of the kHz order) such as the ones in wristwatches and real time computer clocks, the bar shape was first adopted before setting on the tuning fork shape (Reymondin et al., 1999). We do not discuss these oscillators since

---

[1]The Accutron has an amplitude of 35 μm for 25 mm long blades.
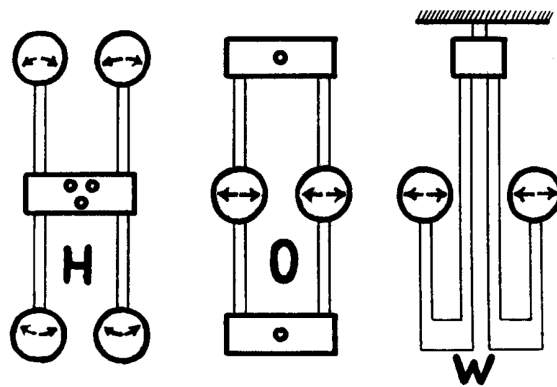
Figure 2.1 – Tuning fork architectures for gravity effect compensation (Hetzel, 1962).

they are not maintained mechanically. With the advent of silicon and Microelectromechanical systems (MEMS), mechanical oscillators reappeared in the clocks of electronic devices, some of which in the shape of tuning forks, see Fig. 2.2. Little information is available but one can see from one manufacturer's data sheet that the gravity-compensating H-shape from Fig. 2.1 has been chosen and that they have a quality factor of 50 000 for a frequency of 524 kHz.[2]
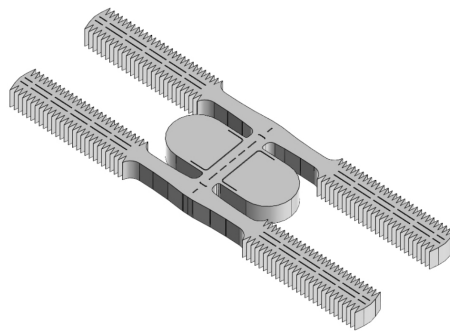
Figure 2.2 – Tuning fork MEMS oscillator of type SiTime SiT1252.[2]

The high frequency and small amplitude of the tuning fork at small scale is often considered to be the factor preventing its sustaining with a mechanical system (Perotto, 2009). Nevertheless, a project from the beginning of the 2010s investigated the feasibility of using a magnetic escapement (Vardi, 2012) or a mechanical escapement (Vardi, 2013) to sustain a watch-size tuning fork. No article has been published but the mechanical solution was preferred and a working prototype was successfully built (Ilan Vardi, personal communication, October 15, 2019). The silicon prototype had a frequency of 84 Hz, a quality factor of approximately 400 and an architecture similar to that depicted in Fig. 2.3.

A more recent variant of the tuning fork for mechanical watches is depicted in Fig. 2.4 (Born et al., 2016). It consists of two masses connected symmetrically to an intermediate body by flexure pivots, the intermediate body being connected elastically to the fixed frame. The

---

[2]Documentation: www.sitime.com/datasheet/SiT1252.

patent also shows an escapement that looks very similar to the one used by Vardi and Déhon (2015). The use of flexure pivots raises isochronism issues, see Sec. 2.2.2, and Winkler et al. (2017) suggested to use short flexures instead of crossed pivots for better isochronism.
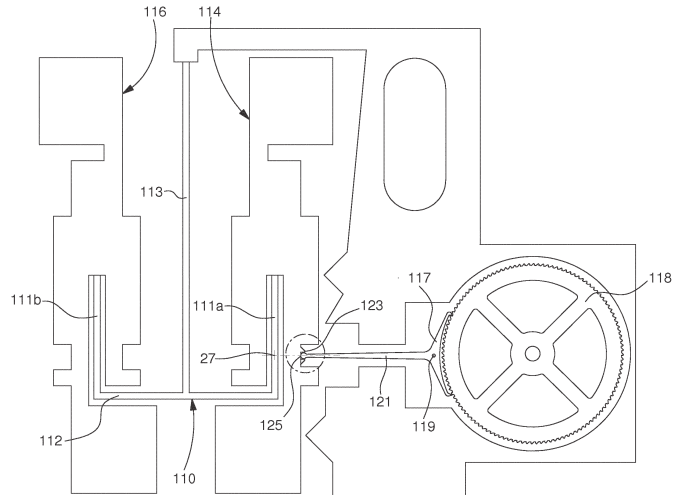
Figure 2.3 – Mechanically sustained silicon tuning fork (Vardi and Déhon, 2015).
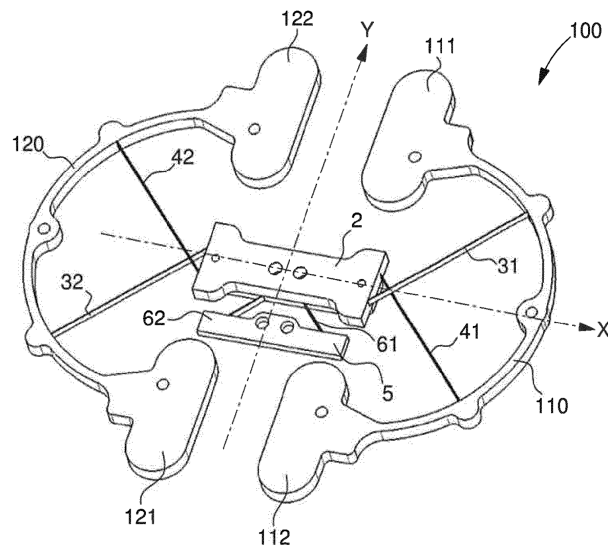
Figure 2.4 – Variant of the tuning fork using flexure pivots (Born et al., 2016).

2.2 The flexure pivot oscillator

2.2.1 The Genequand system

The first application of a flexure pivot oscillators as time base was a 2014 mechanical watch prototype called "Genequand system" (Barrot et al., 2014, 2015). This mechanism already validated some expectations of flexure-based oscillators as it increased the quality factor to about

1000 and watch autonomy from 7 days to potentially 30 days. The basis of the Genequand system was a flexure-based escapement, similar to the grasshopper escapement invented by Harrison around 1722 (Hastings, 1993). The crossed flexure pivot, introduced by Wittrick (1948) and depicted in Fig. 2.5a, was added at a later stage in order to implement the system at a watch scale. This pivot, detailed in Sec. 3.2.1 consists of a rigid-body attached to the ground by two symmetrically-crossed leaf springs that block all degrees-of-freedom but rotation about an axis defined by the intersection of the flexures.[3] The oscillator is gravity-insensitive thanks to a particular value of the crossing point of its leaf springs (Henein and Kjelberg, 2015; Wittrick, 1951) but has a nonlinear restoring torque resulting in an isochronism defect. A system was developed by Henein and Schwab (2014) to address this defect as well as the one caused by the escapement, see Fig. 2.5b. It is indeed known that escapements introduce isochronism defects and this property has already been used in clocks to compensate the intrinsic defect of pendulums (Beckett, Lord Grimthorpe, 1903, pp. 33-34) (Woodward, 1995, pp. 79-80). This is also why, in this thesis, we are interested in controlling the isochronism defect of the oscillator rather than minimizing it.

(a)   (b)
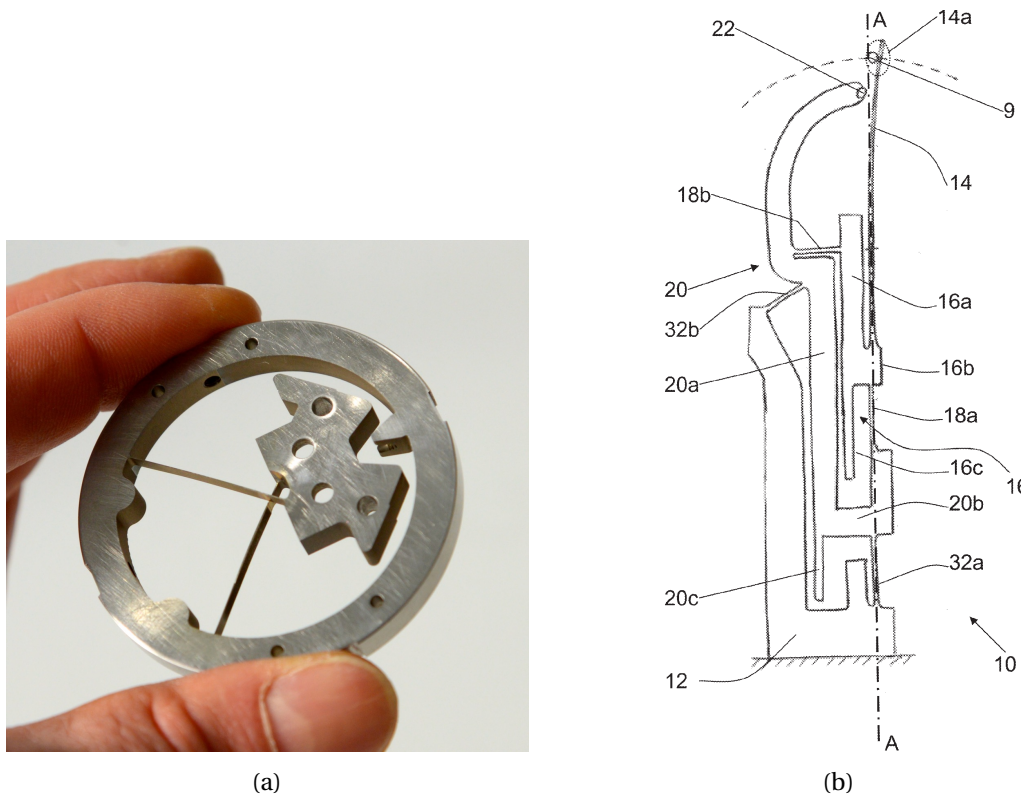
Figure 2.5 – Constituting elements of the Genequand system's time base: (a) crossed flexure pivot with crossing point minimizing its gravity sensitivity (Henein and Kjelberg, 2015; Wittrick, 1951) and (b) isochronism corrector (Henein and Schwab, 2014).

---

[3]A leaf spring is defined as any prismatic beam of rectangular cross section having a width b and length l at least ten times greater than its thickness h: $b > 10h$ and $l > 10h$ (Cosandier et al., 2017).

The isochronism corrector developed for the Genequand system uses flexible blades that come in contact with the escapement anchor for part of the stroke, introducing a discrete change in stiffness. Since the anchor is always in contact with the oscillator, the change directly affects the oscillator. Figure 2.5b shows the contact between pin 9 of the anchor and blade 14. Due to the mechanical stop 22, the contact happens only when the pin is to the right of axis A. The discrete stiffness variation always happens at the same angular position, such that the ratio of time that the oscillator spends with one stiffness to the time spent with the other stiffness depends on the amplitude of oscillation. This introduces a variation of frequency with amplitude that can be used to correct the isochronism. The tool relies on three setting inputs and is complex to tune. It also introduces shocks at the contact point 14a that can have undesired consequences.

2.2.2 Crossed flexure pivot oscillators

Following the Genequand system, a lot of attention has been given to the crossed flexure pivot (CFP) oscillator in the watchmaking world. As most of the research was done in an industrial context, most of the information is obtained from patents. Solutions were developed to make the CFP oscillator isochronous without using an external corrector mechanism such as in the Genequand system. It is known that changing the crossing point of the leaf springs changes the restoring torque nonlinearity of the CFP, see Fig. 5.3, but this also changes its parasitic shift (Zhao and Bi, 2010a) and thus its gravity sensitivity. Di Domenico et al. (2016) suggested to use the angle between the leaf springs in addition to their crossing point to set the isochronism defect while minimizing gravity sensitivity, as depicted in Fig. 2.6a. Chabloz (2018b) proposed to use the variation of the leaf springs' cross-section in addition to the angle between them and their crossing point in order to set the isochronism defect, minimize gravity sensitivity and minimize the equivalent stress in the flexures.

The use of a cartwheel flexure, also known as joined crossed flexure pivot, as mechanical time base has been studied by Robuschi et al. (2017). This particular case of the CFP where the two leaf springs are connected at their crossing is depicted in Fig. 2.6b. Compared to a crossed flexure pivot with same dimensions of the leaf springs, the cartwheel flexure depicted in Fig. 2.6b is four times stiffer and has a four times higher stress in the flexures for the same angular displacement (Cosandier et al., 2017, Chap. 5). This effect can be seen in the relatively low 6 degree maximal amplitude and relatively high 25 Hz frequency of the oscillator. This article computed a quality factor of 2380 though no experimental results confirm this number. The isochronism of the time base is discussed in the article though the effect of the restoring torque nonlinearity, which is not negligible for this kind of flexure, seems to have been omitted.

2.2.3 Serial crossed flexure pivots

A number of existing flexure pivot architectures use serial combinations of crossed flexure pivots placed in a symmetrical way. The symmetry has the advantage of compensating the
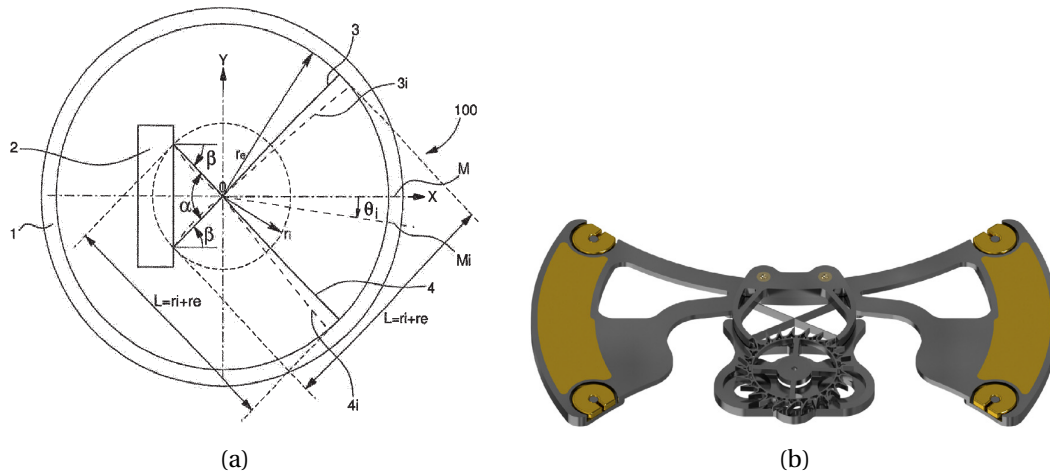
Figure 2.6 – (a) Crossed flexure pivot oscillators whose angle α between the leaf springs is used to minimize the isochronism defect (Di Domenico et al., 2016) and (b) cartwheel flexure pivot oscillator with escapement by Robuschi et al. (2017).

influence of gravity, see Chapter 6, while the serial combination of redundant pivots has the advantage of decreasing the deflection of each pivot for a given rotation of the inertial body. The latter decreases the stress in the flexures, allowing to reach larger amplitudes, and decreases the rotational stiffness, allowing to reach lower oscillation frequency. Both characteristics facilitate compatibility with existing escapements, see Sec. 1.5.4.

The simplest architecture consists of two crossed-flexure pivots mounted head-to-tail, such as depicted in Fig. 2.7a. Combinations of more pivots are obtained by either increasing the number of serial pivots in a planar design, such as the "butterfly" architecture (Henein et al., 2003) depicted in Fig. 2.8b and used in various oscillators (Weeke et al., 2016; Semon et al., 2017; Barrot et al., 2018), or stacking them on several planes such as seen in Fig. 2.7b.
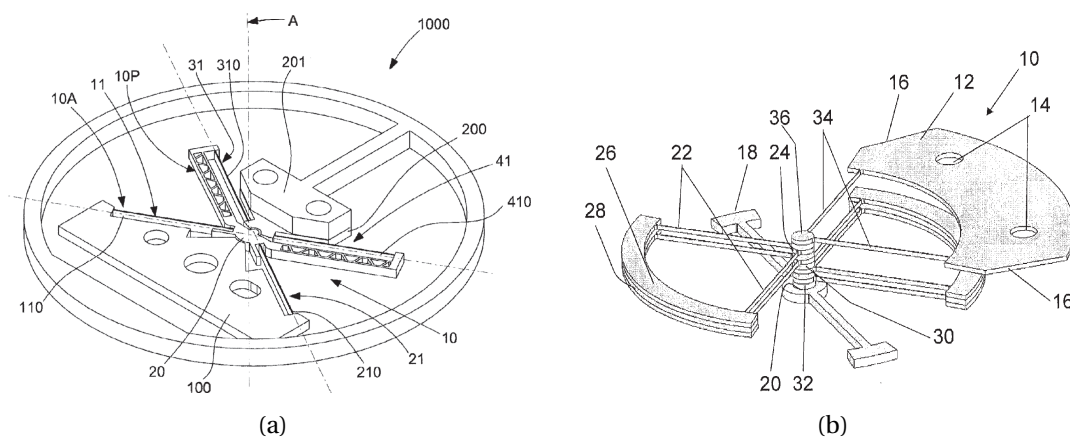
Figure 2.7 – Oscillators using serial combinations of crossed flexure pivots (a) in one plane (Di Domenico et al., 2017) and (b) stacked (von Gunten et al., 2015).

18
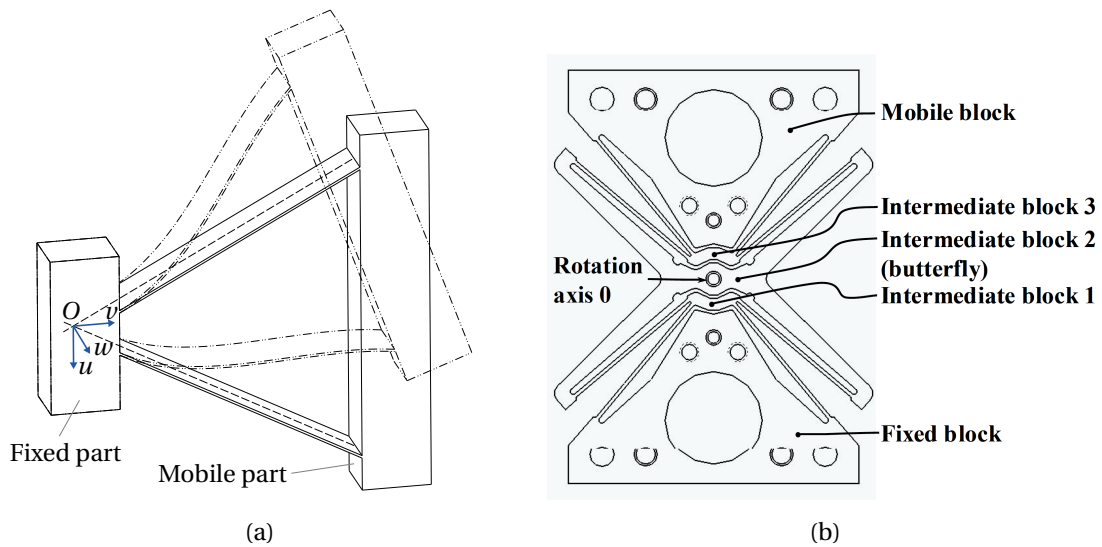
Figure 2.8 – (a) Remote Center Compliance (RCC) flexure pivot in undeflected position (solid lines) and rotated about the w-axis (dashed lines) and (b) "butterfly" flexure pivot consisting of 4 RCC flexure pivots in series (Henein et al., 2003).

Note that these architectures use a particular case of the CFP called *Remote Center Compliance* (RCC) flexure pivot (Cosandier et al., 2017) or *isosceles-trapezoidal flexural pivot* (Pei et al., 2008), where the flexures cross symmetrically outside of their physical structure, see Fig. 2.8a. The intersection of the flexures defines (to a first approximation) the axis of rotation of the pivot (Haringx, 1949), for instance axis w in Fig. 2.8a. More details are given in Sec. 3.2.1.

2.2.4 Overconstrained flexure pivot oscillators

The overconstrained flexure pivot category encompasses a variety of patented architectures which have in common that their mobility, obtained through Grübler's formula (Grübler, 1917) is less than their actual DOF. A basic example is a crossed pivot with more than two leaf springs such as depicted in Fig. 2.10a. A similar architecture with a rotational symmetry of order four has been chosen for the "CR4" oscillator depicted in Fig. 2.10b (Barrot et al., 2018; Cosandier et al., 2018). In this architecture, the flexures are placed in series, which brings the advantages listed in Sec. 2.2.3. Additionally, the distance from the extremities of the flexures to their virtual crossing point can be used to set the isochronism of the pivot (Cosandier et al., 2018), in a similar manner to setting the crossing point of the CFP leaf springs in Fig. 5.3.

An overconstrained pivot also occurs when crossed pivots are connected in parallel without adding a DOF. A simple example is the extension of the flexure pivot oscillator with three leaf springs depicted in Fig. 2.10a to four non-parallel leaf springs, which is equivalent to having a two RCC pivots connecting in parallel the center to the outer ring. Another example would occur if the mobile and fixed blocks of the "butterfly" pivot of Fig. 2.8b were connected together and the intermediate block 2 was used as mobile part. This is essentially equivalent

to the architecture depicted in Fig. 2.9a, where two chains of serial RCC pivots are connected in parallel. Figure 2.9b shows a similar configuration with three parallel chains of two serial RCC pivots. Note that one way of reducing these overconstraints is to add degrees-of-freedom between the elements that are connected in parallel such as in the prototype of Fig. 2.12b or in our architectures of Sec. 3.3.

(a)   (b)
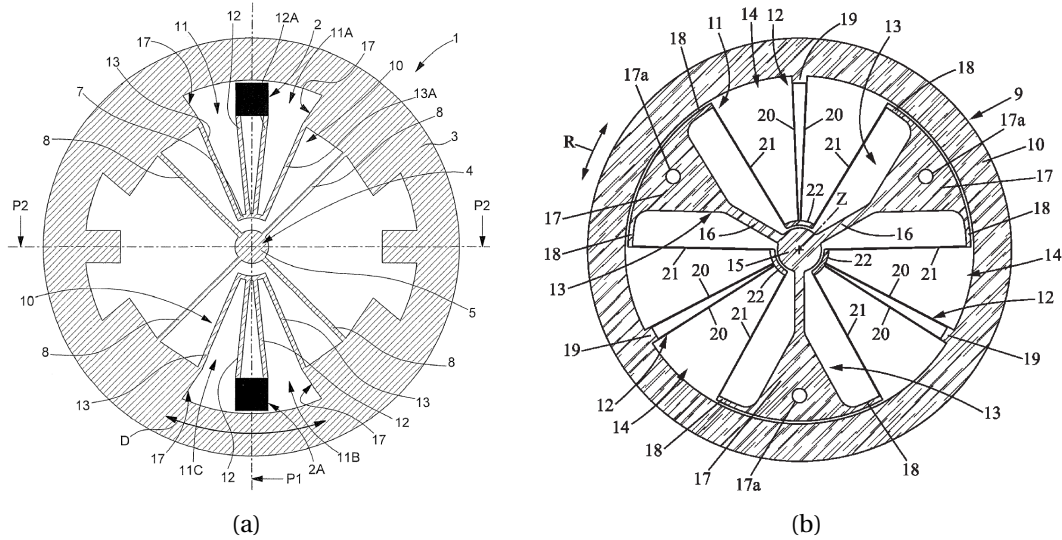
Figure 2.9 – Overconstrained oscillators with crossed flexures connected in parallel: (a) two parallel chains of two serial crossed pivots where the black squares are connected to the fixed frame (Cusin et al., 2012), and (b) three parallel chains of two serial crossed pivots (Semon et al., 2016).

(a)   (b)
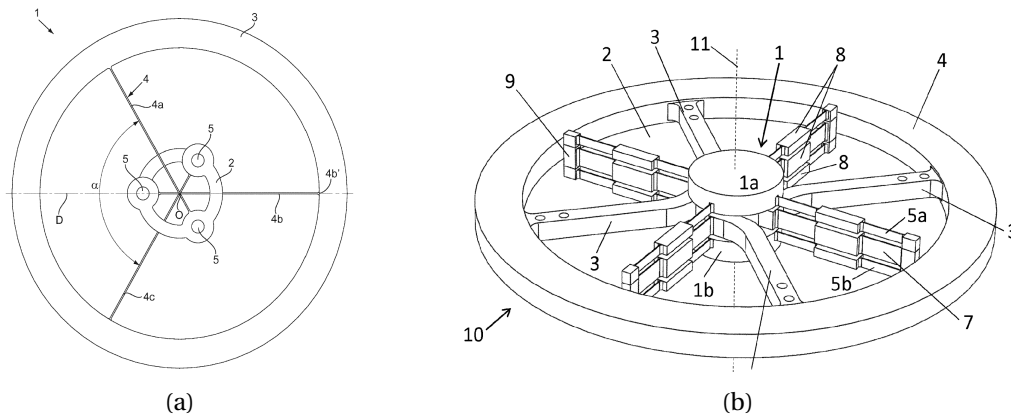
Figure 2.10 – Overconstrained flexure pivot oscillators with (a) three leaf springs (Chabloz, 2018a) and (b) four flexures (Cosandier et al., 2018).

2.2.5 Coupled flexure pivot oscillators

Another way of obtaining a symmetry which is advantageous for compensating gravity effects while keeping one DOF is to couple symmetrically-placed oscillators. These oscillators can

either be coupled such that they oscillate symmetrically (both move in the same direction) as depicted in Fig. 2.11a or asymmetrically (the oscillators move in opposite directions) as depicted in Fig. 2.11a and in (Mercier et al., 2019). The antisymmetric oscillation mode, similar to that of the tuning fork described in Sec. 2.1, has the advantage that the system cannot be excited by angular accelerations, one of the major drawbacks of rotational oscillators. Similarities can be seen with the flexure pivot implementation of the tuning fork in Fig. 2.4. the main difference is that the inertial elements of the tuning fork are connected through the base whereas here they are connected to each other by another elastic element.

(a)	(b)
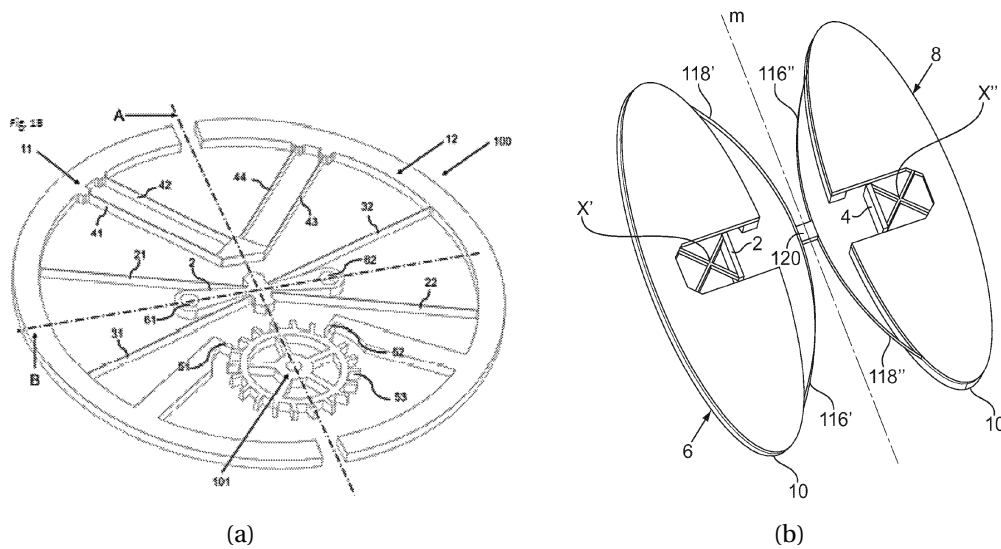
Figure 2.11 – Oscillators made of two flexure pivot oscillators coupled (a) symmetrically (Ypma and Weeke, 2019) and (b) antisymmetrically (Bayat et al., 2018).

2.2.6 Manufactured prototypes

Most of the architectures described in the previous sections have not been implemented in publicly described prototypes. The only prototypes released in watches are the Genequand system (Barrot et al., 2014) shown in Fig. 2.12a, the "Defy Lab" shown in Fig. 2.12b (Semon et al., 2017) and the "Freak NeXt" shown in Fig. 2.12c (von Gunten et al., 2015). Other prototypes such as the "CR4" (Barrot et al., 2018) depicted in Fig. 2.10b and the "force balanced oscillator" shown in Fig. 2.12d (Weeke et al., 2016) have been manufactured but not implemented in a timekeeper. The latter consists of a "butterfly" pivot coupled to symmetrically placed sliding masses. This 27 Hz oscillator seeks to improve the ratio of out-of-plane to in-plane stiffness and the frequency tuning in comparison to oscillators with rotating masses by using sliding masses. It is worth noting that all these prototypes have been manufactured in silicon. Unfortunately, scientific information is lacking to further comment on the performance of these prototypes.

(a)

(b)

(c)

(d)
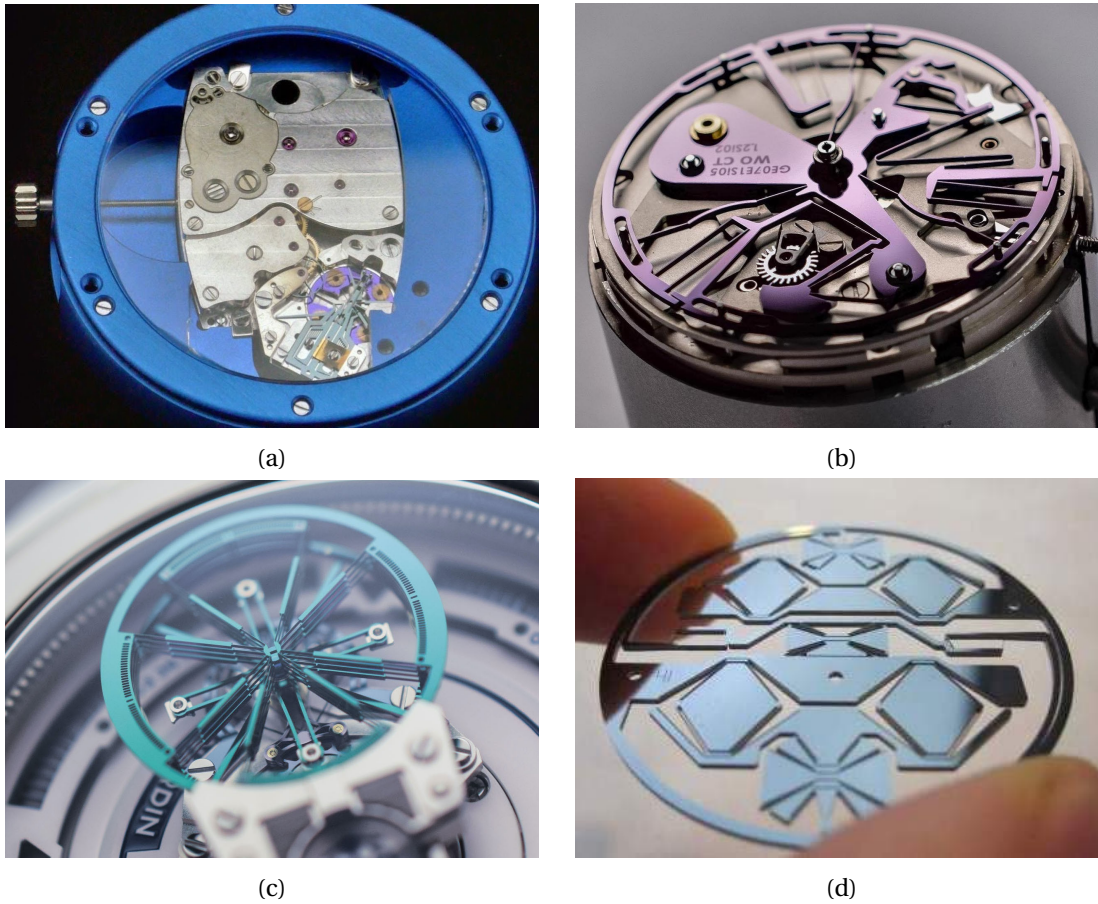
Figure 2.12 – Manufactured flexure pivot oscillator prototypes: (a) Genequand system (Barrot et al., 2015), (b) "Defy Lab" (Semon et al., 2017), image credit (Markl, 2017), (c) "Freak NeXt" (von Gunten et al., 2015), image credit (Markl, 2019), and (d) "Force balanced oscillator" (Weeke et al., 2016).

2.2.7 Limitations of existing flexure pivot oscillators

In order to highlight our contributions to the field of flexure pivot oscillators, it is important to point out the limitations of the existing architectures.

There is a long history in horology of minimizing the need for isochronous oscillators by using so-called *constant force escapements*. This is especially true for pendulum clocks, since the oscillator is intrinsically non-isochronous. In theory, these mechanisms provide impulses of repeatable energy quanta to the oscillator regardless of the driving torque of the mechanism, thereby stabilizing oscillator amplitude and solving the problem of isochronism. Constant force escapements are used for precision pendulum clocks, in particular, gravity escapements (Woodward, 1995). For watches, these escapements add significant complexity to the already complex escapement mechanism and are rarely commercialized (Déhon, 2009; von Gunten and Gubler, 2016; Zanaty, 2018).

In order to be able to account for isochronism perturbations that are external to the oscillator, it is important to be able to tune the isochronism of the time base without affecting its other crucial properties. The methods described in Sec. 2.2.2 do not qualify as isochronism tuning since changing the crossing point or the angle between the flexure also affects the gravity sensitivity and center shift of the crossed pivot, see Eq. (4.11) and (Zhao and Bi, 2010a; Pei et al., 2008).

The serial architectures, such as shown in Fig. 2.7 offer a symmetry that is advantageous for gravity sensitivity. The angle between the leaf springs can then be used to tune the isochronism of the pivot (Di Domenico et al., 2017), provided that this tuning is practically feasible. However, these architectures have redundant degrees-of-freedom that can be excited by external forces and affect the stroke of the pivot or start vibrating, thus disturbing the oscillator. For instance, the intermediate bodies 20 in Fig. 2.7a, 26 in Fig. 2.7b and 9 in Fig. 2.10b) can move without moving the inertial part of the oscillator.

The overconstrained architectures listed in Sec. 2.2.4 have more flexures defining the position of the inertial body than the minimum necessary. This can lead to unpredictable variations of their stiffness and give rise to important stresses in their flexures (Cosandier et al., 2017).

The coupled architectures presented in Sec. 2.2.5 address some of the limitations mentioned above but present the issue that the inertia of the system is likely to change as it oscillates. It is indeed known that flexure pivots present a parasitic shift of the center of rotation. As a result, the centers of mass of each inertial element move towards or away from each other as the system oscillates, which can cause significant isochronism defects, see Sec. 5.5. Tuning the isochronism in a decoupled way is also complex since changing the crossing of the flexures or the angle between them will affect the restoring torque nonlinearity as well as the inertia variation through the parasitic shift. Alternatively, tuning the isochronism through changes in the mass distribution without affecting the nominal frequency and gravity-sensitivity of the oscillator is complex. Additionally, the motion of the coupling element can create isochronism and gravity defects if its mass is not negligible.

2.3 The IsoSpring

The IsoSpring introduced by Henein et al. (2014) differs from existing mechanical time bases by having two degrees-of-freedom. Its design is based on the harmonic oscillator first described in 1687 by Isaac Newton in Principia Mathematica (Newton, 1802, Book I, Proposition X) consisting of a point mass subject to a central linear force producing an elliptical trajectory depicted in Fig. 2.13. Since the restoring force of the system follows Hooke's law, the system is isochronous (i.e. the period of a particle is independent of its energy), making it an ideal candidate for a time base. This theoretical system can be embodied using flexures to provide the necessary central restoring force (Rubbert et al., 2016) and have the low friction necessary for a high quality factor, see Sec. 1.4.1. Figure 2.14 shows two flexure-based implementations of the IsoSpring.
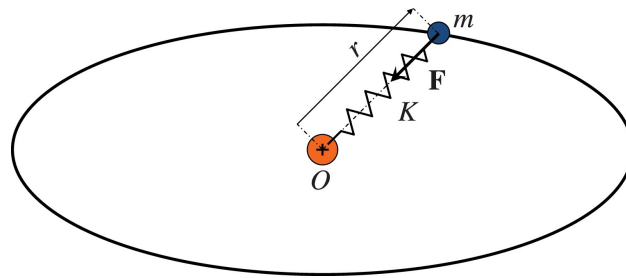
Figure 2.13 – Elliptical orbit under central Hooke Law used as basic principle for the IsoSpring concept (Rubbert et al., 2016).

| (a) | (b) |
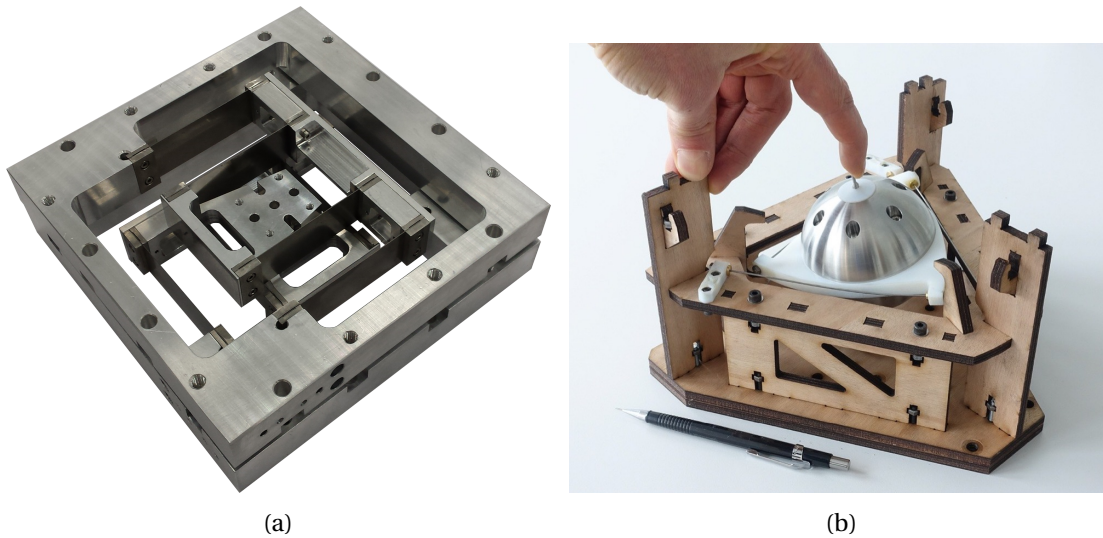
Figure 2.14 – Flexure-based (a) planar and (b) spherical embodiments of the IsoSpring (Rubbert et al., 2016; Vardi et al., 2018).

Since the trajectories of the IsoSpring are unidirectional, the sustaining mechanism of the oscillator can be greatly simplified, see Sec. 1.5.4, paving the way for improvements in efficiency and simpler architectures (Henein et al., 2014). The concept has been validated on clock prototypes and the current research focuses on implementing it at the watch scale.[4]

---

[4]A video is available at https://youtu.be/7XRCTzdvfSk

3 New flexure pivot oscillator designs

Chapter 1 explained how flexure pivot oscillators have the potential to improve the accuracy of mechanical watches and Chapter 2 identified the existing flexure pivot oscillator designs and their limitations. In this chapter, three new flexure pivot oscillator designs aiming to overcome these limitations are presented:

1. The *Gravity-Insensitive Flexure Pivot* (GIFP) lays the groundwork for minimizing the influence of the orientation of gravity on the frequency of flexure pivot oscillators, thus addressing one of the principal challenges of portable timekeepers.

2. The *co-RCC* flexure pivot oscillator uses GIFP concepts to minimize the influence of gravity and establishes a new way of tuning isochronism using the second order stiffness terms of flexures, thus addressing another key challenge of timekeepers.

3. The *Rotation-Dilation Coupled Oscillator* (RDCO) uses GIFP concepts to minimize the influence of gravity, uses co-RCC concepts for isochronism tuning using second order stiffness terms, and introduces a new way of tuning isochronism using inertia variation of the oscillator.

3.1   The GIFP

The GIFP oscillator was introduced in (Kahrobaiyan et al., 2016, 2018). It is based on the design principle that its flexures are placed symmetrically, such as to minimize the influence of the orientation of gravity on its rotational stiffness. The simplest design, shown in Fig. 3.1, consists of a rigid body and five rod flexures blocking all but one DOF: the pivoting motion. The rod flexure depicted in Fig. 3.2a is one of the fundamental building blocks of flexure-based mechanisms. Its stiffness is high for displacements along its neutral axis z and low for any other displacement and it is thus considered to block one DOF. The constituting elements of the GIFP are depicted in Fig. 3.3: a rigid-body (1) is attached to the ground (0) by four bending rods (2-5) and one torsional rod (6). The mechanism is statically determinate (isostatic) as there is only one DOF, rotation about the z axis, and no redundant constraints. Taking

advantage of the elasticity of the rod flexures, if the main rigid body has a non-zero inertia J, this flexure pivot behaves as a rotational oscillator. This behavior was validated qualitatively on the prototype of Fig. 3.1.

Figure 3.1 – GIFP prototype.

(a)

(b)
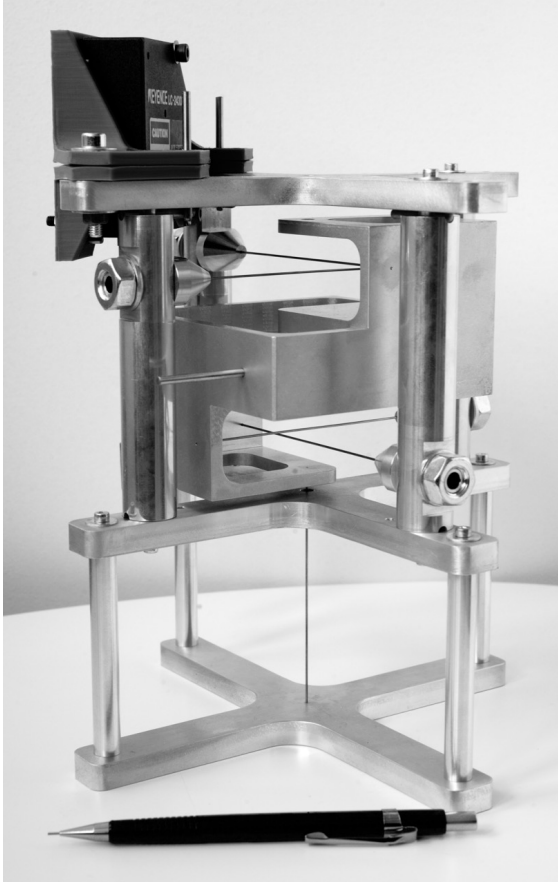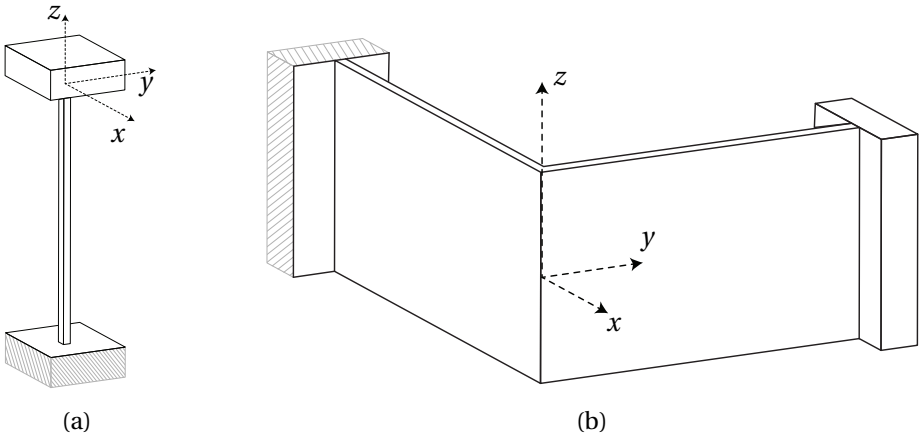
Figure 3.2 – (a) Rod flexure and (b) equivalent L-shaped flexure.

(a)

(b)
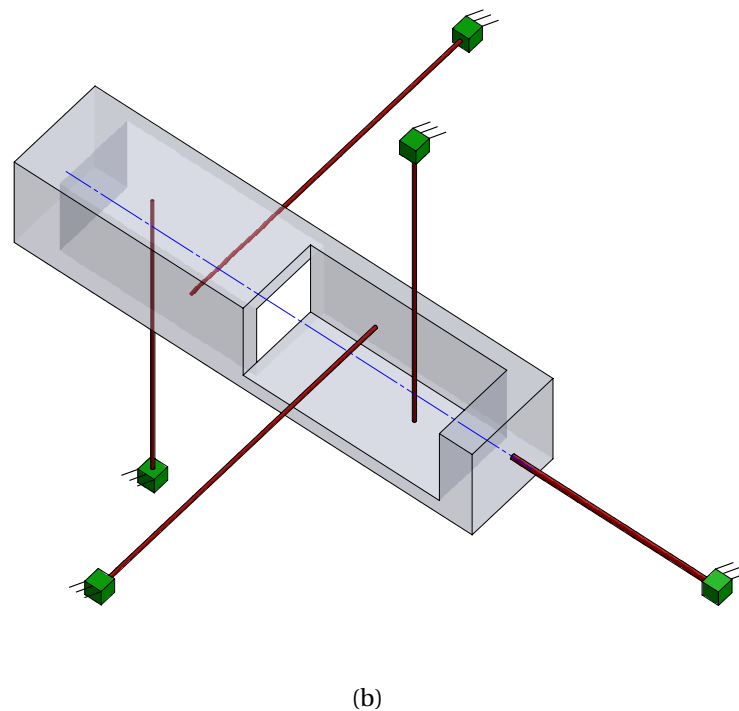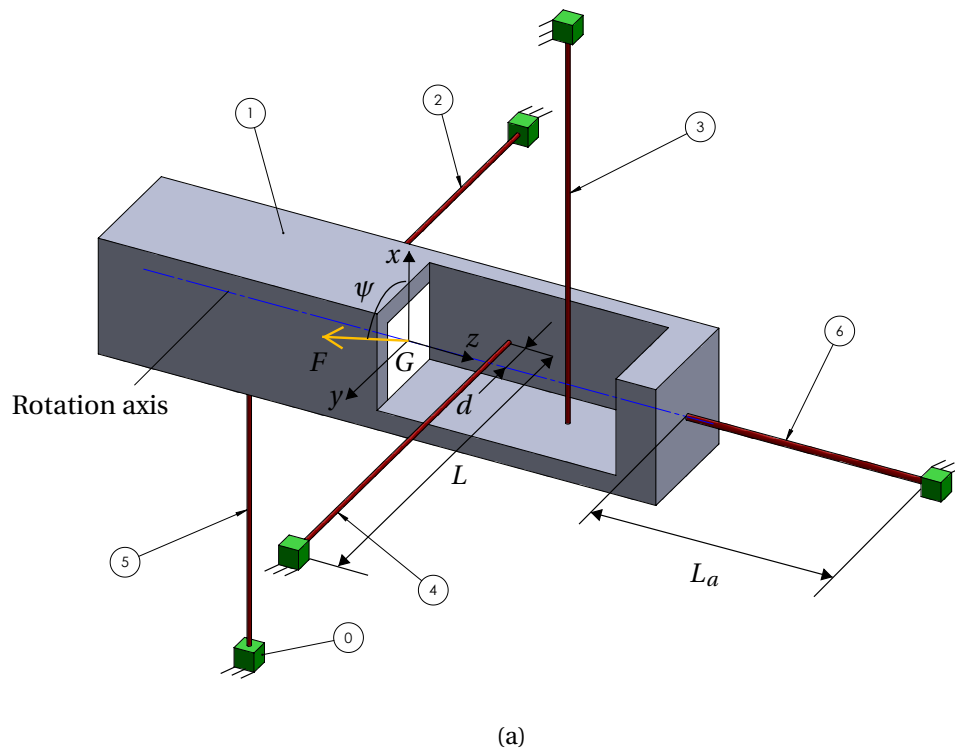
Figure 3.3 – (a) Design of the GIFP and (b) transparent view showing the attachment points of the rod flexures (Kahrobaiyan et al., 2016, 2018).

The bending rods are placed in symmetrical pairs, at a 180° rotation with respect to the COM, see pair (3) and (5) and pair (2) and (4) in Fig. 3.3a. This configuration allows to cancel out the effect of their axial shortening on the position of the COM as the oscillator rotates, a desired property to minimize the influence of gravity, see Sec. 6.2. The benefits of this configuration can also be seen from the canceling of first order effect of gravity on the rotational stiffness of the pivot, see Sec. 4.2.2. The planes formed by the two pairs of symmetrical rods are placed orthogonally (xz and yz-planes in Fig. 3.3a), which provides the second property needed to minimize the influence of gravity, see Sec. 6.2. Note that this design is only meant to minimize the effect of gravity in the xy-plane.

3.1.1   Compact architectures

As mentioned in Sec. 1.5.7, we try to make our designs planar such that they can be miniaturized and are compatible with silicon microfabrication. The design presented in Fig. 3.1 and 3.3 can be modified to keep its functionality while having an architecture that is close to being planar (so-called *2.5D designs*), with a few three-dimensional elements (whose height is less than that of the wafer) that can be manufactured by double-sided etching of silicon-on-insulator (SOI) wafers (Maluf and Williams, 2004). We present here two examples that have not been previously published, namely the compact GIFP architectures with L-shaped flexures of Fig. 3.4 and 3.5 respectively.
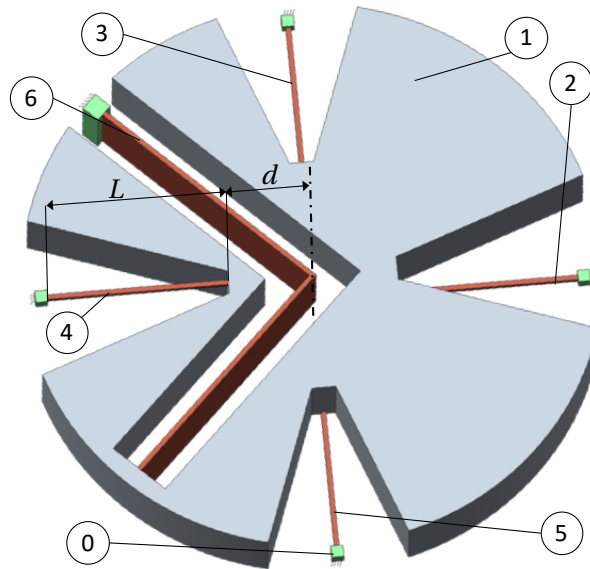
Figure 3.4 – Compact GIFP architecture with a L-shaped flexure replacing the torsional rod.

In the architecture presented in Fig. 3.4, the torsional rod (6) of Fig. 3.3a is replaced by an L-shaped flexure consisting of two perpendicular leaf springs in series, see Fig. 3.2b. The stiffness of this flexure element is high for a translation of the mobile part along the z axis

formed by the intersection of the mid-planes of perpendicular leaf springs (blocked DOF) and low for any other motion (Cosandier et al., 2017). It has thus the same five degrees-of-freedom as the rod flexure and has an equivalent behavior when the respective z axes are parallel, as depicted in Fig. 3.2. This architecture is better suited for minimizing the influence of gravity in any orientation of space than the one presented in Fig. 3.3. Indeed, the stiffness of the L-shape flexure is the same for positive or negative loads along the z axis whereas the torsional rod would be loaded either in tension or in compression. The effect of the transverse load on the bending stiffness of the L-shape flexure is of second order (Van Eijk, 1985), thus following the guidelines for spatial gravity effect minimization of Sec. 6.5.2.

Another way of making the architecture more planar is to replace one pair of bending rods by a pair of L-shaped flexures, as depicted in Fig. 3.5. In this case, the in-plane gravity effect minimization is maintained since they are symmetrically placed and the effect of load along their blocked DOF is of second order (Van Eijk, 1985), see Sec. 6.2.
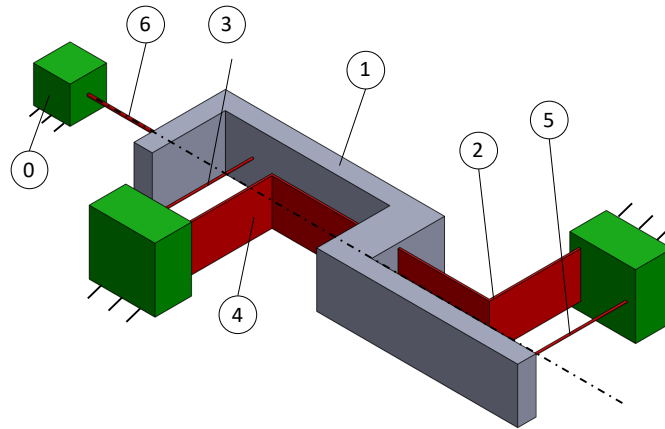
Figure 3.5 – Compact GIFP architecture with a pair of L-shaped flexures replacing a pair of bending rods.

3.1.2 Crossing ratio

The key parameter describing the characteristics of the GIFP is the crossing ratio $\delta = d/L$, where L is the length of the bending rods and d is the distance between their crossing point and their mobile extremity, see Fig. 3.3a. When $\delta \leq 0$, the rotation axis passes through the bending rods, as depicted in Fig. 3.3, and when $\delta > 0$, the rotation axis lies outside of the physical spring structure, see Fig. 3.4. It is analogous to the crossing ratio of the crossed flexure pivot described in Sec. 3.2.1. This parameter has a direct influence on the gravity sensitivity, stroke, restoring torque nonlinearity and parasitic shift of the pivot.

Remark 3.1.1. Due to interchangeability of the rotating rigid body and the fixed frame, it is sufficient to analyze the behavior of the pivot in the range $\delta \geq -0.5$. The results presented here are also valid for all other configurations by using $\delta' = -\delta - 1$.

3.2   The co-RCC

The co-RCC oscillator was introduced in (Thalmann et al., 2020). It is based on the design principle that two RCC flexure pivots "collaborate" to form a pivot with superior properties: the parasitic center shift of the RCC is used to tune the isochronism of the oscillator and its effect on the position of the COM is minimized, thus also minimizing the influence of gravity on the oscillator frequency. The co-RCC architecture is depicted in Fig. 3.6, where the flexures are represented by their pseudo-rigid-body equivalent (Howell et al., 2013). The rigid bars with pin joints and rotational springs at their extremities have equivalent force-deflection characteristics to the leaf springs used in the physical embodiment of Fig. 3.12.
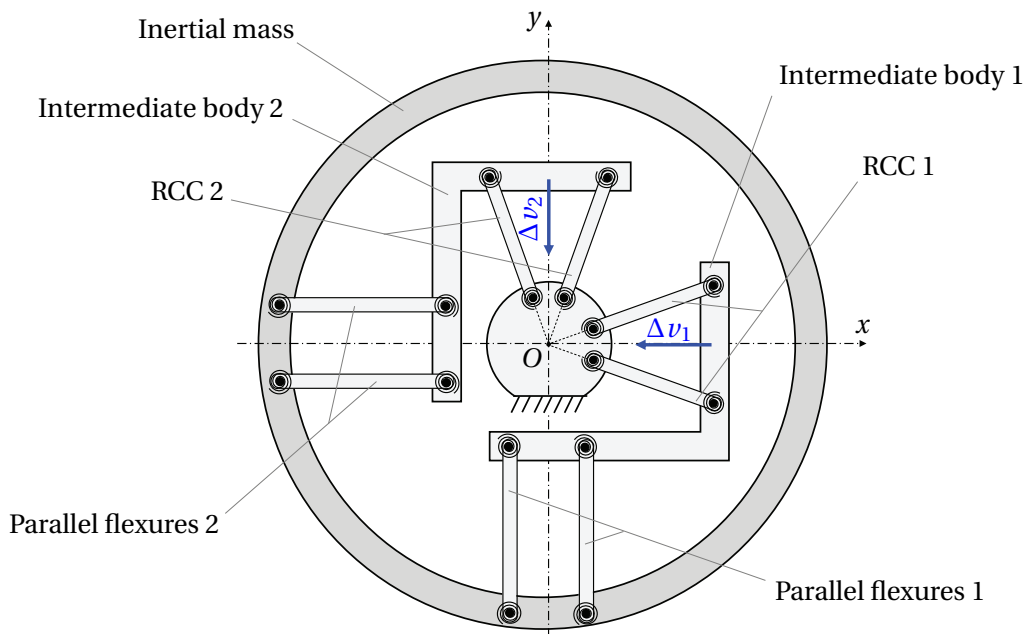
Figure 3.6 – Pseudo-rigid-body model of the co-RCC flexure pivot oscillator (Thalmann et al., 2020).

In the co-RCC design, the parasitic shift of the RCC flexures (labelled Δv_1 and Δv_2 in Fig. 3.6) deforms the neighboring parallel flexures, resulting in a nonlinear contribution of their stiffness to the restoring torque of the system that is of same order as the isochronism defect. The isochronism of the system can thus be tuned, without affecting any other crucial property (such as nominal stiffness, operating stroke, gravity sensitivity and center of rotation shift) by changing the stiffness of the parallel flexures. More details are given in Sec. 5.4.

We explain the design of the co-RCC by decomposing it into sub-elements. We start by describing its fundamental building block, the CFP (of which the RCC is a particular case), in Sec. 3.2.1. We then add a slider to it to form the half co-RCC in Sec. 3.2.2, and finally combine two of these elements in parallel to form the co-RCC in Sec. 3.2.3.

3.2.1 The crossed flexure pivot

The CFP, already introduced in Sec. 2.2.1, consists of a rigid-body attached to the ground by two symmetrically-crossed leaf springs, as shown in Fig. 3.7. The intersection of the flexures defines (to a first approximation) the axis of rotation of the pivot (Haringx, 1949). In the co-RCC architecture, the RCC configuration of the CFP depicted in Fig. 2.8a and 3.7b is used. This particular case has an advantageous planar architecture and a negative restoring torque nonlinearity (Thalmann et al., 2018) that will be used to tune the isochronism of the co-RCC, see Sec. 5.4.

(a) $\delta \leq 0$ (b) $\delta > 0$
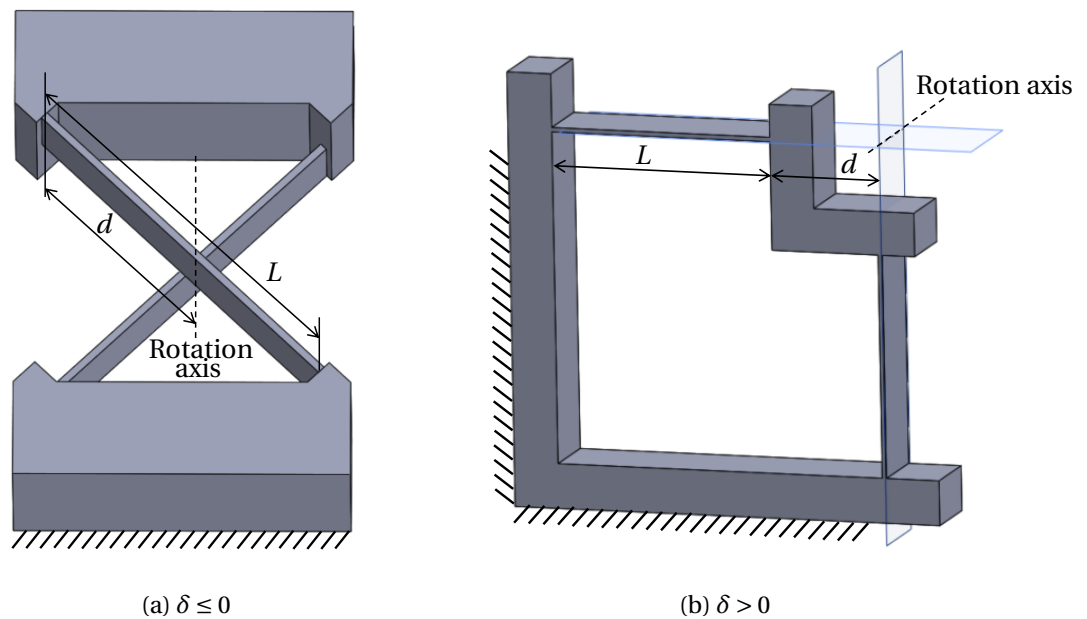
Figure 3.7 – CFP with (a) $\delta \leq 0$ and (b) $\delta > 0$ (RCC configuration).

Crossing ratio

The crossing ratio of the leaf springs is key to characterizing the behavior of the CFP and has a direct influence on its gravity sensitivity, stroke, restoring torque nonlinearity and parasitic shift. It is described by the parameter $\delta = d/L$, where L is the length of the bending rods and d is the distance between their crossing point and their mobile extremity, see Fig. 3.7. When $\delta \leq 0$, the rotation axis passes through the bending rods, as depicted in Fig. 3.7a, and when $\delta > 0$, the rotation axis lies outside of the physical spring structure, corresponding to the RCC configuration depicted in Fig. 3.7b. This is analogous to the crossing ratio of the GIFP described in Sec. 3.1.2 and Remark 3.1.1 also applies.

Remark 3.2.1. The pivots depicted in Fig. 3.7 have a 90 degree angle between the leaf springs. This is a particular case and it is sometimes convenient to use a different value, see Sec. 2.2.2 and Sec. 5.4. We use the parameter α to indicate the half angle between the leaf springs, see Fig. 4.4.

Parasitic shift

We define a local coordinate system for the CFP whose origin lies at the intersection of the neutral axes of the leaf springs as depicted in Fig. 2.8a. Axis v is parallel to the bisector of the angle formed by the leaf springs, axis w is perpendicular to the plane holding the neutral axes and u is the third orthogonal axis.

We mentioned in Sec. 2.2.2 that the motion of the CFP closely approximates a rotation with axis lying on the intersection of the midplanes of the leaf springs at rest position, as depicted in Fig. 3.7. In reality, a translation of the rotation axis along the uv-plane occurs as the pivot rotates, the so-called parasitic shift. Zhao and Bi (2010a) give analytical expressions for the components of the parasitic shift along the u and v axes. For small rotations of slender flexures such as leaf springs ($l > 10h$), the v-component is of second order of the rotation angle and the u-component, which is of third order, can be neglected.

3.2.2 The half co-RCC

The half co-RCC element depicted in Fig. 3.8 is obtained by adding a slider between the RCC and the main rigid body, where the axis of the slider is parallel to the v-axis of the RCC. This element has two degrees-of-freedom: one rotation around center O and one translation along v. As we will see in Sec. 3.2.3, the additional DOF allows to tune the isochronism of the oscillator, to minimize the influence of gravity and to avoid overconstraining.
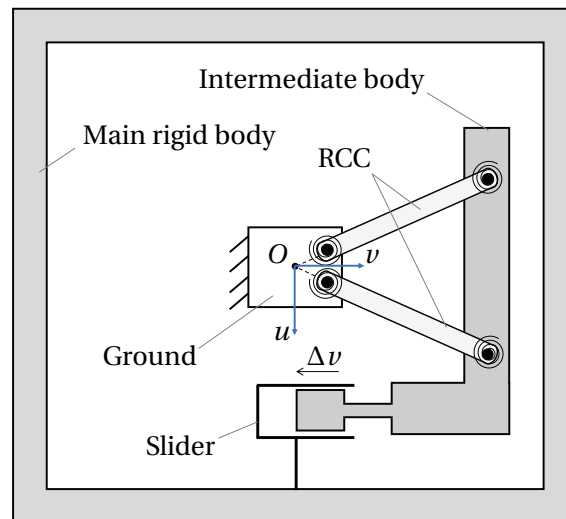
Figure 3.8 – Design of the half co-RCC.

3.2.3 The co-RCC flexure pivot

The co-RCC depicted in Fig. 3.9 consists of two half co-RCC arranged in parallel, at a 90 degree angle, with coinciding axes of rotation. The first half co-RCC consists of the "RCC 1" in series

with the "Slider 1" and the second consists of the "RCC 2" in series with the "Slider 2". They share the same main rigid body and the COM of the system is placed at its center of rotation O. We assume that the intermediate bodies have negligible mass. The system has one DOF and no overconstraint in the xy-plane. Note that the out-of-plane overconstraints can be overlooked assuming that the mechanism is monolithically fabricated. Taking advantage of the elasticity of the RCC flexures, if the main rigid body has a non-zero inertia J, this flexure pivot behaves as a rotational oscillator.
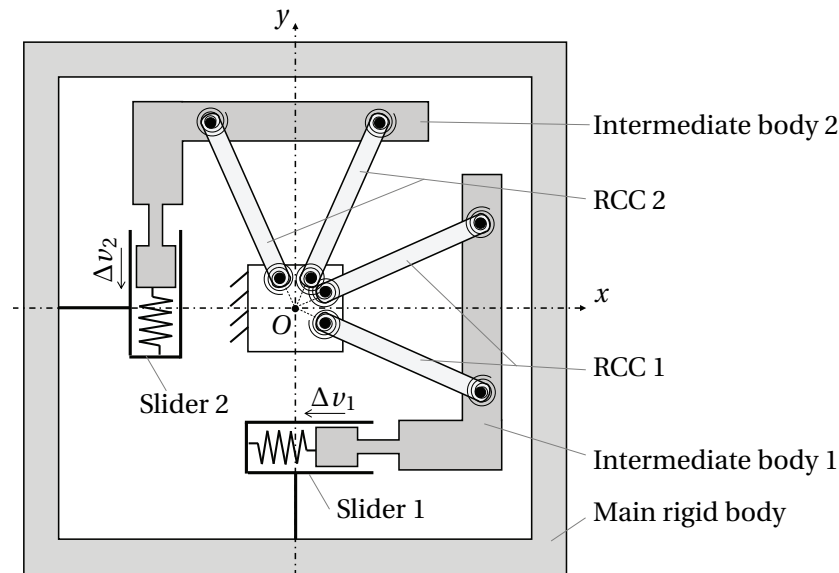
Figure 3.9 – Design of the co-RCC flexure pivot.

Through the parallel arrangement of two half co-RCC elements, the translation of the main rigid body allowed by one half co-RCC is blocked by the other one. As a result, when the system rotates, the parasitic shift of the RCC pivots, which is along the sliding axis of their respective half co-RCC (see Sec. 3.2.1), does not affect the main rigid body (as this motion is blocked by the other half co-RCC). The motion of the main rigid body closely approximates a rotation about point O, which we define as the rotation of the co-RCC.

As in the GIFP, The fact that the parasitic motion of the COM is minimized is one of the properties used to minimize the influence of gravity on the oscillator frequency. Again, this effect can be seen from the canceling of first order effects of gravity on the rotational stiffness of the pivot in Sec. 4.3.1. The second property used to minimize the influence of gravity is that the two half co-RCC elements are placed orthogonally, see Sec. 6.2.

Since the translation of the main rigid body is blocked, the parasitic shifts of each RCC pivot results in a relative linear motion between the main and intermediate bodies, labelled Δv_1 and Δv_2 in Fig. 3.9. In the flexure implementation of Fig. 3.12, the sliders are realized with parallel leaf springs which are known to closely approximate a sliding motion (Cosandier et al., 2017, Sec. 4.1).[1] The deflection of these flexures caused by the RCC parasitic shift is of second

---

[1] The parallel leaf springs also exhibit a parasitic motion that is of second order of the sliding motion (Cosandier

order of the rotation angle (Zhao and Bi, 2010a) and their stiffness, depicted as linear springs in Fig. 3.9, can be used to tune the isochronism of the oscillator, see Sec. 5.4.

3.2.4 Generalization

The design can be generalized by using any type of CFP, by changing the order of the joints of the half co-RCC such as depicted in Fig. 3.10a, or by using rotational joints instead of slider joints such as depicted in Fig. 3.10b. Additionally, any type of flexures that have the force deflection characteristic of the pseudo-rigid-body model depicted in Fig. 3.6 and 3.10 can be used. Figure 3.11 shows examples of how the ideal connecting rod (a) can be realized with a leaf spring (b), or by replacing its pivots with notch flexure hinges (c), cartwheel flexure hinges (d), crossed flexure pivots (e), RCC flexure pivots (f), or a combination of the previous pivots (g) (Cosandier et al., 2017).
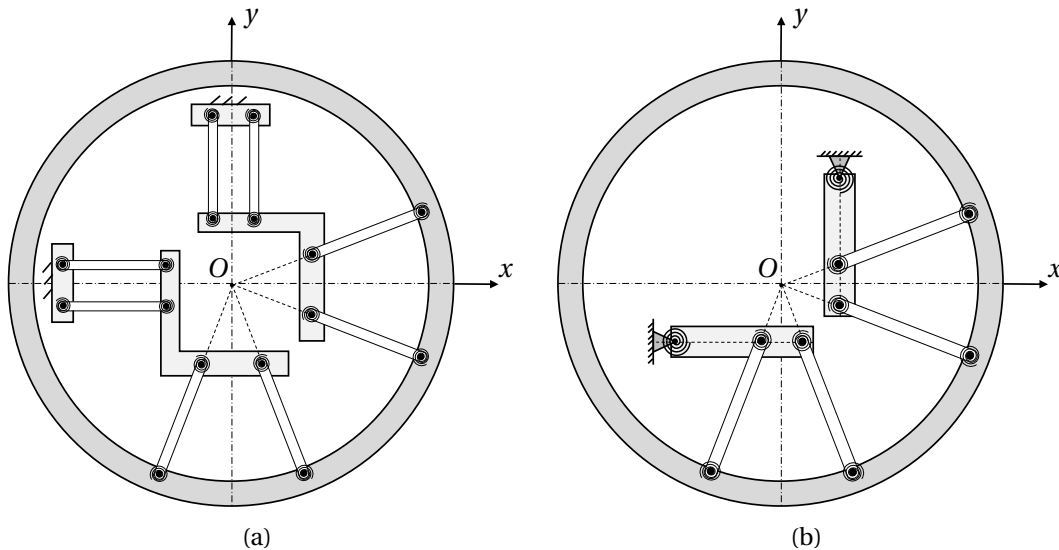
Figure 3.10 – Examples of co-RCC architectures where (a) the order of the joints of the half co-RCC are inverted and (b) rotational joints are used instead of slider joints in comparison to the design in Fig. 3.6 (Kahrobaiyan et al., 2020).

3.2.5 Qualitative design validation

We manufactured a mock-up to validate qualitatively the kinematics of the co-RCC pivot. Figure 3.12 shows a mock-up manufactured by laser cutting a 5 mm thick Polyoxymethylene (POM) sheet. It has an outer diameter of 150 mm and an admissible angular stroke of ±26 degrees. This hardware showed that the system behaves qualitatively as a pivot (one DOF and a motion of the main body closely approximating a rotation about point O) while having a linear relative motion between the intermediate bodies and the main body, see Fig. 3.12b.

---

et al., 2017). In the co-RCC geometry, this motion is of fourth order of the rotation angle and can thus be neglected.
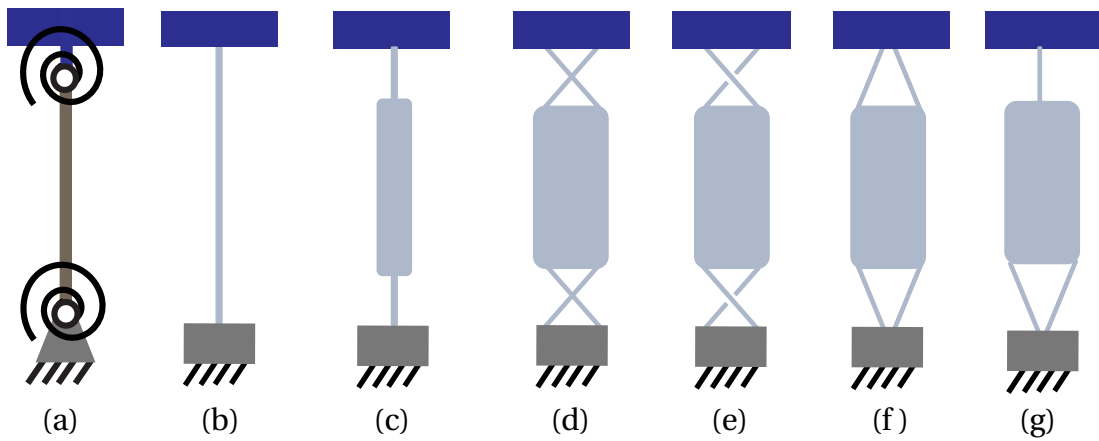
Figure 3.11 – Flexure equivalents for the ideal connecting rod (a).
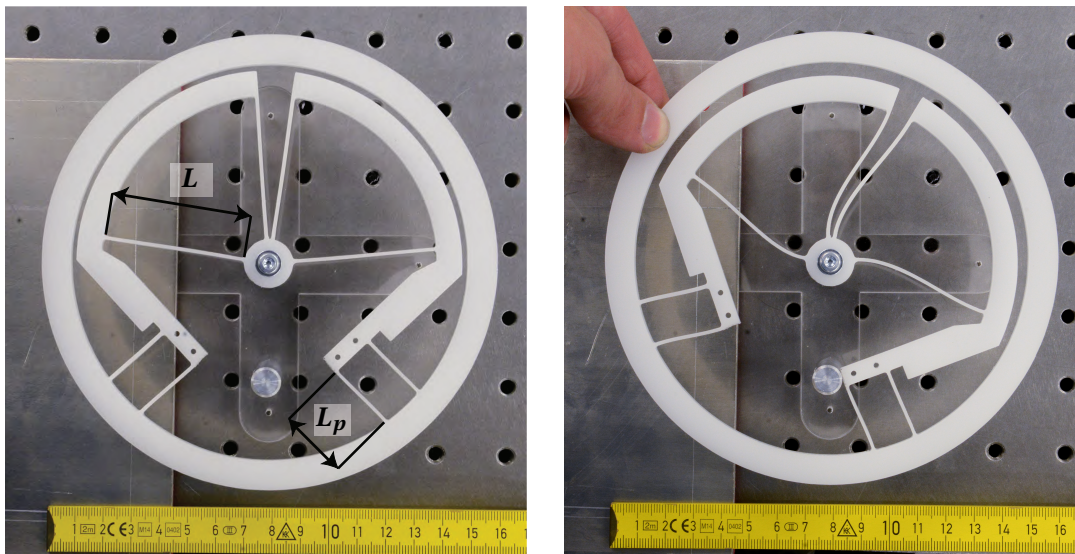
(a) Mock-up at rest position. The length L_p is used to tune isochronism. To make our results independent of scale, we quantify this using the dimensionless parameter $\lambda = L_p/L$ (with L constant).

(b) Mock-up rotated by 26 degrees. An increased gap between the inertial mass and the intermediate bodies and a deformation of the parallel leaf springs can be observed as a result of the parasitic shift of the RCC pivots ($\Delta \nu_1$ and $\Delta \nu_2$ in Fig. 3.6).

Figure 3.12 – Mock-up of the co-RCC flexure pivot oscillator demonstrating its qualitative behavior.

3.3 The RDCO

The Rotation-Dilation Coupled Oscillator depicted in Fig. 3.13a has been introduced in (Thalmann and Henein, 2019) together with all the design variants of this section. The RDCO is a rotational oscillators whose inertia changes as it rotates. This inertia variation affects the isochronism of the oscillator and can be used to tune it. As in the co-RCC, the deflection of some of its flexures is of second order of the rotation angle and this property can also be used to tune the isochronism of the oscillator. Additionally, the architecture exhibits a rotational symmetry that minimizes the influence of gravity in the plane of oscillation on the frequency, see Sec. 6.2.
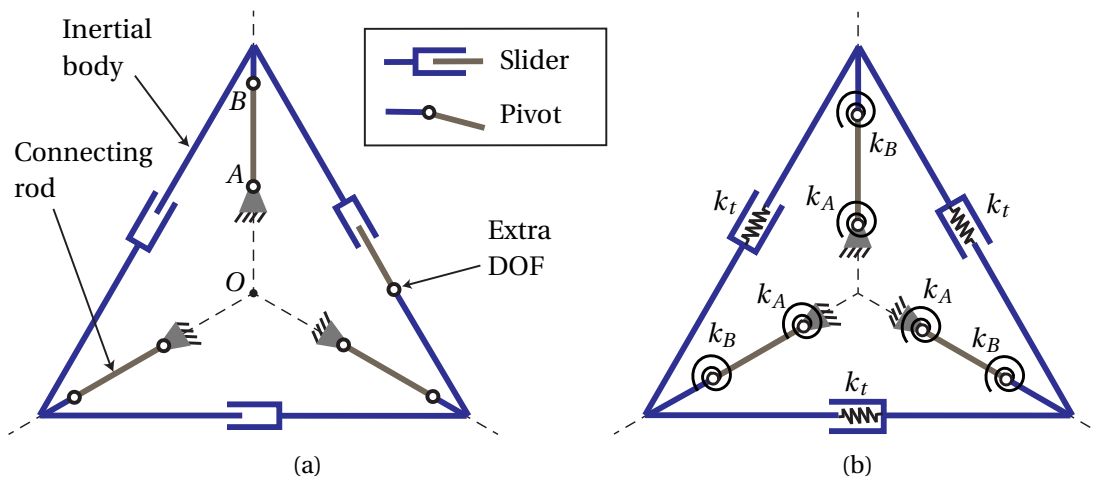
Figure 3.13 – Kinematic diagram of the RDCO using (a) ideal joints and (b) elastic joints.

Figure 3.13 shows a kinematic diagram of the RDCO. The mechanism consists of $n \geq 3$ inertial bodies linked to each other by sliders (prismatic joints) to form a loop ($n = 3$ in Fig. 3.13). Each rigid body is linked to the ground by a connecting rod with a pivot at both extremities, one connected to the ground (pivot A) and the other to the inertial body (pivot B). The joints are placed such that they have rotational symmetry of order n with respect to the center O of the system. An extra DOF is added by allowing a pivoting motion in one of the sliders, see Fig. 3.13a. The sole purpose of this extra DOF is to avoid overconstraining the system; it is not activated during the motion of the system. Note that the extra DOF is neglected in the following figures to simplify the representations.

In order for this system to act as a mechanical oscillator, spring components must be added. This happens naturally when the ideal linkages of Fig. 3.13a are implemented with flexure linkages and is represented schematically in Fig. 3.13b. Rotational springs are added to the ideal pivot joints and linear springs are added to the ideal sliders. This applies to all the kinematic diagrams presented in this section. Examples of flexure implementation are shown in Sec. 3.3.3.

3.3.1 Rotation-dilation coupling

The kinematic behavior of the system is determined by the dimensionless ratio $\delta = d/L$, where d and L are described in Fig. 3.14. We define d as the distance from the center O of the system to the axis of pivot A. We define L as the distance from the axis of pivot A to the axis of pivot B. The signs of d and L are defined with respect to the direction from O to B, represented by axis y in Fig. 3.14.

We classify the RDCO architectures according to three domains of the parameter δ, summarized in Fig. 3.14 and Table 3.1.

(a) When $\delta > 0$, d and L are of same sign. The connecting rods are connected to the ground between the inertial loop and point O.

(b) When $-1 < \delta < 0$, d and L are of opposite sign and $d < L$. The connecting rods cross each other inside of the inertial loop.

(c) When $\delta < -1$, d and L are of opposite sign and $d > L$. The connecting rods are connected to the ground outside of the inertial loop.
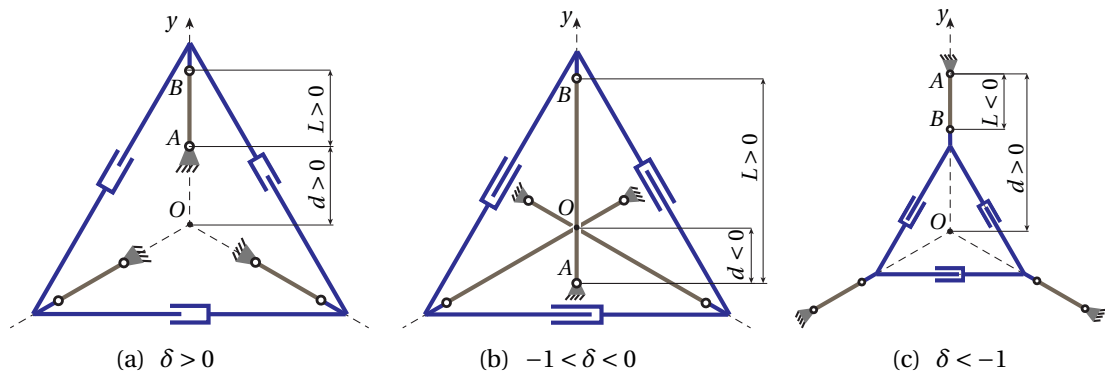
Figure 3.14 – Definitions of d, L and $\delta = \frac{d}{L}$ for the RDCO.

Figure 3.15 shows the motion of the system as it is displaced from its rest position. We call this motion *rotation-dilation coupling*, where the rotation is defined by the angle θ swept by a vector from the center O to a point P on the inertial body and the dilation is defined by the change of length of this vector. As shown in Table 3.1, the parameter δ influences this dilation:

- When $\delta > 0$, $\left\|\overrightarrow{OP(\theta)}\right\| < \left\|\overrightarrow{OP(0)}\right\|$ and the inertial bodies move towards each other. We call it a *negative dilation*.

- When $\delta < 0$, $\left\|\overrightarrow{OP(\theta)}\right\| > \left\|\overrightarrow{OP(0)}\right\|$ and the inertial bodies move away from each other. We call it a *positive dilation*.
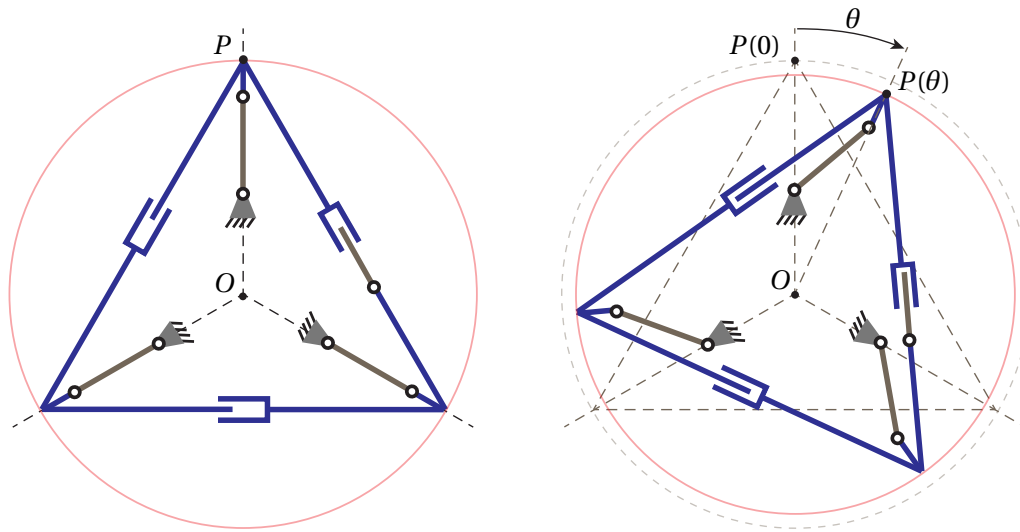
Figure 3.15 – Rotation-dilation coupling.

	(a) $\delta > 0$	(b) $-1 < \delta < 0$	(c) $\delta < -1$
Nominal position			
Rotated			
	Negative dilation	Positive dilation	Positive dilation

Table 3.1 – Influence of the parameter δ on the kinematics of the RDCO.

Particular case: $\delta = 0$

When $\delta = 0$, the connecting rods are attached to the ground at the center of the system and the size of the system stays constant as it rotates (no dilation).

Particular case: $\delta = -1$

The kinematics depicted in Fig. 3.16 corresponds conceptually to the case when $\delta = -1$, i.e., d and L are of opposite sign and go to infinity. It is noted that circular motion becomes straight line motion when the radius goes to infinity. This straight line motion can be implemented by replacing the pivots that attach the connecting rods to the ground by sliders with axis tangential to a circle with center O. The figure is the same for cases (b) and (c) of Fig. 3.14. Note that since $\delta < 0$, the dilation of this system is positive.

(a) Nominal position   (b) Rotated
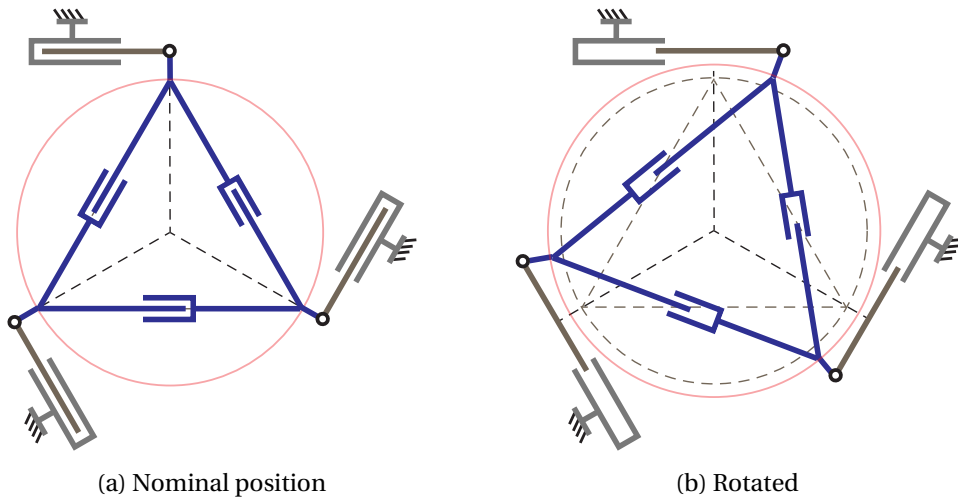
Figure 3.16 – Translational RDCO ($\delta = -1$).

3.3.2 Order of symmetry

The RDCO can be realized with any order of rotational symmetry $n \geq 3$. The order n of the rotational symmetry corresponds to the number of inertial bodies and connecting rods. Fig. 3.17 shows variants with $n = 3$ to 5.

(a) $n = 3$ (b) $n = 4$ (c) $n = 5$
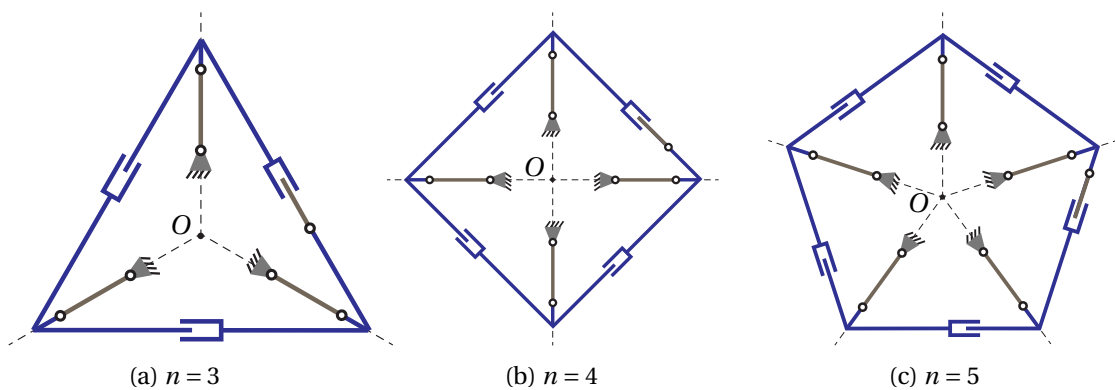
Figure 3.17 – RDCO with different orders of symmetry.

3.3.3 Examples of flexure implementation

In terms of flexure implementation, any kind of flexures presenting equivalent properties to the ideal kinematic diagrams presented here can be used. Figure 3.11 shows different flexure equivalents for the connecting rods, as explained in Sec. 3.2.4. The sliders can for example be implemented with parallel leaf springs, as in the co-RCC architecture.

A wide range of variants arises from the combination of the designs described in Table 3.1 with the different orders of symmetry depicted in Fig. 3.17 and the different flexure elements described in Fig. 3.11. They offer different properties and certain combinations can be particularly interesting, as will be discussed in Sec. 5.5.3. Figure 3.18 shows 4 examples with order of symmetry $n = 4$. Note that in these designs, the extra DOF is omitted assuming that there is enough flexibility in the system to release the overconstraint.

(a) $\delta < -1$, notch hinges

(b) $\delta > 0$, notch hinges

(c) $\delta > 0$, notch hinge and CFP

(d) $\delta > 0$, notch hinge and RCC pivot
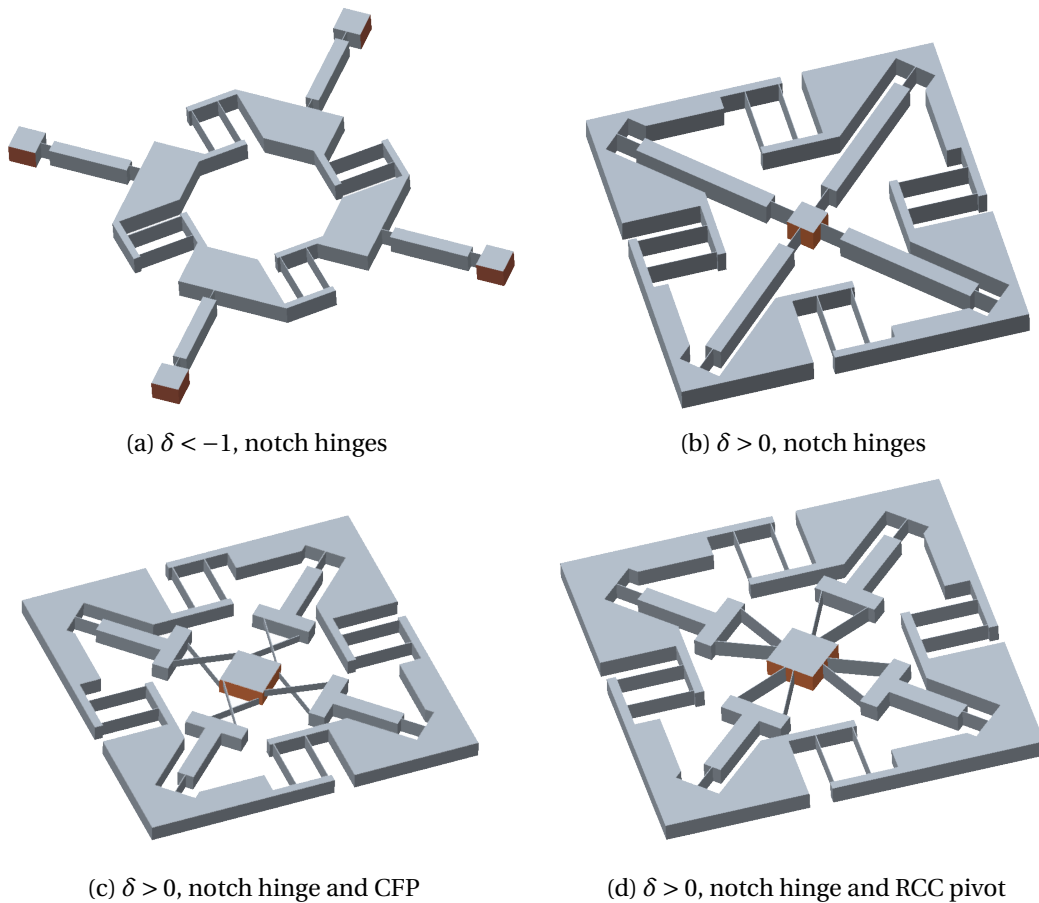
Figure 3.18 – Examples of flexure implementations of the RDCO with $n = 4$. The connections to the fixed frame are represented in orange.

Figure 3.19 shows three ways of implementing the configuration with $-1 < \delta < 0$ (where the connecting rods cross each other in Table 3.1) while keeping the design planar. This can be of advantage for manufacturing and compactness. In designs 3.19a and 3.19b the rigid part of

the connecting rods is used to go around the attachment point of the other connecting rods. In design 3.19c, the remote center of rotation property of the RCC pivot is used to virtually place the pivot of the connecting rods on the other side of the center of the system O.
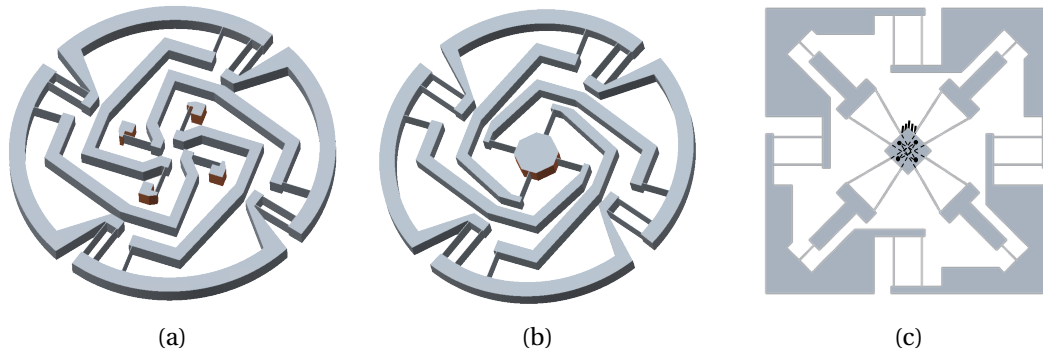
Figure 3.19 – Planar designs for the RDCO with $-1 < \delta < 0$ and $n = 4$ using connecting rods with (a, b) notch hinges and (c) a notch hinge and a RCC pivot. The connections to the fixed frame are represented in orange.

3.3.4 Qualitative design validation

We manufactured mock-ups to validate qualitatively the kinematics of the RDCO. The configurations (a) and (b) of Table 3.1 are shown in Fig. 3.20 and 3.21 respectively. The mock-ups were manufactured by laser cutting a 5 mm thick Polyoxymethylene (POM) sheet. They have an outer diameter of 200 mm and an admissible angular stroke of approximately ± 20 degrees for the configuration with $\delta > 0$ and ± 25 degrees for the configuration with $-1 < \delta < 0$. This hardware showed that the system behaves qualitatively as predicted: the system has one DOF and a motion of the main body closely approximating a rotation about point O coupled to a dilation. The variation in diameter of the mock-ups can be observed relatively to the red circle printed in the background. The two systems confirm that the dilation is negative when $\delta > 0$, see Fig. 3.20, and positive when $-1 < \delta < 0$, see Fig. 3.21.

Remark 3.3.1. For reference purposes, pairs of parallel leaf springs were placed behind the functional ones in the mock-up of Fig. 3.20. These flexures are only connected on one side and do not deflect with the oscillator. They enable to highlight the deflection of the parallel leaf springs as the pivot rotates, as can be seen in Fig. 3.20b. This motion is of second order of the rotation angle and plays a role in the restoring torque nonlinearity of the pivot, see Sec. 5.5.4.

Remark 3.3.2. Due to its three-dimensional design, the mock-up of Fig. 3.21 had to be assembled in multiple parts. As a result, the connecting rods do not cross perfectly in the center in the nominal position and one of the parallel leaf springs was removed to prevent overconstraining the pivot. This is equivalent to the extra DOF of Fig. 3.13a.

(a)   (b)
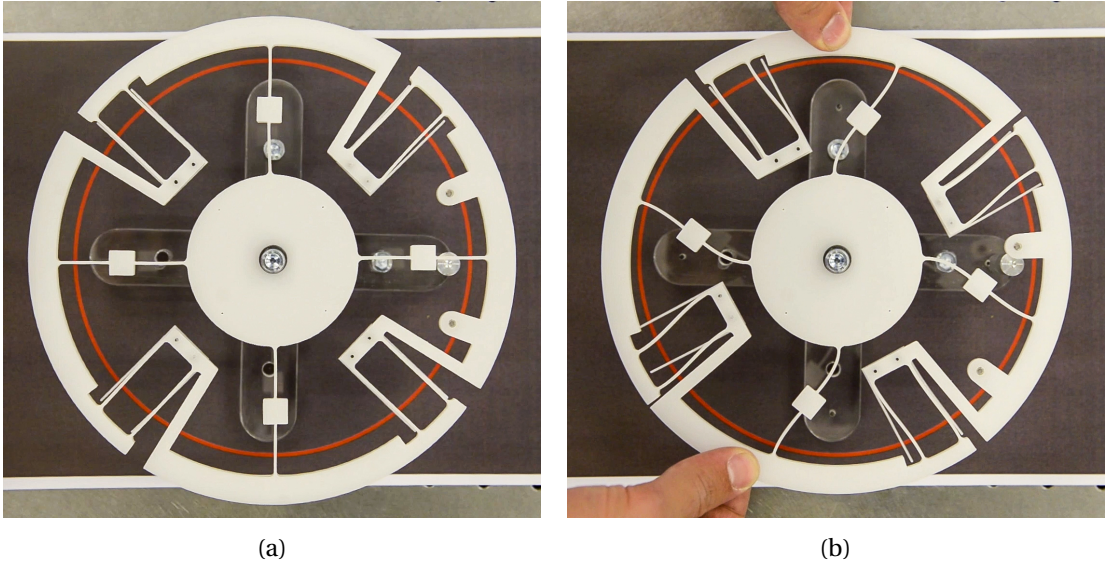
Figure 3.20 – Mock-up of the RDCO with $\delta > 0$ and $n = 4$ in (a) nominal position and (b) rotated showing a negative dilation.

(a)   (b)
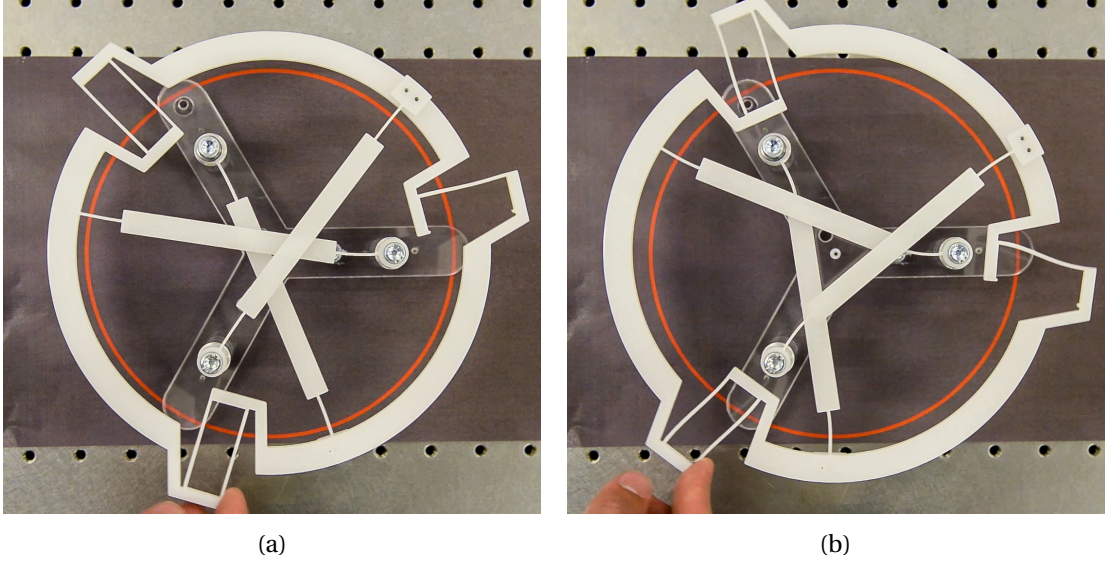
Figure 3.21 – Mock-up of the RDCO with $-1 < \delta < 0$ and $n = 3$ in (a) nominal position and (b) rotated showing a positive dilation.

3.4 Chapter conclusion

In this chapter, the three new families of flexure pivot watch oscillators of this thesis were introduced. Pseudo-rigid-body models were used to describe their general design and kinematics. Examples of variants and flexure implementations were given. The kinematics of the three oscillators were validated qualitatively on mock-ups, that is: one DOF in rotation for all oscillators, a second order motion of the parallel leaf springs for the co-RCC and RDCO, and a variation in diameter as it rotates for the RDCO.

4 Rotational stiffness

As introduced in Chapter. 1, the main limitations to the introduction of new flexure pivot oscillators as mechanical watch time bases are their isochronism defect and the influence of gravity on their frequency. The principal way that these effects occur is though variations in the rotational stiffness of the oscillators.

In the ideal case, the simple rotational harmonic oscillator satisfies

$$J\ddot{\theta} + k\theta = 0, \tag{4.1}$$

which has solution

$$\theta(t) = \Theta \sin(\omega_0 t + \Phi), \tag{4.2}$$

where Θ is the amplitude, $\omega_0 = \sqrt{k/J}$ is the angular frequency and Φ is a phase depending on initial conditions. The stiffness k and inertia J stay constant in all conditions and the frequency ω_0 is constant, leading to ideal timekeeping performance.

In reality however the stiffness k can be function of angular displacement θ, a common property for flexure pivots, that leads to an isochronism defect. This will be treated in detail in Chapter 5. It can also happen that the stiffness of the oscillator is function of the orientation of the oscillator with respect to gravity, leading to an undesired timekeeping defect linked to the position of the oscillator that will be treated in detail in Chapter 6.

In this chapter, formulas are derived for the rotational stiffness of the new oscillators presented in Chapter 3 on which the analyses of Chapters 5 and 6 will be based.

4.1 Rotational stiffness of the crossed flexure pivot

The first step to analysing the rotational stiffness of our new pivots is to analyse that of the crossed flexure pivot (CFP) introduced in Sec. 2.2.2 and 3.2.1. This step is motivated by the following reasons:

- The CFP, which is the first flexure pivot oscillator used in a mechanical watch (Barrot et al., 2014), serves as benchmark to highlight the improvements brought by the new designs in terms of isochronism tuning and gravity sensitivity.

- Applying our modelling method on a well studied case allows to validate it before applying it to our new designs.

- The results will be reused to calculate the rotational stiffness of the GIFP in Sec. 4.2 as its crossed bending rods behave in the same manner.

- The results will be reused to calculate the rotational stiffness of the co-RCC in Sec. 4.3 as the CFP (in RCC configuration) is one of the building blocks of its design, see Sec. 3.2.3.

We derive the rotational stiffness of the loaded CFP under the following assumptions:

(a) All flexures have identical length L and moment of inertia of the cross-section I and are made of the same material with Young's modulus E.

(b) The rotations are small and terms can be expressed using series expansions around $\theta = 0$.

(c) The load F on the pivot is small and terms can be expressed using series expansions around $F = 0$.

(d) The COM of the system is at point O and remains constant during rotation. The effect of gravity can thus be represented by a force F applied to point O.

(e) We consider the flexure elements to be elastic and the other bodies as rigid.

(f) The flexures are not subject to shear or torsion and, with Assumption (b), Euler-Bernoulli beam theory can be used to calculate their deflection behavior.

(g) The out-of-plane bending stiffness of the pivot is much higher than the in-plane (uv-plane) bending stiffness. We only consider in-plane mechanical behavior and assume no out-of plane motion. The u, v, w coordinate system is defined in Fig. 2.8a.

(h) We only consider the effect of loads in the uv-plane since the out-of-plane components of the loads will be treated separately.

(i) The parasitic shift is small and the terms associated with the parasitic shift in the lateral deflections of the beams produce negligible restoring torques. Note that this is a standard assumption in the analysis of flexure pivots (Zhao and Bi, 2010a,b).

(j) During oscillation, rotation of the pivot gives rise to shear forces and leads to slight changes in axial loads caused by the load F. We consider this effect to be negligible.

The development consists of the following steps:

1. Express the rotational stiffness of the CFP considering each flexure as a loaded cantilever beam.
2. Apply an external force at the center of rotation.
3. Express the rotational stiffness of the pivot for small loads and small displacements using series expansion.
4. Verify the results using the finite element method.
5. Improve the model using the findings from the finite element method.

4.1.1 Cantilever beam model

Figure 4.1 shows a crossed flexure pivot subject to a rotation of angle θ. Note that in the rotated position, the center of rotation is located at the crossing point O' of the tangents to the beams at their mobile extremities. This translation of the rotation axis as the pivot rotates corresponds to the parasitic shift described in Sec. 3.2.1.

(a)   (b)
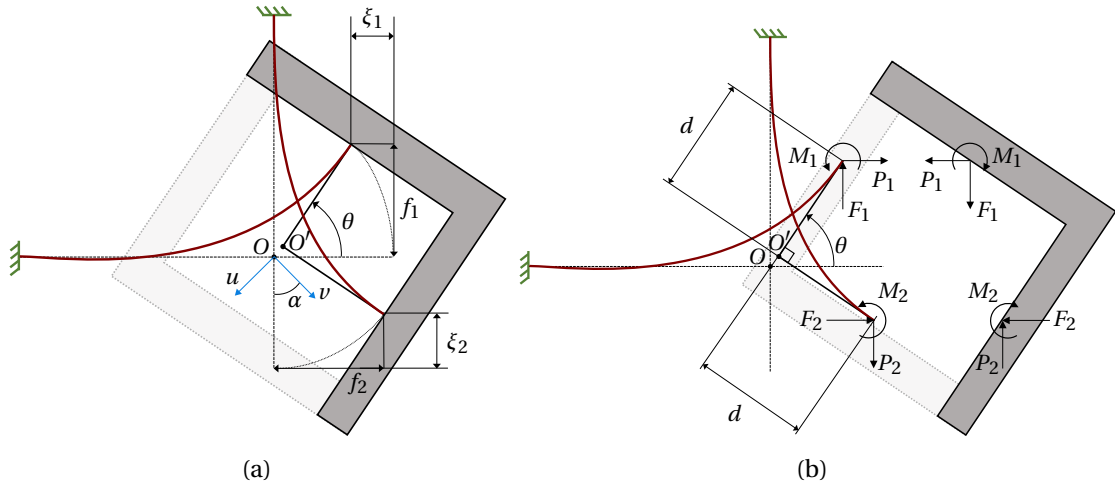
Figure 4.1 – (a) Top view and (b) exploded view of a crossed flexure pivot subjected to a rotation of angle θ around axis x.
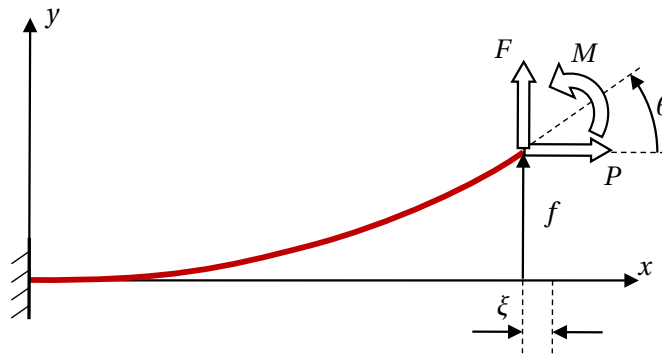
Figure 4.2 – Cantilever beam under axial load P, shear force F and bending moment M with axial shortening ξ, lateral deflection f and slope θ at its mobile extremity.

Each flexure of this pivot can be modelled as a cantilever beam under an axial load P with lateral deflection f and slope θ at its mobile extremity, see Fig. 4.2. For such beam, Euler-Bernoulli beam theory gives the following force-displacement relationship (Awtar et al., 2007; Plainevaux, 1956):

$$\begin{pmatrix} FL^2/EI \\ ML/EI \end{pmatrix} = \mathbf{K} \begin{pmatrix} f/L \\ \theta \end{pmatrix}, \tag{4.3}$$

where M and F denote respectively the bending moment and shear force at the mobile

extremity of the cantilever beam and $\mathbf{K}$ is the stiffness matrix

$$\mathbf{K} = \frac{\sqrt{\lambda}}{2\left(1 - \cosh\sqrt{\lambda}\right) + \sqrt{\lambda}\sinh\sqrt{\lambda}} \begin{pmatrix} \lambda\sinh\sqrt{\lambda} & \sqrt{\lambda}\left(1 - \cosh\sqrt{\lambda}\right) \\ \sqrt{\lambda}\left(1 - \cosh\sqrt{\lambda}\right) & \sqrt{\lambda}\cosh\sqrt{\lambda} - \sinh\sqrt{\lambda} \end{pmatrix}, \qquad (4.4)$$

where $\lambda = PL^2/EI$ is the normalized axial load. Note that we consider the axial load P to be positive when it is tensile and negative when it is compressive.

We derive the rotational stiffness k_r of the crossed flexure pivot by dividing the restoring torque about point O' by the rotation angle θ. Summing the effects of the loads at the extremities of the two cantilever beams depicted in Fig. 4.1b yields

$$k_r = \frac{M_1 + M_2 + (F_1 + F_2)\,d\cos\theta - (P_1 + P_2)\,d\sin\theta}{\theta}, \qquad (4.5)$$

where the subscripts 1 and 2 refer to the two respective beams.

Remark 4.1.1. In this work we define the rotational stiffness by the *secant stiffness*, that is the restoring torque divided by the angular displacement $k_{\text{sec}} = \frac{M(\theta)}{\theta}$. This quantity should not be confused with the *tangent stiffness*, that is the derivative of the restoring torque $k_{\text{tan}} = \frac{dM}{d\theta}$. The difference between the two definitions is graphically illustrated in Fig. 4.3.
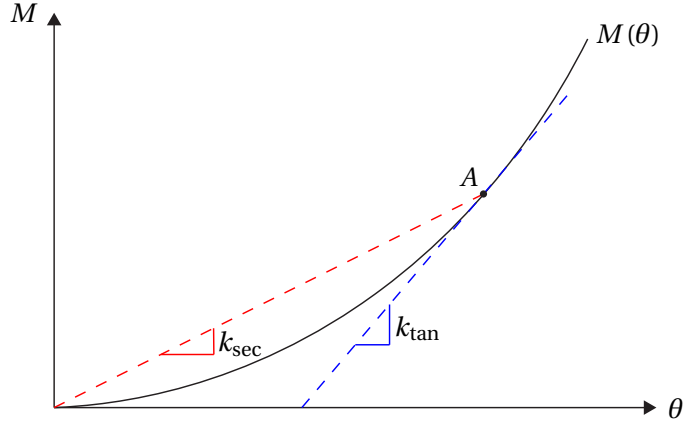
Figure 4.3 – Definition of secant stiffness k_{sec} and tangent stiffness k_{tan} at point A.

The lateral deflections of the beams depicted in Fig. 4.1a are

$$f_1 = d_c\sin\theta - \overrightarrow{OO'}\cdot\mathbf{e}_2, \quad f_2 = d_c\sin\theta + \overrightarrow{OO'}\cdot\mathbf{e}_1, \qquad (4.6)$$

where $\mathbf{e}_1$ and $\mathbf{e}_2$ denote the unit vectors along the neutral axes of beams 1 and 2 respectively. Using Assumption (i), this becomes $f_1 = f_2 = d_c\sin\theta$ and substituting Eq. (4.3) into Eq. (4.5) yields

$$k_r = \frac{EI}{L}\left[\begin{pmatrix} -\delta\cos\theta & 1 \end{pmatrix}(\mathbf{K}_1 + \mathbf{K}_2)\begin{pmatrix} -\delta\frac{\sin\theta}{\theta} \\ 1 \end{pmatrix} + \delta\,(\lambda_1 + \lambda_2)\frac{\sin\theta}{\theta}\right]. \qquad (4.7)$$

The stiffness matrices $\mathbf{K}_1$ and $\mathbf{K}_2$ can be calculated by using the respective value of λ for

each flexure in Eq. (4.4). Note that the sign of δ is defined in Fig. 3.7 and that $\delta = -\frac{|d|}{|L|}$ in the configuration of Fig. 4.1.

4.1.2 Central loading

Following Assumption (d), the effect of gravity corresponds to a force F applied on the mobile part in point O, at an angle φ such as depicted in Fig. 4.4. When the pivot is not rotated ($\theta = 0$), the shear forces are zero ($F_1 = F_2 = 0$) and the axial loads of the beams are

$$P_1 = \frac{F}{2}\left(-\frac{\sin\varphi}{\sin\alpha} + \frac{\cos\varphi}{\cos\alpha}\right) \quad \text{and} \quad P_2 = \frac{F}{2}\left(\frac{\sin\varphi}{\sin\alpha} + \frac{\cos\varphi}{\cos\alpha}\right), \quad (4.8)$$

where φ is the angle between the gravity load and the ν axis and α is the half angle between the RCC flexures.
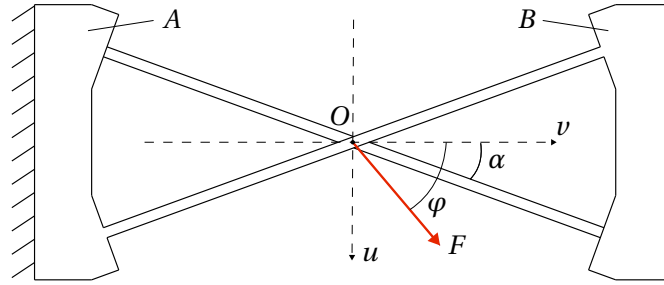
Figure 4.4 – Top view of a crossed flexure pivot with gravity load F acting on rigid body B at its center of rotation.

4.1.3 Approximation by series expansion

In order to characterize the behavior for small loads, we use the series expansion of the hyperbolic functions in Eq. (4.4) to obtain the following formula for the stiffness matrix

$$\mathbf{K} = \mathbf{K}_0 + \frac{\lambda}{30}\begin{pmatrix} 36 & -3 \\ -3 & 4 \end{pmatrix} - \frac{\lambda^2}{12\,600}\begin{pmatrix} 18 & -9 \\ -9 & 22 \end{pmatrix} + \mathcal{O}\left(\lambda^3\right), \quad (4.9)$$

where $\mathbf{K}_0$ is the stiffness matrix of a cantilever beam undergoing no axial load

$$\mathbf{K}_0 = \begin{pmatrix} 12 & -6 \\ -6 & 4 \end{pmatrix}. \quad (4.10)$$

Substituting Eq. (4.9) into Eq. (4.7) with the respective axial loads in each flexure given by Eq. (4.8) and using the series expansion of trigonometric functions around $\theta = 0$, we arrive at

49

the following formula for the rotational stiffness of crossed flexure pivot:

$$
\begin{aligned}
k_r = k_{r,0} + \frac{EI}{12\,600L} & \left[1680 \left(9\delta^2 + 9\delta + 1 \right) \bar{F} \frac{\cos\varphi}{\cos\alpha} - \left(9\delta^2 + 9\delta + 11 \right) \bar{F}^2 \left(\frac{\cos^2\varphi}{\cos^2\alpha} + \frac{\sin^2\varphi}{\sin^2\alpha} \right) \right. \\
& - 100\,800 \left(2\delta^2 + \delta \right) \theta^2 - 420 \left(24\delta^2 + 7\delta \right) \bar{F}\theta^2 \frac{\cos\varphi}{\cos\alpha} \\
& \left. + 3 \left(2\delta^2 + \delta \right) \bar{F}^2 \theta^2 \left(\frac{\cos^2\varphi}{\cos^2\alpha} + \frac{\sin^2\varphi}{\sin^2\alpha} \right) \right] + \mathcal{O}\left(\theta^4\right) + \mathcal{O}\left(\bar{F}^3\right),
\end{aligned}
\tag{4.11}
$$

where

$$
k_{r,0} = 2\frac{EI}{L} \begin{pmatrix} -\delta & 1 \end{pmatrix} \mathbf{K}_0 \begin{pmatrix} -\delta \\ 1 \end{pmatrix} = \frac{8EI}{L} \left(3\delta^2 + 3\delta + 1 \right)
\tag{4.12}
$$

is the nominal stiffness of the pivot in absence of gravity, i.e., the limiting stiffness as $\theta \to 0$ and $\bar{F} = 0$, and $\bar{F} = FL^2/EI$ is the normalized load exerted on the flexure pivot. Note that the first order effect of the gravity load $\bar{F}$ on the stiffness of the pivot depends on the orientation φ of gravity.

Remark 4.1.2. The value $\delta = \frac{\sqrt{5}}{6} - \frac{1}{2} \approx -0.127$ satisfies the equation $9\delta^2 - 9\delta + 1 = 0$ and minimizes the effect of gravity on the rotational stiffness. It cancels the first order terms of $\bar{F}$ and the terms of greater order are less important for our small load and small rotation assumptions. Note also that the second order terms of $\bar{F}$ are independent of φ when $\alpha = \frac{\pi}{4}$ ($\cos\alpha = \sin\alpha$). These values of δ and α were thus chosen for the crossed flexure pivot oscillator of the Genequand system, see Sec. 2.2.1.

Remark 4.1.3. The nominal stiffness $k_{r,0}$ is minimal when the flexures cross at midpoint and $\delta = -0.5$.

4.1.4 Numerical validation

The method applied here to calculate the rotational stiffness of the CFP will also be used for the other oscillators. It is thus important to validate it, which is done by comparison with the finite elements method (FEM). The CFP is simulated using the commercial FEM software ANSYS (ANSYS, 2018) with a mesh of 40 elements of type BEAM188 for each flexure, see Fig. 4.5. Since we are interested in the nonlinear behavior of our system, the structural analysis is performed with the large deflection setting.

The nominal stiffness given in Eq. (4.12) is well known from literature (Zhao and Bi, 2010b; Cosandier et al., 2017) and we showed a good match with FEM results in (Kahrobaiyan et al., 2018). The nonlinear effects of the rotation angle and the effects of gravity are treated separately by assuming no external load ($F = 0$) in the first case and amplitude approaching zero (θ^2 is negligible) in the second case. This assumption is reasonable since the terms combining F and θ have order > 2 in Eq. (4.11) and are thus negligible under Assumptions (b) and (c).
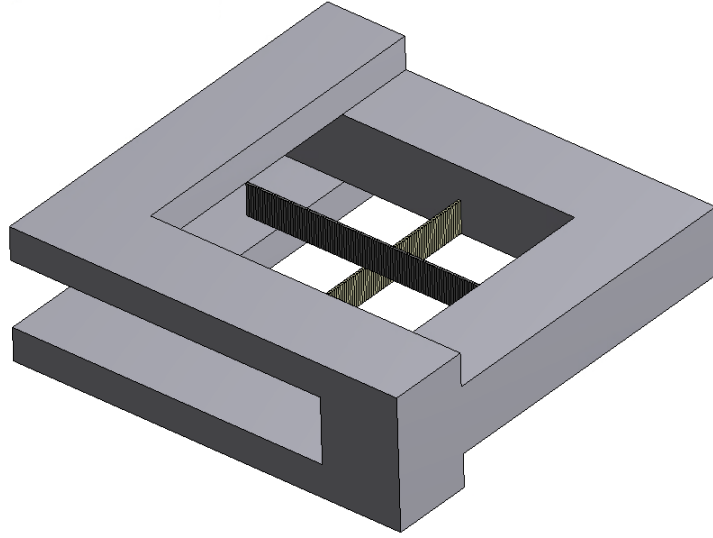
Figure 4.5 – FEM model of the CFP.

Restoring torque nonlinearity

In order to normalize the stiffness variation of a flexure pivot, we use the following definition of *relative restoring torque nonlinearity*:

$$\mu = \frac{k_2}{k_0}, \tag{4.13}$$

where k_0 is the *nominal stiffness* and k_2 the *restoring torque nonlinearity*. This definition applies to a flexure pivot whose restoring torque M is expressed by a power series having only odd terms (assuming the restoring torque to be antisymmetric with respect to equilibrium position)

$$M = k_0 \theta + k_2 \theta^3 + \mathcal{O}\left(\theta^5\right), \tag{4.14}$$

where the higher order terms are negligible for small rotations θ.

Equation (4.11) yields the following analytical expression for the relative restoring torque nonlinearity of the CFP:

$$\mu_{\text{r,analytical}} = \frac{2\delta^2 + \delta}{3\delta^2 + 3\delta + 1}. \tag{4.15}$$

The FEM values for the relative restoring torque nonlinearity of the CFP are obtained by applying 50 incremental displacement values from 0 to 10 degrees on the mobile end of the pivot and calculating the reaction torque on the fixed frame. We then fit an odd cubic polynomial to the torque-angle relationship, see Eq. (4.14), and extract the relative nonlinearity using Eq. (4.13). The results are displayed in Fig. 4.6.

The analytical and FEM results plotted in Fig. 4.6 do not match. The difference can be explained by the use of the Euler-Bernoulli beam theory in the analytical model, which assumes
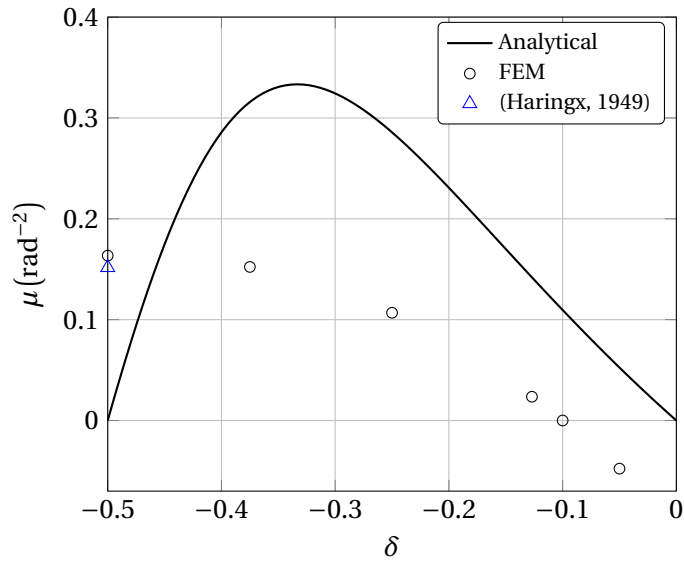
Figure 4.6 – Relative restoring torque nonlinearity μ of an example of CFP versus the geometric parameter δ. Analytical and FEM results are shown for a CFP with $\alpha = 45$ degrees, Poisson's ratio $\nu = 0.3$ and leaf springs dimensions $L = 2$ mm, $h = 0.02$ mm and $b = 0.26$ mm.

that the bending moment and shear force are linear functions of the bending angle and deflection, see Eq. (4.3). This is not the case in reality. Other nonlinear effects play an important role in leaf springs, such as anticlastic curvature (Ashwell, 1950).[1] As it is essential for this research to capture these nonlinear effects correctly, we will use the FEM results in the rest of the study.

Remark 4.1.4. As can be seen in Fig. 4.6, the analytical solution derived by Haringx (1949, Eq. 37) for the nonlinear torque-angle relationship of the CFP with $\delta = -0.5$ validates our FEM results. Haringx's analytical model is however limited to CFP with $\delta = -0.5$ since he used the inherent symmetry which holds only for this CFP in order to solve the nonlinear equations.

Remark 4.1.5. In the analytical formula of Eq. (4.15), the dimensions and elastic properties of the flexures do not affect the relative restoring torque nonlinearity. In reality, the dimensions of the flexures and Poisson's ratio for the material have a significant impact on nonlinear effects such as anticlastic curvature.

Remark 4.1.6. The analytical formula of Eq. (4.15) does not predict an influence of the half-angle α between the flexures on the restoring torque nonlinearity of the CFP. This angle has however a significant effect, as shown in Fig. 4.7, that has been used previously to minimize the isochronism defect of CFP oscillators, see Fig. 2.6a. Figure 4.7 was obtained with the FEM model of the RCC pivot used for the dimensioning of the co-RCC prototype in Chapter 7. Note that Poisson's ratio was set to $\nu = 0$ in order to highlight the geometrical effect of α on the

---

[1] When a beam is bent, the differential lateral contraction caused by Poisson's effect creates a curvature of opposite sign in orthogonal direction called *anticlastic curvature*. In other words, the part of the beam under compression expands laterally while the part under compression contracts, leading to a saddle-shaped curvature. This effect is especially significant for leaf springs with high slenderness of cross-section.

nonlinearity. The prototype is actually fabricated in anisotropic silicon whose Poisson ratio depends of the orientation of the flexures and hence of α, see Eq. (7.1).
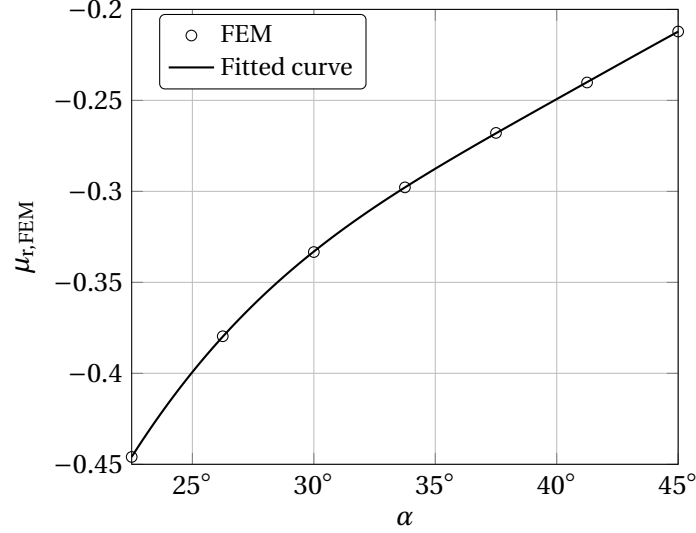
Figure 4.7 – Relative restoring torque nonlinearity $\mu_{\text{r,FEM}}$ versus α of the RCC pivot with dimensions from Sec. 7.2.1 and Poisson's ratio $\nu = 0$. The FEM results are fitted with a Fourier model (with period π due to symmetry): $\mu_R(\alpha) = -2.6 + 0.14\cos 2\alpha + 3.1\sin 2\alpha + 0.76\cos 4\alpha - 0.17\sin 4\alpha$.

Influence of external load orientation

FEM is also used to validate the influence of the orientation of an external load, such as gravity, on the CFP predicted by the analytical model. The COM of the CFP used for the FEM simulation is placed at the intersection of the flexures, see Fig. 4.5. An acceleration corresponding to the desired normalized load $\bar{F}$ is applied on the pivot at an angle φ such as to reproduce the situation in Fig. 4.4. A torque is applied on the pivot corresponding to a rotation $\theta \approx 0.1$ degree and the actual rotation angle obtained is used to compute the stiffness of the pivot. In order to cancel the effect of changing loading conditions as the pivot rotates, the same torque is applied in both directions and the stiffness is averaged, see Assumption (j). Note that a similar averaging effect also happens during one swing of the oscillator. The FEM and analytical results obtained with Eq. (4.11) and $\theta = 0.1$ degree are compared in Fig. 4.8. The results are expressed in terms of relative stiffness variation in parts-per-million (ppm) with respect to a reference stiffness k_{ref}

$$\epsilon = \frac{k - k_{\text{ref}}}{k_{\text{ref}}} \cdot 10^6. \tag{4.16}$$

The stiffness at $\varphi = \pm 90$ degrees is arbitrarily chosen as reference. Both methods show a good match which validates the gravity component of the analytical model. Note that the use of the normalized force $\bar{F} = FL^2/EI$ makes the results independent of the dimensions of the flexures.
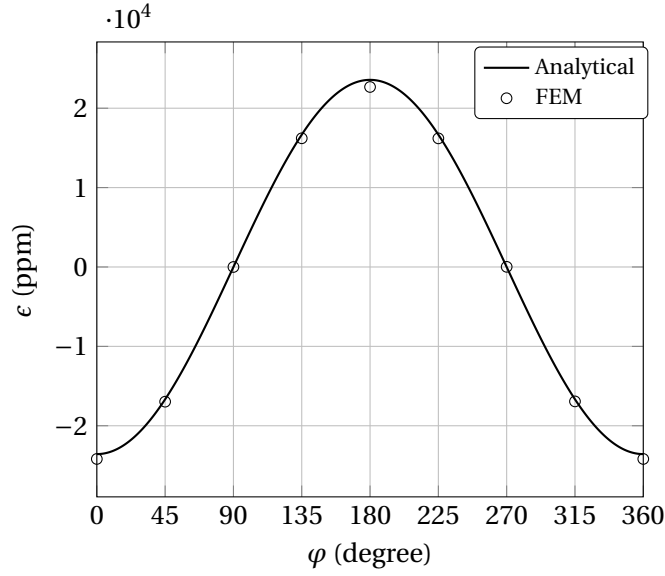
Figure 4.8 – Relative stiffness variation ϵ of the CFP for varying orientations φ of the normalized central load $\bar{F} = 0.2$. Analytical and FEM results are shown for a pivot with $\delta = -0.5$ and $\alpha = 45$ degrees.

Remark 4.1.7. Figure 4.8 shows that the stiffness variation of the CFP is maximal for loads acting along the ν axis ($\varphi = 0$ degrees and $\varphi = 180$ degrees). In this orientation, the flexures are either both in tension or both in compression.

4.1.5 Semi-analytical stiffness formula

Figure 4.8 showed that Eq. (4.11) captures well the effect of load on the CFP stiffness but Fig. 4.6 showed that the restoring torque nonlinearity is not well described. We therefore propose a semi-analytical formula

$$
\begin{aligned}
k_r = k_{r,0}(1 + \mu_{\text{r,FEM}}\theta^2) + \frac{EI}{L}\Bigg[& \frac{2}{15}\left(9\delta^2 + 9\delta + 1\right)\bar{F}\frac{\cos\varphi}{\cos\alpha} \\
& - \frac{\left(9\delta^2 + 9\delta + 11\right)}{12\,600}\bar{F}^2\left(\frac{\cos^2\varphi}{\cos^2\alpha} + \frac{\sin^2\varphi}{\sin^2\alpha}\right)\Bigg] + \mathcal{O}\left(\bar{F}\theta^2\right) + \mathcal{O}\left(\bar{F}^3\right) + \mathcal{O}\left(\theta^4\right)
\end{aligned}
\tag{4.17}
$$

that uses the relative restoring torque nonlinearity $\mu_{\text{r,FEM}}$ obtained by FEM to improve the model. Note that $\mu_{\text{r,FEM}}$ needs to be computed separately for each set of CFP dimensions. Interpolation, such as shown in Fig. 4.7, can be used to ease the dimensioning.

Remark 4.1.8. Note that, according to Assumptions (b) and (c), the terms of combined order of F and θ that is greater than 2 have been neglected in Eq. 4.17.

4.2 Rotational stiffness of the GIFP

In this section, we derive the rotational stiffness of the GIFP introduced in Sec. 3.1. We use the same method as for the CFP in Sec. 4.1, under the same assumptions.

4.2.1 Cantilever beam model

The five rod flexures shown in Fig. 3.3a block all but one DOF which closely approximates a rotation about the z axis. As a result, the four bending rods deflect in the same way as the CFP flexures depicted in Fig. 4.1 and the method of Sec. 4.1 can be applied to find their stiffness. The stiffness of the torsional rod can then be added separately.

We derive the expression for the rotational stiffness of the GIFP by modifying Eq. (4.7) to take into account the four bending rods and adding the stiffness of the torsional rod

$$k_g = k_a + \frac{EI}{L} \left[\begin{pmatrix} -\delta\cos\theta & 1 \end{pmatrix} (\mathbf{K}_{1+} + \mathbf{K}_{1-} + \mathbf{K}_{2+} + \mathbf{K}_{2-}) \begin{pmatrix} -\delta\frac{\sin\theta}{\theta} \\ 1 \end{pmatrix} \right.$$
$$\left. + \delta\,(\lambda_{1+} + \lambda_{1-} + \lambda_{2+} + \lambda_{2-})\,\frac{\sin\theta}{\theta} \right], \tag{4.18}$$

where subscripts 1 and 2 refer to the orientation of the bending rods (e.g. along the x or y axes in Fig. 3.3a) and subscripts + and − refer to the direction in which they are connected from the fixed frame to the mobile part (e.g. rod (5) is in + direction and rod (3) in − direction in Fig. 3.3a). The stiffness of the torsional rod is $k_a = G_a J_a / L_a$, where L_a is its length, G_a its shear modulus and J_a its polar area moment of inertia.

4.2.2 Co-differential concept

We explained in Sec. 3.1 that the symmetric flexure arrangement of the GIFP allows to minimize the influence of gravity on its rotational stiffness. This principle was formalized in (Kahrobaiyan et al., 2018) under the name *co-differential*. The co-differential concept consists in placing two identical flexures subjected to the same kinematic boundary conditions in such way that their axial loads (due to gravity) are opposite (same magnitude but opposite signs). In other words, when one flexure is subjected to tensile axial load, the other one is subjected to compressive axial load of equal magnitude. This results in a cancellation of the first order effect of gravity on the bending stiffness of the flexures.

This effect can be seen on the symmetrical pairs of bending rods of the GIFP with same orientation (orientation 1 or 2). When one rod is under compression, the other one is under tension, i.e., $\lambda_{1+} = \lambda_{1-}$ and $\lambda_{2+} = \lambda_{2-}$. As a result, the last term of Eq. (4.18) is canceled out and the stiffness of one co-differential element is

$$\mathbf{K}_{\mathrm{cd}} = \mathbf{K}_+ + \mathbf{K}_- = 2\,\mathbf{K}_0 - \frac{\lambda^2}{6300} \begin{pmatrix} 18 & -9 \\ -9 & 22 \end{pmatrix} + \mathcal{O}\left(\lambda^3\right), \tag{4.19}$$

where the stiffness matrix of a cantilever beam $\mathbf{K}$ is obtained with Eq. (4.9). The rotational stiffness of the GIFP in Eq. (4.18) can then be re-written as

$$k_g = k_a + \frac{EI}{L}\begin{pmatrix} -\delta\cos\theta & 1 \end{pmatrix}\left(\mathbf{K}_{\text{cd,1}} + \mathbf{K}_{\text{cd,2}}\right)\begin{pmatrix} -\delta\frac{\sin\theta}{\theta} \\ 1 \end{pmatrix}. \tag{4.20}$$

The cancellation of the λ term in Eq. (4.19) and Eq. (4.20) shows the effectiveness of the co-differential concept.

4.2.3 Stiffness under central loading

We model the effect of in-plane gravity loading as a force F applied at the center G of the pivot with an angle φ with respect to the bisector of the planes formed by the bending rods, as depicted in Fig. 4.4.[2] Using series expansion of Eq. (4.20) and replacing the nonlinear terms of θ^2 with FEM results as done in Sec. 4.1.5, the rotational stiffness of the GIFP becomes

$$\begin{aligned} k_g = {} & k_{g,0}(1 + \mu_{\text{g,FEM}}\theta^2) - \frac{EI}{L}\frac{\left(9\delta^2 + 9\delta + 11\right)}{6300}\bar{F}^2\left(\frac{\cos^2\varphi}{\cos^2\alpha} + \frac{\sin^2\varphi}{\sin^2\alpha}\right) + k_a \\ & + \mathcal{O}\left(\bar{F}\theta^2\right) + \mathcal{O}\left(\bar{F}^3\right) + \mathcal{O}\left(\theta^4\right), \end{aligned} \tag{4.21}$$

where α is the half angle between the planes formed by the bending rods, $k_{g,0} = 2k_{r,0}$ is the nominal stiffness obtained from Eq. (4.12) and $\mu_{\text{g,FEM}}$ is the relative restoring torque nonlinearity of the GIFP obtained by FEM.

In order for the GIFP stiffness to be insensitive to the orientation φ of gravity, we design the pivot with $\alpha = \frac{\pi}{4}$, such that $\cos^2\alpha = \sin^2\alpha$ in Eq. (4.21). Applying the trigonometric identity $\cos^2\varphi + \sin^2\varphi = 1$, the rotational stiffness of the GIFP becomes

$$k_g = k_{g,0}(1 + \mu_{\text{g,FEM}}\theta^2) - \frac{EI}{L}\frac{\left(9\delta^2 + 9\delta + 11\right)}{3150}\bar{F}^2 + k_a + \mathcal{O}\left(\bar{F}\theta^2\right) + \mathcal{O}\left(\bar{F}^3\right) + \mathcal{O}\left(\theta^4\right), \tag{4.22}$$

where the parameter φ is not present. Hence, the stiffness of the GIFP does not depend on the orientation of gravity.

4.3 Rotational stiffness of the co-RCC

In this section, we derive the rotational stiffness of the co-RCC introduced in Sec. 3.2. We will reuse the results of Sec. 4.1, as the CFP (in its RCC configuration) is one of the building blocks of the co-RCC, with the addition of the following assumptions:

---

[2]Since the GIFP is designed with a 90 degree angle between the planes formed by the bending rods ($\alpha = \frac{\pi}{4}$), the orientation of the load is indicated with angle $\psi = \frac{\pi}{4} - \varphi$ in Fig. 3.3a.

(k) We consider the flexure elements of the co-RCC as springs and the other bodies as rigid. Figure 4.9 shows such model where the RCC pivots have a rotational stiffness k_{RCC1} and k_{RCC2} and the sliders have a translation stiffness k_{p1} and k_{p2}.

(l) The motion of the sliders (Δv_1 and Δv_2) corresponds to the parasitic motion of the RCC pivots along their local v axis, see Sec. 3.2.1.

(m) The system is symmetric: $k_{\text{RCC1}} = k_{\text{RCC2}} = k_r$, $k_{p1} = k_{p2} = k_p$ and $\Delta v_1 = \Delta v_2 = \Delta v$.

(n) The parallel leaf springs do not transmit any force along their sliding axis. This assumption is reasonable knowing that their stiffness is much smaller than that of the "blocked" degrees-of-freedom of the flexure joints. It is assumed that the possible stiffening of the parallel leaf springs caused by gravity is not sufficient to invalidate this assumption.
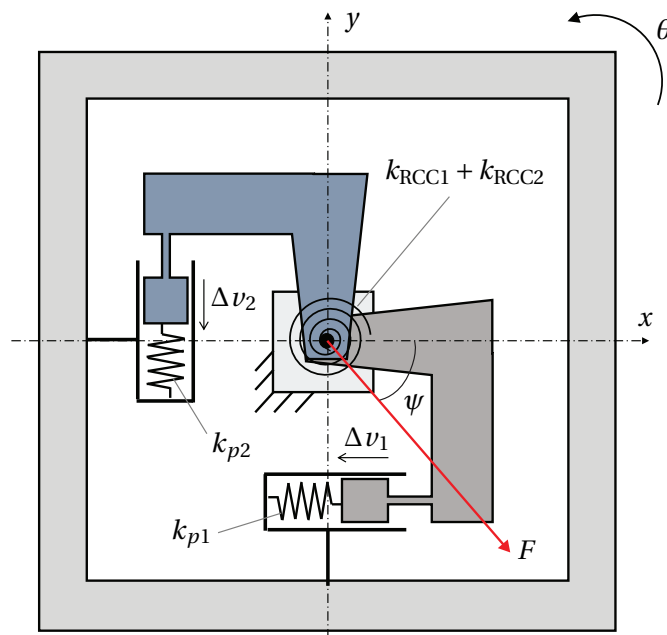
Figure 4.9 – Spring model of the co-RCC.

We proceed with the following steps:

1. Express the restoring torque of the RCC elements of the co-RCC for a given rotation and gravity load.
2. Express the restoring force and motion of the parallel leaf springs of the co-RCC for a given rotation and gravity load.
3. Express the strain energy of the co-RCC for a given rotation.
4. Derive the rotational stiffness of the co-RCC from its total strain energy.

4.3.1   Restoring torque of the RCC spring elements

Following Assumption (d), the effect of gravity corresponds to a force F applied on the mobile part in point O, at an angle ψ such as depicted in Fig. 4.9. Following Assumption (n), the slider

placed between each RCC and the body on which the gravity load is applied allows only for forces along the local u axis to be transmitted to the RCC, see Fig. 3.8. The resulting restoring torque of each half co-RCC is obtained by substituting $\varphi=90$ degrees in Eq. (4.17), giving

$$M_h\left(\theta, \bar{F}_i\right) = \left(k_{r,0} - \frac{EI}{L}\frac{\left(9\delta^2 + 9\delta + 11\right)}{12\,600\sin^2\alpha}\bar{F}_i^{\,2}\right)\theta + k_{r,0}\,\mu_{\text{r,FEM}}\,\theta^3$$
$$+\,\mathcal{O}\left(\bar{F}_i\theta^3\right) + \mathcal{O}\left(\bar{F}_i^{\,3}\theta\right) + \mathcal{O}\left(\theta^5\right), \tag{4.23}$$

where F_i is the force along the local u axis of the respective RCC.

Since the two half co-RCC are placed at a 90 degree angle, the RCC pivots 1 and 2 support the component of the load along their local u-axis, respectively the y and x axes in Fig. 3.9, namely

$$F_1 = F\sin\psi \qquad \text{and} \qquad F_2 = F\cos\psi. \tag{4.24}$$

The restoring torque of each RCC can thus be obtained by substituting the respective force from Eq. (4.24) into Eq. (4.23).

Remark 4.3.1. The co-RCC architecture follows the co-differential concept introduced in Sec. 4.2.2. In the GIFP, the first order effect of gravity on the rotational stiffness of the pivot is eliminated by placing the flexures symmetrically at a 180 degree rotation. In the co-RCC, the same compensating effect is obtained through the fact that the sliders do not transmit any load along their axis of motion, see Assumption (n). Thus, when an external load acts on the main rigid body, each half co-RCC element is only loaded with the component of that force along its local u-axis and the RCC leaf springs are loaded with equal but opposite forces. This effect can be seen in Eq. (4.23), where the first order effect of F_i from Eq. (4.17) has been canceled.

4.3.2 Restoring force and motion of the parallel leaf springs

As was done for the RCC pivots, the restoring force of the parallel leaf springs can be expressed by series expansion having only odd terms of displacement (assuming the restoring force to be antisymmetric with respect to equilibrium position). With the addition of a linear dependence of the translational stiffness on the transverse normalized load $\Delta k_p\left(\bar{F}_i\right)$ (Cosandier et al., 2017, Eq. 4.15), this restoring force becomes

$$M_p\left(\Delta v, \bar{F}_i\right) = \left(k_{p,0} + \Delta k_p\left(\bar{F}_i\right)\right)\Delta v + k_{p,2}\,\Delta v^3 + \mathcal{O}\left(\Delta v^5\right). \tag{4.25}$$

The displacement of the parallel springs for a given rotation θ of the system corresponds to the parasitic motion of the RCC pivots along v given by Zhao and Bi (2010a):

$$\Delta v = -\frac{(9\delta^2 + 9\delta + 1)L}{15\cos\alpha}\theta^2 + \mathcal{O}\left(\theta^4\right). \tag{4.26}$$

4.3.3 Strain energy

Now that the stiffness and displacements of all the elastic elements for a rotation θ of the co-RCC is known, the strain energy of the system can be computed as the sum of the strain energies of each spring

$$U = \int_0^\theta M_h\left(v, \bar{F}_1\right) dv + \int_0^\theta M_h\left(v, \bar{F}_2\right) dv + \int_0^{\Delta v} M_p\left(\Delta v, \bar{F}_1\right) dv + \int_0^{\Delta v} M_p\left(\Delta v, \bar{F}_2\right) dv, \quad (4.27)$$

which, when substituting with Eq. (4.23)–(4.26), yields

$$\begin{aligned}
U &= \left(k_{r,0} - \frac{EI}{L}\frac{9\delta^2 + 9\delta + 11}{25\,200\sin^2\alpha}\bar{F}^2\left(\sin^2\psi + \cos^2\psi\right)\right)\theta^2 \\
&\quad + \left(\frac{1}{2}k_{r,0}\,\mu_{\mathrm{r,FEM}} + \frac{(9\delta^2 + 9\delta + 1)^2 L^2}{225\cos^2\alpha}k_{p,0}\right)\theta^4 + \mathcal{O}\left(\bar{F}\theta^4\right) + \mathcal{O}\left(\bar{F}^3\theta^2\right) + \mathcal{O}\left(\theta^6\right) \\
&= \left(k_{r,0} - \frac{EI}{L}\frac{9\delta^2 + 9\delta + 11}{25\,200\sin^2\alpha}\bar{F}^2\right)\theta^2 + \left(\frac{1}{2}k_{r,0}\,\mu_{\mathrm{r,FEM}} + \frac{(9\delta^2 + 9\delta + 1)^2 L^2}{225\cos^2\alpha}k_{p,0}\right)\theta^4 \\
&\quad + \mathcal{O}\left(\bar{F}\theta^4\right) + \mathcal{O}\left(\bar{F}^3\theta^2\right) + \mathcal{O}\left(\theta^6\right).
\end{aligned} \quad (4.28)$$

4.3.4 Rotational stiffness

The rotational stiffness of the co-RCC is the derivative of the strain energy U with respect to θ divided by θ

$$\begin{aligned}
k_c = \frac{1}{\theta}\frac{dU}{d\theta} &= 2k_{r,0} - \frac{EI}{L}\frac{9\delta^2 + 9\delta + 11}{12\,600\sin^2\alpha}\bar{F}^2 + \left(2k_{r,0}\,\mu_{\mathrm{r,FEM}} + \frac{4(9\delta^2 + 9\delta + 1)^2 L^2}{225\cos^2\alpha}k_{p,0}\right)\theta^2 \\
&\quad + \mathcal{O}\left(\bar{F}\theta^2\right) + \mathcal{O}\left(\bar{F}^3\right) + \mathcal{O}\left(\theta^4\right).
\end{aligned} \quad (4.29)$$

Note that this corresponds to the definition of secant stiffness, see Remark 4.1.1.

Substituting the nominal stiffness of the parallel leaf springs in Eq. 4.29 with the expressions from (Cosandier et al., 2017, Eq. 4.9)

$$k_{p,0} = \frac{24E_p I_p}{L_p^3}, \quad (4.30)$$

yields

$$\begin{aligned}
k_c &= k_{c,0} - \frac{EI}{L}\frac{9\delta^2 + 9\delta + 11}{12\,600\sin^2\alpha}\bar{F}^2 + \left(2k_{r,0}\,\mu_{\mathrm{r,FEM}} + \frac{32(9\delta^2 + 9\delta + 1)^2 E_p I_p L^2}{75\cos^2\alpha L_p^3}\right)\theta^2 \\
&\quad + \mathcal{O}\left(\bar{F}\theta^2\right) + \mathcal{O}\left(\bar{F}^3\right) + \mathcal{O}\left(\theta^4\right),
\end{aligned} \quad (4.31)$$

where I_p is the area moment of inertia of the cross-section of the parallel leaf springs, L_p is their length (see Fig. 3.12a), E_p is their Young's modulus (which can be different from that of the RCC leaf springs if using an anisotropic material), $k_{c,0} = 2k_{r,0}$ is the nominal stiffness of

the oscillator obtained from the nominal stiffness of the RCC pivots in Eq. (4.12) and $\mu_{\text{r,FEM}}$ is the relative restoring torque nonlinearity of the RCC pivots obtained by FEM, see Sec. 4.1.4.

Remark 4.3.2. As for the GIFP, one can see that the stiffness of the oscillator insensitive to the orientation ψ of the load. This effect was obtained by combining the co-differential concept, which cancels the first order effect of gravity in Eq. (4.23), with an orthogonal arrangement of the flexures, which cancels the ψ terms in Eq. (4.28) through the trigonometric identity $\cos^2\psi + \sin^2\psi = 1$.

Remark 4.3.3. Since the parallel leaf springs follow a second order motion of the rotation angle, the influence of the load on their stiffness Δk_p in Eq. (4.25) becomes a negligible higher order term $\mathcal{O}\left(\bar{F}\theta^2\right)$.

4.4 Rotational stiffness of the RDCO

In this section, we derive the rotational stiffness of the RDCO introduced in Sec. 3.3 under the following assumptions:

(i) We consider the flexure elements of the RDCO as springs and the other bodies as rigid. Figure 3.13b shows such model.

(ii) The system is symmetric: all pivots A have rotational stiffness k_A, all pivots B have rotational stiffness k_B and all the sliders have translational stiffness k_t.

(iii) The restoring force or restoring torque of the flexure elements can be expressed by series expansion having only odd terms of displacement, see see Eq. (4.14).

(iv) The rotations θ are small and terms can be expressed using series expansions around $\theta = 0$.

(v) No external force (such as gravity) is acting on the oscillator. We focus our analysis on the isochronism of this oscillator and assume that its rotational symmetry minimizes the influence of gravity on its restoring torque according to the arguments outlined in Sec. 6.2.1.

In the same manner as Sec. 4.3, the restoring torque of the oscillator is derived from the strain energy of the system. The development consists of the following steps:

1. Derive the motion of the two pivots of the connecting rod for a given rotation of the oscillator.
2. Derive the motion of the sliders for a given rotation of the oscillator.
3. Express the strain energy of the system for a given rotation of the oscillator.
4. Compute the restoring torque of the system from its total strain energy.

4.4.1 Motion of the pivots of the connecting rod

The angles θ_A and θ_B swept by the pivots of the connecting rod when the system rotates by an angle θ can be obtained by trigonometry, see Fig. 4.10. They can be expressed using series

expansions for small displacements:

$$\theta_B = \arcsin \frac{d \sin \theta}{L} = \delta \theta + \frac{1}{6} \delta \left(\delta^2 - 1 \right) \theta^3 + \mathcal{O}\left(\theta^5\right)$$
$$\theta_A = \theta + \theta_B = (1 + \delta) \theta + \frac{1}{6} \delta \left(\delta^2 - 1 \right) \theta^3 + \mathcal{O}\left(\theta^5\right).$$

(4.32)
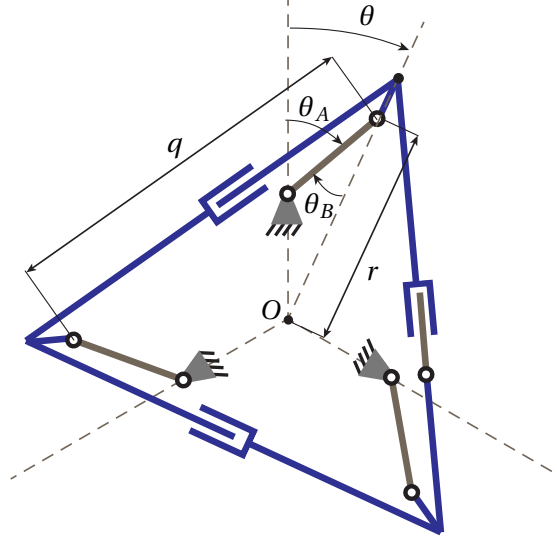
Figure 4.10 – Parameters for the RDCO rotational stiffness computation.

4.4.2 Motion of the sliders

The motion of the sliders corresponds to the change in distance q between the pivots of the inertial bodies, see Fig. 4.10. We first derive the distance from the center of the oscillator to these pivots as the oscillator rotates

$$r(\theta) = d \cos \theta + L \cos \theta_B = L(\delta + 1) \left(1 - \frac{\delta}{2} \theta^2 \right) + \mathcal{O}\left(\theta^4\right) = R_0 \left(1 - \frac{\delta}{2} \theta^2 \right) + \mathcal{O}\left(\theta^4\right),$$

(4.33)

where $R_0 = L + d$ in Fig. 3.14. We then get the motion of the sliders

$$\Delta q(\theta) = q(\theta) - q(0) = 2 \sin \frac{\pi}{n} \left(r(\theta) - r(0) \right) = -R_0 \, \delta \, \sin \frac{\pi}{n} \theta^2 + \mathcal{O}\left(\theta^4\right),$$

(4.34)

where n is the order of symmetry of the oscillator, see Fig. 3.17.

Remark 4.4.1. These two equations show that the sign of the dilation is the opposite of the sign of δ, as already mentioned in Sec. 3.3.1.

Remark 4.4.2. The results are expressed in terms of R_0 instead of d or L as this parameter is more representative of the size of the oscillator and thus more convenient for dimensioning.

4.4.3 Strain energy

Following Assumption (iii), the restoring force of the flexures are expressed by series expansion:

$$M_A(\theta) = k_{A,0}(1 + \mu_A \theta^2)\theta + \mathcal{O}(\theta^5),$$
(4.35)

$$M_B(\theta) = k_{B,0}(1 + \mu_B \theta^2)\theta + \mathcal{O}(\theta^5),$$
(4.36)

$$F_t(\Delta q) = k_{t,0}(1 + \mu_t \Delta q^2)\Delta q + \mathcal{O}(\Delta q^5).$$
(4.37)

The strain energy of the system for a rotation θ follows from the sum of the strain energies of each elastic joint

$$U = n\left(\int_0^{\theta_A} M_A(v)\,dv + \int_0^{\theta_B} M_B(v)\,dv + \int_0^{\Delta q} F_t(v)\,dv\right).$$
(4.38)

4.4.4 Rotational stiffness

Substituting Eq. (4.32)-(4.37) into Eq. (4.38) and deriving and dividing the strain energy U by θ yields the rotational stiffness of the RDCO

$$
\begin{aligned}
k_{\text{RDCO}} = \frac{dU}{d\theta} = {}& k_{\text{RDCO},0} + \frac{1}{3}n\theta^2\bigg(2\delta(\delta+1)(\delta^2-1)k_{A,0} + 2\delta^2(\delta^2-1)k_{B,0} \\
& + 3(\delta+1)^4 k_{A,0}\mu_A + 3\delta^4 k_{B,0}\mu_B + 6\delta^2 k_{t,0}R_0^2\sin^2\left(\frac{\pi}{n}\right)\bigg) + \mathcal{O}(\theta^4),
\end{aligned}
$$
(4.39)

where

$$k_{\text{RDCO},0} = n\left((\delta+1)^2 k_{A,0} + \delta^2 k_{B,0}\right)$$
(4.40)

is the nominal stiffness of the oscillator, i.e., the limiting stiffness as rotation angle goes to zero.

4.5 Chapter conclusion

In this chapter, beam theory was used to compute expressions for the rotational stiffness of the three flexure pivot architectures of this thesis, in terms of angular displacement and gravity loading. Finite element analysis showed that the resulting expressions do not accurately describe the second order effects of angular displacement on the rotational stiffness. The numerical results are thus used to represent these terms in the analytical formulas, resulting in so-called semi-analytical formulas, which can be used to compute the isochronism defect of our oscillators. The terms derived for the influence of gravity on the stiffness of our oscillators were validated numerically and can be used to assess their gravity sensitivity.

5 Isochronism

In Chapter 3, we presented new flexure pivot oscillators aimed at reaching the goal of Sec. 1.1, i.e., breaking through the apparent limit of mechanical watch accuracy. In order to reach this goal, a key aspect of this thesis is to control the isochronism of these new time bases, an essential condition for accurate timekeeping. In this chapter, we give historical context to the problem of isochronism, define it formally and present analytical models for the isochronism defect of the three flexure pivot oscillator families of this thesis.

5.1 Isochronism correction for the pendulum

Isochronism, the independence of period from amplitude, was first identified by Galileo around 1600 as he observed the swinging motion of a chandelier in a church in Pisa. He timed the oscillations of the chandelier with his pulse and found that they seemed to take the same amount of time, regardless of the amplitude of swing. This fact was however contradicted by Mersenne and Descartes in 1636, who observed that the period of the pendulum slightly increases with amplitude (Matthews, 1994). In 1656, Huygens confirmed mathematically Mersenne and Descartes' observation that the pendulum was not isochronous and devised an isochronous pendulum in three stages (Vardi, 2015).

1. He sought the curve from A to B shown in Fig. 5.1 down which an object will slide from rest without friction under gravity to point B in the same time, irrespective of its starting point between A and B. He showed that this so-called *tautochrone curve* is a cycloid.[1]
2. He introduced the notion of involute, the curve traced by the end of a string wrapping around another curve (the evolute).
3. He showed that the involute of a cycloid is another cycloid.

The result is a pendulum consisting of a suspension thread that wraps around cycloidal cheeks and a bob that consequently follows the tautochrone curve, see Fig. 5.2a. Huygens

---

[1]Forty-one years later, Johann Bernoulli proved that this was also the *brachistochrone*, i.e., the curve of fastest descent under gravity between two points (Bernoulli, 1697).
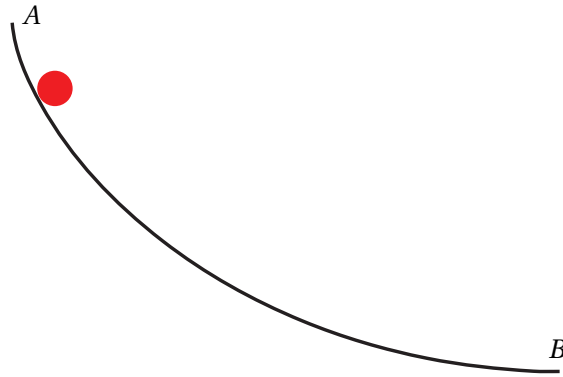
Figure 5.1 – Ball sliding along a cycloid.

implemented this idea in a clock in 1657, see Fig. 5.2b, and published his major results in his *Horologium Oscillatorium* in 1673 (Huygens, 2007). Note that another way to look at the effect of the cycloidal cheeks is that they change the effective length of the pendulum as it swings, thus altering its frequency. This solution is theoretically correct but does not appear to work well in practice (Beckett, Lord Grimthorpe, 1903, p. 24) (Rawlings, 1993, pp. 60-62). It was quickly abandoned in favor of rigid rods with small amplitudes. It should be noted that the small amplitude solution was not considered by Huygens since he was interested in marine chronometers, which necessitated large amplitudes (Leopold, 1996). Subsequently, there was much research on pendulum suspensions and isochronism for precision clocks (Rawlings, 1993, pp. 62-68) (Matthys, 2004, pp. 97-137) (Fedchenko, 1957) but this is beyond the scope of this thesis, which focuses on portable timekeepers.

5.2 The perturbed rotational harmonic oscillator

Chapter 4 showed that the stiffness of flexure pivot oscillators can be a function of the angular displacement θ. The other parameter of the oscillator differential equation, the inertia J in Eq. (4.1), can also be function of θ. A good example is the diameter variation of the RDCO in Fig. 3.20. Hence, instead of the oscillator with constant frequency described by Eq. (4.2), we consider the perturbed harmonic oscillator in which the angular frequency $\omega = \omega(\Theta)$ depends on the amplitude Θ. In this section, we compute the frequency-amplitude relationship of such oscillators and use it to gives an explicit expression for the isochronism of our three flexure pivot oscillators.

5.2.1 Frequency-amplitude relation

We consider the oscillator whose restoring torque can be expressed by a power series using the relative restoring torque nonlinearity $\mu = \frac{k_2}{k_0}$ defined in Eq. (4.13)

$$M = k_0\theta + k_2\theta^3 + \mathcal{O}\left(\theta^5\right) = k_0\theta(1 + \mu\theta^2) + \mathcal{O}\left(\theta^5\right) \tag{5.1}$$

(a)   (b)

Figure 5.2 – Huygens' (a) drawing of the isochronous pendulum in a letter to H. Oldenburg in 1673 (Huygens, 1897, Correspondence N° 1951) and (b) clock design with cycloidal cheeks shown in FIG. II. (Huygens, 2007).

and whose inertia can be expressed by a power series having only even terms (assuming inertia variation is symmetric with respect to equilibrium position)

$$J = J_0 + J_2\theta^2 + \mathcal{O}\left(\theta^4\right) = J_0\left(1 + \iota\theta^2\right) + \mathcal{O}\left(\theta^4\right), \tag{5.2}$$

where we call J_0 the *nominal inertia,* J_2 the *inertia variation* and $\iota = \frac{J_2}{J_0}$ the *relative inertia variation.*

The differential equation of the oscillator follows from Eq. (4.1)

$$\ddot{\theta} = -\frac{k_0\left(1 + \mu\theta^2\right)}{J_0\left(1 + \iota\theta^2\right)}\theta + \mathcal{O}\left(\theta^5\right), \tag{5.3}$$

which, when using again series expansions around $\theta = 0$, becomes

$$\ddot{\theta} = -\frac{k_0}{J_0}\theta - \frac{k_0}{J_0}\left(\mu - \iota\right)\theta^3 + \mathcal{O}\left(\theta^5\right). \tag{5.4}$$

Remark 5.2.1. When the relative restoring torque nonlinearity is equal to the relative inertia variation ($\mu = \iota$), Eq. (5.4) becomes the differential equation of the simple rotational harmonic oscillator without isochronism defect.

Equation (5.4) can be solved using standard methods of perturbation theory (Nayfeh and Mook, 1995, Eq. 2.3.34), yielding the following frequency-amplitude relation

$$\omega(\Theta) = \omega_0 \left(1 + \frac{3(\mu - \iota)}{8} \Theta^2 \right) + \mathcal{O}\left(\Theta^4\right),$$

(5.5)

where $\omega_0 = \sqrt{k_0 / J_0}$ is the nominal frequency of the oscillator as amplitude approaches zero.

Remark 5.2.2. When the amplitude of the oscillator $\Theta(t)$ varies over time, the oscillator satisfies

$$\theta(t) = \Theta(t) \sin\left(\int_0^t \omega\left(\Theta(x)\right) dx + \Phi \right)$$

(5.6)

where $\omega\left(\Theta(t)\right)$ is the instantaneous frequency of the oscillator obtained by substituting $\Theta(t)$ in Eq. (5.5).

5.2.2 Definition of isochronism defect

Equation (5.5) gives an explicit expression for the isochronism defect. In order to provide numerical isochronism data, we choose a *reference amplitude* Θ_1 with corresponding frequency ω_1. One then defines the *daily rate* by (Reymondin et al., 1999)

$$\rho = 86\,400 \frac{\omega - \omega_1}{\omega_1},$$

(5.7)

that is, the gain or loss of the timekeeper, in seconds per day, with respect to the reference frequency. Daily rate gives a precise measure of the (hopefully small) isochronism defect. Applying Eq. (5.5) gives the following explicit formula for the daily rate in terms of amplitude Θ, the reference amplitude Θ_1, μ and ι

$$\rho = 32\,400 \frac{\left(\Theta^2 - \Theta_1^2\right)(\mu - \iota)}{1 + \frac{3}{8}\Theta_1^2(\mu - \iota)}.$$

(5.8)

5.2.3 Definition of isochronism tuning

We define isochronism tuning as the action of altering one parameter of an oscillator that affects its isochronism without significantly affecting any other crucial property of the oscillator such as nominal stiffness or nominal inertia (and consequently nominal frequency), influence of the orientation of gravity, and maximum angular stroke.

Using Eq. (5.5), isochronism tuning can be performed by modifying μ through the restoring torque nonlinearity k_2 without affecting k_0 or by modifying ι through the inertia variation J_2 without affecting J_0. The former will be done on the co-RCC, see Sec. 5.4, and the latter on the RDCO, see Sec. 5.5. Note that the influence of gravity or angular stroke must also not be affected.

5.3 Isochronism of the GIFP

The main factor affecting the isochronism of the GIFP is the nonlinear elastic behavior of its bending rods, represented by the variable $\mu_{\mathrm{g,\,FEM}}$ in Eq. (4.22). These rods behave similarly to the leaf springs of the crossed flexure pivot (CFP) and their restoring torque nonlinearity is thus also highly dependent on the crossing ratio δ, see Fig. 5.3.
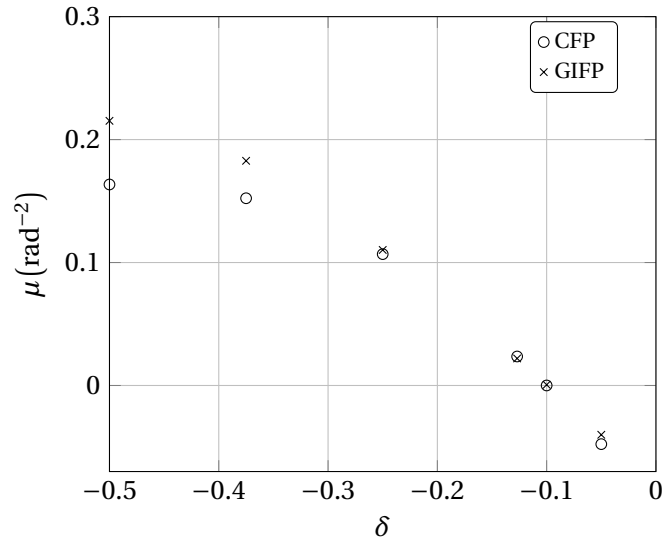
Figure 5.3 – Relative nonlinearity μ of CFP and GIFP versus their geometric parameter δ. The results are obtained by FEM using the method described in Sec. 4.1.4. The CFP leaf springs have dimensions $L = 2$ mm, $h = 0.02$ mm and $b = 0.26$ mm, half angle $\alpha = 45$ degrees between them, and Poisson's ratio $\nu = 0.3$. The GIFP rods have the same dimensions and elastic properties as the CFP flexures, with the exception of having a square cross-section with edge size $h = 0.02$ mm. The GIFP torsional rod is identical to the bending rods.

Remark 5.3.1. The difference between the CFP and GIFP nonlinearity in Fig. 5.3 can be attributed to the difference in cross-section of the flexures, the parasitic angle of the GIFP and the contribution of the torsional rod to its nominal stiffness.

The crossing ratio δ affects the isochronism of the GIFP but cannot be used for tuning according to the definition of Sec. 5.2.3 as it also affects its nominal frequency $k_{g,0}$, see Eq. (4.21) and (4.12). The angle α between the bending rods of the GIFP affects μ without affecting $k_{g,0}$ but modifying its value makes the stiffness of the GIFP sensitive to the orientation of gravity, see Sec. 4.2.3.

The isochronism defect of the GIFP could be tuned by making use of its parasitic angle to modifying its inertia variation J_2. Indeed, the deflection of the bending rods as the pivot rotates cause a shortening of the distance between the fixed frame and the mobile extremity of the flexures. This effect, which results in a translation of the COM in the CFP architecture, see Fig. 4.1, results in an angular shift of the z axis of the GIFP, characterized by angle γ in

Fig. 5.4. This angular shift affects the mass distribution of the pivot about its rotation axis and thus its inertia. However, as this motion is of second order of the rotational angle, only the inertia variation J_2 is affected. Changing the mass distribution of the GIFP along the z axis (while keeping the COM at point G) can be used to alter J_2 without altering the nominal inertia J_0, the mass of the oscillator or the flexures, thus tuning the isochronism defect without altering the nominal frequency or influence of gravity. This concept is not investigated further as the isochronism tuning of the co-RCC and RDCO are better suited for implementation. The purpose of the GIFP oscillator is mainly to introduce the concepts used to minimize the influence of gravity.
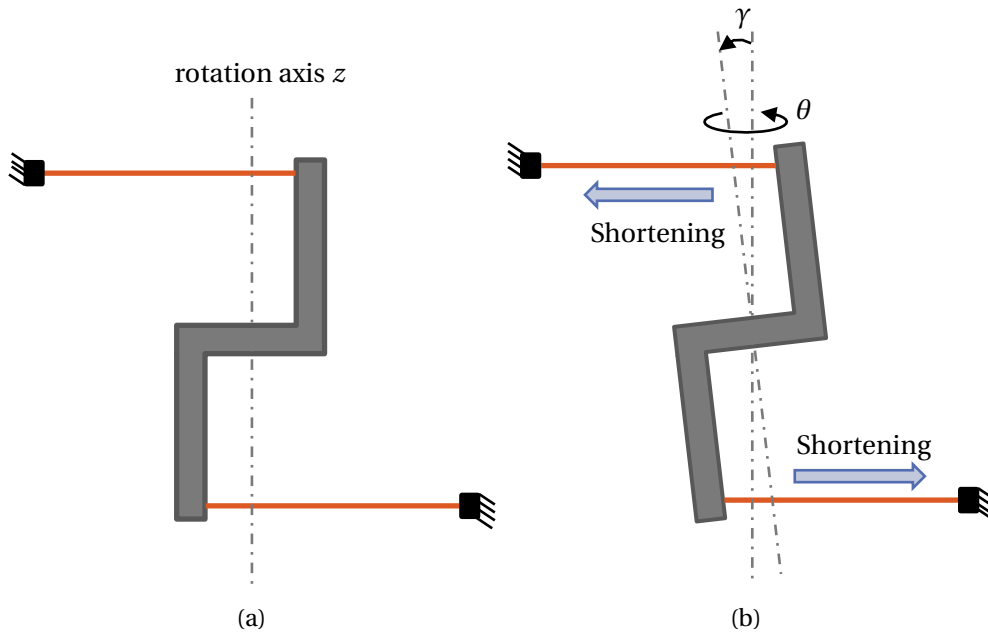
Figure 5.4 – Schematic of the parasitic angle γ of the GIFP in (a) nominal position ($\theta = 0$) and (b) rotated.

5.4 Isochronism of the co-RCC

Equation (4.31) shows that the rotational stiffness of the co-RCC holds second order terms of the rotation angle θ which affect the isochronism of the oscillator ($\mu \neq 0$in Eq. (5.5)). In order to tune the isochronism defect of the co-RCC, we seek to alter the restoring torque nonlinearity

$$k_{c,2} = 2k_{r,0}\,\mu_{\text{r,FEM}} + \frac{32(9\delta^2 + 9\delta + 1)^2 E_p I_p L^2}{75\cos^2 \alpha L_p^3} \tag{5.9}$$

without affecting the nominal stiffness $k_{c,0} = 2k_{r,0}$ or the influence of the gravity load $\bar{F}$. Among the parameters of Eq. (5.9), only those of the parallel leaf springs, E_p, L_p and I_p, will have no effect on the nominal stiffness, gravity effect or angular stroke, which only depend on the geometry of the RCC flexures. The length L_p of the parallel leaf springs is preferred for tuning as it is more flexible than I_p, which is limited by constraints on the flexure thickness h

and height b (in the z-direction) imposed by manufacturing.

The isochronism tuning achieved by modifying L_p is expressed in terms of daily rate by substituting $\mu_c = \frac{k_{c,2}}{k_{c,0}}$ obtained from Eq. (5.9) into Eq. (5.7) assuming no inertia variation ($\iota = 0$)

$$\rho = \frac{32\,400 \left(\mu_{\text{r,FEM}} + \frac{2(9\delta^2+9\delta+1)^2}{75(3\delta^2+3\delta+1)\cos^2\alpha} \frac{E_p I_p}{EI} \left(\frac{L}{L_p}\right)^3 \right) (\Theta^2 - \Theta_1^2)}{1 + \frac{3}{8} \left(\mu_{\text{r,FEM}} + \frac{2(9\delta^2+9\delta+1)^2}{75(3\delta^2+3\delta+1)\cos^2\alpha} \frac{E_p I_p}{EI} \left(\frac{L}{L_p}\right)^3 \right) \Theta_1^2}. \tag{5.10}$$

In order to be able to set the sign of the isochronism defect, the RCC pivot is chosen to have a negative nonlinearity $\mu_{\text{r,FEM}}$ such that the two terms forming the nonlinearity in Eq. (5.9) are of opposite sign. The sign of the defect then depends on the relative magnitude of these two terms. The tuning obtained with Eq. (5.10) is displayed in Fig. 5.5 where the dimensionless ratio $\lambda = L_p/L$ is used to make the results independent of scale. The numerical estimates are calculated in terms of daily rate for a 10% amplitude variation with respect to the reference amplitude $\Theta_1 = 15$ degrees in accordance with the practical watch specifications of Sec. 7.1. The tuning is shown for co-RCC oscillators with different values of RCC relative nonlinearity $\mu_{\text{r,FEM}}$ corresponding to different values of α. One can see that for different choices of RCC pivots, the isochronism can be set to positive or negative values with realistic values of λ, showing that significant defects can be compensated.
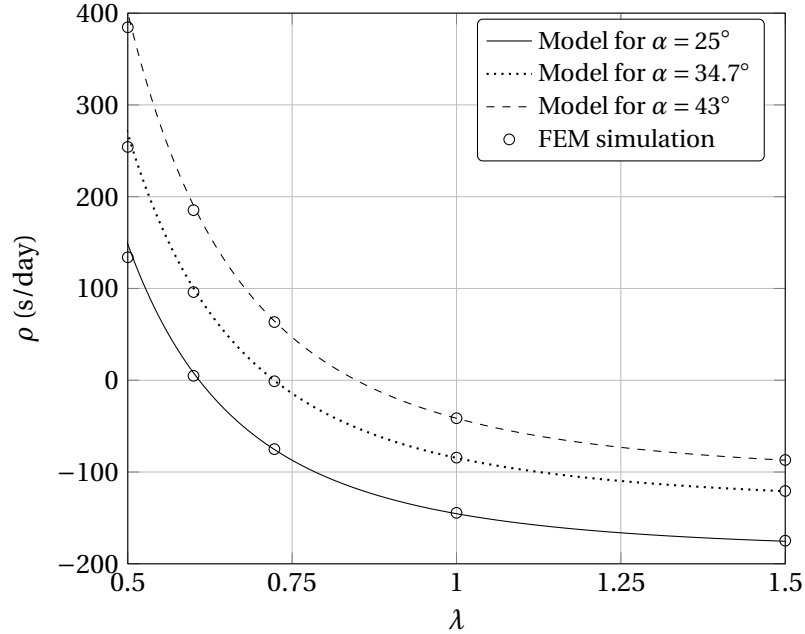
Figure 5.5 – Daily rate ρ versus λ of a co-RCC at $\Theta = 16.5$ degrees with respect to reference amplitude $\Theta_1 = 15$ degrees. The dimensions of the oscillator are given in Sec. 7.2.1.

Remark 5.4.1. The parameter α affects both terms of the co-RCC restoring torque nonlinearity in Eq. (5.9) and can be used as design parameter to offset the isochronism tuning curve, see Fig. 5.5. The expression for $\mu_{\text{r,FEM}}$ with respect to α is obtained by fitting a curve through a set

of FEM-calculated data points depicted in Fig. 4.7.

Remark 5.4.2. In order to be free from the influence of material anisotropy, Young's modulus was set to $E = E_p = 134GPa$ and Poisson's ratio was set to $\nu = 0$ for the analytical and FEM results. This allows to isolate the geometric influence of α on the isochronism curves. The anisotropic effect is however integrated later, in order to compare the models with the experimental results in Fig. 7.20.

Remark 5.4.3. In practice, the assumption that the inertia of the oscillator does not change as it rotates ($\iota = 0$) is not totally accurate as the intermediate bodies do have a non-zero mass. They move closer to the center as the pivot rotates due to the parasitic translation of the RCC pivots and the inertia of the pivot decreases as it moves away from equilibrium ($\iota < 0$), see Fig. 3.12. We assume that this effect is small, the inertia of the intermediate bodies being much smaller than that of the inertial mass, and that it can be compensated by the tuning method presented here.

5.4.1 Tuning resolution

Recall that one of the main goals of this thesis is to design an oscillator capable of being a time base for a timekeeper having 1 s/day accuracy. In order to do this, one must be able to tune the isochronism defect so that the daily rate can be adjusted within a pre-defined oscillator amplitude variation from a reference amplitude. In Sec. 7.1, we make the realistic assumption that the amplitude variation is 10% and that the reference amplitude is 15 degrees.

Figure 5.5 shows that the isochronism defect of the co-RCC can be tuned by changing the length L_p of its parallel leaf springs. The DRIE process, which is used for the manufacturing of silicon parts, and the laser ablation process, which is used to remove matter post-fabrication,[2] typically have a resolution of order 1 μm. We thus define the isochronism tuning resolution by the daily rate variation $\Delta\rho$ obtained with a variation in length of the parallel leaf springs ΔL_p of order 1 μm for a 10% amplitude variation from its reference amplitude 15 degrees, as assumed in Sec. 7.1.

Using Eq. (5.10) and assuming that the RCC leaf springs have a length L of order 1 mm, the tuning resolution is calculated for two isochronous operating points of Fig. 5.5:

1. For $\lambda = 0.72$ and $\alpha = 34.7$ degrees, the slope of $\rho(\lambda)$ is -560 s/day. This means that a variation $\Delta L_p = 1$ μm corresponds to a variation $\Delta\lambda = 0.1\%$ that yields a tuning resolution $\Delta\rho = 0.56$ s/day.
2. For $\lambda = 0.85$ and $\alpha = 43$ degrees, the slope of $\rho(\lambda)$ is -370 s/day. This means that the same variation $\Delta L_p = 1$ μm yields a tuning resolution $\Delta\rho = 0.37$ s/day.

In both cases, the tuning resolution is sufficient to reach the 1 s/day accuracy goal of the thesis.

---

[2]For example, laser ablation is used in the completely automated adjustment of the daily rate of mechanical watches (Conus, 2015).

5.4.2 Numerical validation

The semi-analytical model for the isochronism of the co-RCC in Eq. (5.10) is validated by nonlinear FEM using a mesh of hexahedral elements of type SOLID186 that is refined on the flexures such that there are 3 elements across their thickness h and 6 along their height b. The number of elements along the length of the flexures is chosen such that the elements have a square face. The meshing can be seen in Fig. 5.6. The simulated co-RCC has the dimensions of the prototype of Chapter 7. The daily rate of the FEM model is obtained from its relative restoring torque nonlinearity μ using Eq. (5.8), where μ is obtained using the method described in Sec. 4.1.4. Both methods show similar results, which validates the analytical component of Eq. (5.10).

(a)

(b)
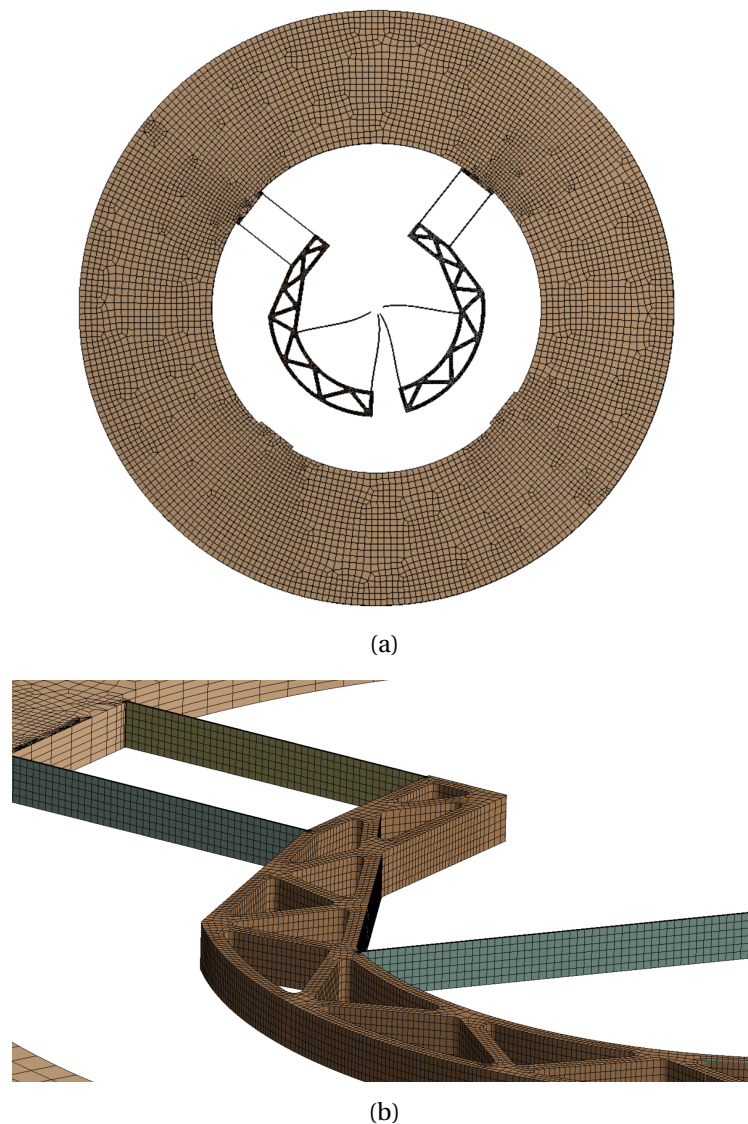
Figure 5.6 – Finite element model of the co-RCC: (a) first mode shape and (b) close-up view of the mesh.

5.5 Isochronism of the RDCO

It was shown in Sec. 3.3.1 that the radius, and thus the inertia, of the RDCO changes as it rotates. According to Eq. (5.5), this affects the isochronism of the oscillator. The derivation of Sec. 4.4 showed that the rotational stiffness of the RDCO changes as it rotates, thus also influencing its isochronism. In this section, we calculate both effects, show that they can be made to compensate each other and show that the isochronism of the RDCO can be tuned by varying either its stiffness variation μ or its inertia variation ι.

5.5.1 Inertia variation

The inertia of the RDCO as it rotates is calculated with the following assumptions:

(a) All the inertial bodies are the same.
(b) All the joints are ideal.
(c) The connecting rods are massless.
(d) The rotations are small and terms can be expressed using series expansions around $\theta = 0$.

The inertia of the RDCO for a rotation θ is

$$J(\theta) = n\left(J_r + m_r s^2(\theta)\right) \tag{5.11}$$

where J_r and m_r are respectively the inertia and mass of one of n inertial bodies and $s(\theta)$ is the distance from the center O of the oscillator to the COM of one inertial body depicted in Fig. 5.7. This distance can be computed as follows

$$\begin{aligned} s^2(\theta) &= S_x^2 + \left(r(\theta) - (R_0 - S_y)\right)^2 = S_x^2 + S_y^2 - \delta R_0 S_y \theta^2 + \mathcal{O}(\theta^4) \\ &= S_0^2 - \delta R_0 S_y \theta^2 + \mathcal{O}(\theta^4), \end{aligned} \tag{5.12}$$

where $r(\theta)$ is given in Eq. (4.33), $S_0 = s(0)$ is the distance from O to the COM of one inertial body at equilibrium and S_y is the projection of that distance against the axis formed by the pivots of the connecting rod, see Fig. 5.7a.

Substituting Eq. (5.12) into Eq. (5.11) yields the inertia of the RDCO as it rotates

$$J(\theta) = n\left(J_r + m_r\left(S_0^2 - \delta R_0 S_y \theta^2\right)\right) + \mathcal{O}(\theta^4) \tag{5.13}$$

with relative inertia variation

$$\iota_{\text{RDCO}} = \frac{-\delta m_r R_0 S_y}{J_r + m_r S_0^2} \tag{5.14}$$

according to the definition of Eq. (5.2). The results obtained with this model are compared to the ones obtained by numerical simulation in Fig. 5.8 and show a good match. The FEM model is described in Sec. 5.5.3.
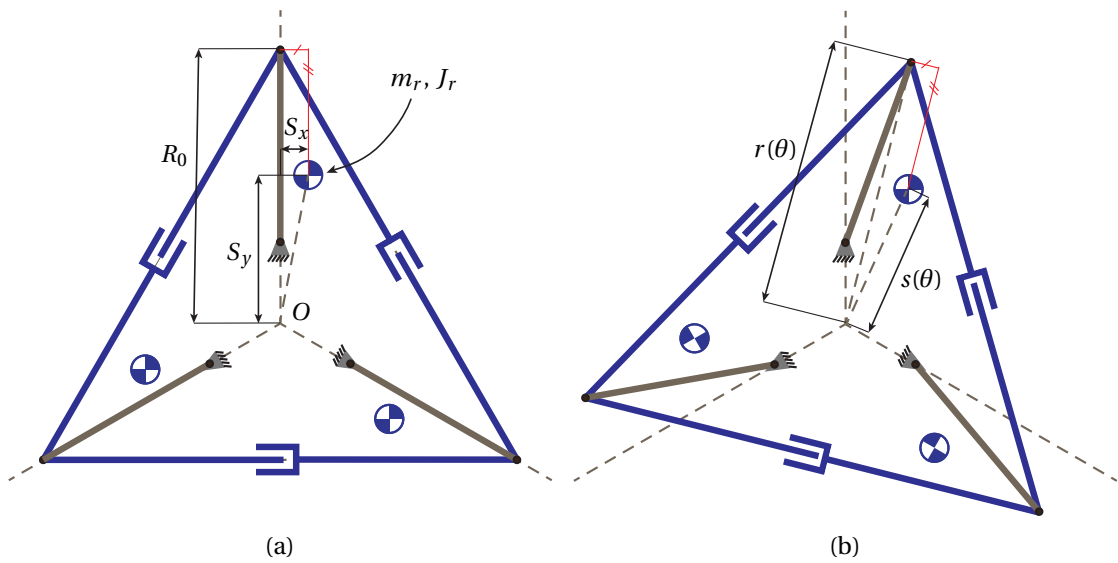
Figure 5.7 – Center of mass position of the inertial bodies of the RDCO (a) in equilibrium position and (b) rotated by angle θ.
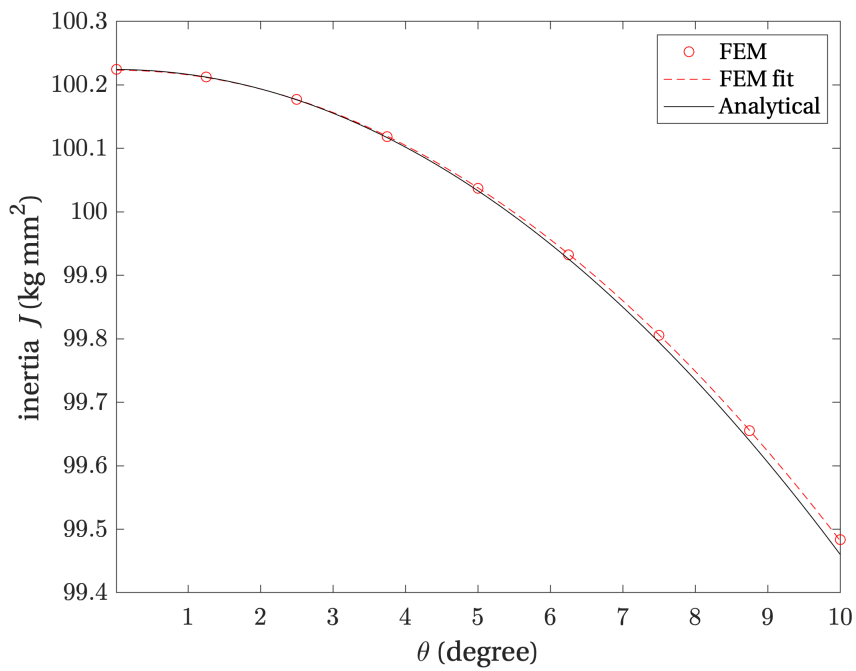
Figure 5.8 – Inertia J of the RDCO versus rotation angle θ obtained by FEM and with the analytical model.

Remark 5.5.1. The sign of the inertia variation in Eq. (5.14) depends on the sign of δ, as was already noted through the sign of the dilation in Sec. 3.3.1.

5.5.2 Stiffness variation

The relative restoring torque nonlinearity of the RDCO is obtained from Eq. (4.39) using the definition of Eq. (4.13):

$$\mu_{\text{RDCO}} = \frac{2\delta(\delta+1)(\delta^2-1)\,k_{A,0} + 2\delta^2(\delta^2-1)\,k_{B,0} + 3\,(\delta+1)^4\,k_{A,0}\mu_A + 6\delta^2\,k_{t,0}R_0^2\sin^2\left(\frac{\pi}{n}\right)}{3\left((\delta+1)^2\,k_{A,0} + \delta^2\,k_{B,0}\right)}. \quad (5.15)$$

Note that the contribution of the relative restoring torque nonlinearity μ_B of the external pivot is neglected assuming that it is small and that δ^4 is small.

5.5.3 Example of implementation

In order to validate the concepts presented in this section, we design a flexure pivot implementation of the RDCO and show that the inertia and stiffness variation can compensate each other in order to reach isochronism. We validated these results by FEM.

Two configurations exist where the inertia and restoring torque defects can compensate each other:

a) $\delta < 0$ and the positive dilation of the system ($\iota > 0$) compensates for the increasing stiffness of the system ($\mu > 0$).

b) $\delta > 0$ and the negative dilation of the system ($\iota < 0$) compensates for the decreasing stiffness of the system ($\mu < 0$).
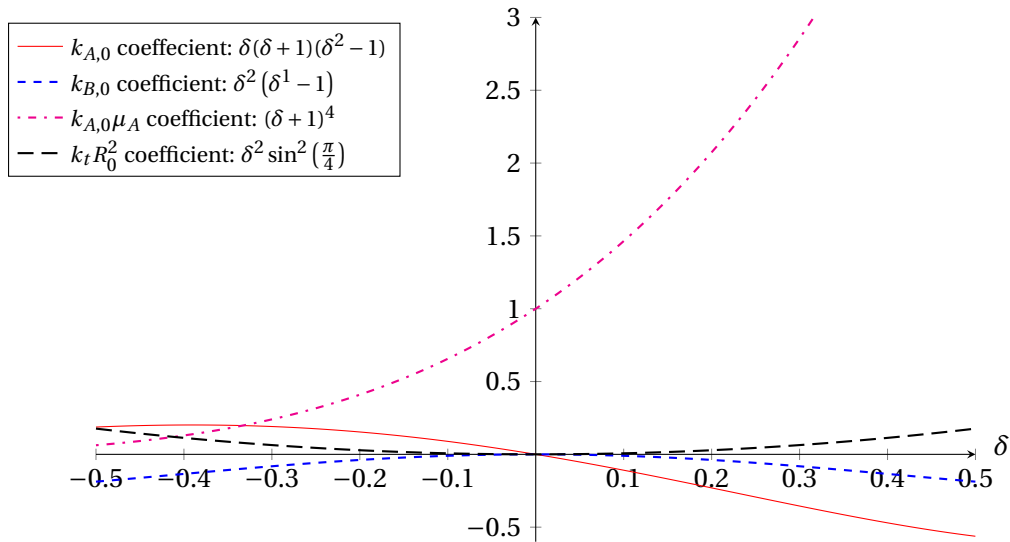
Figure 5.9 – Effect of δ on the four terms forming the restoring torque nonlinearity of the RDCO.

Figure 5.9 shows the contributions of the four terms of the nonlinearity in Eq. 5.15 around $\delta = 0$. There are coefficients with different signs for negative and positive values of δ. This means that the relative weights of the four terms can be adapted to make the sign of the restoring torque nonlinearity match that of the inertia variation. Note that the $k_{0,1}$ term is the only one that changes sign with δ and that it does it in the same way as ι, which is convenient for the desired compensating effect. Note also that the sign of the restoring torque nonlinearity μ_A of pivot A is unknown and will be determined by FEM, as discussed in Sec. 4.1.4.

We choose to implement configuration (b) where $\delta > 0$. This makes the design easier since the connecting rods do not have to cross each other as depicted in Fig. 3.19. The design is shown in Fig. 5.10. It aims at respecting some realistic proportions but does not target watch specifications and has not been validated for fabrication. This effort was instead put into the silicon co-RCC prototype of Chapter 7. The design is intended to demonstrate large nonlinear effects, which is why a relatively large value of $\delta = 0.5$ was chosen.
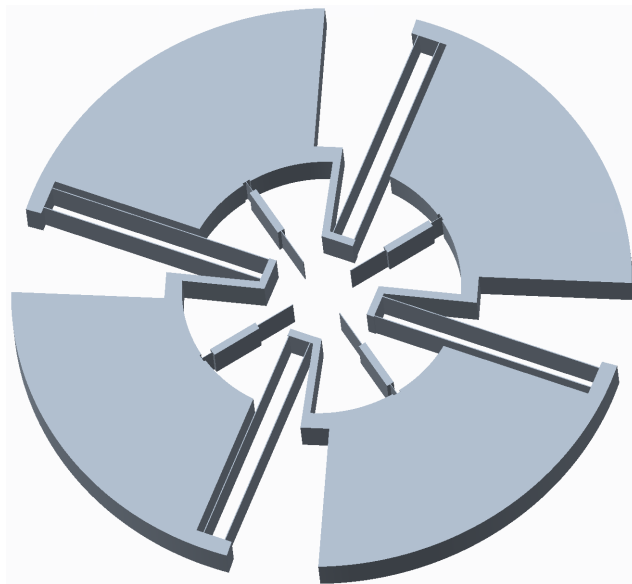
Figure 5.10 – Example of RDCO physical implementation.

The flexure implementation was chosen as follows:

- Leaf springs are used for pivots A of Fig. 3.13 since they perform the greatest deformation, see Eq. (4.32). The stiffness and location of the pivot axis of the flexures were approximated using the pseudo-rigid-body model from (Howell et al., 2013, A.1.5). The dimensions are: thickness of 140 μm, length of 5.4 mm and height of 0.5 mm.

- Truncated circular notches are used for pivots B since their deformation is small in comparison to pivots A and the position of their center of rotation can be known more precisely (at their geometric center). Their stiffness is obtained from (Cosandier et al., 2017, Sec. 3.5.10). The dimensions are: minimum thickness of 50 μm, radius of 13 mm and height of 0.5 mm.

- Parallel leaf springs are used for the sliders. Their stiffness is given in Eq. (4.30). The dimensions are: thickness of 107 μm, length of 30 mm and height of 0.5 mm.

With $\delta = 0.5$ and dimensionless mass parameters $\frac{S_0}{R_0} = 1.76$, $\frac{S_y}{R_0} = 1.75$ and $\frac{J_r}{m_r R_0^2} = 0.413$, Eq. (5.14) returns $\iota = -0.250$. The oscillator was simulated by FEM using shell elements for the leaf spring (pivots A and parallel leaf springs) and solid elements for the circular notches, and assuming all other bodies to be rigid, see Fig. 5.11. An inertia variation $\iota = -0.262$ was obtained with Eq. (5.2) by fitting a polynomial with even coefficients to the FEM data of Fig. 5.8.

(a)

(b)
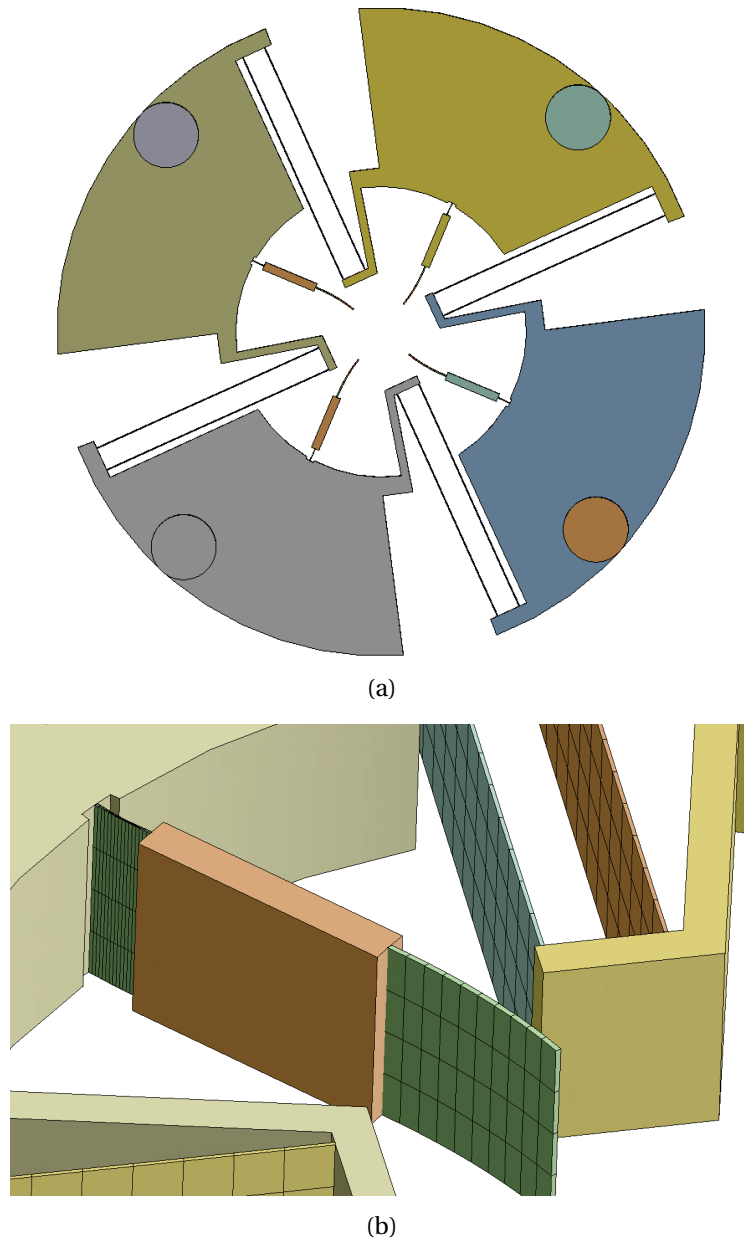
Figure 5.11 – Finite element model of the RDCO: (a) deformed shape for a 10 degrees rotation and (b) close-up view of the mesh.

As mentioned earlier, the nonlinearity μ_A of pivot A is unknown. The dimensions were thus found by using Eq. (5.15) with $\mu_A = 0$ to find a first guess, then adjusting the parameters to find a value of μ_{RDCO} close to ι_{RDCO} and finally fine-tuning μ_{RDCO} by changing the thickness h_t of the parallel leaf springs, see Fig. 5.13. As explained in Sec. 5.5.4, this parameter only affects the restoring torque nonlinearity of the oscillator.

Dimensions were found such that the inertia and stiffness variation compensate each other, hence reaching theoretical isochronism. This is shown in Fig. 5.12. The inertia variation is obtained directly from the data whereas the stiffness variation is obtained either by fitting the restoring torque data with a third order odd polynomial, see Eq. (4.14), or by calculating the secant stiffness for each data point, see Remark 4.1.1. The restoring torque nonlinearity obtained by FEM does not seem to follow the theoretical third order odd polynomial and the results do not match well for small angles. The fact that the slope of k/k_0 obtained with the secant stiffness does not tend to zero as θ goes to zero raises doubt regarding the physical accuracy of the FEM model around equilibrium position. The discrepancies around $\theta = 0$ can be caused by numerical errors or by unmodeled nonlinear effects that could be less significant for less nonlinear designs, for example with smaller values of δ. Nevertheless, the two effects match well above 5 degrees, showing that they can compensate each other.
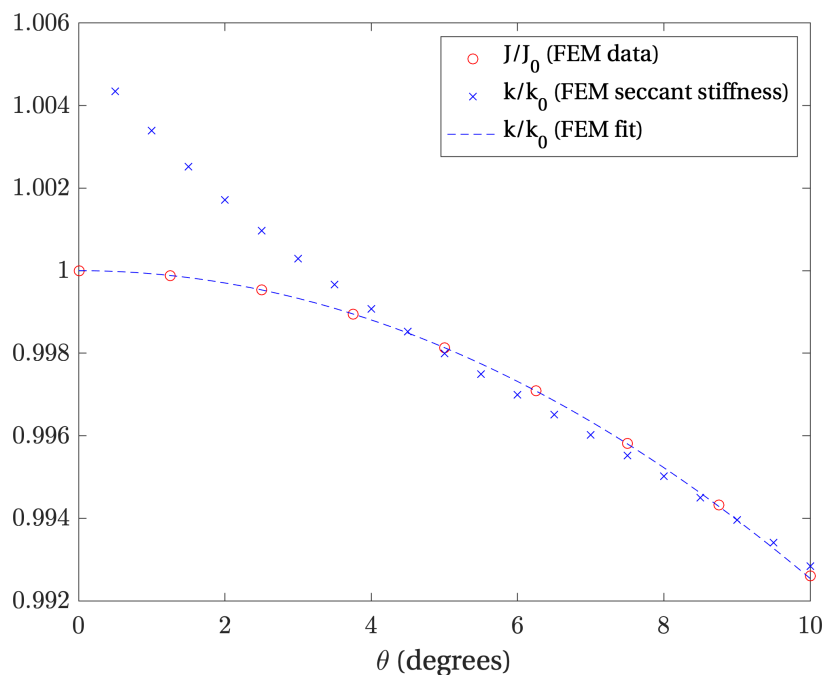
Figure 5.12 – Inertia and stiffness variation of the example RDCO versus rotation angle θ obtained by FEM.

5.5.4   Isochronism tuning

Using the models of Sec. 5.5.1 and 5.5.2, we present two ways of tuning the isochronism of the RDCO, by acting either on the stiffness or the inertia.

Stiffness isochronism tuning

The isochronism of the RDCO can be tuned by varying the relative restoring torque nonlinearity μ_{RDCO} without affecting any other crucial property of the oscillator. As for the co-RCC of Sec. 5.4, this can be done by changing the stiffness k_t of the parallel leaf springs. These flexures perform a second order motion of the rotation angle and thus only contribute to the stiffness variation in Eq. (4.39) without affecting the nominal stiffness. The tuning calculated with Eq. (5.15) is compared to FEM results in Fig. 5.13, showing a good match. The slight difference can be explained by the shift in center of rotation of the leaf springs explained below. Note that the model cannot predict the absolute restoring torque nonlinearity since μ_A is unknown. The results are thus shown in terms of variation of restoring torque nonlinearity $\Delta\mu$ obtained for a relative thickness variation Δh_t of the parallel leaf springs in Fig. 5.13. Note that the relative thickness variation is used to make the results dimensionless.
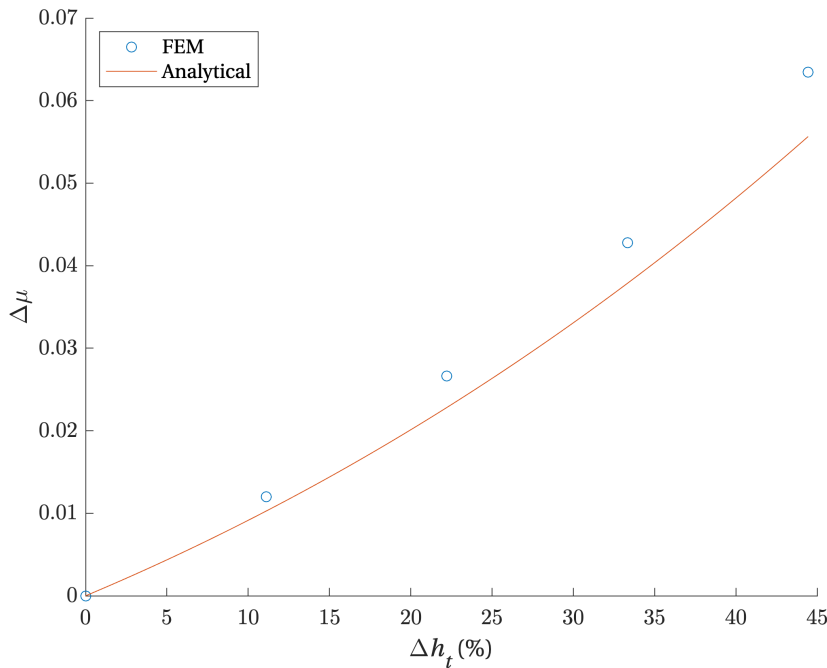
Figure 5.13 – Restoring torque nonlinearity tuning (and thus isochronism tuning) for the RDCO by varying the thickness h_t of the parallel leaf springs. Results obtained by FEM and with the analytical model are displayed.

Inertia isochronism tuning

The isochronism of the RDCO can be tuned by varying the inertia variation ι_{RDCO} without changing any other crucial property of the oscillator. Equation (5.14) shows that this can be done by changing parameter S_y without changing J_r, m_r or S_0. This can be done by moving the COM of the inertial part on a circle centred at point O as depicted in Fig. 5.14. Note that the stiffness properties of the oscillator are not affected by these changes in mass distribution.
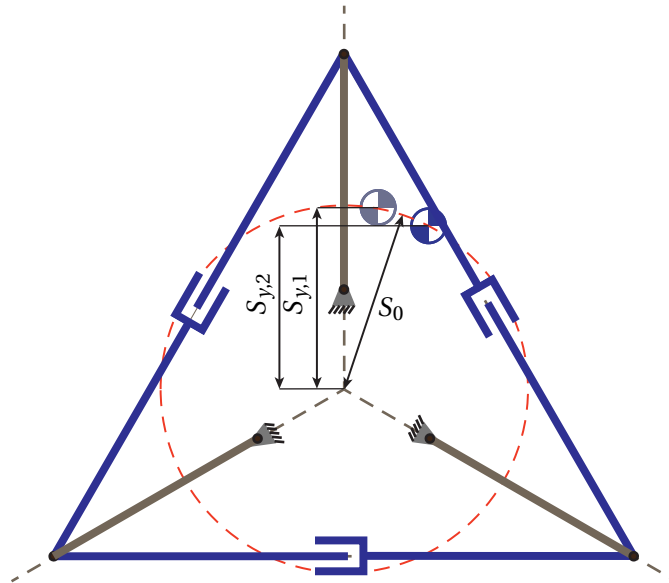
Figure 5.14 – Tuning of the inertia variation ι of the RDCO.

In practice, the tuning can be implemented by moving tuning masses placed on the inertial bodies of the RDCO about a circle centred at point O. Figure 5.15 shows how this is performed on the simulated RDCO: the angular position β of tuning masses is varied. Note that the nominal position $\beta = 0$ is offset with respect to the axis formed by the pivots of the connecting rods such that the tuning can produce either a positive or negative isochronism defect. The results are plotted in Fig. 5.16. They show that the tuning is effective and the tendency corresponds to the predictions of the analytical model. There is a close to constant offset between the two curves that can be easily corrected, for instance by changing the stiffness of the parallel leaf springs as explained above.

Figure 5.17 shows the tuning obtained in terms of daily rate for 10% amplitude variation from reference amplitude $\Theta_1 = 10$ degrees. The masses were chosen such that the correction if of order 1 s/day for the angular range depicted in Fig. 5.15. The tuning can be adjusted by changing the mass ratio, inertia ratio and COM radius ratio between the mobile and fixed parts of the inertial bodies. In this example, the values of 0.44, 0.025 and 0.79 were chosen for these respective ratios.

The tuning slope is different between the two models. This difference can be explained by the fact that the location of the pivoting axis of leaf spring used to implement pivot A is not

exactly known in the equilibrium position and that this axis moves as the oscillator rotates. The pseudo-rigid-body model with fixed axis used is only an approximation (Howell et al., 2013). It is known that leaf springs do not exactly behave as ideal joints and exhibit parasitic motions that are not taken into account in the analytical model and can have a significant impact at this level of precision (frequency variation of order 10 ppm in Fig. 5.17).

(a) $\beta = 0$ (b) $\beta = 13.5$ (c) $\beta = -12.5$
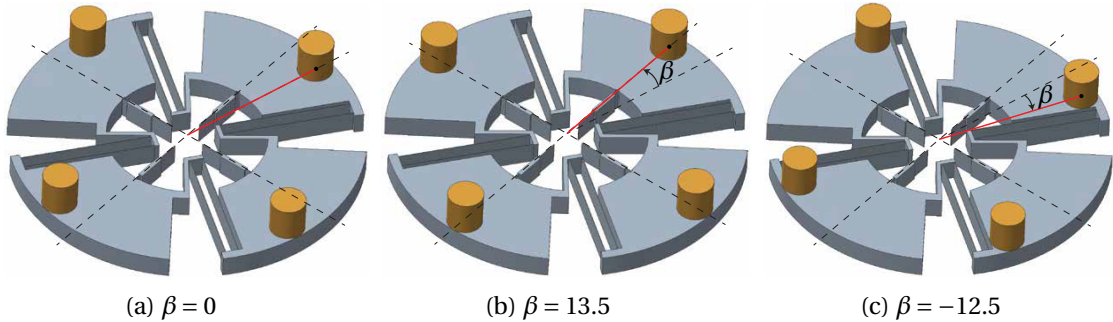
Figure 5.15 – Isochronism tuning masses for the RDCO.
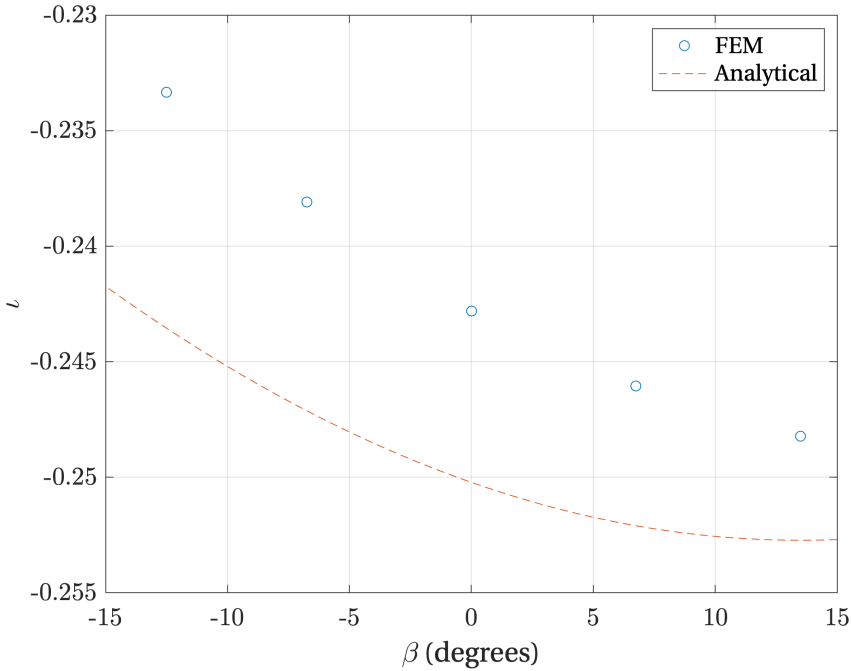
Figure 5.16 – Inertia variation tuning for the RDCO by varying the angular position β of tuning masses. Results obtained by FEM and with the analytical model are displayed.
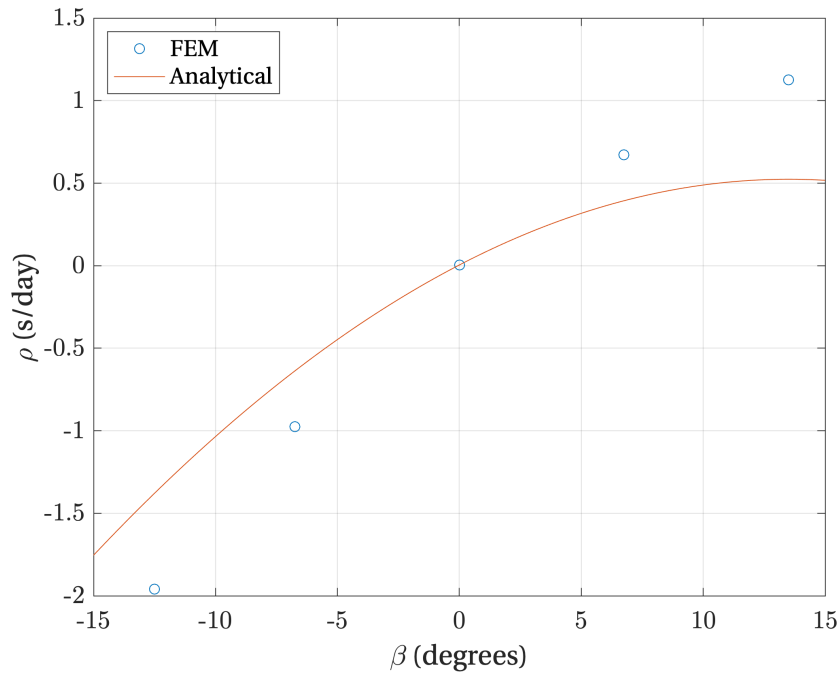
Figure 5.17 – Isochronism tuning for the RDCO by varying the angular position β of tuning masses. Results obtained by FEM and with the analytical model are displayed in terms of daily rate ρ for 10% amplitude variation from reference amplitude $\Theta_1 = 10$ degrees.

5.6 Chapter conclusion

In this chapter, the concept of isochronism tuning using second order terms of stiffness and inertia was formalized and expressions were derived to quantify it. Practical methods of tuning were developed, by modifying dimensions (i.e., the stiffness) of parallel leaf springs for the co-RCC and RDCO and by displacing tuning masses for the RDCO. It was shown that these methods allow to reach a tuning of order 1 s/day, which allows to reach the accuracy goal of this thesis.

6 Gravity sensitivity

In order to implement the new flexure pivot oscillators of this thesis in mechanical watches, one must address one of the principal challenges of making a timekeeper portable: the influence of gravity on the frequency of the time base must be minimized. Flexure-based oscillators are sensitive to gravity due to the fact that

1. they only approximate the motion of ideal linkages, which can lead to a parasitic shift of the center of mass,

2. the elements supporting the mass of the inertial element are not infinitely rigid and thus deform under gravity.

For the traditional balance and hairspring oscillator, the direction of gravity is also an issue, but for different reasons:

1. The sag of the hairspring deforms its spiral shape, which influences its restoring torque.

2. The friction in the bearings of the balance depends on the loading direction (axial versus radial).

For these reasons, mechanical watches are traditionally tested in different positions with respect to gravity.[1]

In this chapter, we present two approaches to analyze the influence of gravity on the stiffness of flexure-based oscillators and use them to provide guidelines for the design of these oscillators. We show how these principles apply to our oscillators and use them to tune the effect of gravity.

---

[1] See the requirements for the "Chronometer" certificate of the Official Swiss Chronometer Testing Institute (COSC) at www.cosc.swiss/en/certification/mechanical-movements. See the requirements for the "Master Chronometer" certificate of the Swiss Federal Institute of Metrology (METAS) at www.metas.ch/dam/data/metas/Dokumentation/rechtliches/zertifizierung-uhren/metas-n001-v-1-1-e.pdf.

6.1 Definition of gravity insensitivity

Ideally, an oscillator would be insensitive to gravity if its oscillation frequency is totally independent of its orientation with respect to gravity. This cannot be achieved in practice and we define a gravity-insensitive oscillator to be

An oscillator whose daily rate varies within 5 s/day in all orientations with respect to gravity,

where daily rate is defined in Eq. (5.7). This error is considered acceptable for a mechanical watch application and corresponds to chronometer certifications by official testing organizations.[1]

Assuming a constant inertia, this condition can be expressed in terms of stiffness variation

$$\rho = 86\,400 \frac{\sqrt{k} - \sqrt{k_1}}{\sqrt{k_1}} \le 5, \tag{6.1}$$

which, considering small stiffness variations ($\sqrt{1 + \epsilon} \approx 1 + \frac{\epsilon}{2}$) can be approximated by

$$\rho = 43\,200 \frac{k - k_1}{k_1} \le 5, \tag{6.2}$$

which, using the relative stiffness variation $\epsilon = \frac{k - k_1}{k_1} \cdot 10^6$ defined in Eq. (4.16), is equivalent to

$$\epsilon \le 120\,\text{ppm}. \tag{6.3}$$

6.2 Design principles for gravity effect minimization

In order to analyze the influence of gravity on the frequency of our oscillators, it is assumed that gravity does not influence the inertia of the oscillator: only the effect on the stiffness is considered. Since gravity is always present, the goal is not to minimize the effect of varying magnitude of gravity force on the frequency of the oscillator but instead to minimize the effect of varying direction of gravity force of constant magnitude. Note that this results in a second order effect of the magnitude of gravity on the frequency, which makes the effect of geographical variations of Earth gravity negligible.

In order to evaluate the effect of gravity on the stiffness of the oscillator, two equivalent approaches are used: an energetic approach and a beam theory approach.

6.2.1 Energetic approach to gravity effect

Gravity can affect the restoring torque of a rotational oscillator by either contributing to the restoring torque of the elastic element (positive stiffness contribution) or providing a torque that drives the oscillator away from its equilibrium (negative stiffness contribution). The

influence of this *gravitational elasticity* was already observed by Hetzel (1962) between the two vertical positions of the tuning fork. The equivalent stiffness of the oscillator resulting from the elastic and gravity components can be evaluated from its total potential energy as it rotates by angle θ

$$U = U_{el} + U_g = \int_0^\theta M(v) \, dv + \int_0^{\Delta_{\text{COM, x}}(\theta)} F \, dx, \tag{6.4}$$

where M is the restoring torque of the elastic elements and the gravitational potential energy corresponds to the work of the gravity force F along the collinear component of the COM shift $\Delta_{\text{COM, x}}$. The rotational stiffness is then obtained by deriving and dividing the total potential energy by θ, as was done in Eq. (4.29).

Equation (6.4) makes the condition to minimize the effect of gravity explicit: the component of the COM shift of the oscillator as it rotates that is collinear to gravity $\Delta_{\text{COM, x}}$ must be the same in all orientations.

Focusing on effects of gravity in the plane of oscillation, the previous condition can be achieved with flexure-based oscillators by following two design guidelines, (a) and (b):

(a) Cancel or compensate the parasitic translations of the flexures.

(b) Design and dimension the flexures such that the stiffness of the "blocked" translational degrees-of-freedom of the oscillator is the same in all directions.

Condition (b) is necessary because the degrees-of-freedom that are considered to be blocked by the flexures actually always have a residual stiffness. Gravity force will thus still result in a shift of the COM along these directions that can have a significant effect at the precision level considered (of order 100 ppm).

One can now summarize how these guidelines are implemented on our oscillators. Note that only the effect of gravity in the plane of oscillation is discussed, out-of-plane effects will be discussed in Sec. 6.5.

The GIFP

The bending rods of the GIFP are placed in sets of identical symmetrical pairs, at a 180° rotation in the xy-plane and equidistant from the COM in the z direction. The consequence is that their parasitic translation, the shortening of the bending rods as the pivot rotates, does not affect the position of the COM, thus following Guideline (a).

The two sets of symmetric rods are placed perpendicularly in the xy-plane and have the same rods. This minimizes the difference in stiffness of the pivot for translations with varying orientation in the xy-plane, thus following Guideline (b).

The co-RCC

In the co-RCC, it is assumed that the parasitic shift of the RCC pivots is along the bisector of the angle formed by its two leaf springs, see Sec. 3.2.1. This motion is prevented from being transmitted to the inertial body by placing a slider with a DOF in this direction between each RCC and the inertial body. The two half co-RCC elements are placed at an angle such that they block each other's translational DOF while keeping the rotational DOF, see Sec. 3.2.3. The inertial body has thus theoretically no parasitic center shift and the co-RCC follows Guideline (a).

The angle between the two half co-RCC elements is chosen to be 90 degrees so as to minimizes the difference in stiffness of the pivot for translations with varying orientation in the xy-plane, thus following Guideline (b).

The RDCO

The rotational symmetry of the RDCO guarantees that the parasitic shift of the flexures compensate each other, thus following Guideline (a).

The rotational symmetry also minimizes the difference in stiffness of the pivot for translations with varying orientation in the xy-plane, thus following Guideline (b). Note that increasing the order of rotational symmetry will reduce this difference, see Sec. 3.3.2.

6.2.2 Beam theory approach to gravity effect

The other approach to gravity sensitivity used in this thesis relies on beam theory to analyze the effect of the forces induced by gravity on the rotational stiffness of the oscillator. This approach is interesting in our context because it allows to compute both the effects of amplitude (isochronism defect) and gravity at the same time, as done in Chapter 4, and to evaluate their potential interactions. Minimizing the effect of gravity corresponds to eliminating the orientation of the gravity from the equation for rotational stiffness.

Focusing on effects of gravity in the plane of oscillation, this can be achieved on flexure-based oscillators with the following two design guidelines, (a) and (b):

(a) Place the flexures in pairs following the co-differential concept of Sec. 4.2.2 to cancel the first order effect of gravity on the rotational stiffness of the pivot.

(b) Have the two co-differential pairs of flexures be identical and place them orthogonally such that the effect of gravity is independent of its angle φ (following the trigonometric identity $\cos^2 \varphi + \sin^2 \varphi = 1$).

The models presented in Sec. 4.2 and 4.3 show how these guidelines result in eliminating the orientation φ of gravity from the rotational stiffness of the GIFP and co-RCC in

Eq. (4.22) and (4.31) respectively. The out-of-plane effects will be discussed in Sec. 6.5.

6.2.3 Equivalence of the two approaches

It can be seen that our oscillators follow the guidelines laid out with both approaches. Indeed, the two approaches are equivalent.

- If two flexures have their shortening in opposite direction and symmetrical with respect to the COM, there will be no parasitic center shift and they will be subjected to equal but opposite axial loads due to gravity, thus following Guideline (a) of both approaches. In the same way, if the parasitic shift is not transferred to the inertial body, as is the case in the co-RCC, then neither is the axial load along this component. Thus, if a parasitic shift is canceled instead of being compensated by an equal but opposite one, the co-differential principle is also respected.

- If the flexures used to achieve the previous point are identical and placed orthogonally, they follow Guideline (b) of both approaches.

The equivalence of the two approaches is also illustrated on the crossed flexure pivot (CFP), where the value of crossing ratio $\delta \approx -0.127$ which minimizes the gravity effect in Eq. (4.11) is also the value that minimizes the parasitic center shift of the pivot in Eq. (4.26).

The architectures suggested by Hetzel (1962) in Fig. 2.1 to cancel the influence of gravity on the tuning fork also show the equivalence of the two approaches. They allow the COM of the tuning fork to stay in the same position and result in having always one blade in compression for one blade in tension.

6.3 In-plane gravity effect numerical validation

Section 6.2 explained how, according to our models, the GIFP and co-RCC follow the guidelines to minimize the effect of gravity in the plane of oscillation on their rotational stiffness. In order to validate these models and be free from their assumptions, the effect of gravity is simulated by FEM. The case of the RDCO is discussed in Sec. 6.5.3.

6.3.1 In-plane gravity effect on the GIFP

Using the same method as in Sec. 4.1.4, the GIFP is subjected to a normalized load $\bar{F} = 0.2$ with varying orientation φ. The results in terms of relative stiffness variation ϵ are shown in Fig. 6.1. Note that the use of the normalized force $\bar{F} = FL^2/EI$ makes the results independent of the dimensions of the flexures. There is a good match between FEM and analytical results, with a difference below 1 ppm, which validates the analytical model. Note that for this crossing ratio ($\delta = -0.5$), the stiffness variation for same normalized load is more than 10^4 times smaller

than for the CFP in Fig. 4.8.

Remark 6.3.1. The difference between FEM and analytical results can be explained by the neglecting, in the analytical model, of the parasitic shift in the lateral deflection of the beams, see Assumption (i) of Sec. 4.1, and other higher order terms.
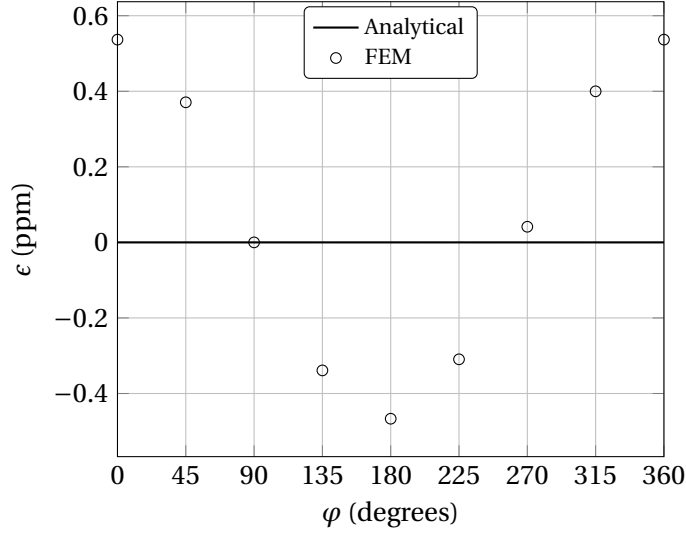
Figure 6.1 – Relative stiffness variation ϵ of the GIFP for varying orientations φ of the normalized central load $\bar{F} = 0.2$. Analytical and FEM results are shown for a pivot with $\delta = -0.5$ and $\alpha = 45$ degrees.

Remark 6.3.2. The benefits of the co-differential concept are illustrated in Fig. 6.2. This figure compares the relative stiffness variation of the CFP and GIFP under central loading with respect to the stiffness with no load for different values of the crossing ratio δ ($k_{\text{ref}} = k_0$ in Eq. 4.16). One can see that the effect is highly dependent on the crossing ratio for the CFP, with variations of order 10^4 ppm, whereas for the GIFP, the effect stays of order 10 ppm for all crossing ratios. This is due to the fact that the co-differential concept cancels the first order term of $\bar{F}$ whereas this is only the case for the CFP when $\delta \approx -0.127$, as mentioned in Remark 4.1.2.

6.3.2 In-plane gravity effect on the co-RCC

The daily rate of the co-RCC for gravity in the xy-plane with respect to operation without gravity is obtained by substituting Eq. (4.31) into Eq. (6.2), yielding

$$\rho = 43\,200 \frac{k_{c,0} - \frac{EI}{L}\frac{9\delta^2+9\delta+11}{12600\sin^2\alpha}\bar{F}^2 - k_{c,0}}{k_{c,0}} = -\frac{3\left(9\delta^2 + 9\delta + 11\right)}{14\left(3\delta^2 + 3\delta + 1\right)\sin^2\alpha}\bar{F}^2 \tag{6.5}$$

where $k_{c,0} = 2k_{r,0}$ is obtained from Eq. (4.12). As in the case of the GIFP, we verify these results by FEM using the model described in Sec. 5.4.2. Instead of calculating the restoring
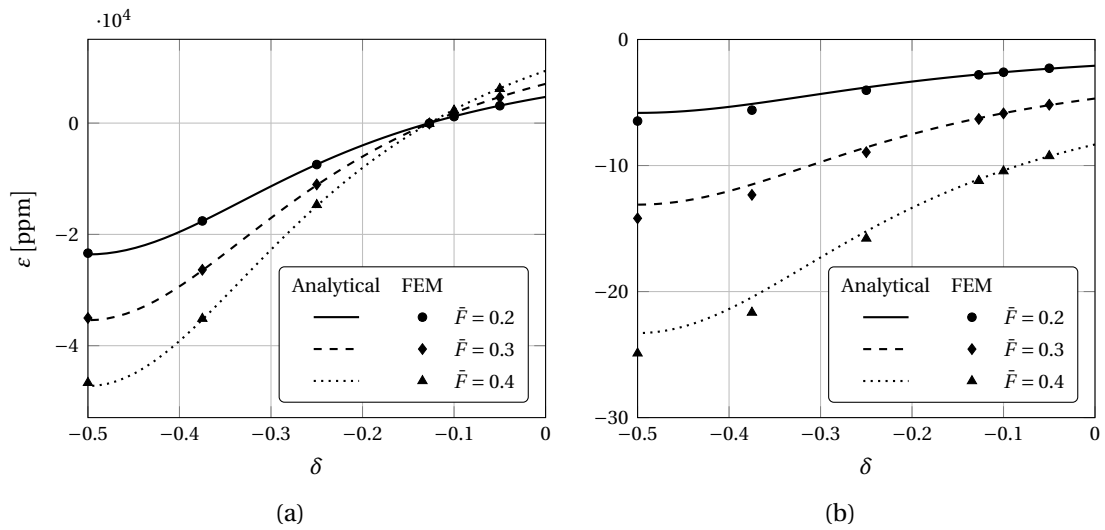
Figure 6.2 – Relative stiffness variation ϵ of (a) the CFP and (b) the GIFP versus crossing ratio δ for different normalized gravity loads. Analytical and FEM results are shown for pivots with $\alpha = 45$ degrees, rotations of $\theta = 0.1$ degrees and gravity acting at an angle $\varphi = 0$.

torque of the oscillator, its frequency is directly obtained by modal analysis when subjected to standard earth gravity with varying orientation, see Fig. 5.6a. In order to be consistent with the theoretical model, the masses of the intermediate bodies are set to zero and the COM is at point O. The data is collected for accelerations in the xy-plane with orientation ψ spanning the interval from 0 to 360 degrees. The daily rate with respect to operation without gravity obtained with Eq. (5.7) is displayed in Fig. 6.3.

For the oscillator dimensions given in Sec. 7.2.1, the gravity sensitivity obtained by FEM varies between -2.4 and -6.4 s/day whereas Eq. (6.5) returns a constant value of -5 s/day. Considering the order of magnitude observed (a 1 s/day rate variation corresponds to a 10 ppm frequency variation), the results are close enough to validate the model. The daily rate of -4.4 ± 2 s/day calculated numerically is within the specifications of Sec. 6.1. Note that the constant offset of -4.4 s/day is not problematic since it can be taken into account in the design.

Remark 6.3.3. The differences between the analytical model and the numerical solution could be explained by a shift of the COM of the pivot due to the u-component of the RCC parasitic shift that is neglected in the model of Sec. 3.2.1 and affects the gravity sensitivity, see Sec. 6.2.1. This assumption is coherent with the symmetric maximum and minimum observed at 45 and 225 degrees, corresponding to the axis of symmetry of the architecture.

6.4   In-plane gravity effect tuning

Figures 6.1 and 6.3 show that there is a gravity effect that is not taken into account by our model. This effect is lower than the timekeeping accuracy specification of Sec. 6.1 and could
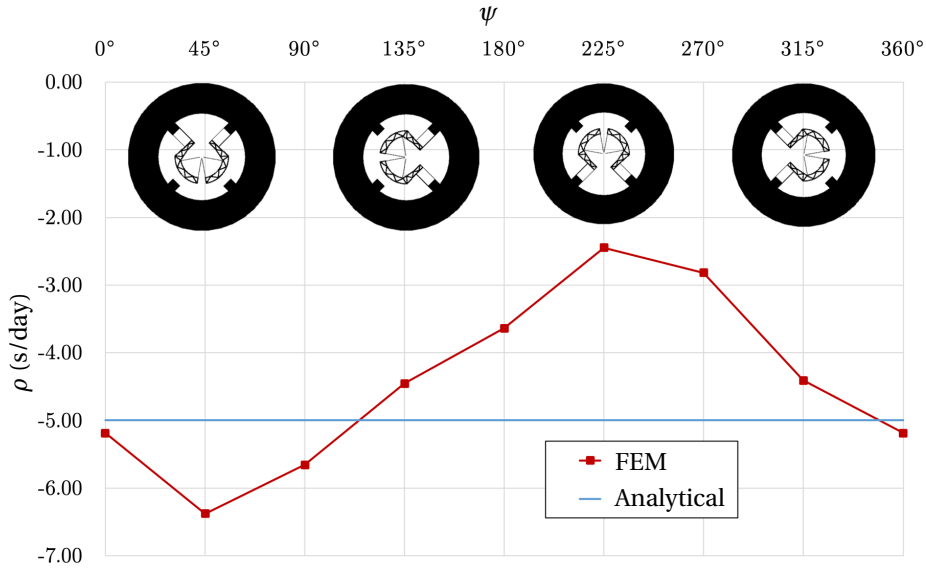
Figure 6.3 – Daily rate ρ of the co-RCC oscillator without intermediate body mass versus the angle ψ of the gravity load in the xy-plane. The reference frequency corresponds to operation without gravity.

be neglected. However, when the mass of the intermediate bodies of the co-RCC is non-zero, as it is the case in practice, the effect of gravity is not negligible: the FEM results show a rate variation of ± 8.9 s/day that is out of the specifications, see Fig. 6.4. Note that these values were obtained with the prototype dimensions of Sec. 7.2.1 where the intermediate bodies are lightened using a truss structure, see Fig. 5.6.

Remark 6.4.1. The extrema of the gravity effect are inverted between Fig. 6.4 and 6.3. According to the energetic approach of Sec. 6.2.1, a logical explanation for this phenomenon is that the parasitic shift of the intermediate bodies is opposed to the parasitic shift of the inertial body and that the first dominates the latter. This seems reasonable since the parasitic shift of the intermediate bodies is of second order of θ, see Eq. (4.26), whereas this motion is supposed to not be transmitted to the inertial body thanks to the DOF of the parallel leaf springs, see Fig. 3.6.

Since the effect of gravity in Fig. 6.4 is antisymmetric, it can be compensated by a gravitational elasticity of opposite sign. This effect, which is analogous to adding a pendulum to the oscillator is depicted in Fig. 6.5. The restoring torque of the ideal pendulum with point mass m and a massless rod of length s depicted in Fig. 6.5a is $M_g = mgs\sin\theta \approx mgs\theta$ for small angles. As a result, the total stiffness when combining it with an oscillator with stiffness k_{el} is

$$k = k_{el} + mgs. \tag{6.6}$$

When gravity acts in the opposite direction, the inverted pendulum situation depicted in Fig. 6.5b occurs, where the additional restoring torque $M_g \approx -mgs\theta$ of the pendulum yields
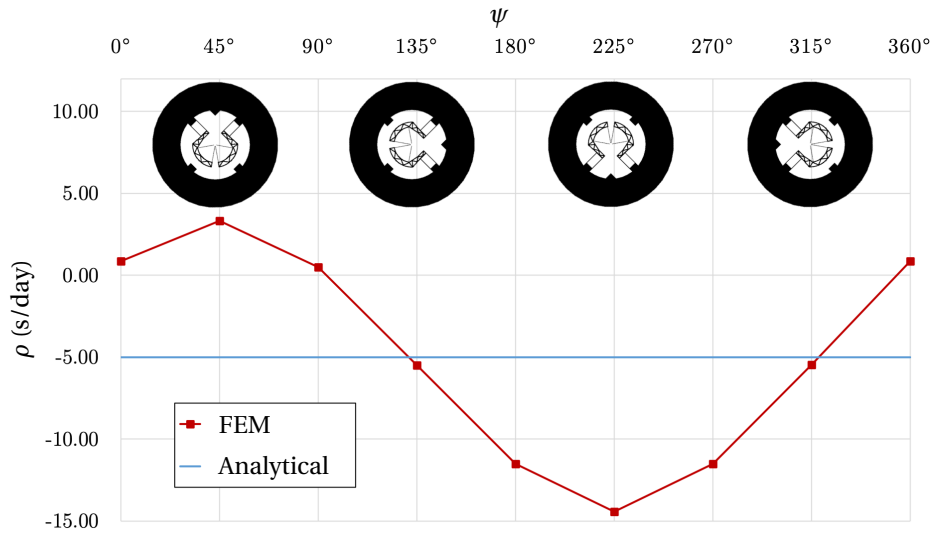
Figure 6.4 – Daily rate ρ of the co-RCC oscillator with intermediate body mass versus the angle ψ of the gravity load in the xy-plane. The reference frequency corresponds to operation without gravity.
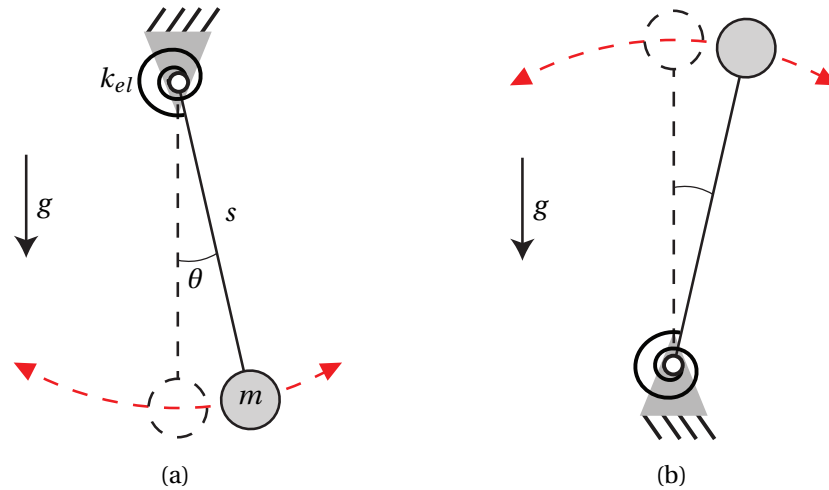
Figure 6.5 – (a) Positive and (b) negative gravitational elasticity caused by the addition of a pendulum to a rotational spring of stiffness k_{el}.

the total stiffness

$$k = k_{el} - mgs. \tag{6.7}$$

This can be realized in practice by moving the COM of the co-RCC away from the center of rotation by a distance s along the axis of symmetry of the oscillator, as depicted in Fig. 6.6. This results in a negative gravitational elasticity when the gravity acts at an angle $\phi = 45$ degrees and positive gravitational elasticity when $\phi = 225$ degrees that will compensate the change in frequency shown in Fig. 6.4.
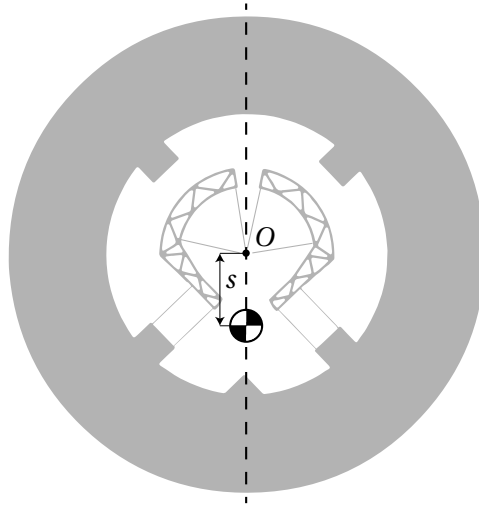
Figure 6.6 – In-plane gravity effect tuning by moving the COM from point O by a distance s along the axis of symmetry of the oscillator. Note that s is enlarged on the figure for visual clarity.

The tuning obtained in the two extreme positions of Fig. 6.5a can be expressed in terms of daily rate by inserting Eq. (6.6) and (6.7) into Eq. (6.2)

$$\rho = 43\,200\frac{k_{el} \pm mgs - k_{el}}{k_{el}} = \pm 43\,200\frac{mgs}{k_{el}}. \tag{6.8}$$

Equation (6.8) gives an expression for the imbalance $B = mgs$ necessary to compensate a given antisymmetric daily rate defect $\pm\rho$. For the oscillator simulated in Fig. 6.4 whose nominal rotational stiffness with the dimensions given in Sec. 7.2.1 is $k_{el} = k_{c,0} = 8.95 \cdot 10^{-5}$ N·m, the imbalance given by Eq. (6.8) to compensate for the $\rho = \pm 8.9$ s/day defect is

$$B = \frac{\rho\, k_{el}}{43\,200} = 18 \text{ nN·m}. \tag{6.9}$$

These results were verified by FEM and are displayed in Fig. 6.7. The best results were obtained with an imbalance $B = 17$ nN·m, close to the 18 nN·m calculated in Eq. (6.9). The in-plane gravity effect on the oscillation frequency is almost completely canceled, which shows the efficiency of the method.

If a greater value of imbalance is chosen, such as 35 nN·m, the gravity effect can even be inverted, showing that important defects can be canceled. For this value, Eq. (6.8) gives a rate correction of ∓ 17 s/day which would change the defect calculated in Fig. 6.4 from ± 8.9 s/day to ∓ 8.1 s/day. The FEM results in Fig. 6.7 show a new rate of ± 8.6 s/day which is close to the prediction of our model and validates this tuning method.

Figure 6.8 shows the difference in mass distribution of the oscillator used to reach the values

of imbalance for the tuning seen in Fig. 6.7. This gives a qualitative indication of the order of magnitude of the correction.

Remark 6.4.2. Note that the mass of the oscillator changes between the different cases, which has an influence on the effect of gravity, but we consider this effect to be negligible because the mass varies by less than 0.5% between the three cases. The change in inertia caused by this tuning method would have to be compensated in order not to alter the nominal frequency of the oscillator. This is a standard procedure in watchmaking that can be done with *inertia blocks* (Berner, 2002).
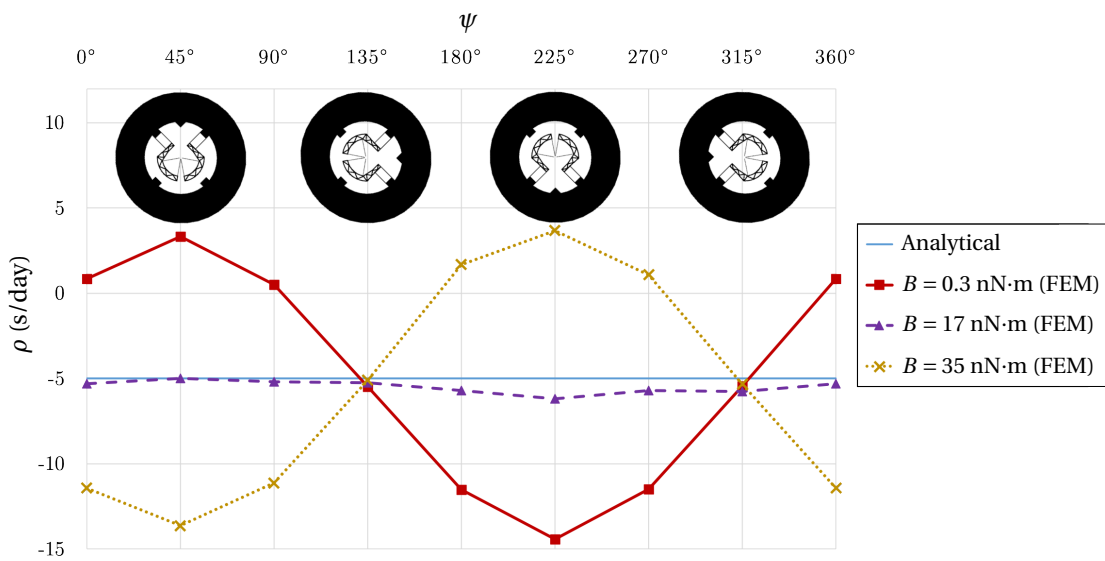
Figure 6.7 – Daily rate ρ of the co-RCC versus the angle ψ of the gravity load in the xy-plane for different values of imbalance B. The reference frequency corresponds to operation without gravity

(a) $B = 0.3$ nN·m   (b) $B = 17$ nN·m   (c) $B = 35$ nN·m
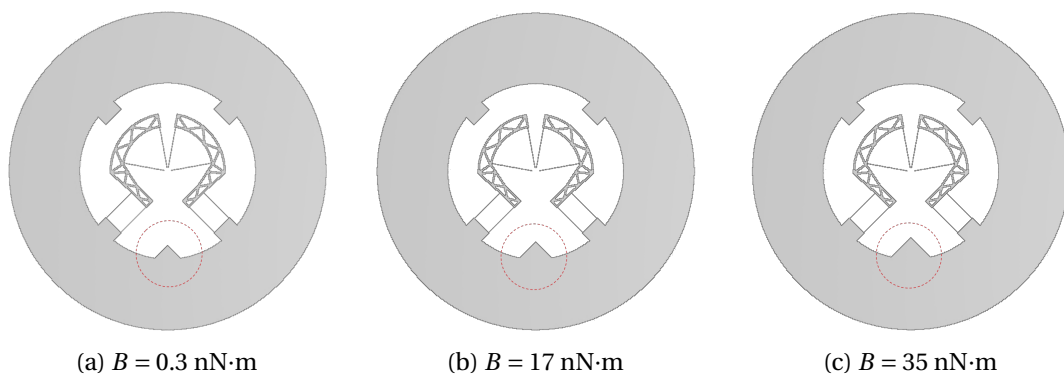
Figure 6.8 – Different values of imbalance B for in-plane gravity effect tuning obtained by asymmetrically adding matter to the inertial body of the co-RCC.

6.5   Out-of-plane gravity effect minimization

Sections 6.2 and 6.4 give practical guidelines to minimize the influence of gravity acting in the plane of oscillation. Yet, in order to reach gravity insensitivity according to the definition of Sec. 6.1, out-of-plane loading must also be considered. The two design guidelines developed using the beam theory approach of Sec. 6.2.2 can thus be generalized to minimize the effect of gravity for any orientation of the oscillator, yielding the following guidelines (a) and (b):

(a) Design the flexures such that the effect of gravity along three orthogonal directions on the rotational stiffness of the oscillator is of order ≥ 2 and independent of the sign of the load.

(b) Dimension the flexures such that the effect of a load along these three orthogonal directions is the same.

Assuming small loads such that the gravity terms of order > 2 are negligible and the superposition principle applies, these guidelines mean that any load can be decomposed into three orthogonal components whose effects sum up to a constant. In other words, if the stiffness of the oscillator is of the form

$$k = k_0 + k_x \left(F_x^2 \right) + k_y \left(F_y^2 \right) + k_z \left(F_z^2 \right) \tag{6.10}$$

where F_x, F_y and F_z are the orthogonal components of the central load and their effect on the stiffness k are constant and equal ($k_x = k_y = k_z = k_F$), the effect of a load F with spherical coordinates θ_F and φ_F is

$$\begin{aligned} k &= k_0 + k_x \left(\cos\theta_F \cos\varphi_F F \right)^2 + k_y \left(\sin\theta_F \cos\varphi_F F \right)^2 + k_z \left(\sin\varphi_F F \right)^2 \\ &= k_0 + k_F F^2 \end{aligned} \tag{6.11}$$

which does not depend on the orientation θ_F and φ_F of the gravity load.

We now discuss how these guidelines can be applied to our new oscillators.

6.5.1   Out-of-plane gravity effect on the GIFP

The GIFP described in Fig. 3.3 only fulfils the condition for gravity insensitivity in the xy-plane. For load components in the z direction, the torsion rod is either in tension or compression, resulting in different effects on its stiffness, i.e., k_z is not constant in Eq. (6.10) and Guideline (a) is not respected. Nevertheless, the effect of gravity on the pivot is small, see Fig. 6.1, and it seems possible to design an oscillator such that the effect on the stiffness is within the 120 ppm of Eq. (6.3) in all orientations.

The GIFP architecture presented in Fig. 3.4 can fulfil the conditions for out-of-plane gravity effect minimization due to the use of the L-shaped flexure instead of the torsional rod. The effect of the z-component of gravity on this flexure is independent of its sign due to symmetry

and is of second order (Van Eijk, 1985), thus respecting Guideline (a).

We do not investigate this issue further on the GIFP as its purpose is mainly to introduce the design principles for in-plane gravity effect cancellation. The topic is explored further on the co-RCC oscillator in the next section.

6.5.2 Out-of-plane gravity effect on the co-RCC

The co-RCC follows Guideline (a) for out-of-plane gravity effect minimization: the in-plane gravity effect was successfully minimized in Fig. 6.7 and the out-of plane effect is symmetric and of order 2 (Van Eijk, 1985, Annex 6.I). Guideline (b) has however not been discussed yet and, when gravity acts along the z axis, the daily rate of the oscillator takes a value of -11 s/day, which is a difference of approximately 6 s/day with the in-plane values, see Fig. 6.9.
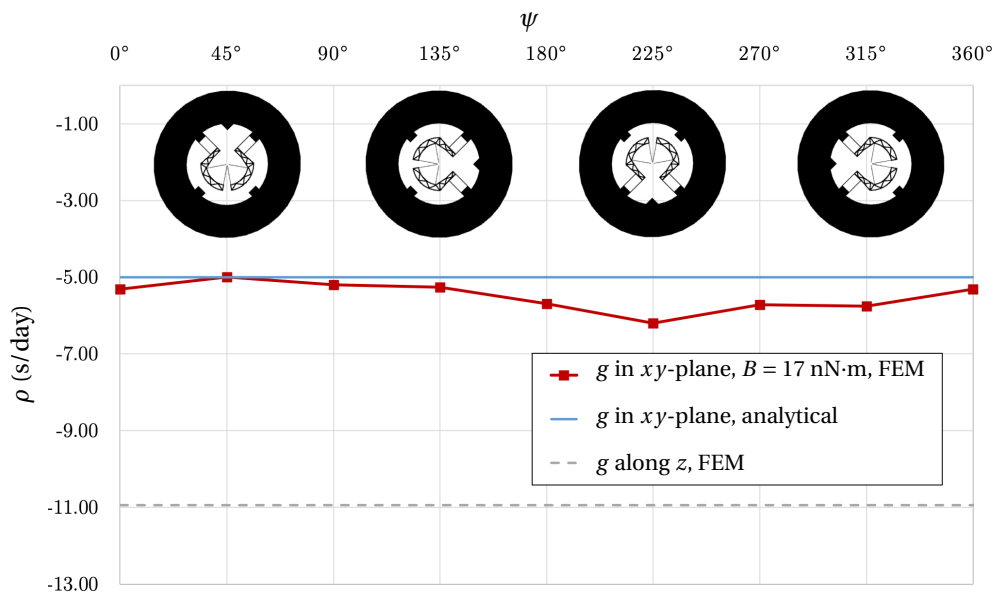
Figure 6.9 – Daily rate ρ of the co-RCC for varying angle ψ of the gravity load in the xy-plane and for gravity acting along the z axis. The reference frequency corresponds to operation without gravity.

One way of matching the effect of gravity along z with the in-plane effect is to increase the height b of the oscillator in the z direction. Indeed, the out-of-plane stiffness of a leaf spring is of third order of its height whereas the in-plane stiffness is proportional to it (Cosandier et al., 2017, Eq. 3.1). The effect of three different oscillator heights b on the influence of gravity along z was simulated by FEM and is displayed in Fig. 6.10.[2] These results show that changing the thickness of the wafer on which the oscillator is manufactured from 0.3 to 0.5 mm allows to reduce the daily rate difference between horizontal and vertical operation of the oscillator from 6 s/day to approximately 2 s/day, which is within the desired specifications.

---

[2]In these simulation, the thickness h of the leaf springs was adapted to always have the same rotational stiffness.
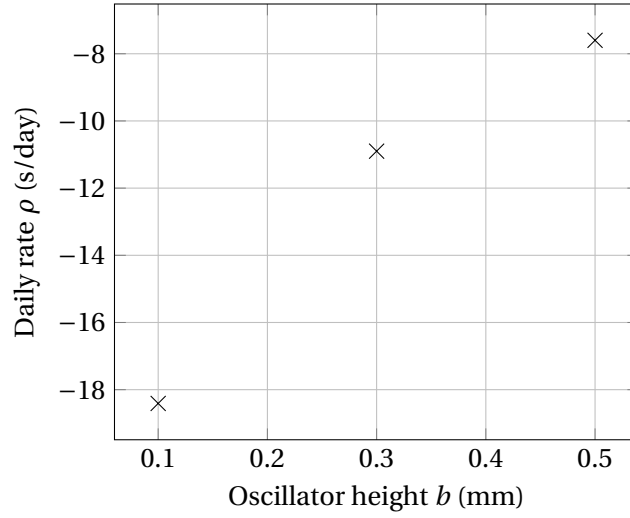
Figure 6.10 – Daily rate of the co-RCC calculated by FEM for gravity acting along the z axis with different values of oscillator height b. The reference frequency corresponds to operation without gravity.

Unfortunately, the thickness of the silicon wafer on which the prototype is fabricated is limited to 0.3 mm by the manufacturing process. A different way of equalizing the gravity effect between horizontal and vertical operation is sought. Since the in-plane gravity effect after tuning is close to the value predicted by Eq. (6.5), this formula can be used to alter the defect such that it matches the out-of-plane one, see Fig. 6.9. In order for this to succeed, a parameter has to be found that affects the in-plane defect without affecting the out-of-plane one. The analytical model developed by Van Eijk (1985) shows that the rotational stiffness of a CFP subjected to a load in the z direction does not depend on the angle between the leaf springs.[3] The parameter α can thus be used to alter the in-plane effect without affecting the out-of-plane one. The value corresponding to a desired daily rate ρ follows from Eq. (6.5)

$$\alpha = \arcsin \sqrt{ -\frac{3\left(9\delta^2 + 9\delta + 11\right)}{14\left(3\delta^2 + 3\delta + 1\right)\rho} \bar{F}^2 }, \tag{6.12}$$

which returns $\alpha = 21$ degrees to match the out-of-plane rate $\rho = -11$ s/day with the prototype dimensions given in Sec. 7.2.1.

With this new value of α, the FEM results return a daily rate $\rho \approx -11 \pm 2$ s/day that shows that the tuning is successful, see Fig. 6.11. Note that the rate for gravity along z also changed slightly to $\rho = -12.1$ s/day but this value is within the ± 2 s/day fluctuation for in-plane gravity and is well within the specifications of Sec. 6.1. Nevertheless, the tuning can still be improved

---

[3]Adapting the model for the rotational stiffness of a CFP subjected to a load in the z direction from (Van Eijk, 1985, Annex 6.I) to our case did not give accurate enough results to be used instead of FEM. This is probably due to the very slender cross-section of our leaf springs that gives rise to highly nonlinear effects that are not taken into account in the model such as anticlastic curvature.

by fine-tuning the parameters. A setting was found with $B = 14$ nN·m and $\alpha = 19.8$ degrees where the simulated daily rate is stable within ± 0.6 s/day. Note that the central value of the rate for in-plane gravity load $\rho = -11.7$ s/day is very close to the 12 s/day predicted by Eq. (6.5) with these values.
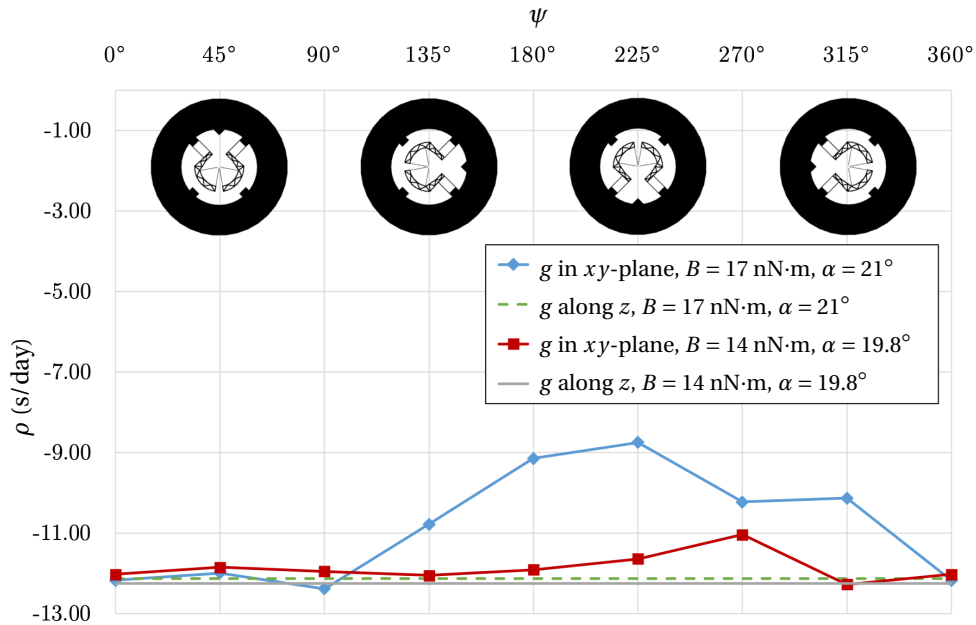
Figure 6.11 – Daily rate ρ of the co-RCC for varying orientations of gravity with varying values of B and α. The results are obtained by FEM and the reference frequency corresponds to operation without gravity.

Remark 6.5.1. The angle α which is used here to equalize the in-plane and out-of plane gravity effects also affect the restoring torque nonlinearity of the co-RCC, see Fig. 4.7. This tuning should thus be done during the dimensioning, before setting the length L_p of the parallel leaf springs for the desired isochronism defect.

The co-RCC now follows the guidelines for out-of-plane gravity effect minimization. It remains to verify that our assumptions are correct and that these guidelines truly enable to minimize the difference in gravity effect for any orientation in space. This was done by simulating by FEM the effect of gravity along 26 evenly distributed directions of space on the rotational stiffness. The results displayed in Fig. 6.12 form a sphere whose radius corresponds to a daily rate of approximately -12 s/day that corresponds to the predictions. Figure 6.12b displays the daily rate with respect to the minimum frequency obtained and shows that the difference stays within 1.6 s/day. This validates our theory within the level of numeric precision of the FEM results (there is a 0.6 s/day difference between the results with g along $z+$ and $z-$, which are supposed to be identical due to symmetry). The effect of gravity on the frequency of the co-RCC has successfully been minimized.
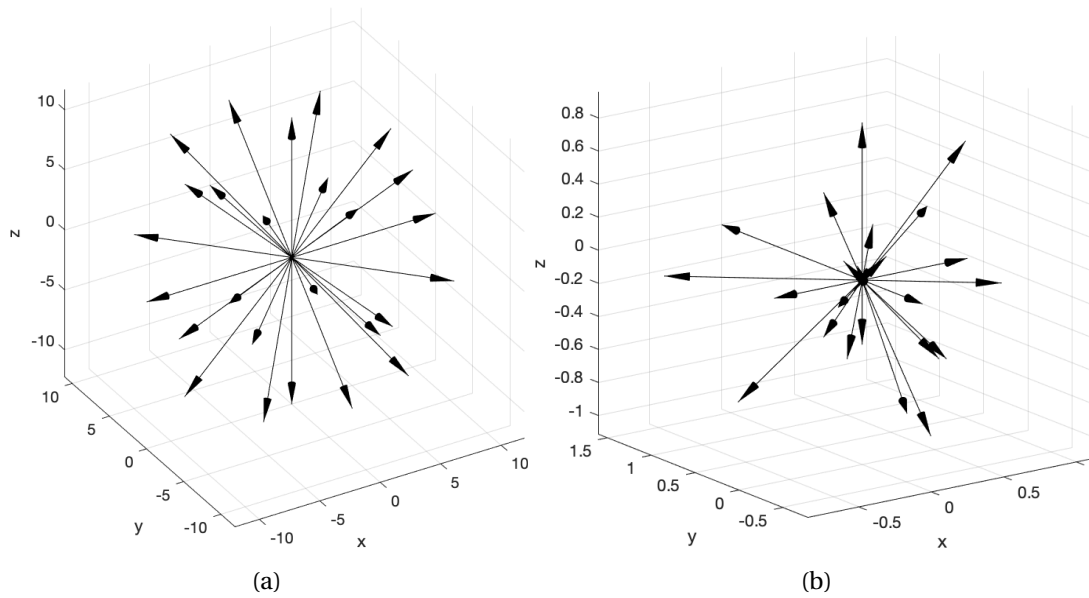
Figure 6.12 – Effect of gravity on the frequency of the co-RCC oscillator for various orientations in space expressed (a) in absolute daily rate (i.e., s/day) with respect to operation without gravity and (b) in daily rate (i.e., s/day) with respect to the minimum calculated frequency. The results are obtained by FEM.

6.5.3 Out-of-plane gravity effect on the RDCO

According to the energetic definition of Sec. 6.2.1, the RDCO is theoretically isochronous for gravity loads in the plane of oscillation. Indeed, the architecture is totally planar and has perfect rotational symmetry. As a result, the position of the COM of the system in the oscillation plane does not change as it oscillates.

For out-of-plane loads, the out-of-plane dimension b of the oscillator should be chosen such that the effect matches the in-plane one. This solution has been validated in Fig. 6.10 and the topic of gravity-sensitivity is not investigated further on the RDCO as the focus of this architecture is to explore the effect of inertia variation on isochronism.

6.6 Chapter conclusion

In this chapter, the concepts used to minimize the effect of gravity were discussed using two approaches, an energetic one and a beam theory one, and practical guidelines were established to implement these concepts in the design of flexure-based oscillators. We showed how these guidelines are implemented on the three oscillators of this thesis and how the effect of gravity is minimized in their analytical models. These results were validated by FEM and a method was presented to cancel remaining defects by modifying the position of the centre of mass of the oscillator.

7 Prototype design and experimental validation

Among the new flexure pivot oscillators presented in Chapter 3, the co-RCC is the most promising one for implementation in a mechanical watch. Its design is relatively simple, consisting of only 8 leaf springs, and suitable for a compact embodiment. Chapter 5 presented a simple way of tuning its isochronism using the length of its parallel leaf springs and Chapter 6 showed that the influence of gravity on its frequency can be minimized. This design was thus chosen for a silicon prototype satisfying typical mechanical watch specifications. The prototype is then used to experimentally validate the concepts and models presented in the previous chapters.

7.1 Practical watch specifications

The following specifications are used as guidelines for our dimensioning:

1. Nominal frequency of 15 Hz.
2. Nominal amplitude of operation of 15 degrees, assuming that this will be sufficient for an escapement to work, see Sec. 1.5.4.
3. Amplitude variation of 10% during normal operation.
4. Isochronism defect of order 1 s/day over the operating stroke.
5. Daily rate stability in all orientations with respect to gravity within 5 s/day.
6. Planar design etched in a 0.3 mm thick wafer.
7. Outer diameter within 20 mm.

7.2   Prototype design

7.2.1   Dimensions and material properties

Our design depicted in Fig. 7.1 has the following dimensions

- $L = 2.59$ mm
- $h = 15$ μm
- $b = 0.3$ mm
- $L_p = 2.27$ mm
- $h_p = 15$ μm
- $D = 20.2$ mm
- $\delta = 0.091$
- $\alpha = 34.7$ degrees
- $J = 1.02 \cdot 10^{-8}$ kg·m^2
- $m = 0.157$ g

and is manufactured in (001) silicon with density $\rho = 2329$ $\frac{\text{kg}}{\text{m}^3}$ (Hull, 1999) and stiffness tensor

$$[c] = \begin{bmatrix} c_{11} & c_{12} & c_{12} & 0 & 0 & 0 \\ c_{12} & c_{11} & c_{12} & 0 & 0 & 0 \\ c_{12} & c_{12} & c_{11} & 0 & 0 & 0 \\ 0 & 0 & 0 & c_{44} & 0 & 0 \\ 0 & 0 & 0 & 0 & c_{44} & 0 \\ 0 & 0 & 0 & 0 & 0 & c_{44} \end{bmatrix}, \tag{7.1}$$

where $c_{11} = 165.7$ GPa, $c_{12} = 63.9$ GPa and $c_{44} = 79.6$ GPa (Cho, 2009).

Figure 7.2 shows the anisotropic characteristic of Young's modulus for (001) silicon and the orientation chosen for the prototype on the silicon wafer. This disposition minimizes the stiffness of the RCC flexures while having the same elastic properties for all flexures of the same type. This choice makes it easier to satisfy the frequency specifications of Sec. 7.1.

7.2.2   Reaching specifications

Frequency

With the above-mentioned dimensions and material properties, the prototype manages to reach the specifications of Sec. 7.1. The nominal stiffness of the prototype according to Eq. (4.31) with $k_{c,0} = 9.07 \cdot 10^{-5}$ N·m where the area moment of inertia of the cross-section of the leaf springs is given by
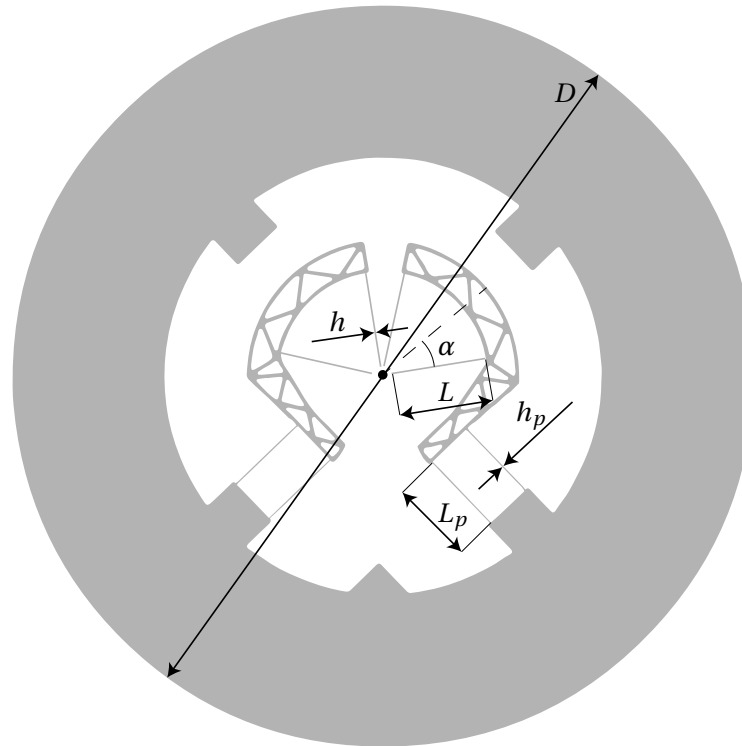
$$I = \frac{bh^3}{12}. \tag{7.2}$$
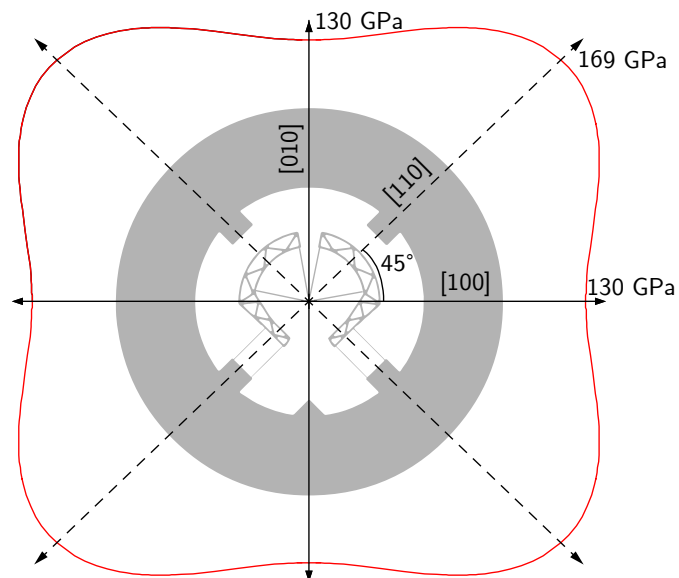
Figure 7.1 – Co-RCC prototype dimensions.

Figure 7.2 – Anisotropic Young's modulus of (001) silicon and prototype orientation on the wafer.

With the inertia J given in Sec. 7.2.1, this rotational stiffness yields a frequency $f = 15$ Hz that satisfies Specification 1.

Angular stroke

Assuming an admissible bending stress of $\sigma_{\text{adm}} = 700$ MPa in the leaf springs,[1] the admissible angular stroke of the oscillator is (Cosandier et al., 2017, Eq. 5.7)

$$\theta_{\text{adm}} = \frac{\sigma_{\text{adm}} L}{E(2h + 3h\delta)} = 22.7 \,\text{degrees,} \tag{7.3}$$

satisfying Specifications 2 and 3.

Isochronism

The isochronism defect of this oscillator is calculated in Sec. 5.4 and shown in terms of daily rate at $\Theta = 16.5$ degrees with respect to reference amplitude $\Theta_1 = 15$ degrees in Fig. 5.5. This corresponds to a 10% amplitude variation with respect to the reference amplitude in accordance with Specifications 2 and 3. Figure 5.5 shows that the length of the parallel leaf springs L_p (quantified by the dimensionless parameter $\lambda = L_p/L$) can be used to introduce a range of positive or negative isochronism defects up to the of order ± 100 s/day. This means that parameters can be found such that the oscillator is isochronous or that significant isochronism defects external to the oscillator can be compensated. Note that $\lambda = 0.88$ was chosen to reach isochronism instead of the value $\lambda = 0.72$ shown in Fig. 5.5 because the restoring torque nonlinearity of the RCC pivot was recalculated with the anisotropic elastic properties of Eq. (7.1).

It was shown in Sec. 5.4.1 that the isochronism tuning resolution $\Delta\rho$ obtained with variations of L_p of order 1 μm, which is compatible with DRIE and laser ablation, is below 1 s/day. This satisfies Specification 4.

Gravity sensitivity

Regarding gravity sensitivity, the dimensions were chosen such that the analytical formula for in-plane gravity effect returns a constant rate of -5 s/day, see Eq. (6.5). The prototype was designed before the tuning principles of Sec. 6.4 and 6.5 were developed and this value was chosen assuming that any deviation would stay of same order and thus satisfy Specification 5. This was confirmed by FEM simulation in Fig. 6.3 when the mass of the intermediate bodies is not taken into account.

However, the mass of the intermediate bodies of the prototype is not negligible and causes

---

[1] This corresponds to a 1.7 safety factor with respect to the 1.2 GPa stress measured by Henein et al. (2011) at the rupture of silicon flexures.

gravity effects that do not meet Specification 5, see Fig. 6.4. We demonstrated in Fig. 6.7 that this effect can be compensated in order to meet the specifications by offsetting the COM of the oscillator. This correction was not integrated in the nominal prototype design but we show how to implement it in Fig. 6.8 and validate it experimentally in Sec. 7.7.1.

The equalizing of in-plane and out-of-plane gravity effect described in Sec. 6.5 was not integrated in the design and cannot be implemented without fabricating new prototypes. Numerical simulations show that the method is effective, see Fig. 6.11 and 6.12 but this remains to be proven experimentally in subsequent prototyping iterations.

7.2.3 Outer dimensions

The prototype is etched in a 0.3 mm thick wafer and the outer diameter is 20.2 mm. This 1% excess in outer diameter dimensions is considered acceptable at this stage. The manufactured prototype is shown in Fig. 7.3. Note that we do not consider the circle involute targets as part of the external diameter constraint as they are an artefact that was added for measurement purposes. They also turned out to be unnecessary, see Remark 7.3.1.

7.3 Experimental method

This section presents the experimental method used to validate the theory and prototype design of this thesis. The method is based on a measurement of the position of the oscillator over time in free oscillation. The oscillator is offset from its equilibrium position by a given angle and released. Its position is then measured until it stops. As mentioned in Sec. 1.5.4, no sustaining mechanism (escapement) is developed and the amplitude decays over time. Figure 7.4 shows four pictures taken during one swing of the prototype on the test bench.

The data obtained from the position of the oscillator over time allows to measure three main characteristics:

1. The quality factor can be extracted from the amplitude decay, see Sec. 7.4.

2. The isochronism defect can be extracted from the frequency-amplitude curve, which is itself extracted from the position-time data in Sec. 7.6.

3. The gravity sensitivity of the oscillator is extracted from the nominal frequency of the oscillator in different positions, where the nominal frequency is obtained from the position-time data in Sec. 7.7.

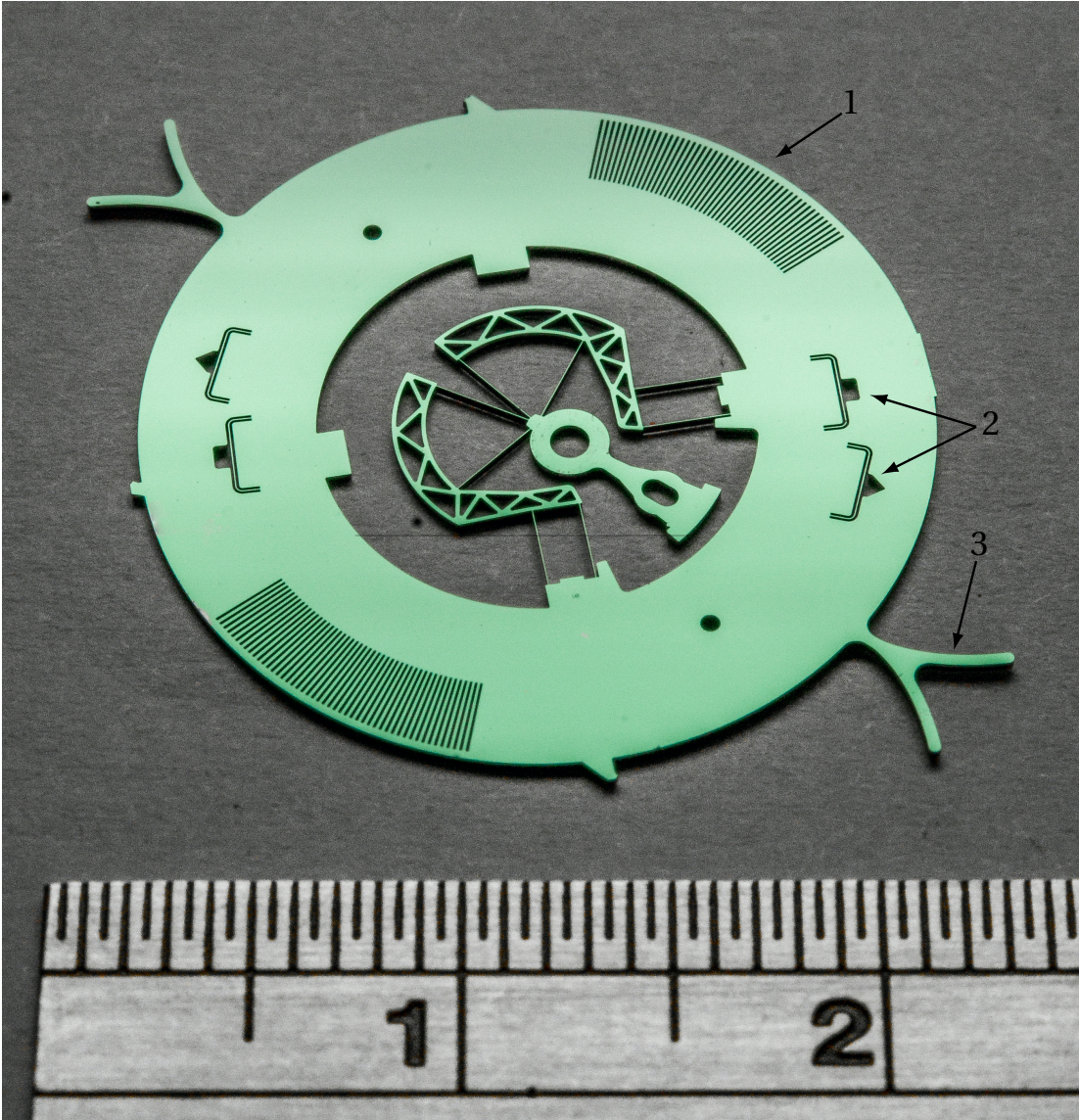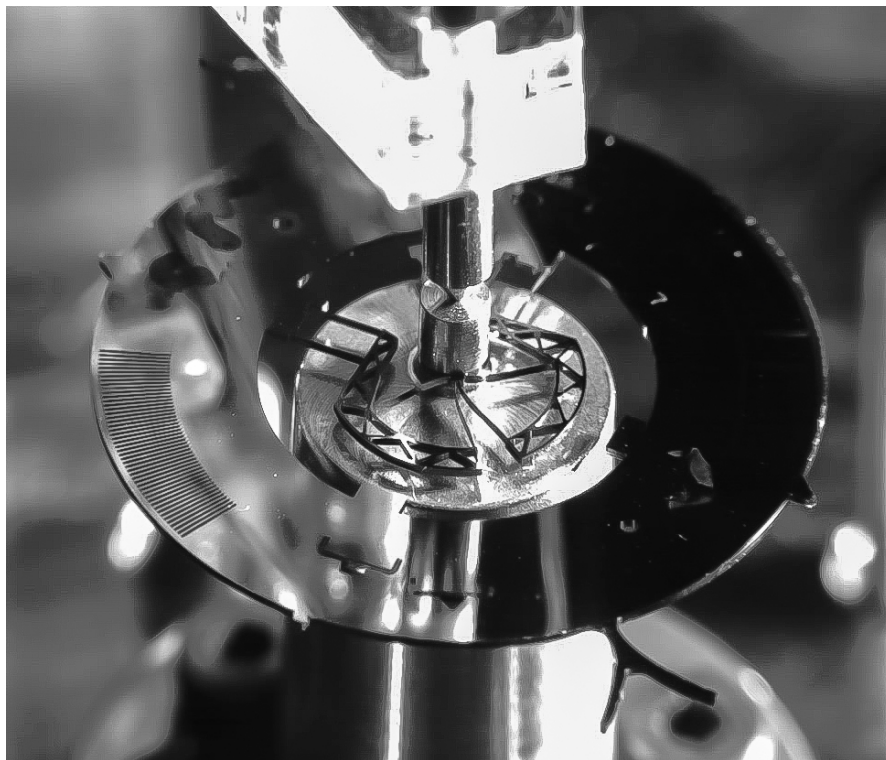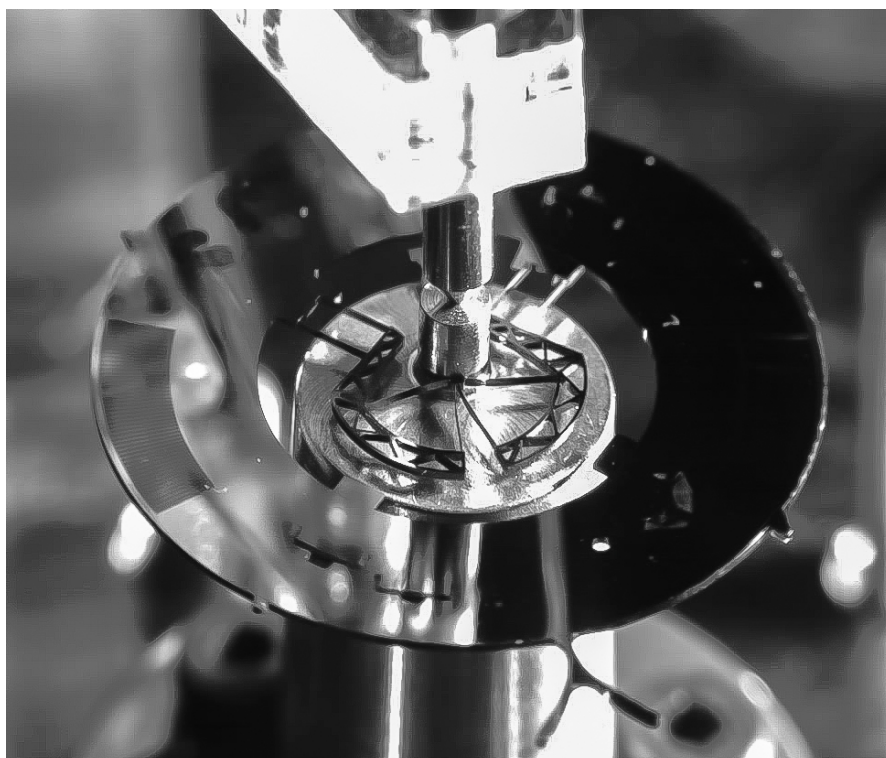Figure 7.3 – Co-RCC prototype manufactured in silicon. The following features were added for experimental purposes: encoder slits (1), clamping features (2) and circle involute targets (3).

(a)

(b)

Figure 7.4 – Frames of prototype free oscillation shot with high speed camera at 250 frames per second.

105
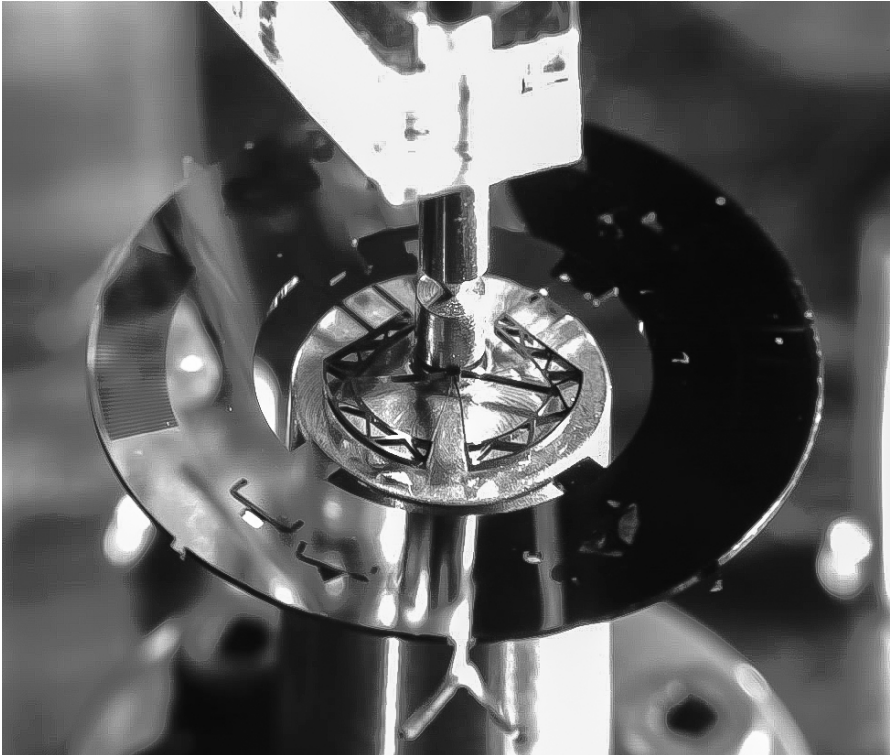
(c)
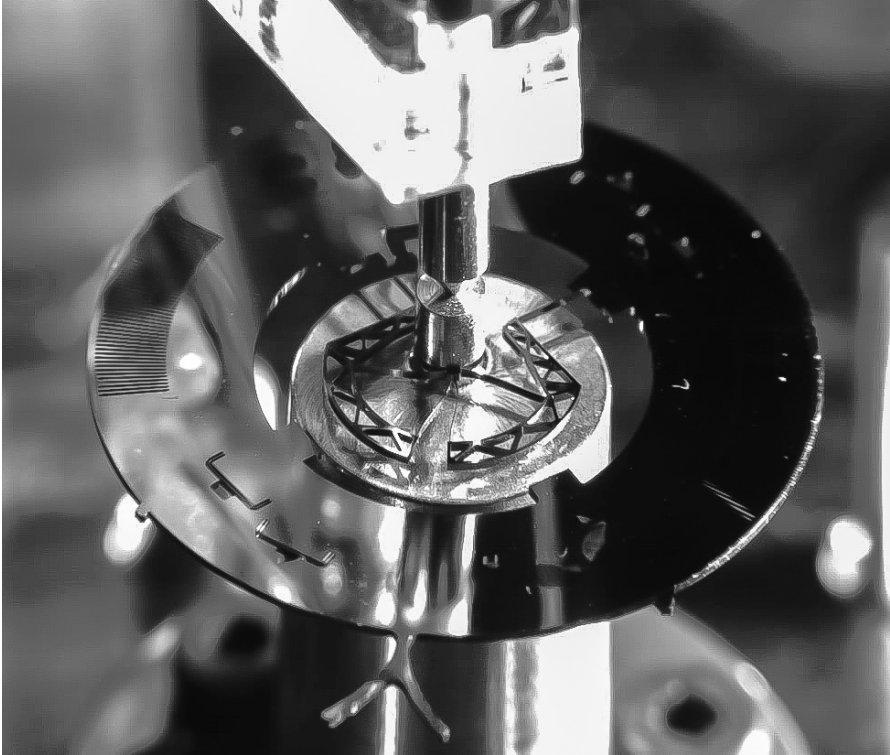
(d)

Figure 7.4 – Frames of prototype free oscillation shot with high speed camera at 250 fps (cont.).

7.3.1 Oscillator position over time

The angular position of the oscillator is measured with an incremental optical encoder of type AVAGO HEDS-9730.[2] A light source is aimed at slits cut into the oscillator and, as the oscillator rotates, the light is either blocked or reaches a receiver through the slits, allowing to detect the motion. As the slits all have the same known size and distance between them, the position of the oscillator with respect to the starting point can be calculated incrementally. The slits can be seen in Fig. 7.3. Their openings corresponds to a rotation of 0.46 degrees of the oscillator. The encoder uses a quadrature output that relies on two light sources with a position offset of a quarter phase (half the width of a slit). This has the advantages of allowing to know the direction of motion in addition to its amplitude and doubling the position resolution to 0.23 degrees. The encoder signal is coupled to a precise clock signal that allows to reconstruct the position of the oscillator over time.[3] Figure 7.5 shows the prototype mounted on the test bench with the optical encoder and Fig. 7.6 shows an example of position of the oscillator over time obtained by decoding the encoder signal.
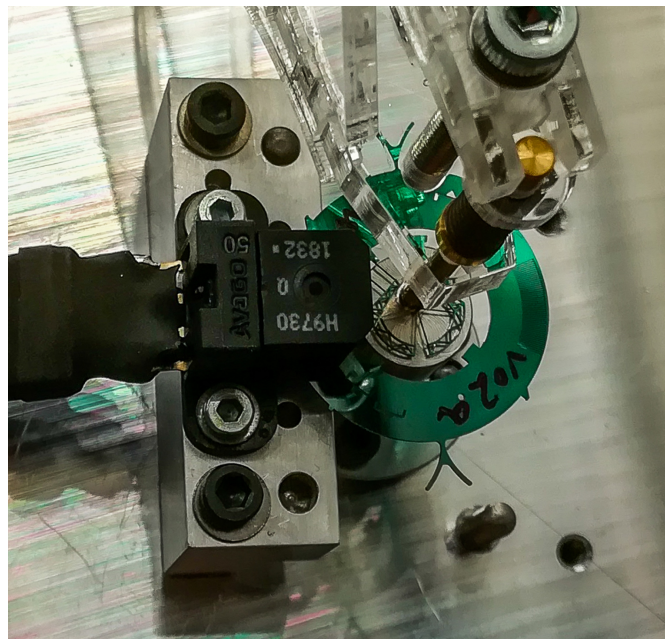
Figure 7.5 – Prototype mounted on experimental bench with optical encoder.

Remark 7.3.1. An alternative position measurement method was tested on the prototype using a laser distance sensor. This sensor measures the distance of a target from the diffuse reflection of a laser beam. We added targets protruding from the external diameter, see Fig. 7.3, such that their distance from the sensor measured in the oscillation plane gives a direct indication of the angular displacement of the oscillator. A circle involute shape was chosen

---

[2]Documentation: https://docs.broadcom.com/docs/AV02-1747EN.

[3]National Instruments NI PXIe 6614 Timer module with a 10 MHz oven-controlled crystal oscillator (OCXO) that has a stability of ±75 ppb (temperature and one year drift). Documentation: https://www.ni.com/pdf/manuals/374078a.pdf.
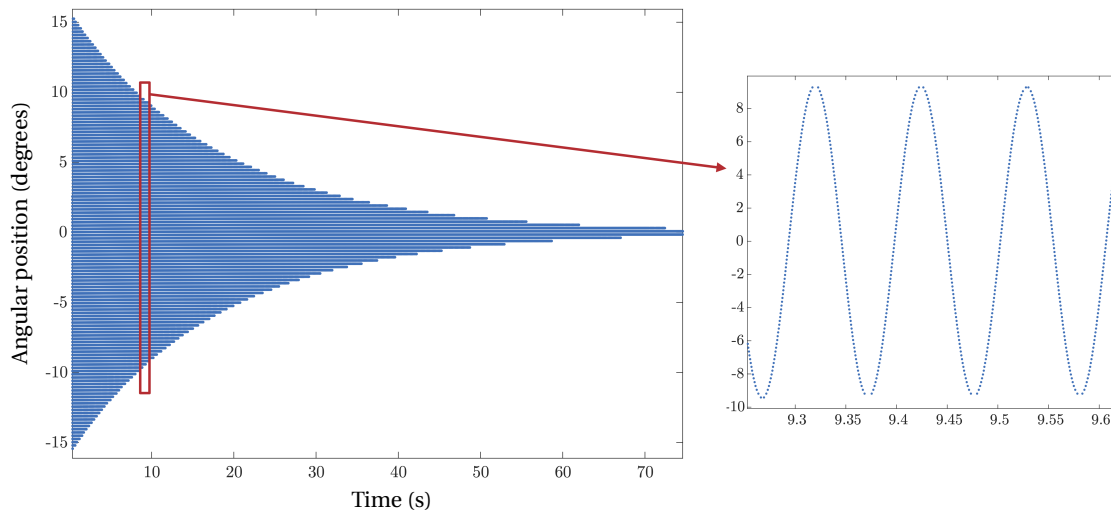
Figure 7.6 – Position-time signal of the prototype decoded from encoder measurement.

such that the surface of the target is always perpendicular to the laser beam (a change in target angle would influence the measurement). This shape offers the additional advantage that the distance measured is directly proportional to the rotation angle of the oscillator, see Fig. 7.7. On the prototype of Fig. 7.3, the target has been made symmetric such as to offer the same air resistance for both directions of oscillation and duplicated at a 180-degree symmetry to maintain the position of the COM of the oscillator. Measurements on this target were not successful as the sensor did not return any reading. This was probably caused by the target surface which is too reflective and too narrow. This method was not investigated further since the encoder method returned satisfactory results.
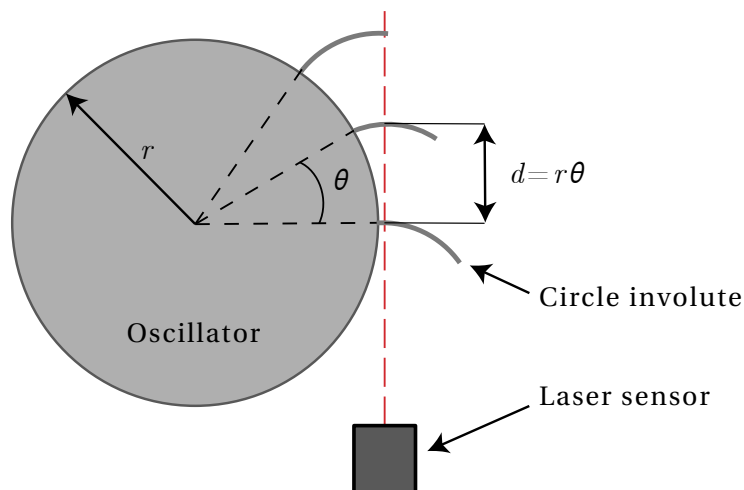
Figure 7.7 – Circle involute target for oscillator position measurement with laser sensor.

7.3.2 Algorithms to extract frequency and amplitude over time

In order to evaluate the three desired characteristics of our prototypes, it is necessary to extract the amplitude and frequency of the oscillator over time. Two different algorithms were tested for this purpose.

Algorithm 1

This algorithm processes the position-time data in subsets by fitting a specified number of samples with a sinusoidal function. The number of samples would typically correspond to a few periods of oscillation, such that the amplitude and frequency of the signal does not vary too much. This window is then moved over the signal, with or without overlap, such as to process the entire dataset, as depicted in Fig. 7.8. For each window n, the algorithm returns a triplet (Θ_n, f_n, t_n) corresponding respectively to the amplitude and frequency of the sinusoidal function fitted on the window and the mean time of the window. From this data, one can the extract the amplitude-time relationship, frequency-time relationship or frequency-amplitude relationship of the oscillator. The sinus function is fitted using the Levenberg-Marquardt algorithm (Weisstein, 2020).
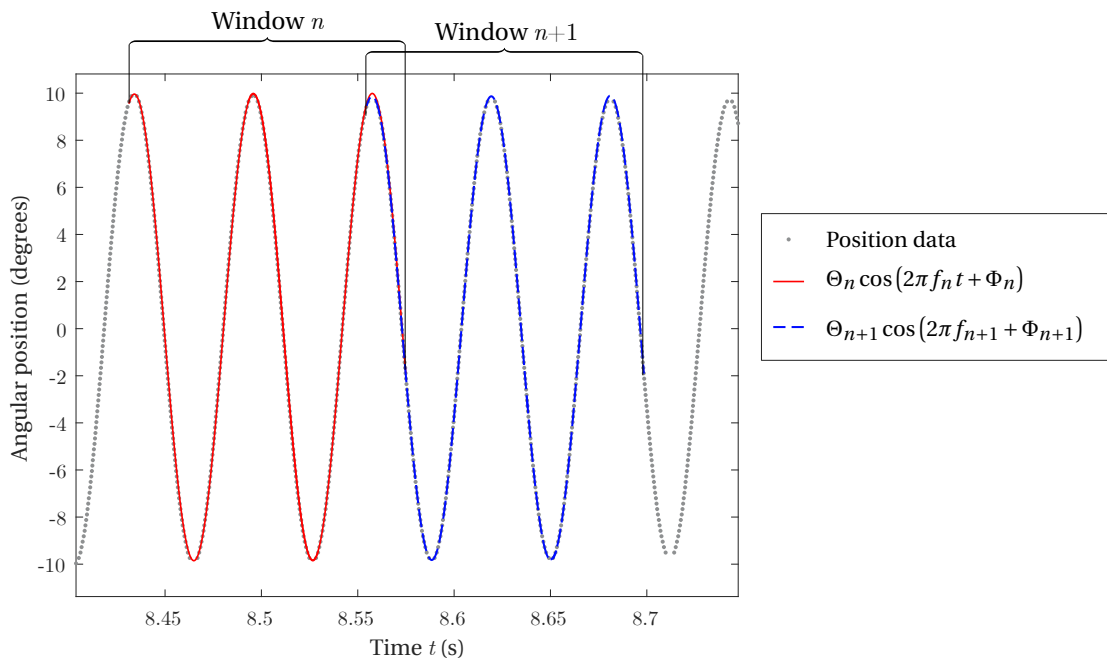
Figure 7.8 – Illustration for Algorithm 1.

Algorithm 2

This algorithm first detects the local position maximum of each oscillation of the oscillator by second order polynomial interpolation. The detected peaks are shown in Fig. 7.9. These peaks are then fitted with an exponential decay model that describes the amplitude-time

relationship of an oscillator undergoing viscous damping

$$\Theta(t) = \Theta_0 e^{-Ct} \tag{7.4}$$

using the Levenberg-Marquardt algorithm (Weisstein, 2020).
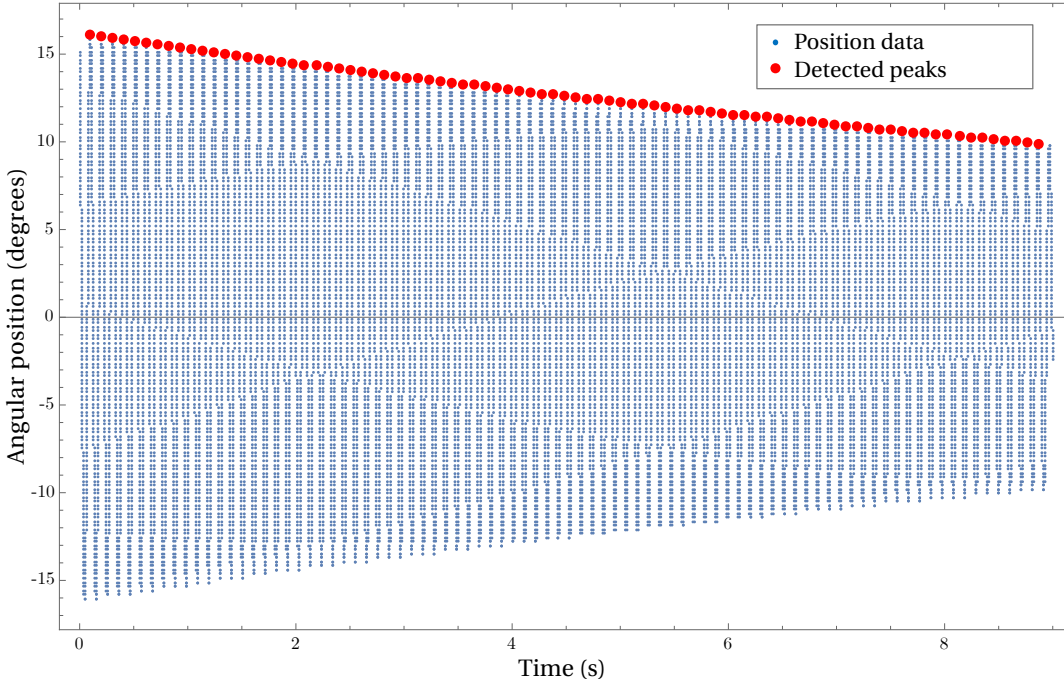
Figure 7.9 – Peak detection for Algorithm 2.

The period of the oscillator over time is then calculated from the time between two successive edge detections of the same slit-edge passing in the same direction, i.e, the time T_n between every other data point with same angular position depicted in Fig. 7.10. For each set of successive edge detection denoted by index n, the algorithm returns a triplet (f_n, Θ_n, t_n) corresponding to the frequency $f_n = 1/T_n$, the mean time between the two edge detections t_n and the value of the fitted amplitude function at this time $\Theta_n = \Theta(t_n)$. From this data, one can the extract the amplitude-time relationship, frequency-time relationship or frequency-amplitude relationship of the oscillator.

7.4 Experimental quality factor measurement

The quality factor Q was introduced in Sec. 1.4.1. It describes the amplitude decay of an oscillator through the relationship (Vardi, 2014)

$$\Theta(t) = \Theta_0 e^{-\pi f_0 t / Q}. \tag{7.5}$$
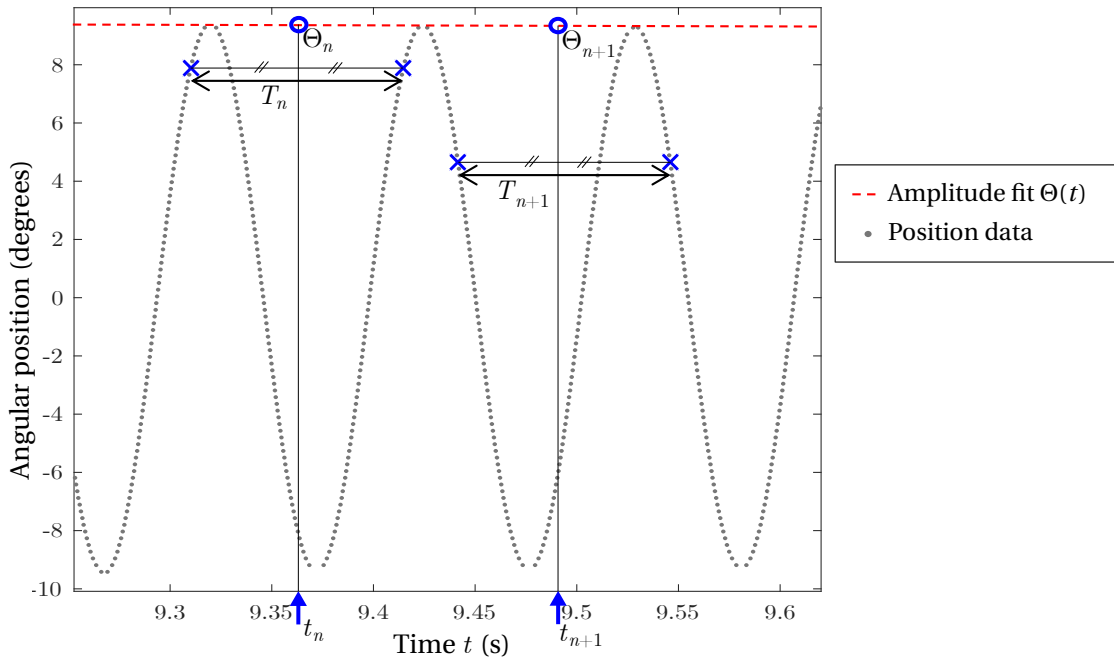
Figure 7.10 – Illustration for Algorithm 2.

As a result, it can be extracted from the fit of Eq. (7.4) in Algorithm 2 and by fitting the amplitude-time output of Algorithm 1 with the same function. The quality factor is then given by

$$Q = \frac{\pi f_0}{C}, \tag{7.6}$$

where C is the exponential decay constant in Eq. (7.4) and f_0 is the nominal frequency, that is, the limiting frequency as amplitude approaches zero, which can be obtained by fitting the frequency-amplitude data, see Eq. (7.15). Alternatively, the Q factor can be obtained by the slope of a linear regression through the log-log plot of the amplitude-time data.

The quality factor measured on three prototypes is shown in Tables 7.1 and 7.2. The prototype variants are described in Sec. 7.6. For each prototype, the measurements were done on 6 launches, 3 of which were performed in each possible winding direction (clockwise or anticlockwise). The sampling rate was set at 100 kHz and the data with amplitude between 19 and 1 degrees was processed with the two algorithms of Sec. 7.3.2.

The results indicate a mean quality factor $Q = 628$ with a low dispersion between prototypes and measurements. According to the standard deviation σ given in the tables, Algorithm 1 shows less dispersion in the results than Algorithm 2. This can be attributed to the fact that amplitude measurement by means of a sinusoidal fit of the data is more accurate than maximum detection by polynomial interpolation.

Prototype	Q	σ
V0	630	0.523
V1	628	0.171
V2	627	0.290
Mean	628	

Table 7.1 – Quality factor measured on 3 prototypes with 6 launches each using Algorithm 1, and corresponding standard deviation σ.

Prototype	Q	σ
V0	630	1.09
V1	626	0.554
V2	628	0.895
Mean	628	

Table 7.2 – Quality factor measured on 3 prototypes with 6 launches each using Algorithm 2, and corresponding standard deviation σ.

7.5 Avenues for quality factor improvement

The quality factor measured on the prototype shows a two to threefold increase with respect to the traditional balance wheel, which typically has a quality factor between 200 and 300. This improvement is significant but does not correspond to the order of magnitude increase in Q required to cross the 1 s/day accuracy threshold according to Fig. 1.4. Note that Fig. 1.4 does not give a precise relationship between Q and accuracy (it displays an apparent correlation on a log-log scale), but gives a good indication of the orders of magnitude involved.

In order to improve the quality factor of the oscillator, it is important to understand the parameters that influence it. For the damped rotational harmonic oscillator satisfying

$$J\ddot{\theta} + c\dot{\theta} + k\theta = 0 \tag{7.7}$$

the quality factor is given by (Vardi, 2014)

$$Q = \frac{\sqrt{Jk}}{c} = \frac{2\pi f_0 J}{c}. \tag{7.8}$$

Since the frequency f_0 should be kept constant to satisfy the specifications of Sec. 7.1, Eq. (7.8) shows that the quality factor can be increased either by increasing the inertia J or by decreasing the viscous damping coefficient c. These two cases are discussed below.

Remark 7.5.1. Equations (7.8) and (7.6) allow to express the exponential decay constant of Eq. (7.4) in terms of c and J

$$C = \frac{c}{2J}. \tag{7.9}$$

7.5.1 Increasing inertia

The inertia of our prototype can be approximated by that of a hollow cylinder of height h, internal radius R_i and external radius R_e:

$$J = \frac{1}{2}\pi\rho b(R_e^4 - R_i^4).$$ (7.10)

It follows that J can be modified without affecting c by modifying the density ρ of the inertial body (the other parameters would change the aerodynamics of the oscillator and hence c). If the stiffness k is also modified such as to keep f_0 constant, Eq. (7.8) shows a quality factor increase proportional to the density increase

$$Q \propto \rho.$$ (7.11)

Note that, in practice, increasing J without affecting c or f_0 is unlikely to happen due to constraints imposed on gravity sensitivity, maximum stroke and dimensions, see Sec. 7.5.3.

7.5.2 Decreasing viscous damping

As shown in Eq. (7.8), the other way of increasing Q is to decrease the viscous damping c. The three main causes for damping in mechanical oscillators are contact friction, internal friction and air friction. These three effects are discussed below in the context of our prototype.

Contact friction

Contact friction has been largely eliminated by the use of flexures to guide the motion of the oscillator. The result can be seen in the two to threefold increase in Q in comparison to the balance and hairspring oscillator. The remaining places where this phenomenon can happen are at the fastening of the oscillator or at the joints between the flexible part and the inertial body if they are made of different parts.

Internal friction

Internal friction usually means energy dissipation connected with deviations from Hooke's law and is quantified by Q^{-1}, the reciprocal of the quality factor, see Eq. (1.1). In fact, a common method of determining internal friction is to measure the rate at which the amplitude of a free-vibrating sample under vacuum decreases, which corresponds to the measurement of Q (Blanter et al., 2007). Hence, internal friction, almost by definition, affects Q.

The internal friction Q^{-1} increases from crystalline solids to glasses and to polymers. It is of order 10^{-6} for quartz, 10^{-5} to 10^{-3} for metals, 10^{-2} for most glasses and 10^{-2} to 10 for high polymers (Zdaniewski et al., 1979). Values for four materials suitable for flexure

Material	Order of magnitude of Q^{-1}	Source
Monocrystalline silicon	10^{-5} to 10^{-6}	Roszhart (1990); Liu et al. (2009)
Titanium 6Al-4V	10^{-4}	Blanter et al. (2007)
Steel X220CrVMo13-4	10^{-4}	Blanter et al. (2007)
Fused silica (glass)	10^{-2}	Zdaniewski et al. (1979)

Table 7.3 – Order of magnitude of internal friction for different materials suitable for flexure mechanisms.

implementations are listed in Table 7.3. These materials are silicon, which was used for our prototype, two metals with high values of the performance index σ_D/E,[4] and one amorphous material that demonstrated attractive properties for flexures (Bellouard, 2011; Zanaty et al., 2019). Finding a value for the internal friction of these materials is a complex task as it depends on their composition and the experimental conditions (temperature, frequency and resonance mode), but data found for similar materials around room temperature allows to specify orders of magnitude. Table 7.3 shows that using a metal or glass instead of silicon for our flexure would decrease the quality factor of the oscillator.

Remark 7.5.2. The addition of a silicon oxide layer for thermal compensation, see Sec. 7.6.1, is likely to increase internal friction as it introduces dislocations and grain boundaries whose motion is a cause of internal friction (Blanter et al., 2007). In fact, any construction that isn't monolithic will increase internal friction due to the interface created.

Air friction

Air friction is linked to the aerodynamics of the oscillator. Estimating c from the geometry of the oscillator is a complex task that is usually performed experimentally. Nevertheless, one can assume that air friction is proportional to the surface area of the inertial body, which can be approximated by the area of a hollow disc $2\pi(R_e^2 - R_i^2)$. With this assumption, it follows from Eq. (7.8) that

$$Q \propto \chi = \frac{\sqrt{Jk}}{R_e^2 - R_i^2}. \tag{7.12}$$

This relationship can be tested by comparing the quality factor measurements on prototype variants V0 and V3, which have significant differences in surface area of the inertial body, see Fig. 7.11.[5] The quality factor measured on prototype V3 is $Q = 504$ with a standard deviation $\sigma = 0.169$ for 6 launches using Algorithm 1. The ratio of measured quality factors of these two prototypes is $\frac{Q_0}{Q_3} = 1.25$ and the ratio according to Eq. (7.12) with the values in Table 7.4 is

---

[4]The performance index σ_D/E, where σ_D is the fatigue limit, is a good indicator of a material's suitability for flexure implementations since it characterizes their maximum deflection (Henein, 2000, Table. B.14) (Cosandier et al., 2017, Chap. 6.2).

[5]Prototype variant V3 was originally designed with a larger mass in order to accentuate gravity effects in case they were too small to be measured. The experimental method turned out to be precise enough to detect the gravity effect of the nominal prototypes and this extra mass was not necessary, see Sec. 7.7.

Prototype variant	Q	J (kg·m^2)	R_i (mm)	R_e (mm)
V0	630	$1.02 \cdot 10^{-8}$	5.35	10.1
V3	504	$4.03 \cdot 10^{-8}$	5.03	14

Table 7.4 – Parameters for the quality factor comparison of prototype variants V0 and V3.[6]

$\frac{\chi_0}{\chi_3} = 1.17$, which suggests that our assumption is reasonable. Note that this relationship would have to be tested on more than two prototypes in order to be validated formally but this is beyond the scope of this thesis and is left for following prototype iterations.
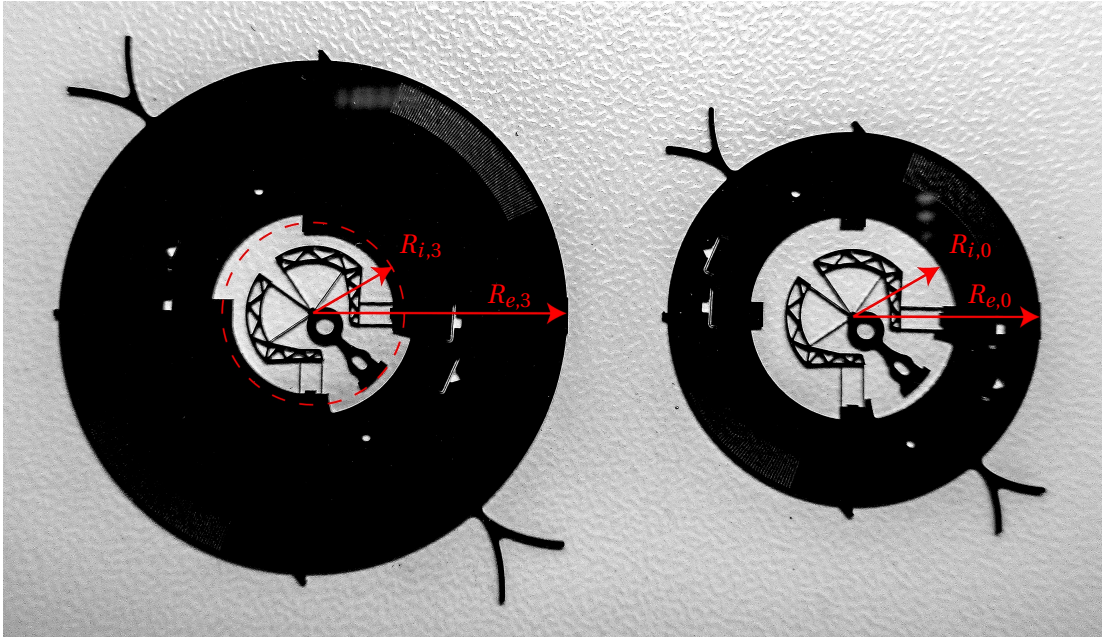
Figure 7.11 – Prototype variant V3 (left) and nominal prototype V0 (right).

Equation (7.12) suggests that the quality factor can be increased by decreasing the surface area of the oscillator without affecting J or k. The area can however not be reduced by increasing the diameter of the oscillator due to the external diameter specification of Sec. 7.1. Isolating R_i in Eq. (7.10) and substituting it into Eq. (7.12) yields

$$Q \propto f_0 b \rho \left(\sqrt{R_e^4 - \frac{2J}{\pi b \rho}} + R_e^2 \right), \tag{7.13}$$

which indicates that Q can be increased by increasing the material density ρ of the inertial body while keeping the frequency f_0, inertia J, outer radius R_e and height b of the oscillator constant.

---

[6]The rotational stiffness k is the same for both prototypes since they have the same RCC blades. The average of the two values of internal radius was taken for prototype V3, as illustrated in Fig. 7.11.

For large densities (e.g. $\rho \geq 10\,000\,\frac{\text{kg}}{\text{m}^3}$), Eq. (7.13) can be approximated by

$$Q \propto f_0 b \rho R_e^2, \tag{7.14}$$

suggesting an increase in Q proportional to the increase in material density. For example, fabricating the inertial body in 22K gold with a density almost 8 times that of silicon (Au925 Pd75, $\rho = 18\,500\,\frac{\text{kg}}{\text{m}^3}$) could increase the quality factor to $Q \approx 5000$. Note that the inertial ring would have a width of 0.3 mm instead of the current 5 mm.

Other steps to improve the aerodynamics of the oscillator include removing the unused circle involute targets visible in Fig. 7.3 or increasing the gap between the oscillator and the opening of the optical encoder, see Fig. 7.12.
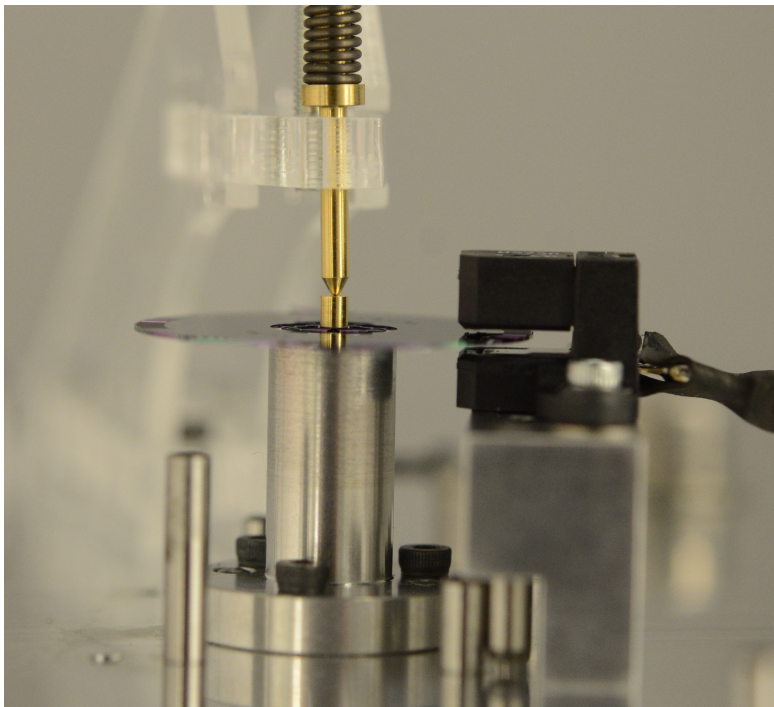
Figure 7.12 – Side view of prototype with optical encoder on the test bench.

Remark 7.5.3. Air friction could be minimized by having the oscillator operate in vacuum. This has been achieved on a concept watch with a 99.8% vacuum inside the case and resulted in a 50% increase in Q (Cartier, 2012; Clymer, 2012). However, it appears to be practically impossible to maintain a vacuum in a mechanical watch using current technology (Ilan Vardi, personal communication, May 20, 2020).

7.5.3 Material choice

Sections 7.5.1 and 7.5.2 show the independent effects of varying J and c on the quality factor. In practice, constraints such as dimensions, stroke and gravity effect result in couplings

Material	ρ (kg/m^3)	E (GPa)	R_i (mm)	L (mm)	δ	α	χ/χ_0	Q
Silicon (V0)	2329	133	5.35	2.59	0.09	34.7	1	630
Silicon (maximized χ)	2329	133	7.99	3.53	0.07	35.8	1.31	825 (est.)
Fused silica (glass)	2200	74	9.00	3.63	0.07	34.6	1.36	857 (est.)
Titanium 6Al-4V	4450	114	9.00	3.25	0.09	33.6	2.76	2281 (est.)
Steel X220CrVMo13-4	7600	196	9.00	3.96	0.07	37.5	4.67	2942 (est.)

Table 7.5 – Estimated (est.) quality factor with different materials based on index χ.

between these two parameters. Additional couplings between the inertial and flexible parts of the oscillator occur when it is manufactured monolithically, which has the advantages of simplifying fabrication and assembly, and eliminating losses at the joints between parts. In order to take into account these elements and to give practical estimates of the potential Q improvement resulting from a different material choice, oscillators were dimensioned for the four materials of Table 7.3 with the objective of maximizing Q. It is assumed that the same minimum thickness of flexures $h = 15\,\mu$m can be manufactured with all materials and the following parameters were kept constant:

- Frequency $f_0 = 15\,Hz$,
- External radius $R_e = 10.1$ mm,
- In-plane gravity effect $\rho = -5$ s/day according to Eq. (6.5),
- Oscillator thickness $b = 0.3$ mm.

Based on the measurements with prototypes V0 and V3, it is assumed that air friction is the dominating damping effect since variant V3 has a significantly lower quality factor than the nominal prototype despite having same RCC flexures (i.e., same internal friction) and a four times greater inertia, see Table 7.4. We thus use χ from Eq. (7.12) as objective function for the dimensioning and as index to estimate the quality factor variation. The results are displayed in Table 7.5.

The comparison in Table 7.5 suggests that using metals with a significantly higher density than silicon could lead to a significant increase in Q despite increasing Young's modulus whereas using materials with a significantly lower Young's modulus while keeping a similar density (such as glass) only leads to a minor increase in Q. It also appears that using χ as objective function in the dimensioning of the silicon prototype could lead to an approximate 30% increase in Q. Note that manufacturing limits have not been considered in this analysis. According to our experience, metallic flexures are typically manufactured by electrical discharge machining (EDM) with a minimum thickness around 40 μm and glass flexures are manufactured using femtosecond laser exposure and chemical etching (Bellouard, 2011) with a minimum thickness around 20 μm. Since the stiffness of leaf springs is proportional to the cube of their thickness h, this would result in larger oscillators (assuming that the frequency is not increased), which does not satisfy the practical watch specifications of Sec. 7.1 and justifies our current material choice.

7.5.4 Summary

The results of Table 7.3 and Eq. (7.14) suggest that the best option to maximize the quality factor of the oscillator is to manufacture the flexures in silicon and the inertial body in a dense material (e.g. gold alloy). If the oscillator is to be manufactured in a single material, Table 7.5 suggests that a higher Q could be obtained by using a metal with a higher density than silicon. This might however not make it possible to reach the external diameter specifications of Sec. 7.1 due to the current limits of micromanufacturing processes for metals, in which case silicon is the next best option. Glasses and polymers are not recommended since their density is of same order as that of silicon but their internal friction is at least two orders of magnitude higher.

7.6 Experimental validation of isochronism tuning

In Sec. 5.4, we presented a way of tuning the isochronism of the co-RCC oscillator by varying the length L_p of its parallel leaf springs. In order to validate this method, variants of the prototype with different lengths of parallel leaf springs were manufactured. Three of these variants are depicted in Fig. 7.13.

(a) V1: $\lambda = 0.5$ (b) V0: $\lambda = 0.88$ (c) V2: $\lambda = 1.5$
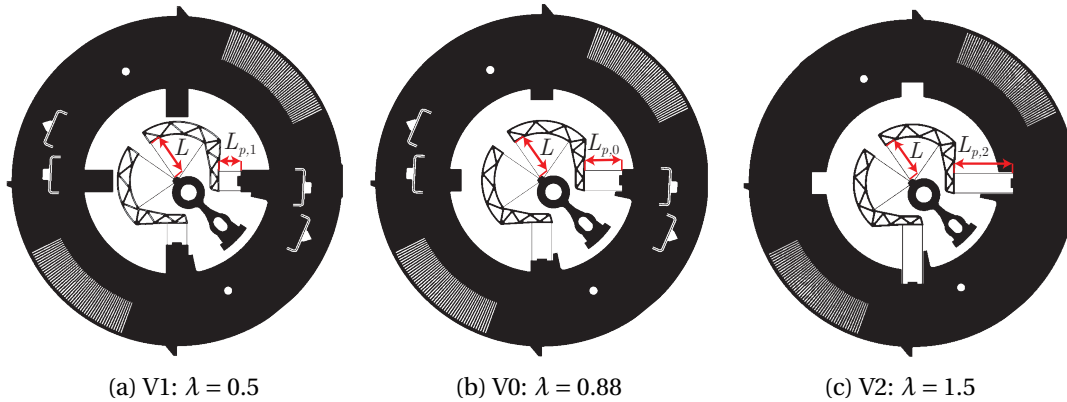
Figure 7.13 – Prototype variants with different length of parallel leaf springs L_p.

As explained in Sec. 5.2.2, the frequency-amplitude relationship of an oscillator gives an explicit description of its isochronism defect. This relationship can be extracted by fitting the amplitude-frequency points obtained after processing the experimental position-time data with the two algorithms of Sec. 7.3.2. Following Eq. (5.5), we choose the following function for the regression

$$f(\Theta) = f_0 + f_2\Theta^2 + f_4\Theta^4, \tag{7.15}$$

where the fourth order terms are added to capture effects that are not taken into account by our model.

The experimental frequency-amplitude relationship obtained with prototypes V0 to V3 for amplitudes between 2.5 and 18 degrees are shown respectively in Fig. 7.14 to 7.17. The

two algorithms give very similar results in terms of fitted frequency-amplitude function, which gives a good indication of the robustness of the method. The results also have a good repeatability, as shown from the data collected on 6 launches in Fig. 7.18.

The isochronism tuning with parameter L_p can already be validated qualitatively from these results: the slope of the frequency-amplitude relationship evolves from positive to negative in decreasing order V1 > V3 > V0 > V2 in the same order as L_p (and λ) increases between the prototype variants.

Remark 7.6.1. The data points obtained with Algorithm 2 in Fig. 7.14b to 7.17b have a large dispersion due to the resolution induced by the sampling frequency. This is however not a problem as the data is normally distributed and the errors compensate each other once the data is fitted, giving a very good estimation of the frequency-amplitude relationship.

Remark 7.6.2. The results seem to diverge slightly between different launches of the same oscillator at large amplitudes (> 15 degrees). This is especially visible in Fig. 7.18c. This phenomenon can be attributed to differences in the way the oscillator is released from its initial position. It was indeed observed during experimentation that out-of-plane forces can be induced during the release, which excite secondary vibration modes. These higher frequency modes are dissipated faster than the main one and do not seem to affect the results at lower amplitudes.

Remark 7.6.3. Prototype V3, which is shown in Fig. 7.11 has the value $\lambda = 0.7$ for the isochronism tuning parameter. This prototype was manufactured with a bigger mass in order to accentuate gravity effects in case they were too small to be measured. This can be seen from its lower frequency in Fig. 7.17 and 7.18d. It is worth noticing that the isochronism tuning is independent of nominal frequency.

(a)

(b)

Figure 7.14 – Experimental frequency-amplitude relationship of Prototype V0 with (a) data from Algorithm 1 and (b) data from Algorithm 2. The Frequency f in Hz is plotted on the vertical axis against the amplitude Θ in degrees.

(a)

(b)

Figure 7.15 – Experimental frequency-amplitude relationship of Prototype V1 with (a) data from Algorithm 1 and (b) data from Algorithm 2. The Frequency f in Hz is plotted on the vertical axis against the amplitude Θ in degrees.

(a)

(b)

Figure 7.16 – Experimental frequency-amplitude relationship of Prototype V2 with (a) data from Algorithm 1 and (b) data from Algorithm 2. The Frequency f in Hz is plotted on the vertical axis against the amplitude Θ in degrees.
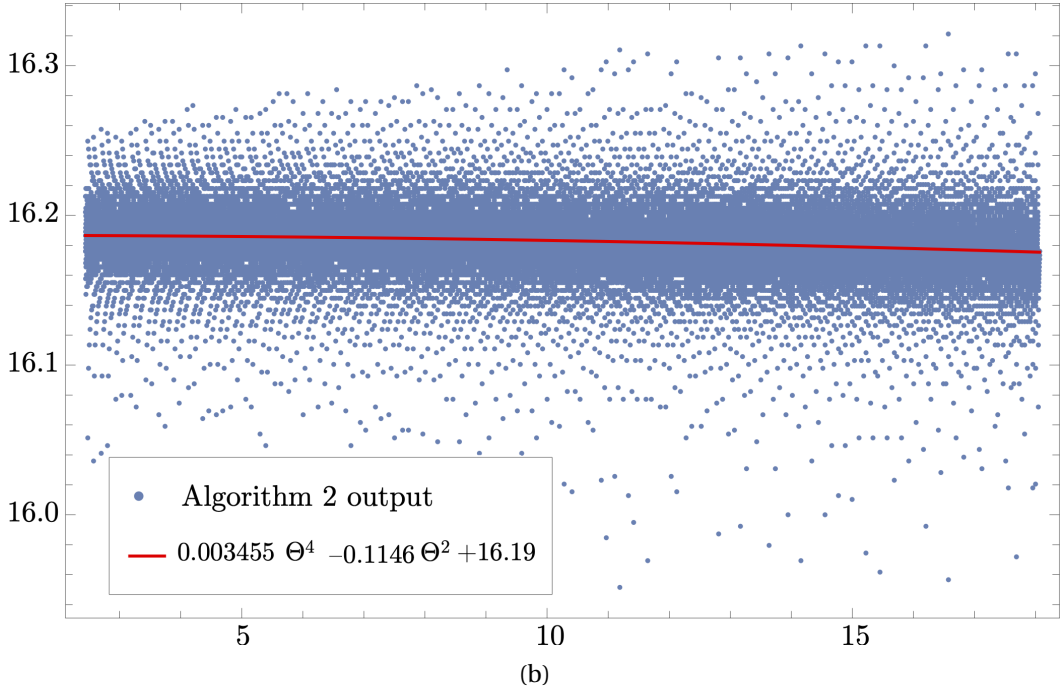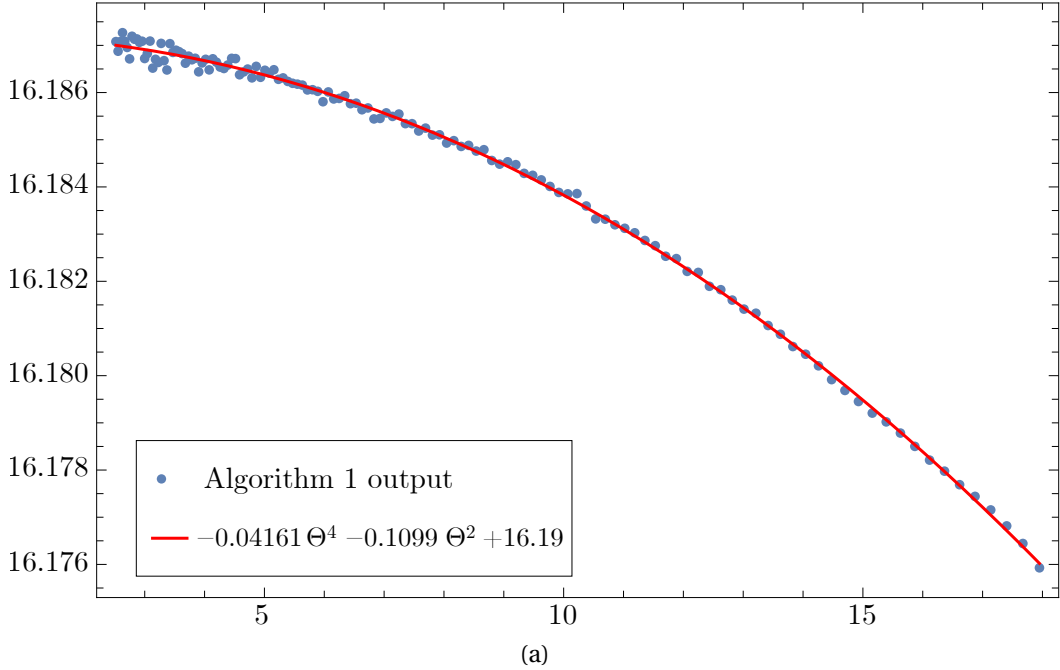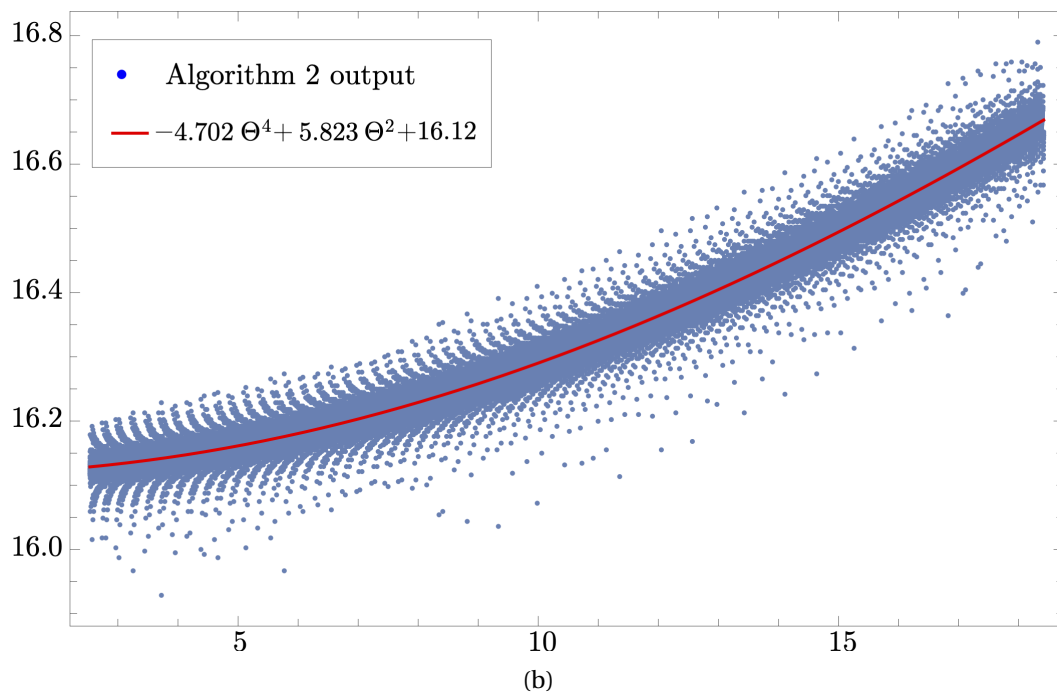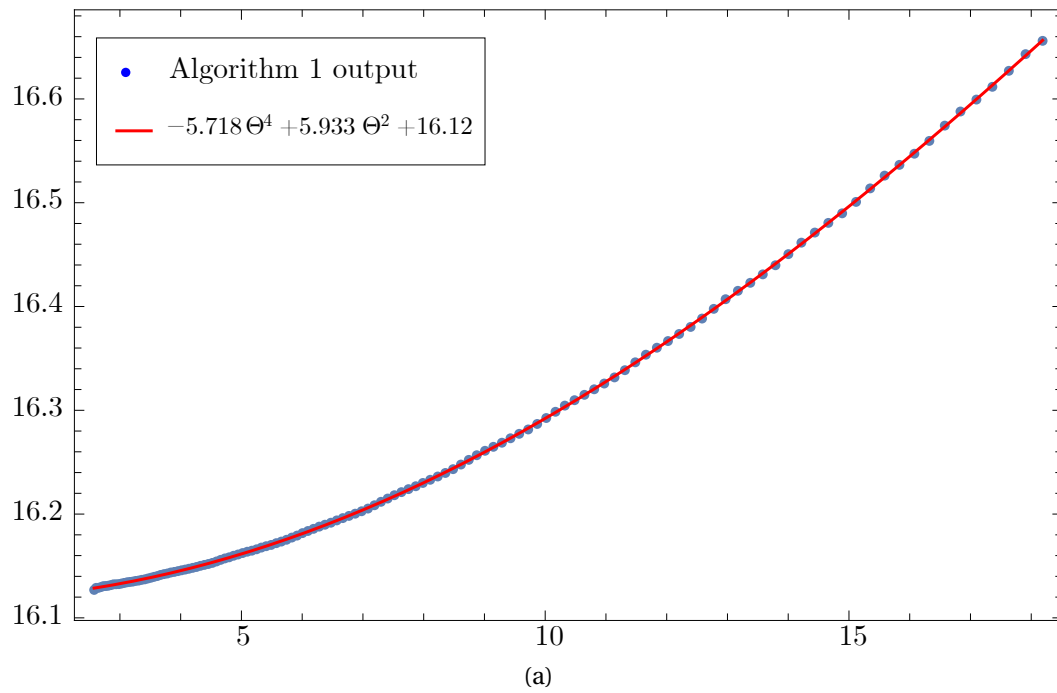
(a)

(b)
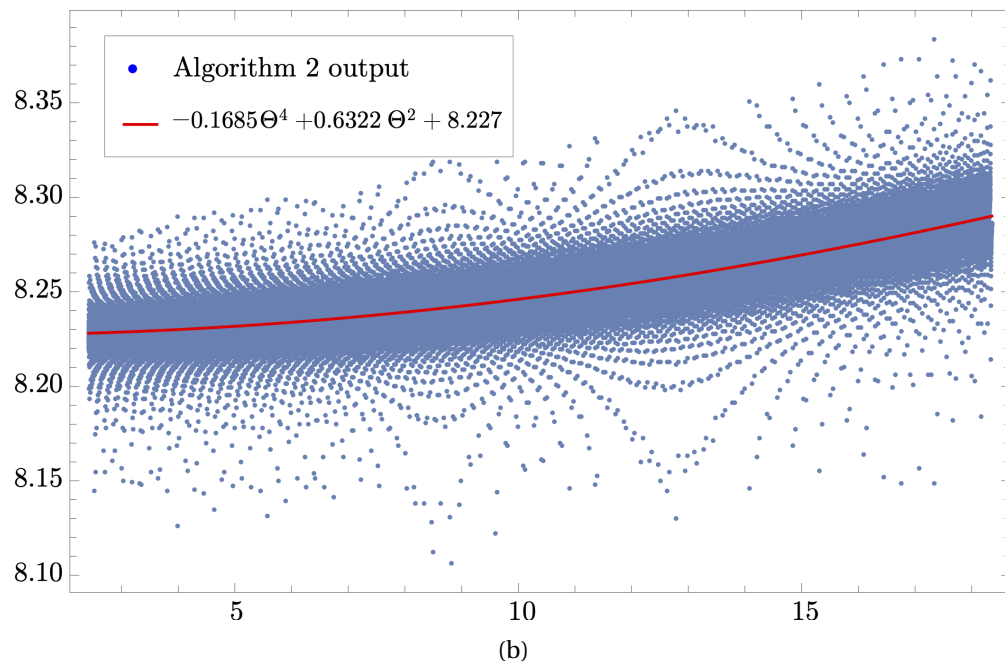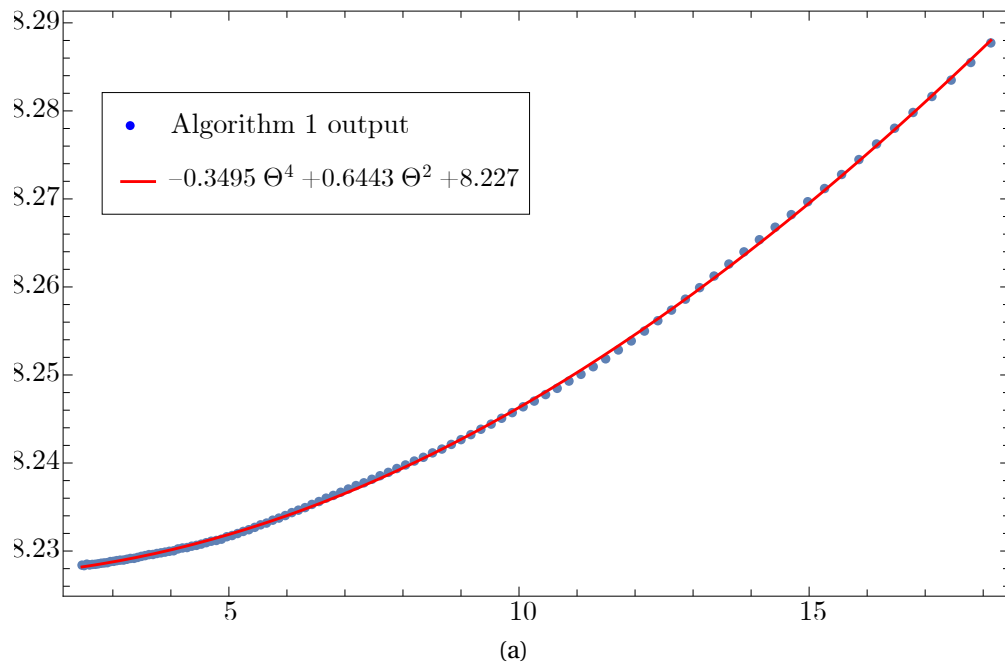
Figure 7.17 – Experimental frequency-amplitude relationship of Prototype V3 with (a) data from Algorithm 1 and (b) data from Algorithm 2. The Frequency f in Hz is plotted on the vertical axis against the amplitude Θ in degrees.
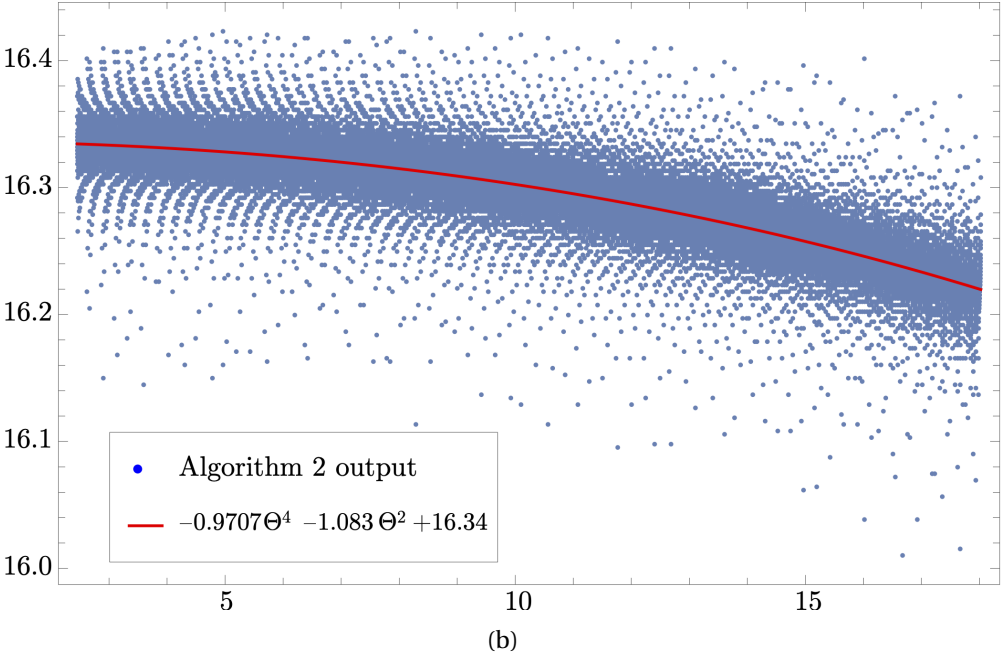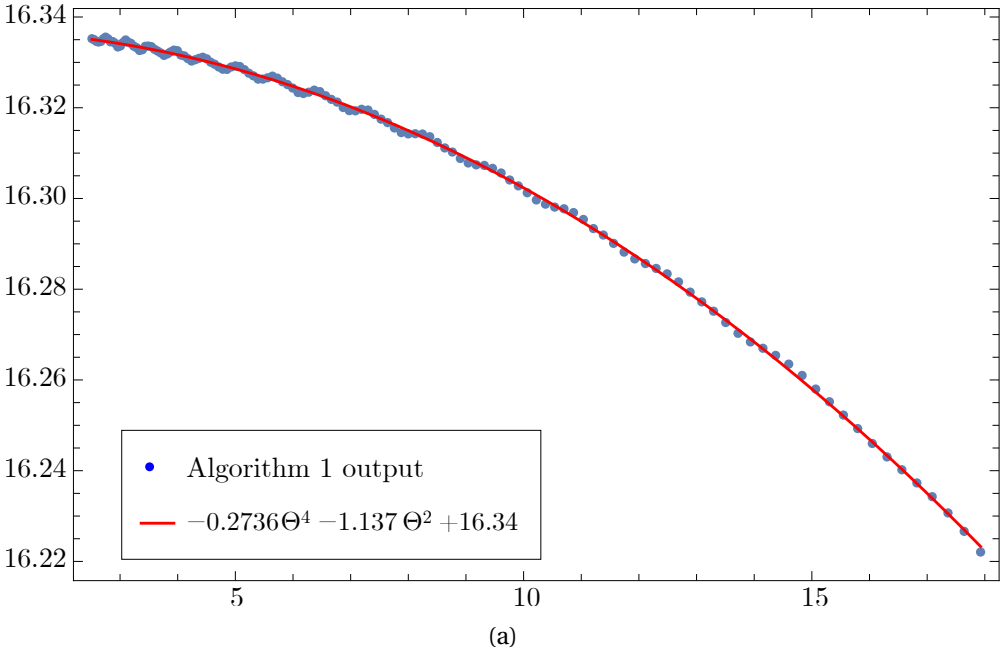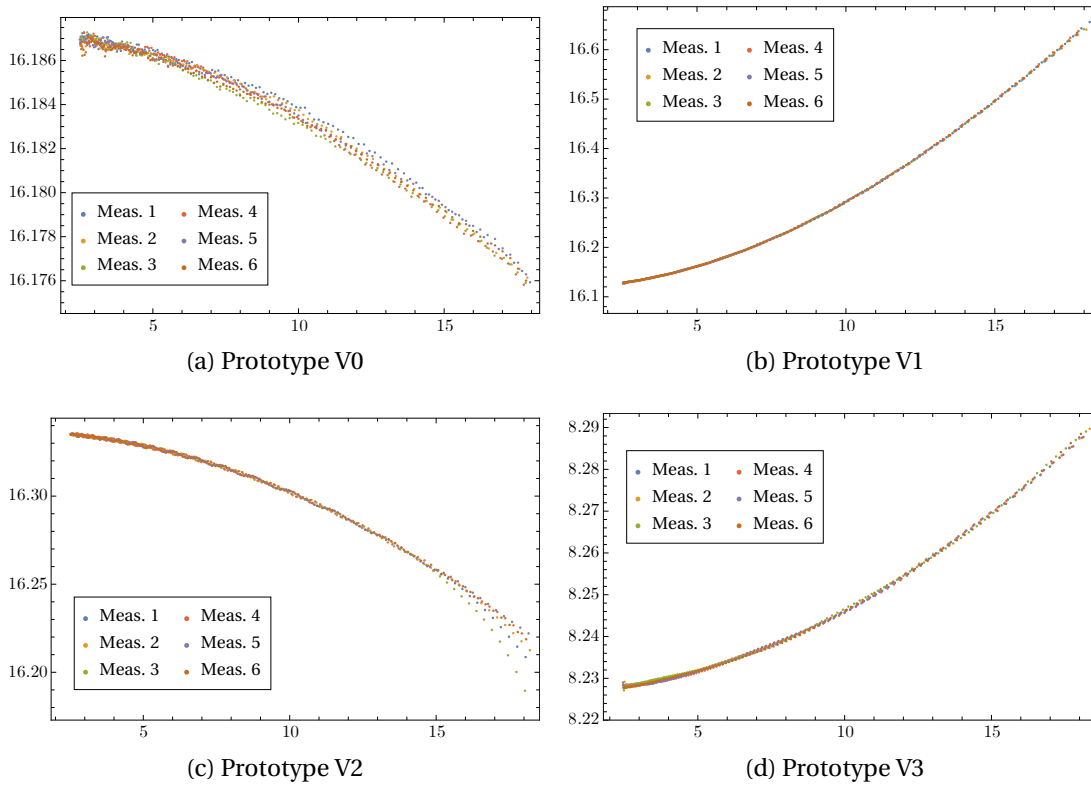
Figure 7.18 – Experimental frequency-amplitude data obtained with Algorithm 1 on 6 launches of (a) prototype V0, (b) prototype V1, (c) prototype V2 and (d) prototype V3. The Frequency f in Hz is plotted on the vertical axis against the amplitude Θ in degrees. The algorithm uses a window corresponding to approximately 3 oscillation periods with no overlap.

The experimental frequency-amplitude curves obtained with the four prototype variants are compared in Fig. 7.19 to the ones obtained with the analytical model of Sec. 5.4. In order to compare the isochronism without being influenced by differences in nominal frequency, the curves are expressed in terms of daily rate with respect to nominal frequency using Eq. (5.7). The effect of the manufacturing tolerances is displayed as confidence interval (CI) on the results of the analytical model. These results are obtained by computing the 95% CI on the mean thickness measured on the manufactured leaf springs and taking the worst case scenarios, i.e., thickest RCC leaf springs with thinnest parallel leaf springs and vice versa, see Sec. 7.6.1. Since the thickness of the leaf springs has a third order effect on their stiffness this dimension is likely to be the source of differences, see Eq. (7.2).

Note that the experimental frequency-amplitude curves of Fig. 7.19 seem to qualitatively match the third order odd coefficient polynomial hypothesis of the analytical model. The results show a slightly different curvature with prototype V1 in Fig. 7.19d, which can be explained from the highly nonlinear characteristic of this oscillator and should not affect results with small defects that would be used in practice.

(a) Prototype V2, $\lambda = 1.4$

(b) Prototype V0, $\lambda = 0.877$

(c) Prototype V3, $\lambda = 0.7$
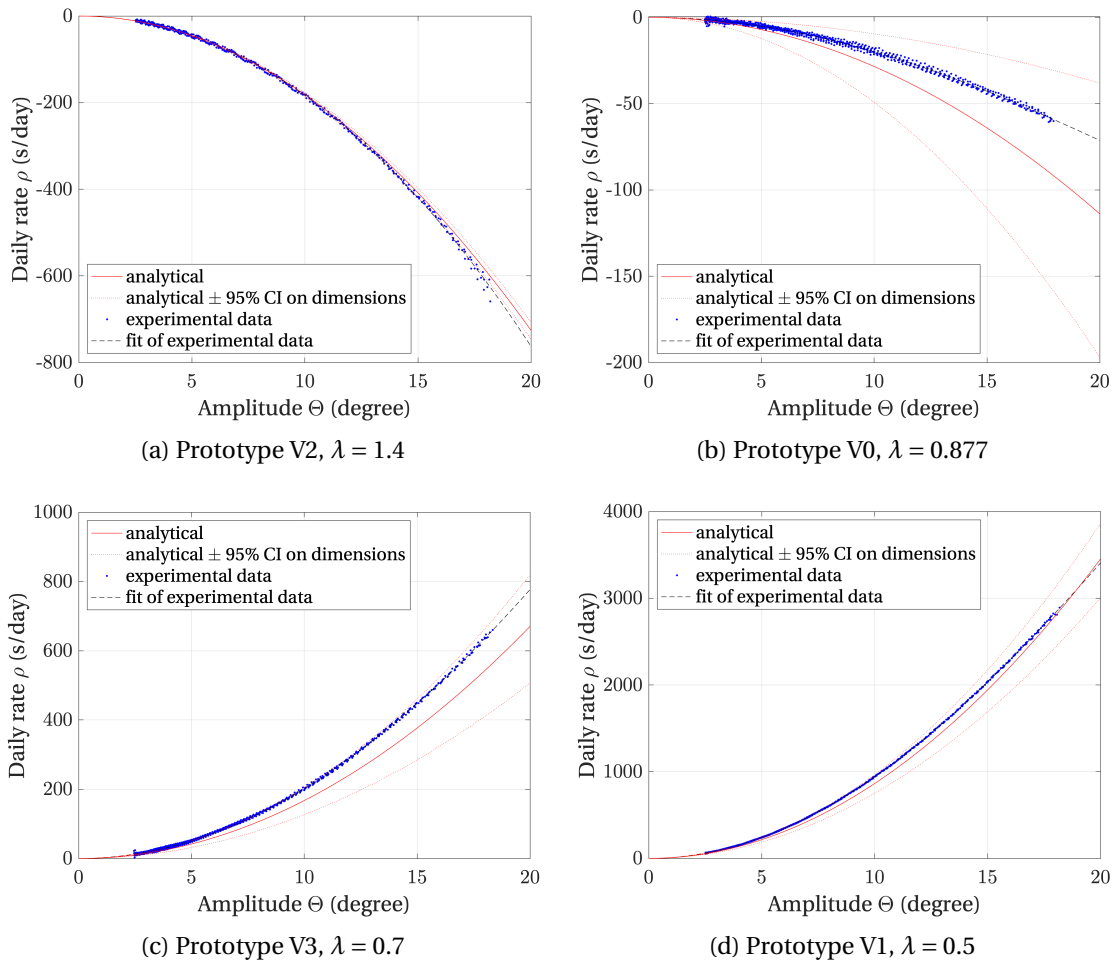
(d) Prototype V1, $\lambda = 0.5$

Figure 7.19 – Isochronism curves of the four prototype variants expressed in daily rate with respect to nominal frequency obtained experimentally and with the analytical model.

In order to give a numerical value to the isochronism defect, we express it in terms of daily rate for a 10% variation from a reference amplitude of 15 degrees, based on the specifications of Sec. 7.1. The results obtained with both algorithms are displayed in Tables 7.6 and 7.7. The results have a standard deviation σ below 5% which gives enough confidence to validate the isochronism tuning that was qualitatively validated previously.

Figure 7.20 compares the isochronism defect measured on the four prototype variants with the results obtained by FEM simulations and with the analytical model. The FEM and analytical results are similar to those already presented in Fig. 5.5, except that the models have been adapted to take into account the anisotropic elastic properties of silicon from Eq. 7.1, the oxide layer and the dimensions measured on the prototypes, see Sec. 7.6.1. Again, the effect of

---

[7] Only four launches were considered for prototype V2 as measurements 1 and 3 seem to have an erratic behavior at large amplitude and were left out, see Fig. 7.18 and Remark 7.6.2. If all the data were considered, the results with prototype V2 would be $\rho = -98.5$ s/day and $\sigma = 12.6$ s/day with Algorithm 1 and $\rho = -103.3$ s/day and $\sigma = 15.5$ s/day with Algorithm 2.

Prototype	ρ (s/day)	σ (s/day)
V0	-8.11	0.642
V1	380	3.29
V2	-91.5	3.70
V3	90.0	1.15
Mean	628	

Table 7.6 – Daily rate ρ at 16.5 degrees with respect to reference amplitude 15 degrees measured on 4 prototypes using Algorithm 1. The mean value and standard deviation σ for 6 measurements with each prototype are given.[7]

Prototype	ρ (s/day)	σ (s/day)
V0	-8.66	0.185
V1	383	3.90
V2	-95.4	4.62
V3	91.7	0.585
Mean	628	

Table 7.7 – Daily rate ρ at 16.5 degrees with respect to reference amplitude 15 degrees measured on 4 prototypes using Algorithm 2. The mean value and standard deviation σ for 6 measurements with each prototype are given.[7]

manufacturing tolerances is displayed as 95% confidence intervals on the analytical results. There is a good match between all the results that shows that isochronism tuning is mastered for the co-RCC and that the analytical model captures well the main nonlinear characteristics of the oscillator.

Remark 7.6.4. There is a difference between the analytical and experimental results for λ=1.4 that is not taken into account by the CI. This offset could have been caused by the inertia variation of the oscillator due to the parasitic translation of the intermediate bodies that is not taken into account by the analytical model. However, the inward motion of the intermediate bodies causes a decrease in inertia that causes a positive isochronism defect ($\iota < 0$ in Eq. (5.8)), the opposite of the observed difference. As the role of the parallel leaf springs on the nonlinearity of the oscillator is small for these large values of λ, the difference can be attributed to errors in the FEM calculation of the RCC pivot nonlinearity. This offset is not critical as it can be compensated by tuning.

7.6.1 Clearance angle and oxide layer

When designing the oscillator in Sec. 7.2, it was assumed that the flexures were made of pure silicon and had a rectangular cross-section. In practice, the leaf springs have a section that resembles a trapezoid due to the DRIE process and an oxide layer (SiO_2) at their surface to compensate for thermal effects, see Sec. 1.5.3. The trapezoidal cross-section is characterized by the clearance angle ξ and the oxide layer by its thickness τ, see Fig. 7.21.

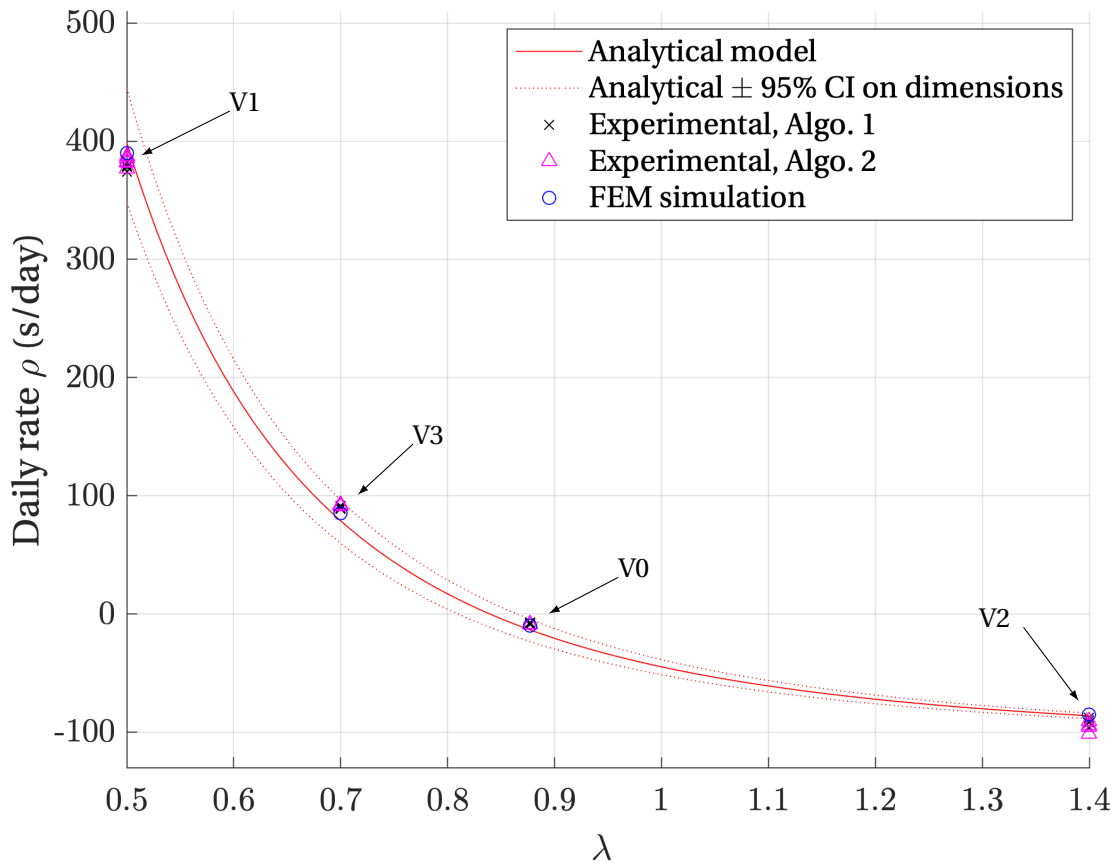Figure 7.20 – Comparison of the isochronism tuning of the co-RCC for varying λ obtained with the analytical model, by FEM simulation and experimentally. The results are expressed in terms of daily rate ρ at 16.5 degrees with respect to reference amplitude 15 degrees.
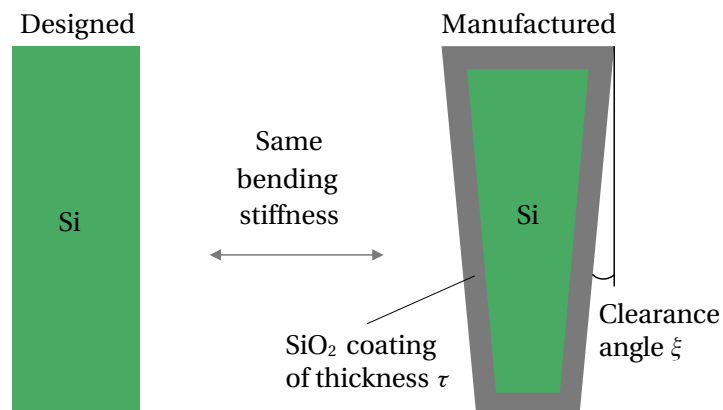

Figure 7.21 – Equivalence between rectangular silicon cross section and trapezoidal silicon cross-section with oxide layer.

In order to be able to alternate between both models, an equivalence is established such that the leaf springs have the same bending stiffness. The stiffness of a cantilever beam subject to rotation, deflection or translation is proportional to EI, where E is Young's modulus and I is the area moment of inertia of the cross-section about the axis relevant to the bending, i.e., axis y in Fig. 7.22 (Cosandier et al., 2017, Eq. 3.1). Assuming that the stiffness of the oxide layer can be added to that of the silicon part (like parallel springs), the condition for equivalent bending stiffness with the two cross-sections of Fig. 7.21 is

$$E_{\mathrm{Si}} I_{\mathrm{rect}} = E_{\mathrm{Si}} I_{\mathrm{Si}} + E_{\mathrm{ox}} I_{\mathrm{ox}} = E I_{\mathrm{eq}}, \qquad (7.16)$$

where E_{Si} is Young's modulus for silicon (see Fig. 7.2) and $E_{\mathrm{ox}} = 70$ GPa is Young's modulus for the SiO$_2$ layer.

The leaf springs with rectangular cross-section have area moment of inertia I_{rect} given in Eq. (7.2),

The manufactured leaf springs have a trapezoidal cross-section with thickness h_{top} on the top surface of the wafer and

$$h_{\mathrm{bottom}} = h_{\mathrm{tot}} - 2\tan\xi\, b. \qquad (7.17)$$

on the bottom surface, see Fig. 7.22. The area moment of inertia of the silicon portion is

$$I_{\mathrm{Si}} = \frac{b}{48}(h_{\mathrm{top,\ Si}} + h_{\mathrm{bottom,\ Si}})(h_{\mathrm{top,\ Si}}^2 + h_{\mathrm{bottom,\ Si}}^2), \qquad (7.18)$$

where

$$h_{\mathrm{top,\ Si}} = h_{\mathrm{top}} - 2\tau \qquad (7.19)$$

is the top thickness and

$$h_{\mathrm{bottom,\ Si}} = h_{\mathrm{bottom}} - 2\tau \qquad (7.20)$$

is the bottom thickness. The area moment of inertia of the oxide layer is

$$I_{\mathrm{ox}} = \frac{b}{48}(h_{\mathrm{top}} + h_{\mathrm{bottom}})(h_{\mathrm{top}}^2 + h_{\mathrm{bottom}}^2) - I_{\mathrm{Si}}. \qquad (7.21)$$

Remark 7.6.5. The difference in height b between the oxide layer and silicon portion of the manufactured part is neglected due to the high slenderness of the cross section and significantly lower influence of this dimension in comparison to the thickness (first order versus third order).

Equation (7.16) is used to switch between the two cross-section models in two cases:

1. To specify the top thickness h_{top} on the manufacturing drawing corresponding to the prototype design with rectangular cross section of Sec. 7.2.1, knowing the clearance angle ξ and oxide thickness τ of the process.

2. To adapt the analytical model of Sec. 5.5 to the dimensions measured on the prototypes.
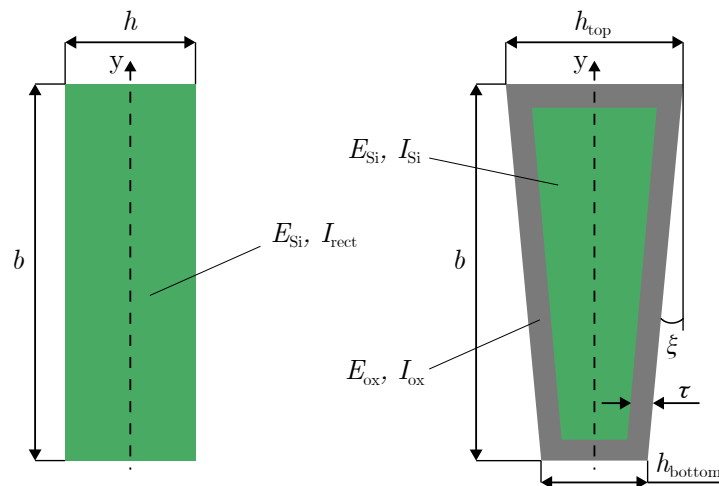
Figure 7.22 – Dimensions of rectangular silicon cross section and trapezoidal silicon cross-section with oxide layer.

In order to perform this second task, the cross-section of one RCC leaf springs of one prototype was measured by scanning electron microscope (SEM). The prototype was coated with a thin layer of gold to increase contrast, cased in a resin, sliced perpendicularly to the leaf springs and polished, see Fig. 7.23. The images showed that the trapezoidal cross-section hypothesis is reasonable and the dimensions near the top and bottom surface of the wafer were measured, see Fig. 7.24. These measurements were performed in five points along the length of the leaf spring, from which a mean value for the top and bottom thickness is computed, see Table 7.8. The measurement of the thickness of the oxide layer returned $1.0 \pm 0.1 \ \mu$m.
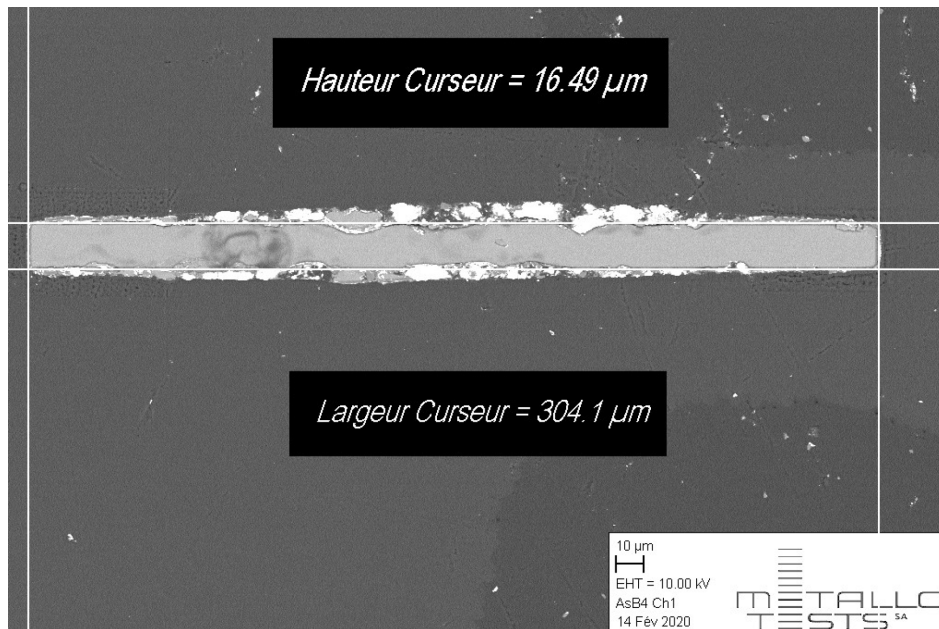
Figure 7.23 – Cross-section of a manufactured RCC leaf spring under SEM.
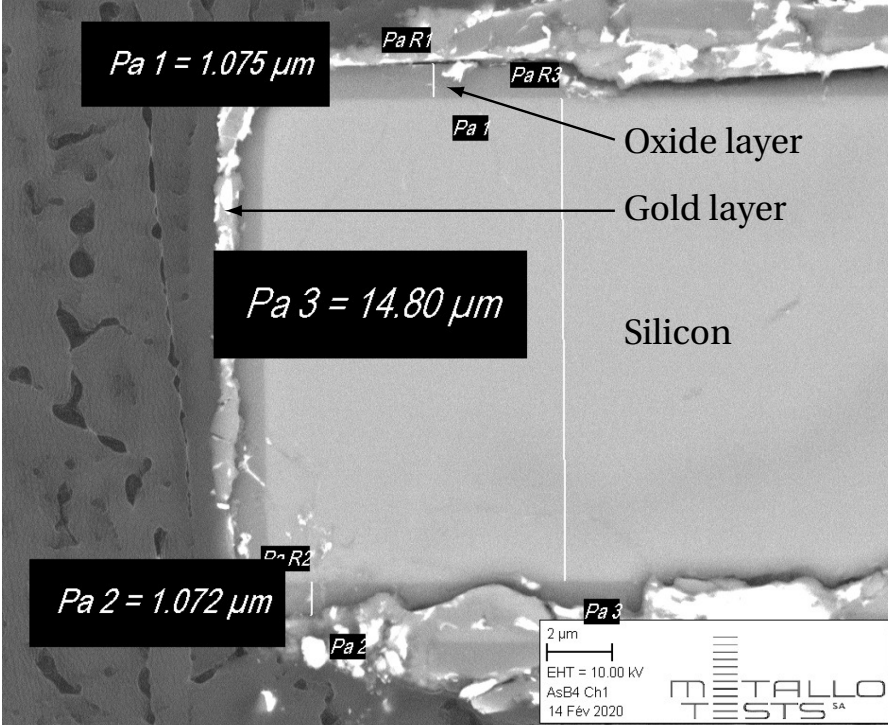
(a)
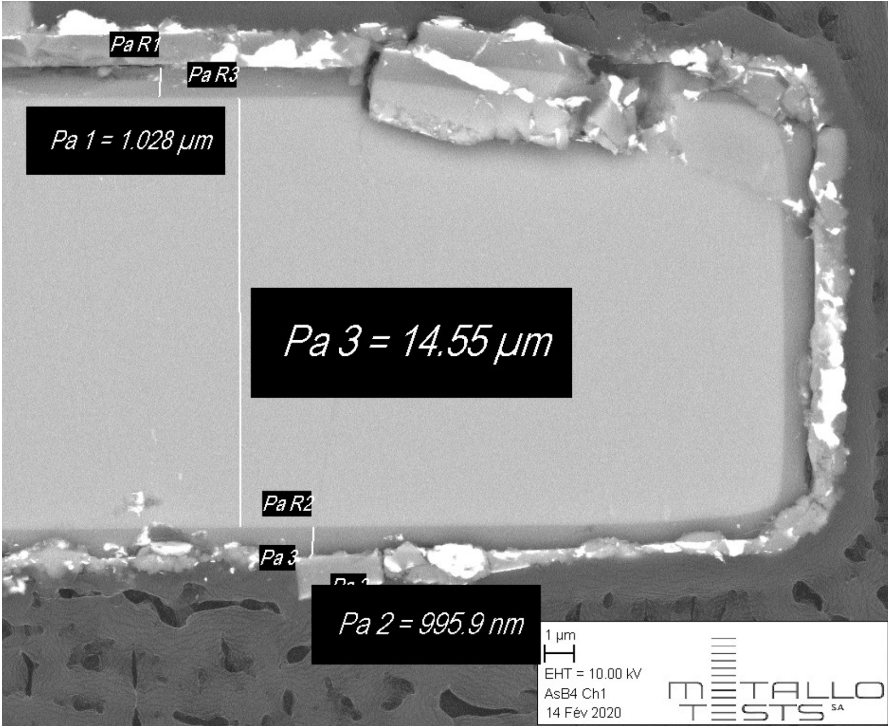
(b)

Figure 7.24 – Measurement by SEM of the thickness of the silicon and oxide parts of the RCC leaf springs near the (a) top and (b) bottom surfaces of the wafer.

Measurement point	Bottom thickness (μm)	Top thickness (μm)
1	16.39	16.87
2	16.47	16.87
3	16.57	16.95
4	16.38	16.91
5	16.15	16.92
Mean	16.39	16.91
Standard dev.	0.16	0.03
95% CI	0.44	0.09

Table 7.8 – Thickness of the measured RCC leaf springs near both surfaces of the wafer.

Since this measurement method is complex and expensive, it was not reproduced for other RCC leaf springs or for the parallel leaf springs. It is thus assumed that the results apply to all RCC flexures and that there is the same difference between the specified and manufactured dimensions for the parallel and RCC leaf springs. Assuming that the dispersion is such that the oscillator behaves as if all the leaf springs of one type (RCC or parallel) have the mean dimensions of that type, the equivalent EI_{eq} ratio for each type of leaf spring is calculated with Eq. (7.16) to (7.21) and used for the analytical results of Fig. 7.19 and 7.20.

In order to account for the manufacturing tolerances, it is assumed that the thickness of the leaf springs follows a normal distribution and 95% confidence intervals on the estimated means are computed using Student's t-distribution (Student, 1908), see Table 7.8. These intervals are then used to compute the uncertainty of the analytical model in Fig. 7.19 and 7.20 by considering the worst case scenarios, that is, thickest parallel leaf springs with the thinnest RCC leaf springs and vice versa. Note that, since there are no measurements on the parallel leaf springs, the same confidence intervals are taken as for the RCC leaf springs.

Remark 7.6.6. The clearance angle ξ of the manufactured leaf springs is smaller than expected, resulting in stiffer flexures than in the design of Sec. 7.2 and a higher nominal frequency of the prototypes than planned (approximately 16 Hz instead of 15 Hz for prototypes V0, V1 and V2 in Fig. 7.18).

7.7 Experimental validation of gravity effect

In order to assess experimentally the effect of gravity on the frequency stability of our prototypes, their position-time relationship is measured in different positions: two horizontal and eight vertical. The oscillator is measured in the two horizontal positions due to the asymmetry induced by the clearance angle of the manufacturing process. The vertical positions correspond to eighth of a full rotation and are determined using an inclinometer as depicted in Fig. 7.25.

The nominal frequency f_0 of the prototype in each position is determined from the frequency-

(a) $\varphi = 0$ degrees

(b) $\varphi = 45$ degrees
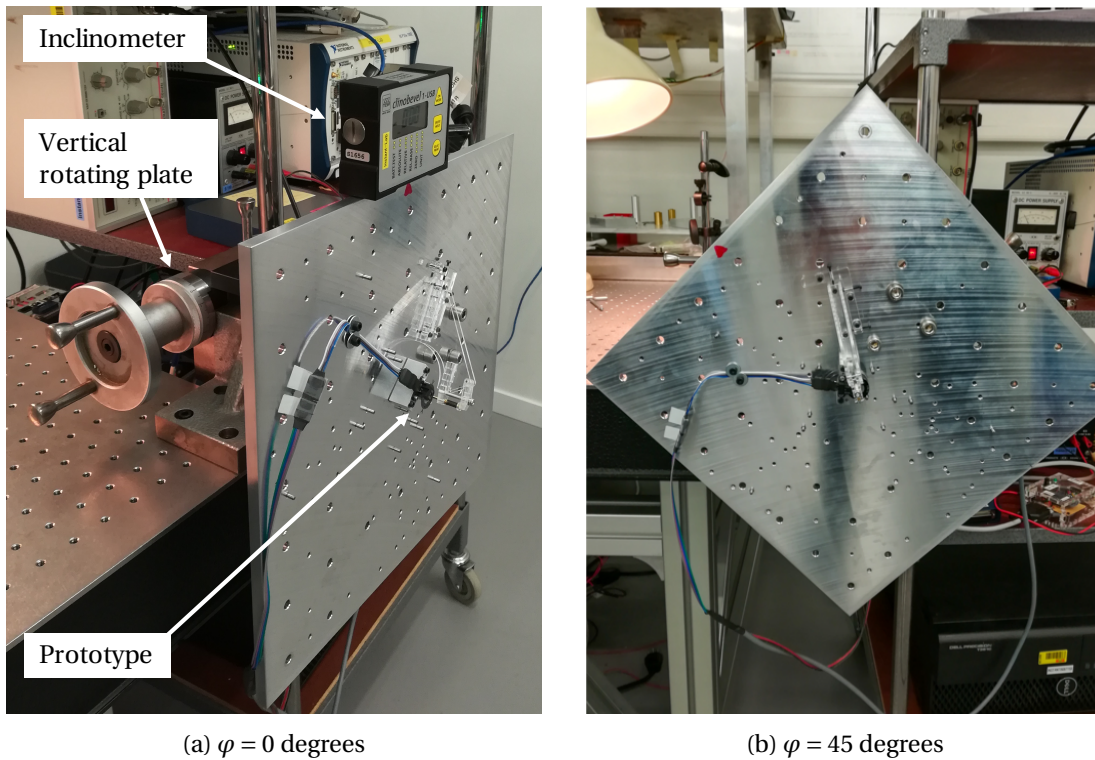
Figure 7.25 – Experimental setup for gravity effect measurement in the oscillation plane.

amplitude relationship, as explained in Sec. 7.6. The influence of gravity is then expressed in terms of daily rate using Eq. (5.7) and the results are plotted in Fig. 7.26. Four measurements were performed in each position. The reference frequency was arbitrarily chosen as the mean frequency measured in horizontal position facing down (gravity in $z+$ direction). This corresponds approximately to the middle of the frequency dispersion.

The finite element model was modified to correspond to the manufactured prototypes, see Fig. 7.27. It takes into account the measurement features, the oxide layer, and the dimensions measured after fabrication in Table 7.8. The FEM results are plotted in Fig. 7.28 and are close to the experimental results of Fig. 7.26. The daily rate stability within ± 5.2 s/day measured experimentally is slightly better than the ± 7.9 s/day of the FEM results. Note that, in both results, there is a difference between both horizontal positions caused by the clearance angle of the manufacturing process.

Remark 7.7.1. The gravity effect measurements were made with a prototype of type V0 but versions V1 and V2 would have given similar results since the stiffness of the parallel leaf springs does not affect the limiting frequency as amplitude approaches zero, see Eq. (4.31).

Figure 7.26 – Experimental daily rate ρ of the co-RCC prototype for varying angle ψ of the gravity load in the xy-plane and for gravity acting along the z axis. Four measurements are done in each position.
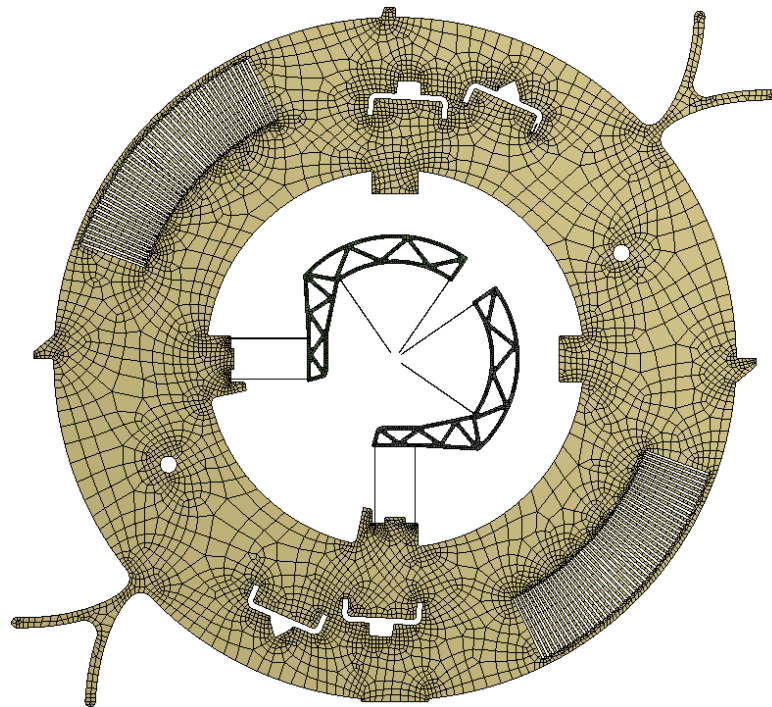
Figure 7.27 – Finite element model of the co-RCC prototype.
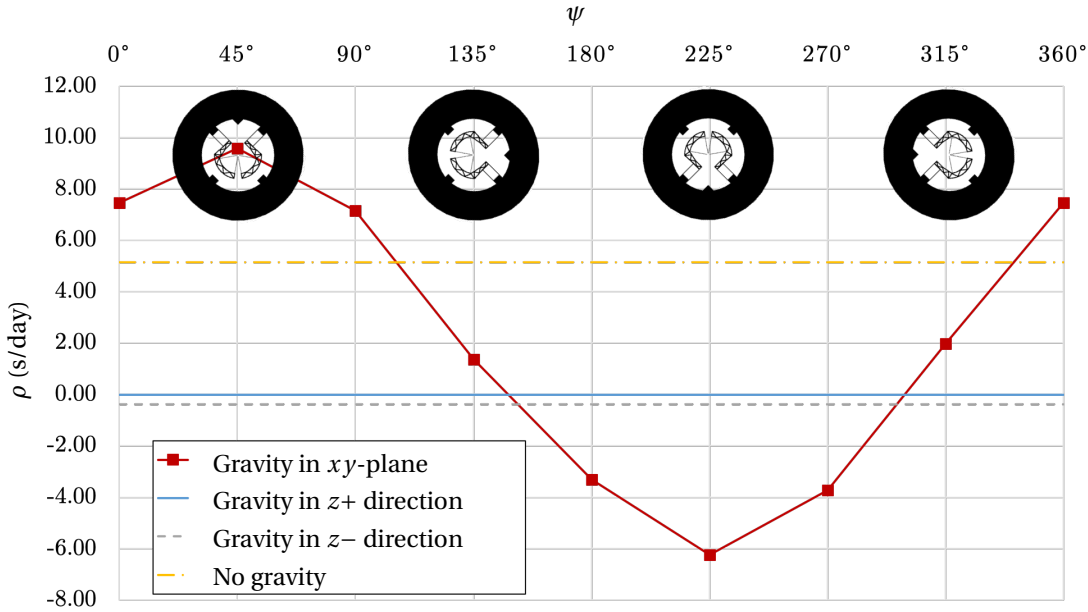
Figure 7.28 – Daily rate ρ of the simulated co-RCC prototype for varying angle ψ of the gravity load in the xy-plane and for gravity acting along the z axis. The reference frequency is the mean frequency with gravity in $z+$ direction.
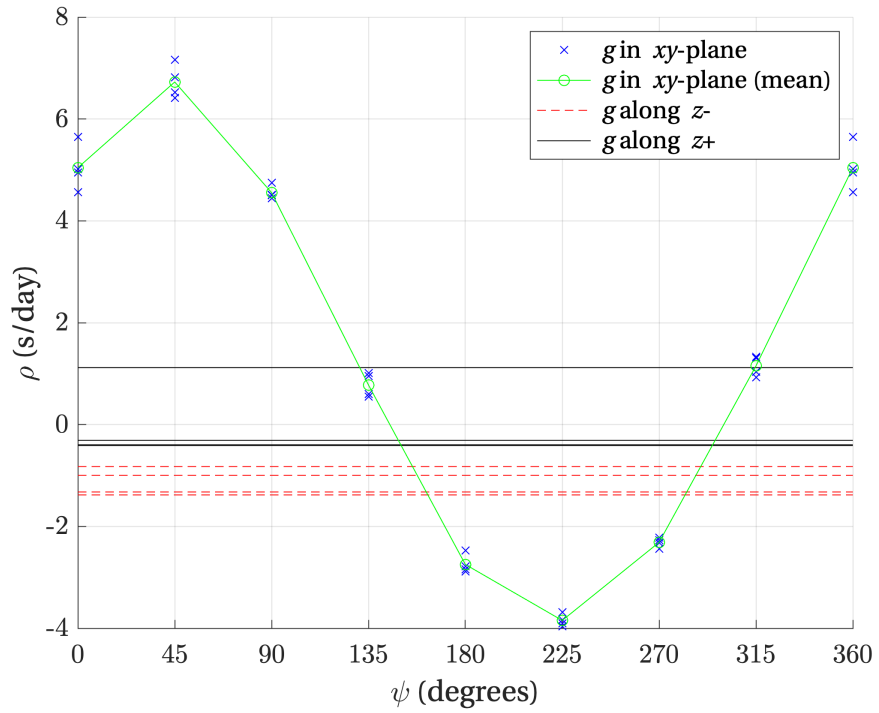
7.7.1 Experimental validation of gravity effect tuning

The gravity effect measured on the prototypes stays within ± 5.2 s/day, which would be reasonable for a watch application. We showed however in Sec. 6.4 that this defect could be decreased by shifting the COM of the oscillator and verify this principle experimentally. This gravity-effect tuning was not yet developed when the prototypes were designed and was not integrated. Nevertheless, external masses can be added to the oscillator using the integrated clamping features, see Fig. 7.3, in order to produce the desired imbalance.

Imbalance masses were produced that allows to shift the COM of the oscillator by a distance s along the axis of symmetry of the flexures without affecting the COM position in any other direction, see Fig. 7.29a. They were manufactured in aluminum alloy and clamped in pairs on each side of the prototypes, see Fig. 7.29b.

Figure 7.30 plots the gravity effect in terms of daily rate for the prototype with imbalance masses. The results show that the tuning is effective since the curve has been inverted from ± 5.2 s/day in Fig. 7.26 to ∓ 2.7 s/day.

The tuning masses were manufactured before the gravity effect on the prototype was measured and an imbalance of $B = 17$ nN·m was chosen based on the FEM results of Fig. 6.7. The manufactured masses have a slightly greater height than specified, resulting in an actual imbalance of $B = 18$ nN·m. According to Eq. (6.8), this gives a rate variation of ∓ 8.7 s/day, which corresponds to a correction from ± 5.2 s/day in Fig. 7.26 to ∓ 3.5 s/day. This is close to the ∓ 2.7 s/day obtained experimentally in Fig. 7.30 and validates our model.
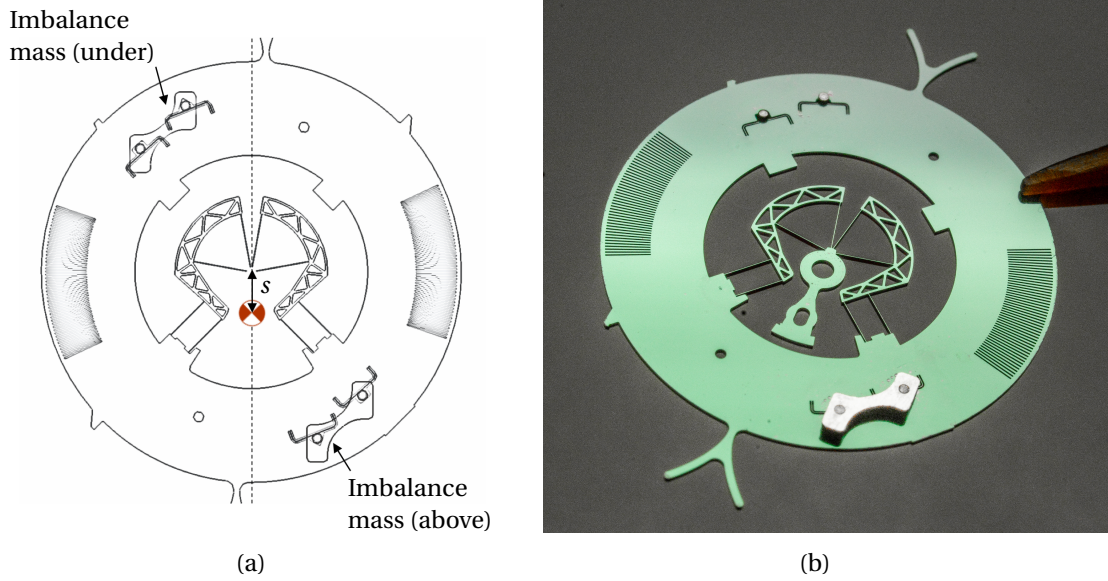
Figure 7.29 – Imbalances masses for in-plane gravity effect tuning seen (a) on a transparent view of the modelled prototype and (b) mounted on the manufactured prototype.
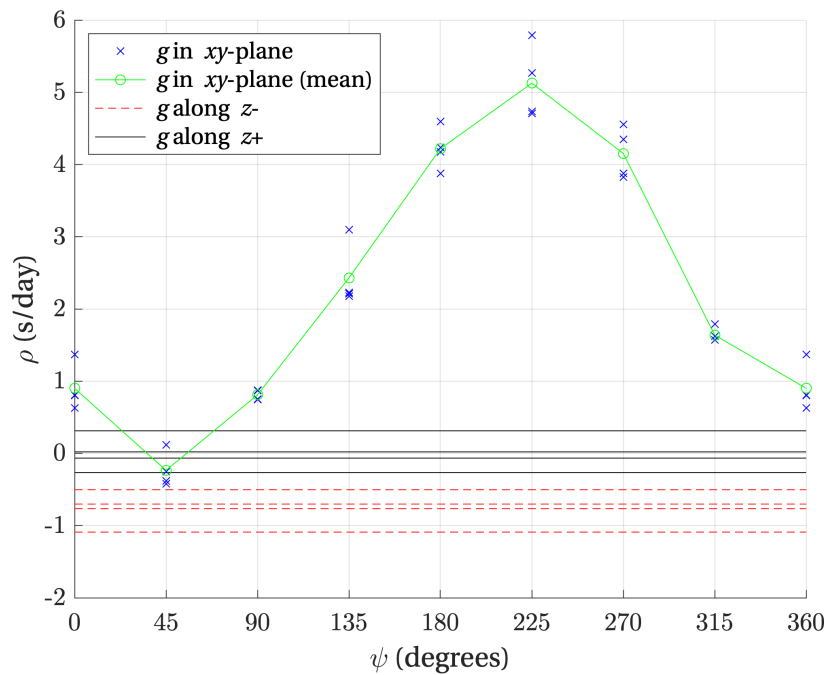
Figure 7.30 – Experimental daily rate ρ of the co-RCC prototype with imbalance mass for varying angle ψ of the gravity load in the xy-plane and for gravity acting along the z axis. Four measurements are done in each position.

The results are very close to the desired watch specifications of Sec. 7.1. Note that these results can still be improved by choosing a smaller imbalance correction and by equalizing the in-plane and out-of-plane effects using parameter α, as explained in Sec. 6.5.

Remark 7.7.2. The imbalance masses used here do not provide a true tuning as they change the mass and inertia of the oscillator. Their goal is to validate the in-plane gravity effect tuning by offsetting the COM. In practice, the imbalance would have to be integrated during the design of the oscillator. Or else this tuning could be part of a system comprising other masses that are used to adjust the nominal frequency of the oscillator. Note that inertia tuning is commonly done in watchmaking using inertia blocks (Berner, 2002).

7.8 Chapter conclusion

In this chapter, a silicon prototype of the co-RCC satisfying practical watch specifications was presented. An experimental method was developed to measure, without a sustaining mechanism, its performance in terms of quality factor, isochronism tuning and gravity effect minimization. The experimental results showed a quality factor around $Q = 630$, isochronism tuning with a resolution below 1 s/day by changing the length of the parallel leaf springs, and a gravity effect within ± 3 s/day that can still be improved by fine-tuning. Avenues for improving the quality factor were discussed. The most promising one seems to be increasing the density of the inertial body, which should lead to the desired order of magnitude improvement in Q with respect to the traditional balance and hairspring oscillator.

8 Contributions and Conclusion

8.1 Contributions

The main contributions of this thesis are:

1. Three new families of flexure pivot watch oscillators.

2. The concept of isochronism tuning (as opposed to minimizing isochronism defect).

3. New ways of tuning the isochronism of flexure-based mechanical time bases: by acting on the second order terms of stiffness and inertia.

4. A silicon flexure pivot oscillator prototype satisfying mechanical watch specifications along with a practical method to tune the isochronism defect post fabrication.

5. A design methodology to make a flexure pivot oscillator insensitive to the effect of gravity and a method to tune this effect.

6. Analytical and numerical models of the new flexure pivot oscillators.

7. Experimental validation of the theoretical concepts of the thesis.

8. A new experimental method to characterize the performance of mechanical oscillators without sustaining mechanism.

9. Categorization and review of the latest stage of development of flexure-based watch oscillators.

8.2 Conclusion

Results

The focus of this thesis was on overcoming the main challenges of the implementation of flexure pivot oscillators in mechanical watches, that is, their isochronism defect and gravity

sensitivity. These issues were treated conceptually, and practical solutions were developed and validated. Three new families of flexure pivot watch oscillators were introduced and examples of embodiments were given. The kinematics of these three oscillators were validated qualitatively on mock-ups.

Expressions for the rotational stiffness of the three flexure pivot architectures in terms of angular displacement and gravity loading were computed using beam theory and improved using finite element analysis. These expressions were then used to assess the isochronism defect and gravity sensitivity of the oscillators. The concept of isochronism tuning using second order terms of stiffness and inertia was formalized and expressions were derived to quantify it. Practical methods of tuning were developed, by modifying the dimensions of flexures or by displacing tuning masses. These methods allow to reach a tuning of order 1 s/day that satisfies the accuracy goal of this thesis. The concepts used to minimize the influence of gravity on the frequency of flexure-based oscillators were discussed and design guidelines were provided for their implementation. Their effectiveness was demonstrated on the oscillators of this thesis and a method was devised to cancel remaining defects.

A silicon prototype of the co-RCC oscillator was presented, allowing to reach practical mechanical watch specifications. A new experimental method was developed in order to measure its performance without a sustaining mechanism (escapement). The experimental results showed a quality factor around $Q = 630$, isochronism tuning with a resolution below 1 s/day, and a gravity effect within ± 3 s/day that can still be improved by fine-tuning. Avenues for increasing the quality factor were discussed, the most promising one being the use of a denser material for the inertial body.

Limitations

A broader goal of this thesis was to invent new flexure pivot oscillators that could eventually replace the traditional balance and hairspring oscillator of industrially produced mechanical watches in order to improve their accuracy. In this respect, the results of this thesis are promising, but, at this stage, it is not possible to assert whether this further goal is reachable with the introduced oscillators. Answering this question would require the implementation of our prototypes in a mechanical watch and measurements of timekeeping performance in wearing conditions. A paramount issue is the compatibility of the oscillator with an escapement and its associated driving gear train. The following critical points are to be mentioned:

- The reduced angular stroke of the flexure pivot (± 15 degrees) compared to classical oscillators (± 270 degrees) allowing for a much shorter interaction path between the escapement and the oscillator.

- The drastically reduced driving torque at the escapement wheel resulting from the drastic increase in quality factor, which makes the fluctuating friction torque of the gear train a potential source of accidental halts of the watch.

- The increased frequency of the oscillator (15 Hz) compared to usual oscillators (typically 4 Hz) which poses challenges that have been addressed in some existing watches, but not in conjunction with reduced angular stroke and reduced driving torque.

Resistance to shocks and frequency stability when subject to angular accelerations are other key issues which remain to be investigated.

Application to other fields

The results of this thesis could find other applications, such as compliant microgrippers, MEMS oscillators for electronic devices, prosthetic joints which approximate the nonlinear behavior of biological materials, MEMS filters using nonlinear resonance phenomena, bistable pivots, constant force mechanisms, and flexure pivots for robotics, space and medical applications.

Final word

Addressing the challenge of breaking through the 1 s/day accuracy limit of mechanical watches by using flexure based oscillators has led to fundamentally novel flexure pivot designs with unequalled properties in terms of restoring torque linearity and gravity sensitivity. Theses results, which constitute important contributions to the field of flexure-based mechanisms, are also promising for the future of mechanical horology.

Bibliography

Académie des inscriptions et belles-lettres (1675). *Le Journal Des Sçavans.* Jean Cusson, Paris, France. gallica.bnf.fr/ark:/12148/bpt6k56526h.

Airy, G. B. (1830). On the Disturbances of Pendulums and Balances, and on the Theory of Escapements. *Transactions of the Cambridge Philosophical Society*, vol. 3, part 1:105–128. members.loria.fr/Roegel/loc/airy1827annotated.pdf.

ANSYS (2018). ANSYS® Workbench, Release 19.2, ANSYS Workbench User's Guide.

Ashwell, D. G. (1950). The Anticlastic Curvature of Rectangular Beams and Plates. *The Aeronautical Journal*, 54(479):708–715, DOI: 10.1017/S0368393100116165.

Awtar, S., Slocum, A. H., and Sevincer, E. (2007). Characteristics of Beam-Based Flexure Modules. *Journal of Mechanical Design*, 129(6):625, DOI: 10.1115/1.2717231.

Barrot, F., Cosandier, F., Musy, G., Giriens, L., Droz, S., and Petremand, Y. (2018). SILOSCAPE—Flexure-based Oscillators for Mechanical Watches. Technical report. www.csem.ch/Doc.aspx?id=124178.

Barrot, F., Dubochet, O., Henein, S., Genequand, P., Giriens, L., Kjelberg, I., Renevey, P., Schwab, P., and Ganny, F. (2014). Un nouveau régulateur mécanique pour une réserve de marche exceptionnelle. In *Journée d'Etude de La Société Suisse de Chronométrie 2014*, pages 43–48. Société Suisse de Chronométrie.

Barrot, F., Musy, G., Cosandier, F., Kjelberg, I., Renevey, P., Giriens, L., Schwab, P., Genequand, P., Petremand, Y., Dubochet, O., Ganny, F., and Hamaguchi, T. (2015). GENEQUAND, a Novel Watch Regulator based on Compliant Mechanisms. Technical report. www.csem.ch/Doc.aspx?id=39670&name=CSEM-STR-2015-p%20103.pdf.

Bateman, D. A. (1977). Vibration theory and clocks. *Horological Journal*, 120-121(seven parts July 1977 to January 1978).

Bayat, D., Pétremand, Y., and Kjelberg, I. (2018). Timepiece Resonator with Two Balances Arranged to Oscillate in a Single Plane. Patent Number: EP3336613A1.

Bibliography

Beckett, Lord Grimthorpe, E. (1903). *A Rudimentary Treatise on Clocks, Watches and Bells.* Crosby Lockwood and Son, D. Van Nostrand Company, London, eighth edition. www.gutenberg.org/ebooks/17576.

Bellouard, Y. (2011). On the bending strength of fused silica flexures fabricated by ultrafast lasers. *Optical Materials Express*, 1(5):816–831, DOI: 10.1364/OME.1.000816.

Bennett, M., Schatz, M. F., Rockwood, H., and Wiesenfeld, K. (2002). Huygens's clocks. *Proceedings of the Royal Society of London. Series A: Mathematical, Physical and Engineering Sciences*, 458(2019):563–579, DOI: 10.1098/rspa.2001.0888.

Berner, G.-A. (2002). *Dictionnaire Professionnel Illustré de l'horlogerie I+ II.* Federation of the Swiss Watch Industry. www.fhs.swiss/berner/?l=en.

Bernoulli, J. (1697). Curvatura radii in diaphanis non uniformibus... In *Acta Eruditorum*, volume 19, pages 206–211. Prostant apud J. Grossium & J. F. Gleditschium. books.google.com/books?id=aTaZHrvK6zIC&dq=Acta%20eruditorum%20Anno%20MDCXCVII&pg=PA206#v=onepage&q&f=false.

Blanter, M. S., Golovin, I. S., Neuhäuser, H., and Sinning, H.-R. (2007). *Internal Friction in Metallic Materials: A Handbook.* Springer Series in Materials Science. Springer-Verlag, Berlin Heidelberg, DOI: 10.1007/978-3-540-68758-0.

Born, J.-J. (2019). Protection antichoc d'un résonateur à lames à pivot RCC. Patent Number: CH714936A2.

Born, J.-J., Di Domenico, G., Hinaux, B., Favre, J., and Léchot, D. (2016). Clock oscillator with tuning fork. Patent Number: EP3035127A1.

Breguet, L. F. C. (1866). Des procédés applicables à l'horlogerie et au réglage de la vitesse des machines. Patent Number: FR73414A.

Cartier (2012). ID Two. Press release. en.worldtempus.com/article/watches/innovation-and-technology/cartier-id-two-12973.html.

Chabloz, D. (2018a). Timepiece Component with a Flexible Pivot. Patent Number: EP3410229A1.

Chabloz, D. (2018b). Timepiece Component with Flexible Pivot. Patent Number: WO2018109584.

Ching, H. and Ko, P. H. (2016). Silicon hairspring. Patent Number: US20160238994A1.

Cho, C.-H. (2009). Characterization of Young's modulus of silicon versus temperature using a "beam deflection" method with a four-point bending fixture. *Current Applied Physics*, 9(2):538–545, DOI: 10.1016/j.cap.2008.03.024.

142

Clymer, B. (2012). Introducing The Cartier ID Two Concept Watch. *Hodin-kee.* www.hodinkee.com/articles/in-depth-introducing-the-cartier-id-two-concept-watch-watchm.

Conus, T. (2007). *Conception et Optimisation Multicritère Des Échappements Libres Pour Montres-Bracelets Mécaniques.* PhD thesis, DOI: 10.5075/epfl-thesis-3806.

Conus, T. (2015). Swatch Sistem51. In *Journée d'Etude de La Société Suisse de Chronométrie 2015*, pages 105–111. Société Suisse de Chronométrie.

Cosandier, F., Domine, E., Musy, G., and Barrot, F. (2018). Mechanical oscillator for a horological movement. Patent Number: US20180088529A1.

Cosandier, F., Henein, S., Richard, M., and Rubbert, L. (2017). *The Art of Flexure Mechanism Design.* EPFL Press, Lausanne, Switzerland.

Cusin, P., Charbon, C., and Verardo, M. (2012). Oscillating mechanism e.g. escapement drive, for timepiece, has rigid elements fixed to different elements of movement, where rigid elements, elastic return units and intermediate rigid element are coplanar on plane and deformed on plane. Patent Number: CH703464A2.

Defossez, L. (1946). *Les savants du XVIIe siècle et la mesure du temps.* Édition du Journal suisse d'horlogerie et de bijouterie.

Déhon, N. (2009). Escapement mechanism. Patent Number: EP2105806A1.

Di Domenico, G., Favre, J., Léchot, D., Hinaux, B., Matthey, O., and Born, J.-J. (2018). Optimised Clock Movement. Patent Number: EP3316046A1.

Di Domenico, G., Hinaux, B., Klinger, L., and Helfer, J.-L. (2016). Timepiece Resonator with Crossed Blades. Patent Number: WO2016096677A1.

Di Domenico, G., Léchot, D., Helfer, J.-L., and Winkler, P. (2017). Timepiece Resonator Mechanism. Patent Number: EP3206089A1.

Ditisheim, P. (1920). Demonstration of (a) A New Balance for Compensating the Temperature Error of Watches and Chronometers, and (b) A Centre-seconds Marine Chronometer with Electric Contacts. *Proceedings of the Physical Society of London*, 32:261, DOI: 10.1088/1478-7814/35/1/337.

Drake, S. (1995). *Galileo at Work: His Scientific Biography.* Dover Pubns, New York.

Eastman, F. S. (1935). *Flexure Pivots to Replace Knife Edges and Ball Bearings, an Adaptation of Beam-Column Analysis,.* Engineering Experiment Station Series. University of Washington, Seattle, USA.

Fedchenko, F. M. (1957). Astronomical Clock AChF-1 with Isochronous Pendulum. *Soviet Astronomy*, 1:637. adsbit.harvard.edu//full/1957SvA.....1..637F/0000637.000.html.

Bibliography

Feldmann, H. (2008). Die Geschichte der Stimmgabel - Teil 1: Die Erfindung der Stimmgabel, ihr Weg in der Musik und den Naturwissenschaften. *Laryngo-Rhino-Otol*, 76(02):116–122, DOI: 10.1055/s-2007-997398.

Forster, D. and Rolland, J. (2019). Accelerated ageing of the Swiss Lever Escapement – a case study. In *Congrès International de Chronométrie 2019*. Société Suisse de Chronométrie.

Gould, R. T. (2013). *The Marine Chronometer*. Antique Collectors' Club Ltd, Woodbrige, England, second edition.

Green, E. I. (1955). The story of Q. *American Scientist*, 43(4):584–594. www.jstor.org/stable/27826701.

Grübler, M. (1917). *Getriebelehre: Eine Theorie Des Zwanglaufes Und Der Ebenen Mechanismen*. Springer-Verlag, Berlin Heidelberg. www.springer.com/gp/book/9783662329535.

Guillaume, C.-E. (1920). Nobel Lecture: Invar and Elinvar. old.nobelprize.org/nobel_prizes/physics/laureates/1920/guillaume-lecture.html.

Haringx, J. A. (1949). The cross-spring pivot as a constructional element. *Flow, Turbulence and Combustion*, 1(1):313, DOI: 10.1007/BF02120338.

Harrison, J. (1767). *The Principles of Mr. Harrison's Timekeeper, with Plates of the Same*. W. Richardson. https://books.google.com/books?id=aB8OAAAAQAAJ.

Hastings, P. (1993). A Look at the Grasshopper Escapement. *Horological Journal*, 136(2):48–53.

Henein, S. (2000). *Conception Des Structures Articulées à Guidages Flexibles de Haute Précision*. PhD thesis, EPFL, Lausanne, DOI: 10.5075/epfl-thesis-2194. https://infoscience.epfl.ch/record/32670.

Henein, S., Barrot, F., Jeanneret, S., Fournier, R., Giriens, L., Gumy, M., Droz, S., and Toimil, M. (2011). Silicon Flexures for the Sugar-Cube Delta Robot. In *Proceedings of the 11th Euspen International Conference*, page 4, Como. www.euspen.eu/resource/silicon-flexures-for-the-sugar-cube-delta-robot/.

Henein, S. and Kjelberg, I. (2015). Timepiece oscillator. Patent Number: US9207641B2.

Henein, S. and Schwab, P. (2014). Isochronism corrector for clockwork escapement and escapement provided with such a corrector. Patent Number: US8672536B2.

Henein, S., Spanoudakis, P., Droz, S., Myklebust, L. I., and Onillon, E. (2003). Flexure Pivot for Aerospace Mechanisms. In *Proceedings of the 10th ESMATS*. citeseerx.ist.psu.edu/viewdoc/summary?doi=10.1.1.542.8369.

Henein, S., Vardi, I., Rubbert, L., Bitterli, R., Ferrier, N., Fifanski, S., and Lengacher, D. (2014). IsoSpring : Vers la montre sans échappement. In *Journée d'étude de La Société Suisse de Chronométrie 2014*. Société Suisse de Chronométrie. infoscience.epfl.ch/record/201790.

Hetzel, M. (1962). Le diapason et son influence sur l'horlogerie. *Bulletin annuel de la société suisse de chronométrie*, IV-1962:666–679.

Howell, L. L., Magleby, S. P., Olsen, B. M., and Wiley, J. (2013). *Handbook of Compliant Mechanisms*. Wiley Online Library, DOI: 10.1002/9781118516485.

Hull, R. (1999). *Properties of Crystalline Silicon*. Institution of Electrical Engineers. https://books.google.com/books?id=C_TWB_0rRLgC.

Huygens, C. (1897). *Oeuvres Complètes*, volume VII, Correspondance 1670-1675. Publiées par la Société Hollandaise des Sciences, Martinus Nijhoff, La Haye. www.dbnl.org/tekst/huyg003oeuv07_01/colofon.php.

Huygens, C. (2007). Horologium Oscillatorium [Latin with English translation by Ian Bruce]. www.17centurymaths.com/contents/huygenscontents.html.

Jaspers, H. (1986). The evolution of regulators for precision timekeeping. *Bulletin of the Scientific Instrument Society*, 11:4–5. static1.squarespace.com/static/54ec9b40e4b02904f4e09b74/t/567fd957d8af10f8899e2353/1451219287821/SIS_Bulletin_011.pdf.

Kahrobaiyan, M., Rubbert, L., Vardi, I., and Henein, S. (2016). Gravity insensitive flexure pivots for watch oscillators. In *Congrès International de Chronométrie 2016*. Société Suisse de Chronométrie. infoscience.epfl.ch/record/222491.

Kahrobaiyan, M. H., Thalmann, E., and Henein, S. (2020). Flexure Pivot Oscillator Insensitive to Gravity. Patent Number: WO2020016131.

Kahrobaiyan, M. H., Thalmann, E., Rubbert, L., Vardi, I., and Henein, S. (2018). Gravity-Insensitive Flexure Pivot Oscillators. *Journal of Mechanical Design*, 140(7):075002–9, DOI: 10.1115/1.4039887.

Léchot, D., Winkler, P., Di Domenico, G., and Born, J.-J. (2018). Protection of a blade resonator mechanism against axial shocks. Patent Number: US20180136607A1.

Leopold, J. (1996). The Longitude Timekeepers of Christiaan Huygens. In Andrewes, W. J. H., editor, *The Quest for Longitude: The Proceedings of the Longitude Symposium Harvard University, Cambridge, Massachusetts, November 4-6, 1993*, pages 101–114. Harvard University, Cambridge, Massachusetts, second edition.

Liu, X., Haucke, H., Vignola, J. F., Simpson, H. J., Baldwin, J. W., Houston, B. H., and Photiadis, D. M. (2009). Understanding the internal friction of a silicon micro-mechanical oscillator. *Materials Science and Engineering: A*, 521-522:389–392, DOI: 10.1016/j.msea.2008.10.065.

Maluf, N. and Williams, K. (2004). *An Introduction to Microelectromechanical Systems Engineering*. Artech House. http://epdf.pub/an-introduction-to-mems-engineering.html.

Bibliography

Markl, X. (2017). Zenith DEFY LAB, 3 Centuries of Regulation & Chronometry Revolutionized with a Radically New Oscillator. *Monochrome Watches*. http://monochrome-watches.com/zenith-defy-lab-revolutionary-oscillator-technical-review-video-price/.

Markl, X. (2019). Introducing Ulysse Nardin Freak NeXt. *Monochrome Watches*. http://monochrome-watches.com/ulysse-nardin-freak-next-a-new-concept-with-revolutionary-3d-flying-oscillator-live-pics/.

Matthews, M. R. (1994). *Science Teaching: The Role of History and Philosophy of Science*. Routledge, New York.

Matthys, R. J. (2004). *Accurate Clock Pendulums*. Oxford University Press, Oxford.

McKie, R. (2015). Clockmaker John Harrison vindicated 250 years after 'absurd' claims. *The Observer*, ISSN: 0029−7712. www.theguardian.com/science/2015/apr/19/clockmaker-john-harrison-vindicated-250-years-absurd-claims.

Mercier, T., Semon, G., Ypma, W. J. B., and Weeke, S. L. (2019). Dispositif Pour Piece D'horlogerie, Mouvement Horloger Et Piece D'horlogerie Comprenant Un Tel Dispositif. Patent Number: FR3071075A1.

Musy, J.-P., Maier, F., and Krüttli, A. (2008). Echappement et spiral réalisés en Silinvar®. In *Journée d'Etude de la Société Suisse de Chronométrie 2008*, pages 51–54. Société Suisse de Chronométrie.

Nayfeh, A. and Mook, D. (1995). *Nonlinear Oscillations*. Wiley, New York, wiley classics library edition.

Newton, I. (1802). *Mathematical Principles of Natural Philosophy*. A. Strahan.

Niaudet-Breguet, N. (1866). Application du diapason à I'horlogerie. *Comptes rendus de seances de l'Academie des Sciences*, 63:991.

Noell, W., Clerc, P.-A., Jeanneret, S., Hoogerwerf, A., Niedermann, P., Perret, A., and de Rooij, N. (2004). MEMS for a watches. In *Maastricht MEMS 2004 Technical Digest*, page 39904, Maastricht, Netherlands. IEEE, DOI: 10.1109/MEMS.2004.1290507.

Oldenburg, H. (1675). *Philosophical Transactions of the Royal Society*, volume X.

Pei, X., Yu, J., Zong, G., Bi, S., and Yu, Z. (2008). Analysis of Rotational Precision for an Isosceles-Trapezoidal Flexural Pivot. *Journal of Mechanical Design*, 130(5):052302, DOI: 10.1115/1.2885507.

Pellaton, J. C. (1949). *Cours d'échappements*. Technicum Neuchatelois.

Perotto, J.-F. (2009). Les bases de temps horlogères. *Bulletin de la Société Suisse de Chronométrie*, 61:21–26.

Plainevaux, J. E. (1956). Etude des déformations d'une lame de suspension élastique. *Il Nuovo Cimento (1955-1965)*, 4(4):922–928, DOI: 10.1007/BF02746178.

Rawlings, A. L. (1993). *The Science of Clocks & Watches.* British Horological Institute, Upton, UK, third and revised edition.

Reymondin, C.-A., Monnier, G., Jeanneret, D., and Pelaratti, U. (1999). *The Theory of Horology.* Swiss Federation of Technical Colleges.

Robuschi, N., Braghin, F., Corigliano, A., Ghisi, A., and Tasora, A. (2017). On the dynamics of a high frequency oscillator for mechanical watches. *Mechanism and Machine Theory*, 117:276–293, DOI: 10.1016/j.mechmachtheory.2017.07.013.

Roszhart, T. (1990). The effect of thermoelastic internal friction on the Q of micromachined silicon resonators. In *IEEE 4th Technical Digest on Solid-State Sensor and Actuator Workshop*, pages 13–16. DOI: 10.1109/SOLSEN.1990.109810.

Rubbert, L., Bitterli, R., Ferrier, N., Fifanski, S., Vardi, I., and Henein, S. (2016). Isotropic springs based on parallel flexure stages. *Precision Engineering*, 43:132–145, DOI: 10.1016/j.precisioneng.2015.07.003.

Semon, G., Van Zoest, W. P., and Tolou, N. (2016). Monolithic Timepiece Regulator, Timepiece Movement and Timepiece Having Such a Timepiece Regulator. Patent Number: WO2016079068A1.

Semon, G., Ypma, W. J. B., Weeke, S. L., and Tolou, N. (2017). Device for a Timepiece, Timepiece Movement and Timepiece Comprising a Device of Said Type. Patent Number: WO2017157870A1.

Student (1908). The Probable Error of a Mean. *Biometrika*, 6(1):1–25, DOI: 10.2307/2331554.

Su, S. and Du, R. (2007). Signature analysis of mechanical watch movements. *Mechanical Systems and Signal Processing*, 21(8):3189–3200, DOI: 10.1016/j.ymssp.2007.04.006.

Thalmann, E. and Henein, S. (2019). Conceptual design of a rotational mechanical time base with varying inertia. Preprint, engrXiv, DOI: 10.31224/osf.io/kjhbx.

Thalmann, E., Kahrobaiyan, M. H., and Henein, S. (2018). Flexure-Pivot Oscillator Restoring Torque Nonlinearity and Isochronism Defect. In *ASME 2018 International Design Engineering Technical Conferences and Computers and Information in Engineering Conference*, volume 5A, page V05AT07A013. American Society of Mechanical Engineers, DOI: 10.1115/DETC2018-85863.

Thalmann, E., Kahrobaiyan, M. H., Vardi, I., and Henein, S. (2020). Flexure Pivot Oscillator With Intrinsically Tuned Isochronism. *Journal of Mechanical Design*, 142(7), DOI: 10.1115/1.4045388.

Bibliography

Van Eijk, J. (1985). *On the Design of Plate-Spring Mechanisms*. PhD thesis, TU Delft, Delft, The Netherlands. citeseerx.ist.psu.edu/viewdoc/download?doi=10.1.1.1025.65&rep=rep1&type=pdf.

Vardi, I. (2012). Magnetic Resonator for a Mechanical Timepiece. Patent Number: WO2012080413.

Vardi, I. (2013). Resonator Having a Tuning Fork for a Mechanical Clock Movement. Patent Number: WO2013045573.

Vardi, I. (2014). Le facteur de qualité en horlogerie mécanique. *Bulletin de la Société Suisse de Chronométrie*, 75:9. infoscience.epfl.ch/record/263995.

Vardi, I. (2015). Mathematics, the Language of Watchmaking. *Watch Around*, 20:90–94. infoscience.epfl.ch/record/213702.

Vardi, I. and Déhon, N. (2015). Oscillating System for Horological Movement with a Pallet Escapement. Patent Number: WO2015197411.

Vardi, I. and Henein, S. (2019). A la recherche du temps précis : La découverte de l'oscillateur. In *Congrès International de Chronométrie 2019*. Société Suisse de Chronométrie. infoscience.epfl.ch/record/271525.

Vardi, I., Rubbert, L., Bitterli, R., Ferrier, N., Kahrobaiyan, M., Nussbaumer, B., and Henein, S. (2018). Theory and design of spherical oscillator mechanisms. *Precision Engineering*, 51:499–513, DOI: 10.1016/j.precisioneng.2017.10.005.

von Gunten, S. and Gubler, Q. (2016). Mechanism and method for adjusting a speed in a watch movement. Patent Number: EP3037894A1.

von Gunten, S., Gygax, P., and Humair, L. (2015). Oscillateur mécanique. Patent Number: EP2273323B1.

Weeke, S. L., Tolou, N., Semon, G., and Herder, J. L. (2016). A Fully Compliant Force Balanced Oscillator. In *ASME 2016 International Design Engineering Technical Conferences and Computers and Information in Engineering Conference*, page V05AT07A008. American Society of Mechanical Engineers, DOI: 10.1115/DETC2016-59247.

Weisstein, E. W. (2020). Levenberg-Marquardt Method. In *MathWorld–A Wolfram Web Resource*. Accessed on 21/03/2020. mathworld.wolfram.com/Levenberg-MarquardtMethod.html.

Winkler, P. and Helfer, J.-L. (2019). Protection antichoc d'un mécanisme résonateur d'horlogerie à guidage flexible rotatif. Patent Number: CH714922A2.

Winkler, P., Helfer, J.-L., and Di Domenico, G. (2018a). Rotating resonator with flexure bearing maintained by a detached lever escapement. Patent Number: WO2018095593A2.

Winkler, P., Helfer, J.-L., Di Domenico, G., and Conus, T. (2017). Isochronous Timepiece Resonator. Patent Number: EP3254158A1.

Winkler, P., Helfer, J.-L., Léchot, D., and Born, J.-J. (2018b). Protection of Blades of a Mechanical Watch Resonator. Patent Number: EP3324247A1.

Wittrick, W. (1948). The Theory of Symmetrical Crossed Flexure Pivots. *Australian Journal of Scientific Research A Physical Sciences*, 1:121. http://adsabs.harvard.edu/full/1948AuSRA...1..121W.

Wittrick, W. (1951). The properties of crossed flexure pivots, and the influence of the point at which the strips cross. *The Aeronautical Quarterly*, 2:272–292, DOI: 10.1017/S0001925900000470.

Woodward, P. (1995). *My Own Right Time: An Exploration of Clockwork Design*. Oxford University Press, Oxford.

Ypma, W. J. B. and Weeke, S. L. (2019). Mechanical Watch Oscillator. Patent Number: WO2019156552A1.

Zanaty, M., Fussinger, T., Rogg, A., Lovera, A., Lambelet, D., Vardi, I., Wolfensberger, T. J., Baur, C., and Henein, S. (2019). Programmable Multistable Mechanisms for Safe Surgical Puncturing. *Journal of Medical Devices*, 13(2), DOI: 10.1115/1.4043016.

Zanaty, M. G. A. A. (2018). *Programmable Multistable Mechanisms: Design, Modeling, Characterization and Applications*. PhD thesis, EPFL, Lausanne, Switzerland, DOI: 10.5075/epfl-thesis-9055.

Zdaniewski, W. A., Rindone, G. E., and Day, D. E. (1979). The internal friction of glasses. *Journal of Materials Science*, 14(4):763–775, DOI: 10.1007/BF00550707.

Zhao, H. and Bi, S. (2010a). Accuracy characteristics of the generalized cross-spring pivot. *Mechanism and Machine Theory*, 45(10):1434–1448, DOI: 10.1016/j.mechmachtheory.2010.05.004.

Zhao, H. and Bi, S. (2010b). Stiffness and stress characteristics of the generalized cross-spring pivot. *Mechanism and Machine Theory*, 45(3):378–391, DOI: 10.1016/j.mechmachtheory.2009.10.001.

Etienne Thalmann

Ch. du Liaudoz 34
1009 Pully, Switzerland
thalmann.etienne@gmail.com
www.linkedin.com/in/ethalmann

EDUCATION	**Ph.D. Candidate in Microengineering**	2017 - 2020

Swiss Federal Institute of Technology (EPFL), *Lausanne, Switzerland*

Title: Flexure Pivot Oscillators for Mechanical Watches.
Supervisors: Prof. Simon Henein and Dr. Ilan Vardi.

M.Sc. in Mechanical Engineering — 2013 - 2015
EPFL, *Lausanne, Switzerland*

Specialization in Control and Mechatronics.
Master's thesis in industry at CSEM SA: *Robust Control of Mechatronic Systems.*

B.Sc. in Mechanical Engineering — 2010 - 2013
EPFL, *Lausanne, Switzerland*

Exchange student at Carnegie Mellon University, Pittsburgh, USA.
Bachelor Thesis: Design of a roof shingling robot.

Scientific Federal Baccalaureate — 2007 - 2010
Gymnase de Chamblandes, *Pully, Switzerland*

Bilingual Bac. French-German. Distinction.

EMPLOYMENT	**Doctoral Assistant**	May 2017 - Present

EPFL, Instant-Lab, *Neuchâtel, Switzerland*

- Conceptual design, modelling, manufacturing, numerical simulation and experimental characterization of flexure pivot oscillators for mechanical watches.
- Lecturer and teaching assistant for undergraduate Design of Mechanisms course.

Scientific Assistant — May 2016 - April 2017
EPFL, Instant-Lab, *Neuchâtel, Switzerland*

- Theoretical and experimental work on 2-DOF flexure-based watch oscillators.
- Development of an energetic theory of mechanical watch escapements.

International Intern — September - December 2015
Sirena Technologies, *Bangalore, India*

- Modelling of a servomotor and design of its position controller.
- Dynamic modelling of a humanoid robot and gait generation.

Mater's Thesis Intern — February - August 2015
CSEM SA, *Neuchâtel, Switzerland*

- Design and testing of a robust control algorithm on a new type of MEMS.
- Design of a control law for the mobile stage of weather satellite interferometer.

151

Research Assistant   August - October 2014
EPFL, STI robotics competition, *Lausanne, Switzerland*

- Development of an Arduino test platform for mechatronic components.
- Writing of a tutorial for students.

Intern   August - September 2013
Constellium Valais SA, *Chippis, Switzerland*

- Machining using mill and lathe.
- Numerical Control of machine tools.

ACADEMIC ACTIVITIES

Lecturer, Design of Mechanisms   November 2017, 2018, 2019
EPFL, *Lausanne, Switzerland*

- Lectures on power transmission.

Student Internship Supervisor
EPFL, *Lausanne, Switzerland*

- Dimensioning and simulation of a flexure pivot oscillator.   Summer 2019
- Fabrication of flexure pivot oscillator mock-ups.   Summer 2019
- Finite element modelling of mechanical oscillators.   Summer 2018
- Mechanical oscillator driven by light.   Summer 2016

Teaching Assistant
EPFL, *Lausanne, Switzerland*

- Design of Mechanisms project (2nd year students). Spring semesters 2017 - 2020
- Design of Mechanisms (2nd year students).   Fall semesters 2016 - 2019
- Probabilities and statistics (2nd year students).   Fall semesters 2013 - 2014
- Linear algebra (1st year students).   Fall semester 2014

Technical Reviewer   2018 - Present
Peer reviewing activities for:

- Mathematical Problems in Engineering (scientific journal).
- ASME International Design Engineering and Technology Conferences.
- Precision Engineering (scientific journal).

HONORS & AWARDS

- Hilti Mechatronics Award: Master's thesis.
- Swiss Society for Automatic Control Award: 2nd prize, Master's thesis.
- 1st prize of the US National Safety Council robotics challenge: Bachelor project.
- Texas Instrument Student Prize 2015: 2nd prize, Embedded systems project.
- College of Engineering Dean's List: 2013, Carnegie Mellon University.
- Best overall results award: Baccalaureate, Gymnase de Chambandes.

PUBLICATIONS

Publications in Peer-reviewed Scientific Journals

Thalmann, E., M. H. Kahrobaiyan, I. Vardi, and S. Henein. 2020. "Flexure Pivot Oscillator With Intrinsically Tuned Isochronism." Journal of Mechanical Design 142 (7). DOI: 10.1115/1.4045388.

Kahrobaiyan, M. H., **E. Thalmann**, L. Rubbert, I. Vardi, and S. Henein. 2018. "Gravity-Insensitive Flexure Pivot Oscillators." Journal of Mechanical Design 140 (7). DOI: 10.1115/1.4039887.

Vardi, I., R. A. Bitterli, L. Convert, **E. Thalmann**, and S. Henein. 2018. "Echappements à Impulsion Virtuelle." Bulletin de La Société Suisse de Chronométrie 85: 25–32. infoscience.epfl.ch/record/255796.

Peer-reviewed Conference Proceedings

Thalmann, E., M. H. Kahrobaiyan, and S. Henein. 2018. "Flexure-Pivot Oscillator Restoring Torque Nonlinearity and Isochronism Defect." Proceedings of the ASME 2018 International Design Engineering Technical Conferences and Computers and Information in Engineering Conference. Quebec City, Quebec, Canada. DOI: 10.1115/DETC2018-85863.

Thalmann, E., Y. Regamey, and A. Karimi. 2016. "High Performance Control of a Corner Cube Reflector by a Frequency-Domain Data-Driven Robust Control Method." In 2016 American Control Conference (ACC), 455–60. DOI: 10.1109/ACC.2016.7524956.

Preprint

Thalmann, Etienne, and Simon Henein. 2019. "Conceptual Design of a Rotational Mechanical Time Base with Varying Inertia." engrXiv. DOI: 10.31224/osf.io/kjhbx.

PATENTS

Kahrobaiyan, M. H., **E. Thalmann**, and S. Henein. 2020. Flexure Pivot Oscillator Insensitive to Gravity, Patent Number: WO2020016131.

Kahrobaiyan, M. H., I. Vardi, S. Henein, B. Nussbaumer, and **E. Thalmann**. 2019. Horological Oscillator, Patent Number: WO2019141789.